Author:
Llewellyn, Dan M

Title:
Quantum Information Processing by Programming Optical Nano-Circuits in Silicon

Quantum Information Processing by Programming Optical Nano-Circuits in Silicon

By

DANIEL LLEWELLYN

Department of Physics
UNIVERSITY OF BRISTOL

A dissertation submitted to the University of Bristol in accordance with the requirements of the degree of DOCTOR OF PHILOSOPHY in the School of Physics of the Faculty of Science.

SEPTEMBER 2020

Abstract

Quantum technologies, able to manipulate the individual quantum states of single particles, have the potential to revolutionise science and engineering. The possible applications of these technologies are remarkably broad, ranging from the simulation of the underlying physics that governs our universe, to securing the worlds information, and even to improving health-care through quantum metrology. Though there are many competing quantum technology platforms, quantum platforms based on light are uniquely fascinating due to their low noise and suitability for communications. Modern fabrication methods allow for the production of chip-scale devices that can trap and manipulate single particles of light (photons) to produce complex quantum states on chip. In particular, silicon photonic devices are of interest due to the abundance and supply chains of silicon in the microelectronics industry. Theoretically, these supply chains could be leveraged to mass produce high performance quantum technologies built from silicon photonic components at scale and low cost.

In this thesis we explore current silicon quantum photonic technologies and their applications. In particular, we asses how they can be leveraged to generate pure single photons and how multiple photons can be reliably interfered on a chip. In addition, we introduce many key integrated quantum optic components and explain how, when combined with high quality single photon sources, they can be used to encode quantum information in silicon chips. Several of the fundamental protocols of quantum information theory are benchmarked on state-of-the-art silicon photonic chips and methods for chip-to-chip demonstrations are proposed and verified. Finally, we discuss the scalability of these devices and outline the technologies that are required in order to advance the field of integrated quantum photonic technologies.

ACKNOWLEDGMENTS

This thesis is dedicated to the many wonderful people in my life. Without their support and guidance these words would not exist.

My time at QETLabs has been an incredible experience and I would like to thank all of the incredible people I have met during this adventure. **Jianwei** - thank you for being a great teacher and an inspiring scientist. Your encouragement and energy helped me to grow even during the most challenging times. From you I have learned a great many lessons that I will always cherish. **Stefano** - thank you for sharing your knowledge with me and providing me with so many moments of sudden insight and discovery. **Imad** - I have learned so much from working with you. Thanks for all of the invaluable discussions and endless perfectionism. Thank you **Ben** for all of the camaraderie, the second lunches in between long lab hours and the many gym sessions. A special thanks to all of those I had the honour of sharing a lab with and the countless others in QETLabs for making my time here so enjoyable.

To my supervisory team. **Mark** - thank you for the endless opportunities you have given me and for inspiring the entire photonics community. **John** - you are the coolest professor I have ever met! Thank you for helping me deliver this thesis. **Jorge** - thank you for all of the great advice you have given me during my PhD. Your feedback has greatly improved this thesis. It has been an honour to work with you all.

Thank you to everyone involved in the UK Quantum Communications Hub for supporting my PhD Research, without you all none of this research could exist.

To my **family** - thank you all for the endless support throughout my education. I could not have written this without you. To **Yolanda** - thanks for sharing this wonderful journey with me. Here's to many more.

Author's declaration

I declare that the work in this dissertation was carried out in accordance with the requirements of the University's Regulations and Code of Practice for Research Degree Programmes and that it has not been submitted for any other academic award. Except where indicated by specific reference in the text, the work is the candidate's own work. Work done in collaboration with, or with the assistance of, others, is indicated as such. Any views expressed in the dissertation are those of the author.

SIGNED: .....

DATE: .....

TABLE OF CONTENTS

LIST OF TABLES

TABLE **Page**

List of Figures

Figure **Page**

CHAPTER 1

INTRODUCTION

Nature is not classical. By this I mean that - when you really take a close look at things - the world just does not behave in ways you might expect. Our expectations of the world around us directly translate from our experiences, which is to say that we expect new things to behave in ways that most other things do. Despite our expectations, the deeper you look into nature, the less we are able to rely on our inherent intuitions. Instead, one must develop brand new intuitions. Mathematics has played a key role in the development of these intuitions throughout history and has led to many physical discoveries. At times, mathematical intuition has even preceded physical observation, for example the discovery of anti-matter predicted by Richard Feynman, or more recently gravitational waves predicted by Albert Einstein. Today mathematics has developed a new sense of intuitions which come together to form the theory of quantum mechanics, which remains (even after a century from its inception) the most complete theory of nature. Quantum mechanics, as well as being very precise, is also remarkably counter intuitive and abstract in its ideas. At its core, quantum physics exists in attempt to interpret all of the peculiarities of nature, from the microscopic scale to the macroscopic.

The study of quantum mechanics has already led to the development of some of humanities greatest achievements, such as transistors that power modern computation, LEDs that enable modern displays, and the laser in which countless modern technologies are derived. Though each of these technologies are profound and widespread, they do not require the direct control of individual quantum systems - rather they leverage the understanding of how many quantum particles interact with one another. In recent decades, the study of quantum information has proposed powerful new technologies

that require the direct control of individual quantum systems that, when combined, will allow previously unobtainable control over nature. These technologies, such as quantum computing that offers an exponential speedup for certain computations, and quantum communications that can secure data and detect eavesdroppers, may one day influence almost all aspects of technology.

In an effort to build such technologies, current research involves a growing number of quantum platforms such as the manipulation of atoms [1], trapped ions [2] and superconductors [3], to name a few. The topic of this thesis focuses on one platform in particular - silicon integrated quantum photonics, where single photon quantum states are embed in silicon optical circuits and programmed through modern semiconductor technology [4–14]. The chosen silicon photonic platform is unique due to its compact form-factor (high component densities), compatibility with existing manufacturing techniques (ability to reach scale), and existing integration of many key quantum optic components [15, 16].

One of the great challenges of manipulating quantum systems is that they tend to decohere over time, meaning that they change by interacting with their environment [17, 18]. One of the more fascinating properties of light is its resistance to this decoherence. After all, even the ≈ 13.8 billion year old cosmic microwave background radiation remains polarised [19]. The exploration of quantum states of light is therefore deeply fascinating and integrated photonics provides a powerful platform for both exploring quantum phenomena and building technologies.

This thesis explores several key concepts of quantum information theory and applies them to integrated silicon photons in order to perform some unique quantum experiments. Each of these experiments are designed to be a proof-of-concept towards practical quantum technologies that operate on single photons, with a particular focus on quantum communications and quantum information processing. In the following section, the main high-level motivations for these applications are introduced.

1.1 Motivations

The emergence of quantum information theory has led to the discovery of many quantum science applications such as quantum communications and quantum computing. Since then, these ideas have developed into large fields of science in their own right. In addition, private companies have even bet big on the adoption of quantum technologies that may play a significant role in many sectors such as quantum computing [20, 21], cyber security [22, 23] and even health care with quantum metrology [24]. The following two sections are designed to give the reader a brief overview of the motivations for

studying the fields of quantum communications and quantum computing, which are the main target of this thesis.

1.1.1 Quantum communications

Modern cyber security relies on cryptography methods such as public key encryption and digital signatures [25]. The main premise behind these security measures is that some problems are hard to solve yet easy to verify. Such problems lend themselves to cryptography, since messages can be easily encrypted but where decryption without a key is computationally hard. An example of which is the multiplication of two large prime numbers p_1 & p_2 that can be easily multiplied together such that $p_1 \times p_2 = m$, but are extremely difficult to factorise where m is known but the two prime numbers are unknown.

The security level of these approaches are typically characterised by assumptions about any adversary, such as the efficiency of their factoring algorithms and computational power. Of course such assumptions have a wide margin of error and so typically very conservative estimates are used. However, encrypted messages that are stored for long periods of time may be later decrypted once advancements are made. As a result, most encrypted data has time-limited security. In addition, the very premise that some problems are one-way hard is an unproven problem in computer science. Not only that, but their existence would imply that polynomial time and non-polynomial time complexity classes are not equal to one another, which is one of the biggest unsolved problems in mathematics and computer science [26, 27].

Two popular public key encryption protocols are named RSA and Elliptic curve that can today be ran efficiently on small processors [25, 28]. Typically today very long 1024-bit or 2048-bit length integers are used to encrypt messages. However, in special cases even 1000-bit integers can today be factorised, requiring university supercomputers running for several months [29]. Moreover, despite the lack of efficient classical factorising algorithm, prime factorisation is efficiently achievable on a fault-tolerant quantum computer via Shor's algorithm [30, 31]. This algorithm has now been experimentally verified on several quantum platforms using small-scale quantum processors, though the exact implementations each used small integer values [32–35]. Today, quantum communications protocols have rigorous security proofs based on the laws of physics, which may present a long term solution to Shor's algorithm [36–41]. It is also important to note that, as an alternative approach, post-quantum classical cryptography protocols have also been developed, where there currently exists no known efficient quantum decryption algorithms [42].

One of the significant challenges in the quantum cryptography approach is that the more secure quantum protocols tend to be demanding in their system requirements, and are either difficult to implement or yield low key-rates [43–45]. Such low key-rates would make them redundant in a world where high internet band-widths are widely adopted, however, some highly secure low key-rate protocols could be implemented for specific tasks. On the contrary, some less resource intensive quantum cryptography protocols provide security proofs that are less secure, meaning that they place more trust in one's devices, where a tampered device may be susceptible to attack [41]. In addition, each of these implementations require the efficient long distance transmission of single (or few) photons, where optical losses play a key role in the limit of key generation rate. Moreover, real life implementations of security protocols don't always fall within the bounds of theoretical modeling, and can be subject to device exploitation [46–50].

1.1.2 Linear Optic Quantum Computing

There is no doubt that advanced computation has revolutionised almost all industries, and today reaches almost every corner of human life. This is largely thanks to the continued progress in fabrication processes that lead to devices that are increasingly compact and yet increasingly capable. However, our current classical approach to computation, from a fundamental physics perspective, is arguably deeply flawed. The fundamental problem becomes increasingly apparent the closer one compares computational approaches with fundamental science. In fact this mismatch between computation and science - which will be briefly elaborate on soon - has been apparent for a long time, for example, Richard Feynman in his 1982 transcript on simulating physics quotes [51]

> "Nature isn't classical, dammit, and if you want to make a simulation of nature, you'd better make it quantum mechanical" - Richard Feynman (1982).

As he here points out, the basic problem is that classical computation methods just aren't very efficient at computing the complexities of quantum mechanics.

For example, suppose that we would like to perform a simulation of how we expect the world may behave, one that is based on quantum mechanics. In addition, suppose we are to investigate a system that is particularly sensitive to errors, where we would ideally like our simulation to match the underlying physics as closely as possible. In this case the initial system may have some initial pure state $|\psi\rangle$ that is composed of

N d-dimensional systems. In addition, suppose that there is some time-dependent Hamiltonian $\hat{H}(t)$ which acts to evolve the state over time through an interaction with the environment.

The fundamental issue is that in order to obtain a precise solution to this arbitrary quantum simulation, the computer should store an order of d^N complex amplitudes in memory. At each time interval, these amplitudes should be updated due to the proposed interaction Hamiltonian $\hat{H}(t)$. In fact, even the discretization of time itself is an approximation that causes an unknown discrepancy between the true underlying physics and the simulation. Even for incredibly small-scale systems, if we would like to have a complete picture of the underlying physics, this simulation becomes infeasible.

Suppose instead that we are no longer interested in the exact underlying physical process but we would like to compute some specific outcome. In this case, one could justify a classical computer who gave some probabilistic outcome that when repeated would on average give the correct quantum probability. In other words this computer would in some way directly calculate outcome probabilities rather than keep track of the underlying evolution's. As Feynman details back in 1982, such a system is infeasible due to the negative probability amplitudes associated with quantum mechanics [51].

The solution, as Feynman suggested, is to attempt to directly construct a quantum mechanical system that we have influence over, and that can simulate the system we are interested in. Since then, quantum computing has become a large field of science and progress has been made on many fronts. For example, the coherent control of quantum systems is an ongoing endeavour in many platforms, such as superconducting qubits [3, 52–54], atoms [1, 55] and photons [4, 12, 56–61]. On the theoretical side, there has been a vast amount of progress on quantum algorithms that are able to solve specific problems, such as Shor's algorithm that can efficiently factorise large integers [30], where no efficient classical counterpart is known. The recent task is to construct quantum architectures that can efficiently scale to produce exponentially larger quantum states on chip-scale devices.

With regards to quantum information processing, this thesis is concerned with the field of linear-optic quantum computing with single photons. Single photons as quantum information carriers have many advantages when compared with other systems. For example, photons possess extremely long coherence times and interact very little with their environment. As a result, they can carry very low noise which is crucial for implementing large-scale quantum computing. It is for this reason that photonic systems are one of the only platforms which can operate at room temperature, where the vast amount of demonstrations require a huge amount of cooling power to

decouple qubits from their environment [62]. In addition, the speed of photons makes them a natural choice for any quantum information processing that requires the transfer of information from one place to another, such as the quantum cryptography or distributed quantum computing [41, 63]. On the contrary, the main sticking point for photonics-based quantum computing is the development of scalable architectures that would allow arbitrary complexity.

In 2001, three researchers that initially set out to prove that efficient quantum computation with photons was infeasible, surprisingly found the exact opposite. In their seminal work, Knill, Laflamme and Milburn (KLM) created a scheme which proved that scalable linear optic quantum computing (LOQC) was indeed possible - where efficient here is defined as requiring a polynomial number of resources [64]. The basis of their work utilised the quantum teleportation protocol (see experimental sections 4.3 and 2.3.2), where the teleportation of quantum operations overcomes the lack of deterministic multi-qubit gates. Since then, a whole host of works have added to this initial demonstration in order to bridge the gap between experimental capabilities and theoretical requirements [65–69]. Despite this progress, experimental limitations such as high losses, low quality single photon sources and imperfect detection still creates a disparity between scalable photonic architectures and today's technology.

The topic of this thesis assesses the current state of the art in silicon integrated photonics in the field of quantum information processing - for applications in quantum communications and quantum computing. In chapter 3 we explore the current limitation of quantum interference in silicon due to impure single photon sources. Then later, we go on to investigate the fidelity to which some of the fundamental building blocks of quantum computation can be explored, for example quantum teleportation. Finally, we explore integrated silicon photonics for quantum communications, where qudits are transmitted between devices - which may lead the way for future multi-chip architectures. For example, the remote preparation of initial states may lead to information security in distributed quantum systems such as blind quantum computing [70]. By engineering significantly more advanced integrated photonic systems, the gap between theoretical requirements and real-world device performance will continue to close. In the following section, a chapter-by-chapter breakdown is given in order to guide the reader to area's of their particular interest.

1.2 Thesis Outline

This thesis consists of six chapters, the structure of which is outlined in the following summary.

- **Chapter 2** attempts to provide all essential background information that may guide the reader in understanding the work that is contained in the later chapters. In addition, this chapter will aim at providing key contexts and motivations for the chapters it precedes. In particular, it begins by explaining the fundamentals of quantum information and quantum photonics, as well as introduces some key motivators for quantum technologies - with a focus on the areas where photons are particularly practical. Next this chapter focuses on the platform in which this thesis is based, integrated silicon quantum photonics, and introduces the key technologies in order to understand the experiments introduced within the later chapters.

- Next, **chapter 3** attempts to benchmark current integrated quantum silicon photonic technologies with a focus on the device performance of key quantum photonic components in silicon. In particular, we benchmark the integrated components in the devices used during the experiments of this thesis, which are manufactured at the Technical University of Denmark (DTU). Secondly, we focus on one key aspect of integrated quantum technologies based on photons - the single photon sources. The integrated single photon sources used during this thesis are compared with current state-of-the-art, and context is given as to how these sources should perform for future quantum technology development. Finally, a framework is given to which quantum information experiments can be run by utilising the integrated silicon platform based on imperfect single photon sources and thermally controlled linear optic components.

- **Chapter 4** utilises a four-qubit integrated photon circuit to experimentally demonstrate some of the fundamental building blocks of optical quantum technologies. The goal of this chapter is to construct a toolbox of quantum capabilities that can be applied to diverse applications in an integrated platform, and to give hope for future approaches. We begin with one of the most fundamental concepts in quantum information, quantum bipartite entanglement, and then move on to test the current limits of the technology. We end with the aim to convince the reader that photonics is both a compelling and unique platform for quantum science the subsequent development of technologies.

- Finally, **chapter 5** combines the previous work to demonstrate the practical challenges of quantum communications in an integrated quantum photonic platform that uses heralded single photons. We begin by transmitting small quantum systems between chips and later expand to show the transfer of higher

dimensional quantum states - opening the door to more complex communications protocols and network demonstrations. This chapter shows that integrated photonics, not without its current flaws, is a great platform to explore the foundations of science and to develop its technologies.

- **Chapter 6** draws together the main insights from each of the previous chapters and provides the thesis conclusions.

CHAPTER 2

INTRODUCTION TO QUANTUM INFORMATION THEORY AND INTEGRATED SILICON PHOTONICS

2.1 Quantum Information

Quantum information science is the study of information in the framework of quantum mechanics. Since information is physical, meaning that it is encoded in physical systems that obey the laws of physics, it is feasible to imagine that quantum phenomena should have a direct influence on information storage itself. Quantum information theory incorporates key concepts from quantum science, such as entanglement and superposition, into information theory in order to explore the vast capabilities of communication and computation. In this chapter, we explore the background material necessary to understand the key concepts of this thesis that are a combination of quantum mechanics, quantum information and quantum photonics.

2.1.1 Hilbert Spaces & Dirac Notation

The purpose of this section is to familiarise the reader with the foundational principles of quantum mechanics, where the following material forms a prerequisite to the quantum information theory subjects that lie ahead. Suppose we want to describe the properties of a pure isolated quantum system A. In quantum physics, all that can be known about this pure quantum system is represented by a normalised vector, denoted as a 'ket' in Dirac notation as $|\psi\rangle$. Here ψ is the label that refers to the vector we are interested in. The vector $|\psi\rangle$ lives within the systems Hilbert space H that

contains the set of all orthonormal (orthogonal and normalised) vectors that the state could be measured in. In addition, the vector dual space lives within the Hilbert space, where the dual vector is written as a 'bra' in Dirac notation, $\langle\psi| \equiv |\psi\rangle^\dagger$, where the † operation transforms between the two spaces. Here the † operation is defined as the conjugate transpose $|\psi\rangle^\dagger \equiv |\psi\rangle^{*T}$.

Moreover, there is a well-defined inner and outer product, where the inner product between two vectors $|\phi\rangle$ and $|\psi\rangle$ produces a complex number and is written as

$$|\phi\rangle^\dagger |\psi\rangle \equiv \langle\phi||\psi\rangle \equiv \langle\psi||\phi\rangle^* \qquad \text{Inner Product.} \tag{2.1}$$

The inner product between two orthonormal vectors $\langle\phi||\psi\rangle$ reads 1 where $\phi \equiv \psi$ and 0 otherwise. In contrast, the outer product between two vectors $|\phi\rangle$ and $|\psi\rangle$, written as

$$|\phi\rangle |\psi\rangle^\dagger \equiv |\phi\rangle \langle\psi| \qquad \text{Outer Product,} \tag{2.2}$$

which produces an operator that can act on a vector to product another vector. For example, where the two vectors are orthonormal the above outer product acts on the state $|\psi\rangle$ to give

$$|\phi\rangle \langle\psi||\psi\rangle = |\phi\rangle . \tag{2.3}$$

It is often necessary to describe the behavior of multiple quantum systems, such as systems of many particles. The combined Hilbert space of two or more systems is the tensor product between them. For example, for systems A and B, each with their respective spaces H_A and H_B, have a combined space that is defined as $H_A \otimes H_B$. The tensor product between two vectors $|\phi\rangle$ and $|\psi\rangle$ is written $|\phi\rangle_A \otimes |\psi\rangle_B$, or often in shorthand as $|\phi,\psi\rangle_{A,B}$.

2.1.2 Superposition

Quantum superposition is one of the most interesting features of quantum mechanics, which states that the quantum state of a system may actually be the coherent sum of orthonormal states. In general this is achieved by assigning a complex amplitude α_i to each of the normalised Hilbert space vectors $\{\,|\,i\rangle\}$, where the state of a system may be in the state $|\psi\rangle$

$$|\psi\rangle = \sum_{\forall i} \alpha_i |i\rangle . \tag{2.4}$$

The probability that $|\psi\rangle$ is measured in any particular state $|i\rangle$ is given by the absolute value squared of the complex amplitude $P_i = |\alpha_i|^2$. Thus the list of complex amplitudes $\{\alpha_i\}$ give rise to a probability distribution of states $\{\,|\,\alpha_i|^2\}$, who's sum must be

normalised

$$\sum_{\forall i} |\alpha_i|^2 = 1. \tag{2.5}$$

2.1.3 Measurement

In quantum mechanics, measurements of a system are achieved through physical observables, $\hat{M}$, which take the form of Hermitian (self-adjoint) operators, where $\hat{M}^\dagger = \hat{M}$. The role of these observables is to lay out all possible measurement outcomes, which correspond to the eigenvalues λ_i of $\hat{M}$, as well as the eigenstates $\{ |i\rangle \}$ that correspond to the possible measurement outcomes. When written in terms of the eigenvalues and vectors, $\hat{M}$ is written in its spectral decomposition as

$$\hat{M} = \sum_{\forall i} \lambda_i |i\rangle \langle i|, \tag{2.6}$$

where $|i\rangle \langle i|$ are referred to as the projectors $\hat{P}_i$ onto the eigenstate $|i\rangle$. These projectors are themselves operators that have the following properties $P_i^2 = P_i$, $P_i^\dagger = P_i$ and $\sum_i P_i = \hat{I}$. When written in its spectral decomposition, one can see that the enforcement that $\hat{M} = \hat{M}^\dagger$ is really a statement about its eigenvalues, since

$$\begin{aligned} \hat{M}^\dagger &= \Big(\sum_{\forall i} \lambda_i |i\rangle \langle i| \Big)^\dagger \\ &= \sum_{\forall i} \lambda_i^* |i\rangle \langle i|^\dagger \\ &= \sum_{\forall i} \lambda_i^* |i\rangle \langle i|. \end{aligned} \tag{2.7}$$

As a result, $\hat{M}$ only equals its adjoint when all of its eigenvalues are real and therefore they must satisfy the condition $\lambda_i = \lambda_i^*$. Since the eigenvalues of $\hat{M}$ correspond to the possible measurement values, it is crucial that these values are all real numbers.

Once a given system in state $|\psi\rangle$ is measured with the observable $\hat{M}$, the state after measurement is collapsed onto the corresponding eigenvector. For example, if the measurement outcome is λ_i then the state after the measurement is $|i\rangle$. The probability of this measurement outcome is computed as the absolute value square of the inner product between the eigenvector $|i\rangle$ and $|\psi\rangle$, $p_i = |\langle i|\psi\rangle|^2$. Once the state has collapsed onto the eigenstate $|\psi\rangle \rightarrow |i\rangle$, the subsequent measurement probability of outcomes λ_j is $\delta_{i,j}$.

2.1.4 Quantum Interference

Take the two superposition states $|\psi\rangle = \sum_{\forall i} \alpha_i |i\rangle$ and $|\phi\rangle = \sum_{\forall i} \beta_i |i\rangle$. The probability that each superposition state is measured in the i^{th} state is given by their square

amplitudes $|\alpha_i|^2$ and $|\beta_i|^2$. Therefore one might assume that the probability that each gives the same outcome is the sum of the overlapping amplitudes, i.e.

$$\sum_{\forall i} |\alpha_i|^2 |\beta_i|^2 \leq 1, \tag{2.8}$$

which is consistent with our classical expectation. For example, during the roll of two six-sides die, the probability that the same number arises should be 1/6. We are sure of this since the two outcomes are independent from one another. Therefore given any outcome on the first dice, there is a 1/6 probability that the same outcome occurs on the second. Mathematically, this could be calculated is $P(j = i) = \sum_1^6 (1/6)^2 = 1/6$. This value could be obtained for the quantum state by individually measuring the observable $|i\rangle\langle i|$, which would yield the individual outcome probabilities. By summing over these combined outcomes for the two states, one would arrive at a value predicted by equation 2.8.

However, quantum mechanically, the probability that one state is found in the other is obtained by the absolute value squared of the inner product between the two states, and predicts the following

$$|\langle\phi||\psi\rangle|^2 = \Big|\sum_{\forall i} \beta_i^* \alpha_i\Big|^2. \tag{2.9}$$

Here one finds that the probability depends on the sum of complex numbers, and where the arguments of those complex numbers directly affects the measurement outcome. It is a direct consequence of these complex arguments that gives rise to quantum interference, where measurable outcome probabilities are constructively or destructively altered in ways that cannot be explained classically. This is one of the most fascinating and counter-intuitive aspects of quantum mechanics that occurs as a direct consequence of quantum superposition. The practical and powerful aspects of quantum interference will be highlighted in every chapter of this thesis.

2.1.5 Qubits & Qudits

So far in our discussions we have introduced Hilbert spaces of arbitrary dimensions, however, for many systems there is a well-defined number of orthonormal states that may characterise a system. An example of this is the polarisation of a photon, which has two orthonormal state vectors corresponding to horizontal $|H\rangle$ and vertical $|V\rangle$ polarisation. Quantum systems of this form, which have just two dimensions, are referred to as qubits, i.e. quantum bits. Qubits are a natural representation of quantum information since they allow a natural transition from classical information, encoded in bits of information, to a quantum setting. However, in general, d-dimensional

systems are referred to as qudits in this thesis and are discussed more heavily in chapter 5.

In principle, many systems can be confined to just two modes such as spatial mode, spin and orbital angular momentum, to name a few. In order to keep our discussion general, we will often use the state labels '0' and '1' when referring to qubits. As such, a general qubit can be written as a superposition of these two states

$$|\psi\rangle = \alpha\,|0\rangle + \beta\,|1\rangle\,, \tag{2.10}$$

where $|\psi\rangle$ is normalised such that $\langle\psi||\psi\rangle = 1$, which also gives $|\alpha|^2 + |\beta|^2 = 1$. In quantum information theory, a basis is a set of d orthonormal vectors that span the entire Hilbert space of a given system. As a result, the above state does not have to be written in terms of the $|0\rangle$ and $|1\rangle$ states at all, and can be written in any basis.

To see some frequent examples, consider the three Pauli spin matrices that are defined as follows

$$\hat{\sigma}_z = \begin{pmatrix} 1 & 0 \\ 0 & -1 \end{pmatrix}, \qquad \hat{\sigma}_x = \begin{pmatrix} 0 & 1 \\ 1 & 0 \end{pmatrix}, \qquad \hat{\sigma}_y = \begin{pmatrix} 0 & -i \\ i & 0 \end{pmatrix}, \tag{2.11}$$

where we have used the vector representation of the spin matrices, and where the states $|0\rangle \to (1,0)^T$ and $|1\rangle \to (0,1)^T$. The eigenvalues for each matrix are ± 1 with corresponding eigenvectors $|0/1\rangle$, $|\pm\rangle = (|0\rangle \pm |1\rangle)/\sqrt{2}$ and $|\pm i\rangle = (|0\rangle \pm i\,|1\rangle)/\sqrt{2}$ for $\hat{\sigma}_z$, $\hat{\sigma}_x$ and $\hat{\sigma}_y$, respectfully. The $\hat{\sigma}_z$ eigenstates $|0/1\rangle$ will often be referred to in this thesis as the *computational basis*. Therefore, when written in their spectral decomposition, each matrix reads

$$\begin{aligned} \hat{\sigma}_z &= |0\rangle\langle 0| - |1\rangle\langle 1|\,, \\ \hat{\sigma}_x &= |+\rangle\langle +| - |-\rangle\langle -|\,, \\ \hat{\sigma}_y &= |+i\rangle\langle +i| - |-i\rangle\langle -i|\,. \end{aligned} \tag{2.12}$$

Each of these pairs of eigenvectors form a set of orthonormal basis vectors, for which the state $|\psi\rangle$ can be written. As an example, consider the following basis transformation $|0\rangle = (|+\rangle + |-\rangle)/\sqrt{2}$ and $|1\rangle = (|+\rangle - |-\rangle)/\sqrt{2}$ the state would read

$$|\psi\rangle = \frac{\alpha+\beta}{\sqrt{2}}\,|+\rangle + \frac{\alpha-\beta}{\sqrt{2}}\,|-\rangle\,. \tag{2.13}$$

Finally, the state rewritten in the basis of $\hat{\sigma}_y$ eigenvectors is as follows

$$|\psi\rangle = \frac{\alpha - i\beta}{\sqrt{2}}\,|+i\rangle + \frac{\alpha + i\beta}{\sqrt{2}}\,|-i\rangle\,. \tag{2.14}$$

The act of rewriting a state in a different choice of basis allows for the easy calculation of measurement outcomes. For example, consider the state $|+\rangle$ as defined above,

where $\alpha = \beta = 1/\sqrt{2}$. Clearly, in the computational basis there is a 50% probability of each outcome, which is calculated as $P_0 = |1/\sqrt{2}|^2$ and $P_1 = |1/\sqrt{2}|^2$. When written in the $\hat{\sigma}_x$ basis, the state is an eigenstate $|+\rangle$ and so the corresponding probabilities are $P_+ = 1$ and $P_- = 0$. Finally, for the $\hat{\sigma}_y$ basis we have, $|+\rangle = (1-i)/2\,|+i\rangle + (1+i)/2\,|-i\rangle$ giving the measurement probabilities $P_{+i} = 1/2$ and $P_{-i} = 1/2$. Notice that the chosen state was an eigenstate of the $\hat{\sigma}_x$ basis, and when measured in the other two Pauli bases each outcome was equally likely. This observation turns out to be true for any of the Pauli eigenstates, that when measured in one of the other Pauli basis, each outcome is equally likely. Sets of basis for which this is true are referred to as *mutually unbiased* bases and are key in many quantum information concepts such as quantum key distribution which is discussed later in this thesis.

2.1.6 Mixed States

So far we have discussed only pure quantum states, but in general a system may emit a statistical mixture of quantum states of dimension d. Mixed quantum states of this form are mathematically represented by a $d \times d$ density matrix (also referred to as a density operator) ρ where in general

$$\rho = \sum_{\forall i} p_i \,|i\rangle\langle i| \tag{2.15}$$

where $|i\rangle\langle i|$ is the projector onto the i^{th} basis state with probability p_i. A density matrix is normalised such that the sum of its diagonal elements is 1, $\text{Tr}\rho = 1$.

Consider a quantum state emitter that outputs pure quantum states such that with 50% probability $|0\rangle$ is prepared and the remaining 50% of time time $|1\rangle$ is prepared. In the example above, the given density matrix is therefore

$$\rho = \frac{1}{2}|0\rangle\langle 0| + \frac{1}{2}|1\rangle\langle 1|. \tag{2.16}$$

Suppose that during each emission the state is measured in a particular basis, in general the basis vectors are $|\alpha \pm \beta\rangle \equiv \alpha|0\rangle \pm \beta|1\rangle$. When measured in this basis, the outcome probabilities are the following in the case where the emitted state is $|0\rangle$

$$P(|\alpha+\beta\rangle\,||0\rangle) = |\alpha|^2 \qquad P(|\alpha-\beta\rangle\,||0\rangle) = |\alpha|^2, \tag{2.17}$$

and likewise for the case where $|1\rangle$ is the emitted state

$$P(|\alpha+\beta\rangle\,||1\rangle) = |\beta|^2 \qquad P(|\alpha-\beta\rangle\,||1\rangle) = |\beta|^2. \tag{2.18}$$

The overall probability of measuring each eigenvector can be computed from the above conditional probabilities in the following way

$$
\begin{aligned}
P(|\alpha+\beta\rangle) &= P(|\alpha+\beta\rangle\,||0\rangle)\,P(|0\rangle) + P(|\alpha+\beta\rangle\,||1\rangle)\,P(|1\rangle) \\
&= (|\alpha|^2+|\beta|^2)/2 \\
&= 1/2 \\
P(|\alpha-\beta\rangle) &= P(|\alpha-\beta\rangle\,||0\rangle)\,P(|0\rangle) + P(|\alpha-\beta\rangle\,||1\rangle)\,P(|1\rangle) \\
&= (|\alpha|^2+|\beta|^2)/2 \\
&= 1/2.
\end{aligned}
\tag{2.19}
$$

As a result, we find that the outcome probabilities of each eigenvector are unbiased (50%) for any possible measurement setting. Statistical mixtures of states that have this property are referred to as *maximally mixed*, and occur only when the density matrix that describes them equals the identity matrix up to a normalisation

$$\rho_{max} = \frac{1}{d}\hat{I}_d. \tag{2.20}$$

In direct contrast, a pure quantum state can be represented as a density matrix with only one nonzero element, i.e. $|0\rangle \rightarrow \rho_0 = |0\rangle\langle 0|$. A useful measure of the amount of mixture is the *purity* of a quantum state which is mathematically defined as

$$P(\rho) = \mathrm{Tr}(\rho^2). \tag{2.21}$$

Pure quantum states obtain a purity value of 1, while maximally mixed states evaluate as $1/d$.

For an observable $\hat{A}$ that has eigenvalues λ_i and eigenvectors $|i\rangle$, the probability that each state is found in any particular eigenvector is the following

$$p_i = \mathrm{Tr}(|i\rangle\langle i|\,\rho), \tag{2.22}$$

which is equivalent to $\langle i|\,\rho\,|i\rangle$, since the trace can be taken in any basis. The expectation value of the operator is as follows

$$\langle\hat{A}\rangle = \mathrm{Tr}(\hat{A}\rho). \tag{2.23}$$

2.1.7 State Fidelity

Suppose you purchase a quantum machine that outputs quantum states at a specified time interval, T. The machine is designed such that you may specify exactly which state is to be output, but you are told by the manufacturer that there is some error on

the state. In principle, the state that is output from the machine will be a statistical mixture that can be represented by the density matrix ρ. You may ask, what is the meaning of this manufacturer error and what is a sensible mathematical measure to represent it. There are many such measures in quantum information science, but in this thesis we focus on one in particular, fidelity. The fidelity between a target state σ and measured output state ρ is defined as

$$F(\rho,\sigma) = \left(\mathrm{Tr}\sqrt{\sqrt{\sigma}\,\rho\sqrt{\sigma}}\right)^2. \tag{2.24}$$

However, in this thesis we are primarily interested in target states that are pure quantum states $|\psi\rangle$. Under this condition, the target state may be written $\sigma = |\psi\rangle\langle\psi|$ where, crucially, $\sqrt{\sigma} = \sqrt{|\psi\rangle\langle\psi|} = |\psi\rangle\langle\psi|$. Under this condition

$$\begin{aligned} F(\rho,\sigma) &= \left(\mathrm{Tr}\ \sqrt{|\psi\rangle\langle\psi|\,\rho\,|\psi\rangle\langle\psi|}\right)^2 \\ &= \left(\mathrm{Tr}\ \sqrt{\langle\psi|\,\rho\,|\psi\rangle}\,|\psi\rangle\langle\psi|\right)^2 \\ &= \langle\psi|\,\rho\,|\psi\rangle\,. \end{aligned} \tag{2.25}$$

This evaluates, and can be interpreted, as the probability that the measured state is observed in the target state.

2.2 Quantum States of Light

The following material summarises some of the key states of light which are discussed in this thesis. A basic understanding of this material is necessary for the later chapters and will aid those readers with less background in quantum optics. For more in-depth discussions on these topics it is recommended for the reader to look at the following textbook chapters [71] (chapter 2) and [72–74] (chapters 1-3). We then go on to summarise how some of these states can be approximated on-chip and give a brief discussion as to which requirements are met and which require the most work.

2.2.1 Single Photons & Fock States

Identical single photons are mathematically represented in the Fock basis as the state $|n\rangle_i$, which represents n identical single photon excitation's in the electromagnetic field, each in the i^{th} mode. The absence of photons in a particular mode is often represented by the vacuum state $|\mathrm{vac}\rangle$ which is equivalent to the state $|0\rangle_i$. This particular basis is not to be confused with the logical bases that are also represented by numbered quantum states $|i\rangle$. The use of the Fock basis should be clear from the

context of which the states are introduced, however, where it is not clear the basis choice will be explicitly stated in this thesis.

Photons in any particular mode can be introduced via the creation operator denoted $\hat{a}_i^\dagger$, which acts on the i^{th} mode to increment the number of identical single photons, i.e.

$$\hat{a}_i^\dagger |n\rangle_i = \sqrt{n+1}\,|n+1\rangle\,. \tag{2.26}$$

The annihilation operator is the hermitian conjugate of the creation operator, and acts to lower the number of single photons in the following way

$$\hat{a}_i |n\rangle_i = \sqrt{n}\,|n-1\rangle\,. \tag{2.27}$$

When combined as $\hat{a}_i^\dagger \hat{a}_i$ these two operators form the number operator $\hat{N}_i$ whose eigenvalues are the number of photons in the i^{th} mode. This can be seen from the following

$$\begin{aligned} \hat{N}_i |n\rangle_i &= \hat{a}_i^\dagger \hat{a}_i |n\rangle_i \\ &= \hat{a}_i^\dagger \sqrt{n}\,|n-1\rangle \\ &= n\,|n\rangle\,. \end{aligned} \tag{2.28}$$

In the following sections we will attempt to categorise some of the key states of light based on their measurement statistics, and give a few examples of states that are mathematically represented in terms of the Fock basis.

2.2.2 Counting statistics

In the late nineteenth century (1887) it was observed by Heinrich Hertz that ultraviolet light incident on a metal plate would emit electrons in a discrete manor. Although, it was not until almost 20 years later (1905) that Einstein advanced the theory of the photoelectric effect to include the quantisation of the electromagnetic field. In modern physics, it is well understood that the behaviour of light is such that it comes in discrete packets, called photons, which have well-defined energy levels depending on the photon argular frequency ω, where $E = \hbar\omega$. But when looking from a historical viewpoint, this has not always been obvious, due to the difficulty of untangling the quantisation of the measurement from the fundamental properties of light. In this way, it is often possible to construct semi-classical theories of light (quantisation of measurement but not EM field) which give rise to the correct outcomes for most experiments. In this chapter, and since hindsight is 20/20[1], the discussions will proceed in an order whereby we

[1]Experiments that cannot be explained by semi-quantum theories are well-known today, such a Hong-Ou-Mandel Interference

discuss the quantum photonic states based on their measurement statistics. In the following we make three main distinctions, firstly where the photon counting statistics follow a poissonian distribution, giving rise to a standard deviation in time that is the square root of the mean, $\sigma = \sqrt{\bar{n}}$. Or secondly, whether the photon arrival times are broader (super-poissonian, $\sigma > \sqrt{\bar{n}}$), and finally where the distribution is narrower (sub-poissonian, $\sigma < \sqrt{\bar{n}}$) than the poissonian distribution. For each case we give an example of a state which follows these statistics and in order to give context to the chapters that follow. A example of these counting statistics with a mean of $\bar{n} = 25$ can be seen in figure 2.1.

2.2.2.1 Coherent States & Poissonian Counting Statistics

Here we show that poissonian counting statistics arise from a perfectly stable (fixed power), coherent stream of photons. Say that such a source of photons emits $\bar{n}$ photons per second, and that $\bar{n}$ is sufficiently large such that the mean is a well-known integer value. In a single second, there will be a beam of length $L \approx 3 * 10^8 m$ containing on average $\bar{n}$ photons. Consider partitioning the beam into N sections where $N \gg \bar{n}$ such that only a small number of partitions contain a photon. In this case, it is natural to assume that the probability of any partition containing two or more photons is negligible, and exactly zero in the limit of large N.

In this circumstance, we have a probability $p = \bar{n}/N$ that a photon is in any individual partition, and probability $q = 1 - p = 1 - \bar{n}/N$ that the partition is empty. We ask ourselves, what is the probability that there are n photons (in any order) in the N partitions, which follows the well-known binomial distribution

$$P(n) = \lim_{N\to\infty} \left[\frac{N!}{n!(N-n)!} p(N,\bar{n})^n q(N,\bar{n})^{N-n} \right], \tag{2.29}$$

which becomes

$$P(n) = \lim_{N\to\infty} \left[\frac{N!}{n!(N-n)!} \left(\frac{\bar{n}}{N}\right)^n \left(1 - \frac{\bar{n}}{N}\right)^{N-n} \right], \tag{2.30}$$

for our specific case. Note that here we take the limit of large N due to the assumption that $N \gg \bar{n}$ for any finite $\bar{n}$. This is also required in the assumption that $p^2/p = \bar{n}/N \to 0$. In order to determine the limit, one can notice that

$$\begin{aligned} \lim_{N\to\infty} \frac{N!}{N^n(N-n)!} &= \lim_{N\to\infty} \frac{N(N-1)(N-2)\ldots(N-n+1)}{N^n} \\ &= \lim_{N\to\infty} \frac{N}{N}\left(1-\frac{1}{N}\right)\ldots\left(1-\frac{n+1}{N}\right) \\ &= 1 \end{aligned} \tag{2.31}$$

and

$$\begin{aligned}\lim_{N\to\infty}\left(1-\frac{\bar{n}}{N}\right)^{N-n} &= \lim_{N\to\infty}\left(1-\frac{\bar{n}}{N}\right)^{-n}\left(1-\frac{\bar{n}}{N}\right)^{N} \\ &= 1.\left(1-\bar{n}+\bar{n}^2/4+\ldots\right) \\ &= e^{-\bar{n}}.\end{aligned} \tag{2.32}$$

The result is the following,

$$P(n) = \frac{\bar{n}^n e^{-\bar{n}}}{n!}, \tag{2.33}$$

giving rise to poissonian counting statistics with well-known standard deviation $\sigma = \sqrt{\bar{n}}$.

A stable coherent-wave laser is such a system that gives rise to Poissonian counting statistics. At constant power and centre wavelength, such a sources gives rise to a constant stream of photons emitted in the i^{th} energy eigenstate. The quantum state which represents this is the coherent state $|\alpha\rangle_k$, written in the Fock basis as follows [75]

$$|\alpha\rangle_i = e^{-|\alpha|^2/2}\sum_{n=0}^{\infty}\frac{\alpha^n}{\sqrt{n!}}|n\rangle_i\,. \tag{2.34}$$

The probability that n photons are detected within a coherent state is calculated via the following inner product

$$p_n = |\langle n||\alpha\rangle|^2 = e^{-|\alpha|^2}\frac{\alpha^{2n}}{n!} \tag{2.35}$$

which gives rise to a Poissonian probability distribution in the photon number with mean $\bar{n} = |\alpha|^2$.

2.2.2.2 Thermal States & Super-Poissonian Counting Statistics

Here we show that thermal light, i.e. light which 'thermalises' through the interaction with matter, is an example of super-Poissonian light that has a broader distribution than the Poissonian case. Take the energy levels for the quantum harmonic oscillator at angular frequency ω,

$$E_n = (n+\frac{1}{2})\hbar\omega, \tag{2.36}$$

which describes the an n-photon ($0 \leq n < \infty$) excitation in a particular mode at the angular frequency ω. The probability of each energy is given by the Boltzmann law,

$$\begin{aligned} P_\omega(n) &= \frac{e^{-E_n/k_BT}}{\sum_m e^{-E_m/k_BT}} \\ &= \frac{e^{-(n+\frac{1}{2})\hbar\omega/k_BT}}{\sum_m e^{-(m+\frac{1}{2})\hbar\omega/k_BT}} \\ &= \frac{(e^{-\hbar\omega/k_BT})^n}{\sum_m (e^{-\hbar\omega/k_BT})^m} \\ &= x^n(1-x), \end{aligned} \tag{2.37}$$

where we have used the geometric properties of the substitution $x \equiv e^{-\hbar\omega/k_BT}$, and that the exponent is always negative. In order to rewrite the probabilities in terms of the average number of photons, we can calculate the expectation value:

$$\begin{aligned} \bar{n}_\omega &= \sum_{n=0}^{\infty} nP_\omega(n) \\ &= \sum_{n=0}^{\text{inf}} nx^n(1-x) \\ &= (1-x)x\frac{\mathrm{d}}{\mathrm{d}x}\Big(\sum_{n=0}^{\text{inf}} x^n\Big) \\ &= (1-x)x\frac{\mathrm{d}}{\mathrm{d}x}\Big(\frac{1}{1-x}\Big) \\ &= \frac{x}{1-x} \\ &= \frac{1}{e^{\hbar\omega/k_BT}-1}, \end{aligned} \tag{2.38}$$

giving the Planck formula. Combining equations 2.37 and 2.38 allows us to write the probability that a particular state is occupied in terms of the average photon number $\bar{n}_\omega$,

$$P_\omega(n) = \frac{1}{\bar{n}_\omega + 1}\Big(\frac{\bar{n}_\omega}{\bar{n}_\omega + 1}\Big)^n. \tag{2.39}$$

These statistics are represented by a statistical mixture of quantum states which can be written in the Fock basis for the frequency ω as [75, 76]

$$\rho_\omega = \frac{\bar{n}_\omega^n}{(\bar{n}_\omega + 1)^{n+1}} |n\rangle \langle n| \tag{2.40}$$

2.2.2.3 Squeezed States & Sub-Poissonian Counting Statistics

As mentioned above, sub-poissonian counting statistics arise when the standard deviation in the number of photons over a particular time-period are smaller than

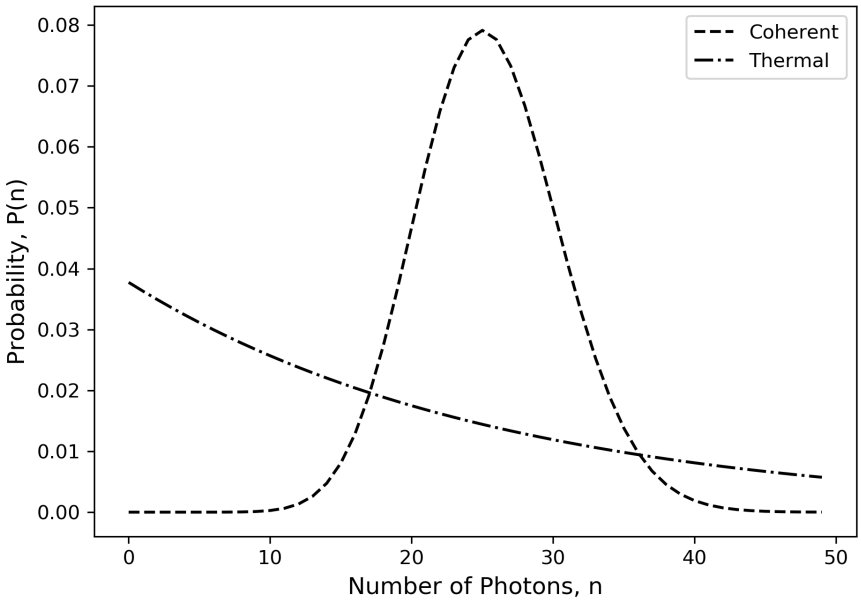

Figure 2.1: A direct comparison of the counting statistics of thermal light (single mode, $\hbar\omega$) compared with a coherent beam for the same average photon number $\bar{n} = 25$.

the square root of the mean, $\sigma < \sqrt{\bar{n}}$. Light with such statistics is referred to as squeezed light, of which there is no classical analogue. The limiting case of this is extremely intuitive, and arises when there is a constant stream of photons at a time interval T. In this instance the measured photon counts over a given time period will remain constant and so the variance will be exactly equal to zero. Quantum photonic states that exhibit lower variance than the coherent state are referred to as squeezed states. Mathematically, squeezed states obey the following mathematical condition. Suppose that two operators $\hat{A}$ & $\hat{B}$ obey the commutation relation $[\hat{A},\hat{B}] = i\hat{C}$, then the following condition holds in terms of the two variances V_A, V_B [77]

$$V_A V_B \geq \frac{1}{4}|\langle\hat{C}\rangle|^2. \tag{2.41}$$

A state is said to be squeezed if either variance obeys one the following inequalities

$$V_A \leq \frac{1}{2}|\langle\hat{C}\rangle| \qquad V_B \leq \frac{1}{2}|\langle\hat{C}\rangle|, \tag{2.42}$$

which can be true for only one of the variances at a time. In the cases of the coherent state and vacuum state, which have been discussed above, each have equal variances where $V_A, V_B = \frac{1}{2}|\langle\hat{C}\rangle|$. Squeezed states are therefore surprising since they can exhibit smaller variances than even the vacuum state and are considered truly quantum, where there is no classical analogue.

Two types of squeezed state are typically considered in quantum optic experiments, the first of which is the single-mode squeezed state (SMS State) which is represented by the parameter $\zeta = re^{i\theta}$ where r is referred to as the squeezer strength $0 \leq r < \infty$, where

$$\hat{S}_{\text{SMS}}(\zeta) = \exp\left[\frac{1}{2}\left(\zeta^* \hat{a}^2 - \zeta \hat{a}^{\dagger 2}\right)\right]. \tag{2.43}$$

However, in this thesis we are concerned primarily with the twin-mode squeezed state (TMS State) who's operator is as follows

$$\hat{S}_{\text{TMS}}(\zeta) = \exp\left[\frac{1}{2}\left(\zeta^* \hat{a}\hat{b} - \zeta \hat{a}^\dagger \hat{b}^\dagger\right)\right], \tag{2.44}$$

which acts to emit spectrally non-degenerate photon pairs where $\hat{a}$ and $\hat{b}$ are the operators for those modes. This twin-mode squeezer acts on the vacuum state $|0\rangle_a |0\rangle_b \equiv |0,0\rangle$ to give [77]

$$\begin{aligned} \hat{S}_{\text{TMS}}(\zeta)|0,0\rangle &\equiv |\zeta\rangle_2 \\ &= \frac{1}{\cosh r} \sum_{n=0}^{\infty} (-1)^n e^{in\theta} (\tanh r)^n |n,n\rangle . \end{aligned} \tag{2.45}$$

In the following sections, we make the substitution $x \equiv e^{i(\theta+\pi)} \tanh r$, where $\text{sech} r = \sqrt{1-\tanh^2 r}$ and gives

$$|\zeta\rangle_2 = (1-|x|^2) \sum_{n=0}^{\infty} x^n |n,n\rangle . \tag{2.46}$$

A discussion on how these states are used to approximately encode qubits on chip is given in chapter 3 and expanded in chapter 4. Finally, the discussion is extended to qudit states in chapter 5.

2.2.3 Spontaneous Four-wave Mixing Sources

Spontaneous four-wave mixing (SFWM) is an optical non-linear process whereby pairs of photons may be emitted spontaneously (with a given probability p) from a non-linear medium via the absorption of a photon-pair, i.e. two photons from the pump field. In this case, for two identical absorbed photons, the energies of the emitted photons are non-degenerate and conserve energy. The reverse process is also possible, this time where the non-degenerate pairs of photons are absorbed by the material and two identical (same colour) photons are produced.

Due to the lack of $\chi^{(2)}$ non-linearity in silicon, the more efficient non-linear process parametric down conversion is not available in integrated silicon photonics. However,

silicon has a relatively high $\chi^{(3)}$ response, which gives rise to the SFWM effect. This means that single photons can be successfully generated on-chip, given a strong enough pump field. Due to the emission of signal and idler pairs of photons during this process, two types of encoding are possible. Either both of the generated photons inside of the waveguides can be used to encode quantum information as two photons (i.e. two qubits), or one of the photon pairs can be used as a trigger in order to declare the presence of the second photon. The latter technique is referred to as a heralded single photon source (HSPS) in this thesis. A HSPS may be particularly useful in many scenarios since the SFWM mechanism is inherently probabilistic, it is therefore often necessary to infer the presence of the signal photon given the detection of an idler.

The unitary of the spontaneous four-wave mixing process is derived in appendix B section B.1 and evaluates as

$$\hat{U} = \exp\left[-\frac{i}{\hbar}\left(A\int \mathrm{d}\omega_s \mathrm{d}\omega_i f_{\mathrm{SFWM}}(\omega_s,\omega_i)\hat{a}_s^\dagger(\omega_s)\hat{a}_i^\dagger(\omega_i) + \mathrm{h.c.}\right)\right], \tag{2.47}$$

where the function $f_{\mathrm{SFWM}}(\omega_s,\omega_i)$ is the joint spectral amplitude and describes the spectral correlations of photons produced by the interaction. The parameter A characterises the strength of SFWM and relates to the pump field strength, $\hat{a}_x^\dagger$ is the creation operator for the signal or idler photons $x \in \{s,i\}$ and all other symbols have their usual meanings.

In general, the SFWM unitary acts on the vacuum state $|\mathrm{vac}\rangle$ to produce multi-mode twin-beam squeezed vacuum states, see section 3.2.2. This gives rise to multiple pairs of signal and idler photons in different spectral modes. However, for low pair production probabilities, the produced state can be approximated by the following bi-photon state when signal and idler photons are measured [78]

$$|\psi\rangle = \int \mathrm{d}\omega_s \mathrm{d}\omega_i f_{\mathrm{SFWM}}(\omega_s,\omega_i)\hat{a}_s^\dagger(\omega_s)\hat{a}_i^\dagger(\omega_i)|\mathrm{vac}\rangle\,. \tag{2.48}$$

This approximation will be used throughout this thesis, where the measured multi-pair terms are low compared with the single pair production. For an explanation of this approximation see appendix B section B.2.

2.3 Quantum Photonic Protocols & Applications

This section summarises some of the key quantum protocols introduced within the later chapters of this thesis. This will serve as a prerequisite for chapters 3-6, but may be skipped for readers who are particularly familiar with quantum entanglement and teleportation.

2.3.1 Quantum Entanglement

Quantum superposition allows for the surprising result that two separate systems can be in a non-separable pure quantum state. In other words, their combined state cannot be factorised in such a way that it can be written in the form $|\psi\rangle_A \otimes |\phi\rangle_B$. An example of this is the superposition state $|\Phi^+\rangle$ which is defined as

$$|\Phi^+\rangle \equiv \frac{1}{\sqrt{2}}\big(|0,0\rangle + |1,1\rangle\big)_{A,B}, \tag{2.49}$$

meaning that the two systems are perfectly correlated when measured in the computational basis. The surprising result, however, is that these perfect correlations also arise in other bases, for example, the same state when written in the eigenbasis of the $\hat{\sigma}_x^{\otimes 2} \equiv \hat{\sigma}_x \otimes \hat{\sigma}_x$ operator is as follows

$$|\Phi^+\rangle \equiv \frac{1}{\sqrt{2}}\big(|+,+\rangle + |-,-\rangle\big)_{A,B}. \tag{2.50}$$

In this basis, you can again see that the two systems remain perfectly correlated with one another, which may seem highly surprising since the computational basis and $\hat{\sigma}_x$ basis are mutually unbiased as we have recently discussed. This is equivalent to an experiment whereby two path entangled photons, initially prepared in the state $|\Phi^+\rangle$, are each incident on two different 50:50 beam splitters[2] operating on four total spatial modes. An experimental demonstration of this example is given in section 4.1.5 of this thesis. Since the probability that each photon is transmitted or reflected is 50%, one would assume that all four path permutations are equally likely with one another, i.e. $\{(T,T),(T,R),(R,T),(R,R)\}$ would all occur with 25% likelihood. Instead, we find that the entangled photons are always together transmitted or together reflected, where only the following outcomes can occur $\{(T,T),(R,R)\}$, each with 50% probability.

In fact, the above state is a special kind of two qubit entangled state called a Bell state, which form the set of maximally entangled states in two-qubits. There are four Bell states that together form a basis of Bell states that span the entire two-qubit Hilbert space. As a result, any two-qubit state can be written as a linear superposition of Bell states, and they form a orthonormal basis on the space. The four Bell states

[2]The optical matrix for the beam splitter is the same as the projector for the $\hat{\sigma}_x$ basis.

are defined as follows

$$
\begin{aligned}
|\Phi^+\rangle &\equiv \frac{1}{\sqrt{2}}\big(|0,0\rangle + |1,1\rangle\big)_{A,B} \\
|\Phi^-\rangle &\equiv \frac{1}{\sqrt{2}}\big(|0,0\rangle - |1,1\rangle\big)_{A,B} \\
|\Psi^+\rangle &\equiv \frac{1}{\sqrt{2}}\big(|0,1\rangle + |1,0\rangle\big)_{A,B} \\
|\Psi^-\rangle &\equiv \frac{1}{\sqrt{2}}\big(|0,1\rangle - |1,0\rangle\big)_{A,B},
\end{aligned}
\tag{2.51}
$$

where each of the Bell states can reproduce each-other via local rotations applied to only one of the qubits, for example

$$
\begin{aligned}
|\Phi^+\rangle &= (\hat{I}\otimes\hat{\sigma}_z)|\Phi^-\rangle \\
&= (\hat{I}\otimes\hat{\sigma}_x)|\Psi^+\rangle \\
&= (\hat{I}\otimes\hat{\sigma}_y)|\Psi^-\rangle\,.
\end{aligned}
\tag{2.52}
$$

The $|\Psi^-\rangle$ state is a particularly interesting example since it exhibits anti-correlations in all product bases. This can be seen directly by considering the basis produced by the two orthonormal vectors $|\alpha \pm \beta\rangle \equiv \alpha|0\rangle \pm \beta|1\rangle$. In fact, when written in terms of these vectors the produced state (after re-normalisation) is

$$
|\Psi^-\rangle = \frac{|\alpha-\beta\rangle\,|\alpha+\beta\rangle - |\alpha+\beta\rangle\,|\alpha-\beta\rangle}{\sqrt{2}},
\tag{2.53}
$$

and so the two qubits are always anti-correlated when measured locally in the same basis. This surprising property names the $|\Psi^-\rangle$ state the singlet state.

Though there are many kinds of entangled state, it turns out that entanglement is a difficult quantity to quantify [79–81]. For example, it would be useful to have a measure of entanglement whereby we could directly compare two states and tell which one has 'more' entanglement than the other. In quantum information theory, a work-around is that states are classified in terms of their properties. In the later sections of this thesis we will discuss two particular kinds of entangled states. The first is the n-qubit entangled state which is classified into the GHZ class, in particular we will explore the following states

$$
|\mathrm{GHZ}_n\rangle = \frac{|0\rangle^{\otimes n} + |1\rangle^{\otimes n}}{\sqrt{2}},
\tag{2.54}
$$

in section 4.4 of this thesis. Later, throughout many parts of chapter 5, we will experimentally discuss entanglement in higher dimensions, in particular the d-dimensional two qudit maximally entangled state

$$
|\Phi_d\rangle \equiv \frac{1}{\sqrt{d}}\sum_{\forall i\in d}|i,i\rangle\,.
\tag{2.55}
$$

In those sections we will discuss the specific motivations of these states, as well as how to experimentally prepare and measure such them on a silicon integrated photonic platform.

2.3.2 Quantum Teleportation

Quantum teleportation is the transfer of a qubit from one system to another without the need to physically transmit the object in which the initial qubit is encoded. This seems immediately counter intuitive and controversial, since at first sight this claim seems to be in contradiction to the no-signaling condition - since information cannot travel faster than the speed of light. However, it is through a combination of shared entanglement and classical communication that the teleportation protocol is achieved, and so no laws of physics are broken here. Quantum teleportation is still very surprising, however, since it allows the direct transfer of a state between systems with low resource requirements, even in instances where the state is unknown to both parties.

The teleportation protocol is as follows. Suppose that two parties, Alice and Bob, each share one particle from a maximally entangled Bell pair $|\Psi^+\rangle_{A,B}$. In addition to this bipartite system, suppose that Alice has the control over a third particle in which she encodes an arbitrary qubit state $|\phi\rangle_{A_2} = \alpha|0\rangle_{A_2} + \beta|1\rangle_{A_2}$. In this case the three particle state is the following

$$\begin{aligned} |\phi\rangle_{A_2} \otimes |\Phi^+\rangle_{A,B} &= \big(\alpha|0\rangle_{A_2} + \beta|1\rangle_{A_2}\big) \otimes \frac{1}{\sqrt{2}}\big(|0,0\rangle + |1,1\rangle\big)_{A,B} \\ &= \Big(\frac{\alpha}{\sqrt{2}}|0,0,0\rangle + \frac{\alpha}{\sqrt{2}}|0,1,1\rangle + \frac{\beta}{\sqrt{2}}|1,0,0\rangle + \frac{\beta}{\sqrt{2}}|1,1,1\rangle\Big)_{A_2,A,B}. \end{aligned} \tag{2.56}$$

The parameters α and β could even be unknown to Alice or Bob, but despite of this, they understand the form of the quantum state compared with the initial qubit state, as written above. Next, Alice would like to perform a joint measurement in the Bell Basis for her two particles. In order to see what effect the outcome of her measurement would yield, we could rewrite the state such that her two particles are in this basis, which can be achieved via the following substitutions

$$\begin{aligned} |0,0\rangle_{A_2,A} &= \frac{1}{\sqrt{2}}\big(|\Phi^+\rangle + |\Phi^-\rangle\big)_{A_2,A}, \\ |1,1\rangle_{A_2,A} &= \frac{1}{\sqrt{2}}\big(|\Phi^+\rangle - |\Phi^-\rangle\big)_{A_2,A}, \\ |0,1\rangle_{A_2,A} &= \frac{1}{\sqrt{2}}\big(|\Psi^+\rangle + |\Psi^-\rangle\big)_{A_2,A}, \\ |1,0\rangle_{A_2,A} &= \frac{1}{\sqrt{2}}\big(|\Psi^+\rangle - |\Psi^-\rangle\big)_{A_2,A}. \end{aligned} \tag{2.57}$$

The rewritten state is as follows

$$
\begin{aligned}
|\phi\rangle_{A_2}\otimes|\Phi^+\rangle_{A,B} = \Big(&\frac{\alpha}{2}\big(|\Phi^+\rangle+|\Phi^-\rangle\big)_{A_2,A}\otimes|0\rangle_B+\frac{\alpha}{2}\big(|\Psi^+\rangle+|\Psi^-\rangle\big)_{A_2,A}\otimes|1\rangle_B+\\
&\frac{\beta}{2}\big(|\Psi^+\rangle-|\Psi^-\rangle\big)_{A_2,A}\otimes|0\rangle_B+\frac{\beta}{2}\big(|\Phi^+\rangle-|\Phi^-\rangle\big)_{A_2,A}\otimes|1\rangle_B,\Big)\\
=&\frac{1}{2}\Big(|\Phi^+\rangle_{A_2,A}\otimes\big(\alpha|0\rangle+\beta|1\rangle\big)_B+|\Phi^-\rangle_{A_2,A}\otimes\big(\alpha|0\rangle-\beta|1\rangle\big)_B\\
&+|\Psi^+\rangle_{A_2,A}\otimes\big(\beta|0\rangle+\alpha|1\rangle\big)_B+|\Psi^-\rangle_{A_2,A}\otimes\big(\beta|0\rangle-\alpha|1\rangle\big)_B\Big).
\end{aligned}
\tag{2.58}
$$

Hence whatever outcome Alice is to measure, Bobs state looks like a local rotation of the initial state $|\phi\rangle$. The exact rotations are actually one of the four operators $\{\hat{I},\hat{\sigma}_x,\hat{\sigma}_y,\hat{\sigma}_z\}$ where the final state is as follows

$$
\begin{aligned}
|\phi\rangle_{A_2}\otimes|\Phi^+\rangle_{A,B} = \frac{1}{2}\Big(&|\Phi^+\rangle_{A_2,A}|\phi\rangle_B+|\Phi^-\rangle_{A_2,A}\big(\hat{\sigma}_z|\phi\rangle\big)_B\\
&+|\Psi^+\rangle_{A_2,A}\big(\hat{\sigma}_x|\phi\rangle\big)_B+|\Psi^-\rangle_{A_2,A}\big(\hat{\sigma}_y|\phi\rangle\big)_B\Big).
\end{aligned}
\tag{2.59}
$$

To complete the teleportation protocol, Alice transmits her Bell measurement outcome to Bob, which requires the transmission of two classical bits. From this result, Bob does not know the state of the original particle $|\phi\rangle$, but he knows what rotation to apply in order to regain the state. Since each of the Pauli operators are self-inverse, Bob needs to only apply the same operator that has already acted on his state, i.e.

Alice's Outcome:	Bob Applies:
$\|\Phi^+\rangle_{A_2,A}$	$\hat{I}$
$\|\Phi^-\rangle_{A_2,A}$	$\hat{\sigma}_z$
$\|\Psi^+\rangle_{A_2,A}$	$\hat{\sigma}_x$
$\|\Psi^-\rangle_{A_2,A}$	$\hat{\sigma}_y$.

(2.60)

Therefore if Alice is capable of measuring in the Bell basis, and if Bob can perform local rotation on his qubit, they are sure that Bobs state is the arbitrary (and perhaps unknown) state initially prepared by Alice. Quantum teleportation is now one of the fundamental protocols of quantum information science, and is the backbone of quantum computing [64, 65] and communications [38].

2.3.3 Entanglement Swapping

A bi-seperable state is a multi-partite state which can be written as the tensor product of two systems $|\psi\rangle_A\otimes|\psi\rangle_B$, where each system A and B contains entangled subsystems

that cannot be factorised. The four particle state $|\Phi^+\rangle_{A,B} \otimes |\Phi^+\rangle_{C,D}$, consisting of two Bell pairs is one such example which has many applications throughout quantum information science. Entanglement swapping is a protocol which can swap the entanglement between different sets of qubits. When applied to the above example, if particles B&C are projected onto a Bell state, then consequently so are A&D. This is of particular interest since there is no requirement for particles A and D to have ever interacted with one another, yet they now experience non-local quantum correlations. One could immediately imagine that this could be utilised to extend the range of entanglement for long-distance quantum communication and network, which forms the basis for the quantum repeater [82, 83]. Another way of viewing this process would be the quantum teleportation of particle B onto particle D, the successful transmission of which would result in systems A and D being in a Bell state.

The exact protocol is as follows. Suppose that four particles are initially prepared in the bi-separable entangled state as introduced above, namely

$$\begin{aligned} |\Phi^+\rangle_{A,B} \otimes |\Phi^+\rangle_{C,D} &= \frac{1}{\sqrt{2}}\big(|0,0\rangle + |1,1\rangle\big)_{A,B} \otimes \frac{1}{\sqrt{2}}\big(|0,0\rangle + |1,1\rangle\big)_{C,D} \\ &= \frac{1}{2}\Big(|0,0,0,0\rangle + |0,0,1,1\rangle + |1,1,0,0\rangle + |1,1,1,1\rangle\Big)_{A,B,C,D} \\ &= \frac{1}{2}\Big(|0,0,0,0\rangle + |0,1,0,1\rangle + |1,0,1,0\rangle + |1,1,1,1\rangle\Big)_{B,C,A,D} \end{aligned} \tag{2.61}$$

where in the final line we have rearranged the ordering of the qubits. Suppose that we wish to perform a Bell measurement on systems B and C and so we rewrite the state in the basis of Bell states for B&C, and separately for A&D. The method for this is outlined in the previous section. In this case the resulting state is

$$\begin{aligned} |\Phi^+\rangle_{A,B} \otimes |\Phi^+\rangle_{C,D} = \Big(&|\Phi^+\rangle_{B,C} \otimes |\Phi^+\rangle_{A,D} + |\Phi^-\rangle_{B,C} \otimes |\Phi^-\rangle_{A,D} \\ &+ |\Psi^+\rangle_{B,C} \otimes |\Psi^+\rangle_{A,D} + |\Psi^-\rangle_{B,C} \otimes |\Psi^-\rangle_{A,D} \Big). \end{aligned} \tag{2.62}$$

When written in this basis, it is clear that by performing the Bell measurement on B&C, the remaining particles must also be in the same entangled state. Moreover, since the Bell pairs are all reproducible via local measurements on one particle, as explained in section 2.3.1, particles A&D can be prepared as any of the Bell states.

The distribution and swapping of entanglement are of fundamental interest in quantum communications, having direct applications in device-independent quantum key distribution, quantum secret sharing and quantum networks [38, 44, 82, 84, 85]. Optical loss in quantum channel limits the distance over which these quantum protocols can operate. A proposed solution is that of the quantum repeater, which can in principle achieve long distances by utilising entanglement swapping and quantum

memory [38, 82, 83]. This phenomena has also been of great interest in fundamental science, since it has been shown that the choice of measurement of particles B&C can even steer particles A&B into the past [86, 87].

2.3.4 Quantum Key Distribution - BB84

Suppose that two people, Alice and Bob, would like to communicate in secrecy with one another. They know that if they each share an identical random string of classical bits they can secure any message by performing a bit-wise XOR operation between their message m and the random bit string b to produce the encrypted string $e = m \times b$. This operation has the quality that if performed twice, the original message is returned $e \times b = m$ and the code is decrypted. If this random bit string is used only once, this encryption technique is referred to as the one-time pad, and is secure against any attack so long as b is known only to Alice and Bob and is truly random [88].

Despite the absolute security of the one-time pad protocol, any two users that would like to implement the protocol require pre-shared random bit strings equal in length to their message. This quickly becomes impractical for many-user networks, since each pair of users would have to store sufficiently long strings to encrypt any message they might want to send each other. A far more practical approach is to find a secure way to distribute a random key between both parties once a message is to be sent. Typically, classical public key cryptography schemes achieve this by creating problems that seem one-way hard, i.e. hard to compute but easy to verify. Quantum key distribution (QKD) is a quantum approach to this problem, where a security proof relies only on the postulates of quantum mechanics. As a result, messages encrypted through QKD are secure so long as the known laws of physics hold - an exciting endeavour no matter the outcome[3]. BB84, the QKD protocol named by its two authors Charles Bennett and Gilles Brassard in 1984, was the first QKD protocol of its kind. Today, there are many such protocols each with their own advantages [36, 44, 89–91], however here we introduce the basic concepts of the BB84 protocol.

Suppose that Alice prepares and sends a stream of qubits to Bob chosen from the two Pauli bases $\hat{\sigma}_z$ and $\hat{\sigma}_x$. Alice prepares a list of random bits and encodes them in qubits such that a 0 corresponds to the +1 eigenvector, $\{|0\rangle, |+\rangle\}$, and a 1 represents a -1 eigenvector, $\{|1\rangle, |-\rangle\}$. However, the basis in which the state is encoded is chosen at random. When Bob receives the qubit, he is forced to make a decision about which basis to measure the particle in. He knows that Alice encoded in one of two basis,

[3] In reality no implementation of a QKD protocol is perfectly accurate and so practical demonstrations can be exploited when they do not match the physical model.

but not which one. If Bob is to measure in the correct basis (the basis in which Alice encoded the qubit), then he will measure the correct eigenvalue with 100% certainty. However, if he measures in the wrong basis then he will receive either outcome with 50% probability because the two bases are mutually unbiased. In the BB84 protocol, after Bob records each of his measurements, Bob publicly announces his choice of basis for each particle. Alice can then verify which particles were measured correctly and an identical random string can be formed between the two parties. The bits corresponding to Bob measuring the wrong basis are discarded.

The security of this protocol comes from the fact that any eavesdroppers attempt to learn the quantum state before it reaches Bob will also have to make a measurement choice. If the eavesdropper chooses the wrong basis then 50% of the time they will measure the wrong eigenvalue. After this the eavesdropper must send the qubit to Bob, but since the quantum state is still unknown to the eavesdropper (since it cannot be precisely measured or cloned) the state may not match Alice's prepared state. By comparing a small subset of their measurement outcomes, Alice and Bob can together assess whether their communication channel was secure. If there are many errors introduced in the string then they can simply abort the communication, however, if the error-rate is low then an eavesdropper could not have made measurements. This protocol demonstrates how some of the peculiar features of quantum information can be used to great advantage in real-world scenarios.

2.4 Quantum Interference with Single Photons

The quantum interference of single photon states is one of the central components of quantum photonic technologies. In the following sections we outline a few key quantum information experiments, where the successful interference depends on a range of factors such as single photon source performance. These experiments, and their demonstrations in chapter 3, will be key to understanding how to achieve better performance in photonic quantum information demonstrations.

2.4.1 Hong-Ou-Mandel Interference

The original Hong-Ou-Mandel experiment [92] showed the fascinating effect that two identical single photons incident on either arm of a balanced beam splitter would deterministically bunch on the output ports. From a classical viewpoint, the probability that each photon is transmitted or reflected is 50% and so the classical theory suggests that if you repeat the experiment N times, approximately $N/2$ times the photons

will leave separate arms and the remaining $N/2$ times they will leave the same arm. Quantum mechanically, however, the two identical photons interfere with one another and the probability that they leave different ports is 0.

The quantum state of two identical photons in different optical modes, i and j, can be written in the Fock basis as $|1,1\rangle_{i,j} = \hat{a}_i^\dagger \hat{a}_i^\dagger |0,0\rangle_{i,j}$. The transformation matrix for a balanced beam splitter maps the creation operators

$$\hat{a}_i^\dagger \to (\hat{a}_i^\dagger + e^{i\pi/2}\hat{a}_j^\dagger)/\sqrt{2} \tag{2.63a}$$

$$\hat{a}_j^\dagger \to (e^{i\pi/2}\hat{a}_i^\dagger + \hat{a}_j^\dagger)/\sqrt{2} \tag{2.63b}$$

and hence the initial state becomes

$$\begin{aligned} \hat{a}_i^\dagger \hat{a}_i^\dagger |0,0\rangle_{i,j} &\to \frac{1}{2}\left(\hat{a}_i^\dagger + e^{i\pi/2}\hat{a}_j^\dagger\right)\left(e^{i\pi/2}\hat{a}_i^\dagger + \hat{a}_j^\dagger\right)|0,0\rangle_{i,j} \\ &= \left(e^{i\pi/2}\hat{a}_i^{\dagger 2} \underbrace{+\hat{a}_i^\dagger \hat{a}_j^\dagger - \hat{a}_j^\dagger \hat{a}_i^\dagger}_{0} + e^{i\pi/2}\hat{a}_j^{\dagger 2}\right) \\ &= \frac{|2,0\rangle_{i,j} + |0,2\rangle_{i,j}}{\sqrt{2}}, \end{aligned} \tag{2.64}$$

up to the global $\pi/2$ phase. The result is that photons only arrive out of the same optical port.

Experimentally, this was demonstrated by introducing an optical delay between one of the single photons. By placing a single photon detector at each output port the anti-bunching state can be measure through the simultaneous arrival of two photons at each output port. When the optical delay is large, the photons arrive at the beam splitter at slightly different time and therefore the counting statistics behave classically since they are transmitting and reflected roughly 50% of the time. However, when the two photons overlap in time and are identical the quantum interference happens and there is zero coincidence counts at zero time delay. In the following sections we will see two more examples of quantum interference experiments with single photons, these slight deviations from the original time-delayed experiment are more practical to achieve on an integrated device and will be explored in chapter 3 of this thesis.

2.4.2 Time-reversed HOM

The standard Hong-Ou-Mandel experiment, as discussed above, generates the initial anti-bunched Fock state in the i and j spatial modes $|1,1\rangle_{i,j}$, and interferes the identical single photons to produce the anti-bunched state $(|2,0\rangle + |0,2\rangle)_{i,j}/\sqrt{2}$. Here we wish to discuss another type of bi-photon quantum interference experiment which

seems to act in reverse of this standard approach. In this approach, which we will refer to as the time-reversed HOM experiment, an initially bunched superposition state becomes anti-bunched by controlling a relative phase shift between the superposition states. This experiment will be later used in order to benchmark the similarities between different integrated sources experimentally in chapter 3 of this thesis.

The details of this experiment are as follows. Suppose that we begin with a two-photon bunched state, where the bi-photons are initially in a coherent superposition of spatial mode i and j, as follows

$$\begin{aligned} |\psi\rangle &= \frac{1}{\sqrt{2}}\left(|2\rangle_i \otimes |0\rangle_j + |0\rangle_i \otimes |2\rangle_j\right) \\ &= \frac{1}{2}\left(\hat{a}_i^{\dagger 2} + \hat{a}_j^{\dagger 2}\right)|0,0\rangle_{a,b} \end{aligned} \tag{2.65}$$

where we have used $\hat{a}^{\dagger n}|0\rangle = \sqrt{n!}\,|n\rangle$. By adding a phase offset $e^{i\phi}$ to the j^{th} spatial mode, each photon picks up a relative phaseshift compared with the i^{th} mode and the state becomes

$$\frac{1}{2}\left(\hat{a}_i^{\dagger 2} + e^{2i\phi}\hat{a}_j^{\dagger 2}\right)|0,0\rangle_{a,b} \tag{2.66}$$

In this experiment, a Hadamard gate $\hat{H}$ is then applied to the above initial state, such that $\hat{a}_i^\dagger \to (\hat{a}_i^\dagger + \hat{a}_j^\dagger)/\sqrt{2}$ and $\hat{a}_j^\dagger \to (\hat{a}_i^\dagger - \hat{a}_j^\dagger)/\sqrt{2}$, which gives

$$\begin{aligned} \hat{H}\frac{1}{2}\left(\hat{a}_i^{\dagger 2} + e^{2i\phi}\hat{a}_j^{\dagger 2}\right)|0,0\rangle_{a,b} &= \frac{1}{4}\left(\left(\hat{a}_i^\dagger + \hat{a}_j^\dagger\right)^2 + e^{2i\phi}\left(\hat{a}_i^\dagger - \hat{a}_j^\dagger\right)^2\right)|0,0\rangle_{a,b} \\ &= \frac{1}{4}\left(\left(\hat{a}_i^{\dagger 2} + \hat{a}_j^{\dagger 2}\right)(1+e^{2i\phi}) + 2\hat{a}_i^\dagger\hat{a}_j^\dagger(1-e^{2i\phi})\right)|0,0\rangle_{a,b} \end{aligned} \tag{2.67}$$

which up to a global phase ($e^{-i\phi}$) gives the state

$$\hat{H}\frac{1}{2}\left(\hat{a}_i^{\dagger 2} + e^{2i\phi}\hat{a}_j^{\dagger 2}\right)|0,0\rangle_{a,b} = \cos\phi\frac{|2,0\rangle_{i,j} + |0,2\rangle_{i,j}}{\sqrt{2}} + \sin\phi\,|1,1\rangle_{i,j}\,. \tag{2.68}$$

Hence by choosing the correct phase offset, the state can be either in the pure anti-bunched state $|1,1\rangle_{i,j}$ or in the original bunched superposition state.

This experiment can also be achieved with non-degenerate single photon states. As we will see in more detail in chapter 3, this allows the experiment to be performed with $\chi^{(3)}$ parametric single photon sources, where signal and idler photon pairs encode the initial bunched state. This experiment has been verified both in bulk [93] and on-chip [94] and has been shown to have direct applications in quantum metrology [95]. In addition, this interference pattern is useful for the deterministic routing of photons [96] and has been proposed as a method of producing path-encoded multi-partite entangled states [97].

2.4.3 Heralded MZI Quantum Interference

The standard HOM experiment, as described above, acts as a photon indistinguishability measurement where the visibility of interference relates to how similar the interfering photons are. The reversed HOM fringe in the previous section is able to infer how similar are the spectra of two photon sources, where identical but impure sources are able to achieve good overlap and high visibility. We therefore require another interference experiment able to determine the spectral purity of the single photons that are emitted from a given single photon source. The details of this purity measurement are outlined more in-depth in section 3.2.4.2, but here we give a brief outline of the procedure.

The idea is that, despite the lack of deterministic single photon sources, parametric sources that emit photon pairs can be used as triggered (or heralded) single photon sources. For example, consider an experiment where two pairs of photon sources produce photon pairs through spontaneous four-wave mixing, where there is some probability that each source simultaneously emits one photon pair. In these instances, there are four photons produced, two at the signal frequency and two and the idler frequency. As a result, the two idler photons can be spatially de-multiplexed (filtered) and when detected can infer the presence of the remaining signal photons. In this example, if single photons are indistinguishable from each other and emitted in the pure quantum state, then the initial state after heralding would become $|1,1\rangle_{i,j}$ in the Fock basis, where i and j represent the different spatial modes that the photons occupy. This is the starting point of the standard HOM experiment, where the presence of an optical delay can choose whether the two measured photons are distinguishable or indistinguishable. However, optical delay lines in integrated devices are largely problematic due to the increased optical losses on the single photons, and the lack of tune-ability on the amount of delay. An alternative method is to input the heralded two photon state onto separate arms of a controllable interferometer. The transformation matrix for an on-chip Mach-Zehnder interferometer, as shown in section 2.5.5, relates to the relative optical phase shift ϕ inside the interferometer as

$$\hat{U}_{\mathrm{MZI}}(\phi) = \begin{pmatrix} \sin(\phi/2) & \cos(\phi/2) \\ \cos(\phi/2) & -\sin(\phi/2) \end{pmatrix}. \tag{2.69}$$

The heralded two photon state that emerges from the interferometer is therefore

(2.70)
$$\begin{aligned}\hat{U}_{\mathrm{MZI}}(\phi)|1,1\rangle_{i,j} &= \hat{U}_{\mathrm{MZI}}(\phi)\ \hat{a}_i^\dagger \hat{a}_j^\dagger |0,0\rangle_{i,j} \\ &= \big(\sin(\phi/2)\ \hat{a}_i^\dagger + \cos(\phi/2)\ \hat{a}_j^\dagger\big)\big(\cos(\phi/2)\ \hat{a}_i^\dagger - \sin(\phi/2)\ \hat{a}_j^\dagger\big)|0,0\rangle_{i,j} \\ &= \sqrt{2}\sin(\phi/2)\cos(\phi/2)\big(|2,0\rangle - |0,2\rangle\big)_{i,j} + \big(\cos^2(\phi/2) - \sin^2(\phi/2)\big)|1,1\rangle_{i,j} \\ &= \sin(\phi)\big(|2,0\rangle - |0,2\rangle\big)_{i,j}/\sqrt{2} + \cos\phi\,|1,1\rangle_{i,j}\,.\end{aligned}$$

Hence the probability of anti-bunched photons is $P_{\mathrm{antibunch}} = \cos^2\phi$ and can be computed on chip via the simultaneous detection of all four photons [98].

2.5 Integrated Quantum Photonics

2.5.1 Introduction

The ultimate goal of quantum photonics is to construct useful and powerful quantum technologies at scale. Specific quantum technologies will require the inclusion of many-thousands if not millions of optical components that is not possible with off the shelf optical equipment. The field of integrated photonics is therefore an ideal candidate to cater for these specific fields. Moreover, integrated platforms such as silicon photonics have proven capabilities in meeting economic requirements such as high yield, small form-factor and low cost, that are inevitably required for mass adoption. In the following section we will introduce several key components in silicon photonics, which will form a foundation for understanding the experiments in the following chapters of this thesis.

2.5.2 Waveguides

Until now, we have used the term waveguides loosely as a term meaning to guide electromagnetic waves in a given medium. In this section we provide a more precise definition of what we mean by waveguides in silicon photonics - specifically how different silicon structures may guide infrared waves of light on chip.

Formally, a waveguide is a medium which is able to confine one or more modes of light in a particular direction with minimal loss of energy or dispersion. In silicon photonics this is achieved via total-internal reflection at an interface between two materials, the core and cladding. In this case, the internal core is always silicon (with a high refractive index) and the cladding is another insulating material such as silica. Here it is crucial that the cladding material have relatively low refractive

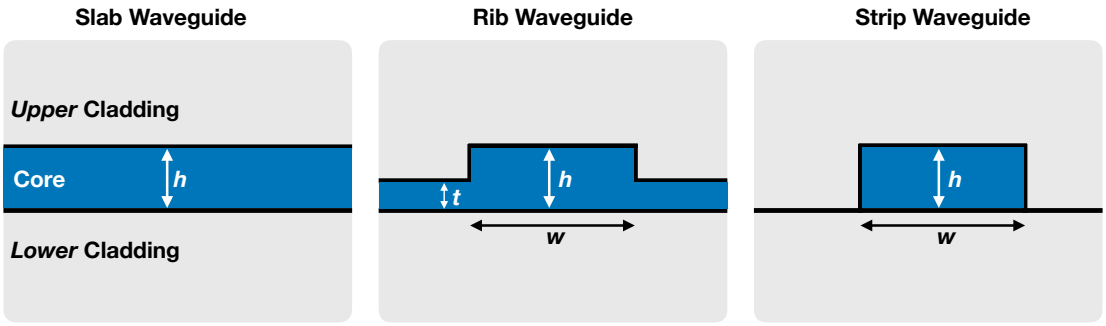

Figure 2.2: Cross-section view of standard waveguide geometries. In each case the transverse electric field is designed to be maximum inside of the core, shown in dark blue. In the slab waveguide, light is confined in one dimension. In contrast, the rib and strip waveguides confine the light inside a two-dimensional area, $h \times w$, and propagate along the z direction (into the page).

index compared with the silicon core so that light is well confined in the structure. This allows high transmission across the circuit and permits designs with relatively tight bends or curves where light may be more likely to be lost to the environment. Figure 2.2 shows a few of the most common waveguide structures in silicon photonics. In this thesis we are most interested in the strip waveguide, since it is the primary structure used to assemble the chips discussed in the later chapters of this thesis.

In order to gain a firm understanding on how light in the C-band (or telecommunication frequency, $1530nm < \lambda < 1565nm$) are confined in silicon waveguides, one must solve the Helmholtz equation under the correct boundary conditions [99]. Unfortunately, this is only analytically feasible for simple waveguide structures such as the slab waveguide, which has simple boundary conditions. However, by utilizing FDTD (Finite-difference time-domain) techniques one can obtain the numerical approximation of more complex waveguide structures in silicon, such as the strip and rib waveguides. Figure 2.3 shows the simulation of the TE and TM modes for the strip waveguide. The results were achieved by Lumerical software, which gave a matrix of values corresponding to the E field components at different x, y values.

These simulations, with perfect components (zero roughness) give estimations of zero losses. The losses one sees in experiment are due to the imperfect fabrication and primarily side-wall roughness which scatters the light. We therefore expect that eigenmode solutions which are concentrated to the outside of the waveguide surface would experience the highest loss and should therefore be avoided in experiments in practice. It can be seen from the figure 2.3 that the fundamental TM mode is highly concentrated towards the waveguide boundary and hence their use-cases should be limited in practical experiments.

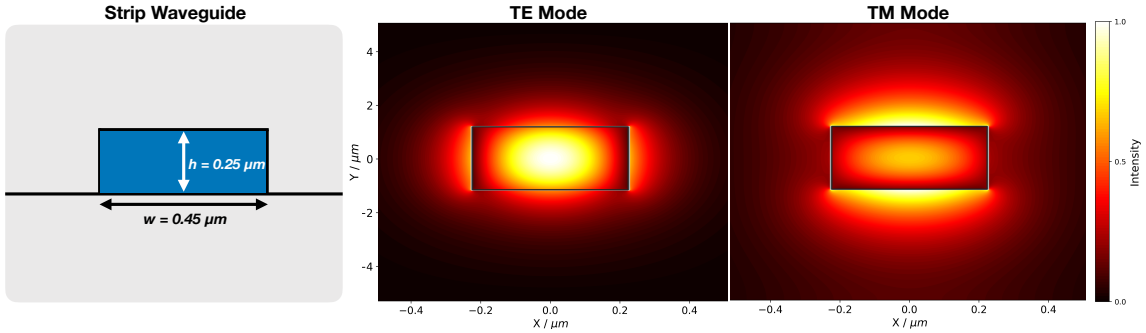

Figure 2.3: FDTD Simulation of a perfect strip waveguide comprised of a solid silicon core and silicon-dioxide cladding. The waveguide dimensions, shown in the left diagram, are $250 \times 450nm$ and are the same dimensions used to fabricate the devices in the later chapters of this thesis. The simulations show the cross section of the waveguide and represent the distribution of the normalised intensity of the electric field inside the waveguide for the lowest order modes TE_0 and TM_0.

In addition, since silicon is not transparent at wavelengths shorter than a micron, the work in this thesis is performed at the telecommunication wavelength $\lambda = 1.55\mu m$. This is a natural choice of operation, since standard off-the-shelf components are typically optimised for this wavelength due to the large telecommunication industry. As a result our experiments gain access to a wide array of fine-tuned lasers and fibre-optic components to see the best results.

2.5.3 Beam Splitters - MMI & DC

Having discussed waveguides in integrated photonics, we would now like to discuss how to construct devices which mimic the linear operation of standard well-known optical components. The two most important devices in linear optics are arguably the 50:50 beam splitter and phase shifter. The beam splitter has two main approaches in integrated optics, the Multi-Mode Interferometer (MMI) and Directional Coupler [100] (DC) [101, 102]. In each case, the structure can be tuned in order to achieve different splitting ratios, here we discuss the situation where light in the input port is split 50:50 between each of the two output ports.

In the case of a directional coupler, two waveguides are brought close together in space over a short period such that the light in each waveguide becomes momentarily coupled. In this approach, when the gap is small, light from either waveguide is able to tunnel across the boundary between different optical modes. The interaction region, that is, the length at which the momentary coupling occurs, can be tuned in order to control the effect of the region and tune the splitting ratio. For a tuned 50:50 beam-splitter the waveguides are separated from one another precisely once the field

amplitudes become equal.

In the case of the MMI coupler, again multiple waveguide modes are brought together into a single spatial region, where they may overlap and interfere. Here the subtle difference is that there is a single well-defined region where the mixing occurs and is therefore easier to fabricate in practice. As a result, such a structure becomes more tolerant to errors and is easier to achieve an accurate 50:50 ratio. On the contrary, these structures typically have higher optical losses than the directional coupler which tend to have similar loss to standard waveguide fabrication.

The trade-off between splitting ratio error tolerance and losses cause difficulties in quantum optic experiments on chip. Since uneven splitting ratios add errors into the desired rotation matrix necessary to perform the experiment. However, low optical transmission in the best case scenario makes the data collection more time consuming. In the worst-case scenario, poor chip stability (temperature or coupling) can give rise to time-varying results, and uneven losses (parts of the chip which experience relatively high losses) can again cause unwanted rotations in ones qubits. Nevertheless, due to the fabrication tolerances which are required for scaling the number of components on-chip, the decision in this thesis is to use the MMI structures to achieve on-chip 50:50 beam splitters.

Due to the precision of the overlapping fields, the interaction region can be tuned such that the light contained in either output ports (compared with the input fields) undergo the exact transformation as of the beam splitter

$$\frac{1}{\sqrt{2}}\begin{pmatrix} 1 & i \\ i & 1 \end{pmatrix}. \tag{2.71}$$

An approximation of the structure can again be seen via FDTD numerical methods using Lumerical software, this can be seen in figure 2.4. A magnified image of these structures in practice can be seen in figure 2.5.

2.5.4 Phase Shifter

One of the most crucial components and building blocks in integrated photonics design is the phase shifter - and specifically, the physical mechanism which is exploited in order to achieve a relative phase difference between two or more waveguides. This is extremely crucial since it has a direct effect on any application or experiment that is possible with the device that is designed. There are a few types of physical effect which may be exploited to achieve relative phase shifts, a few of which are summarised and contrasted below:

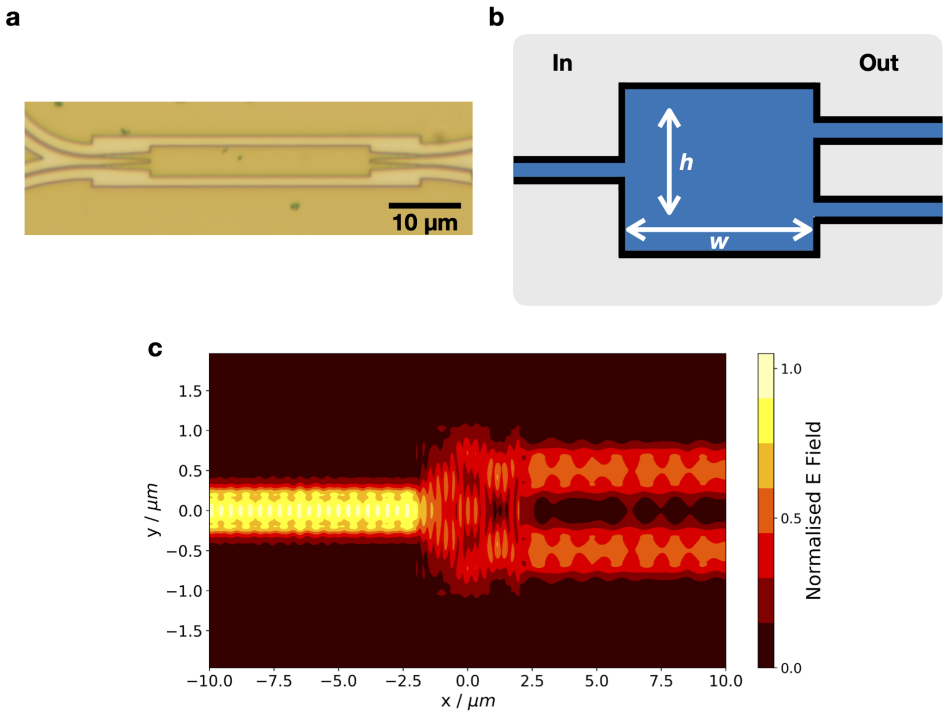

Figure 2.4: MMI design and simulation. **a** Microscope image of an MMI used in this thesis as part of a 4-dimensional receiver design. **b** diagram showing a simplified schematic of a MMI whereby the width and height of the interaction region can be tuned in order to achieve a balanced beam splitter in silicon. **c** numerical simulation of a simple (1×2) MMI, showing that half of the E field is successfully split between the two output waveguides.

- Thermo-optic (TO) phase effect, where a local refractive index change is created by locally heating the waveguide material.
- Electro-optic, where the local refractive index is modified by an induced electric field.
- Magneto-optic, where an induced magnetic field can locally modify the refractive index inside a waveguide.

The thermo-optic effect is one which induces a change in refractive index (locally) upon its change in temperature, and can be approximated as:

$$n(\Delta T) = n_0 + \alpha \Delta T, \tag{2.72}$$

where n_0 is the baseline refractive index at starting temperature T_0 and α is the TO coefficient $\alpha(T, \lambda) = \frac{\mathrm{d}n}{\mathrm{d}T}_{T,\lambda}$. The thermo-optic coefficient has been investigated in silicon at both room temperature $\alpha(300\ K, 1.55\ \mu m) = 1.8 \times 10^{-4}\ K^{-1}$, and at cryogenic temperatures which gave $\alpha(5\ K, 1.55\ \mu m) = 10^{-8}\ K^{-1}$ [103].

The electro-optic effect is a non-linear response of a material to an externally applied electric field. In this response the change in the local refractive index of such a material relates to the electric field in the following manner

$$n(E) = \sum_{i=0}^{\infty} \beta_i E^i, \tag{2.73}$$

where β_i are arbitrary coefficients. The Pockels (2nd order, linear response to applied field) and Kerr (3nd order, quadratic response to the applied field) coefficients are dominant in silicon, and so approximately the relation is

$$n(E) \approx n_0 + \underbrace{\beta_1 E}_{\text{Pockel}} - \underbrace{\beta_2 E^2}_{\text{Kerr}}. \tag{2.74}$$

The work in this thesis utilizes the thermo-optic effect (see fig 2.5), which is achieved by depositing a conductive layer directly on top of the chip. Local heating is caused by applying a current along the resistive film directly above the waveguide. At room temperature, silicon has a sharp change in refractive index for small changes in temperature, allowing effective change in the relative path difference between adjacent waveguides. Throughout this process, and with many thermally tuned heaters on-board a complex device, it is imperative that one controls the overall (average) temperature of the chip in order to conduct heat away from local circuits. This minimizes heat leakage to unwanted parts of the circuit which can introduce errors in the desired operation due to an induced phase difference across unwanted photonic components. This effect is referred to in this thesis as thermal cross-talk, and is a typical problem with thermo-optic phase shifters.

Thermo-optic phase shifters have the advantages that they are reliable, easy to control, high precision, full 2π phase shift. Their disadvantages are thermal cross-talk (largely dependent on circuit design), and relatively low switching speeds (kHz), since one has to wait for the local heating to equilibriate. By constructing a network of linear-optic components, along with integrated phase shifters, it is possible to program and externally control the optical circuitry. This is typically achieved by varying the linear operations achieved in the circuit by varying the phase shifters which are integrated into the device. This is the basic idea behind the external control of devices within this thesis.

2.5.5 Mach-Zehnder Interferometer

A Mach-Zehnder interferometer (MZI) consists of an optical phase shifter between two optical beam splitters. In the Silicon on Insulator (SOI) platform, this can be achieved

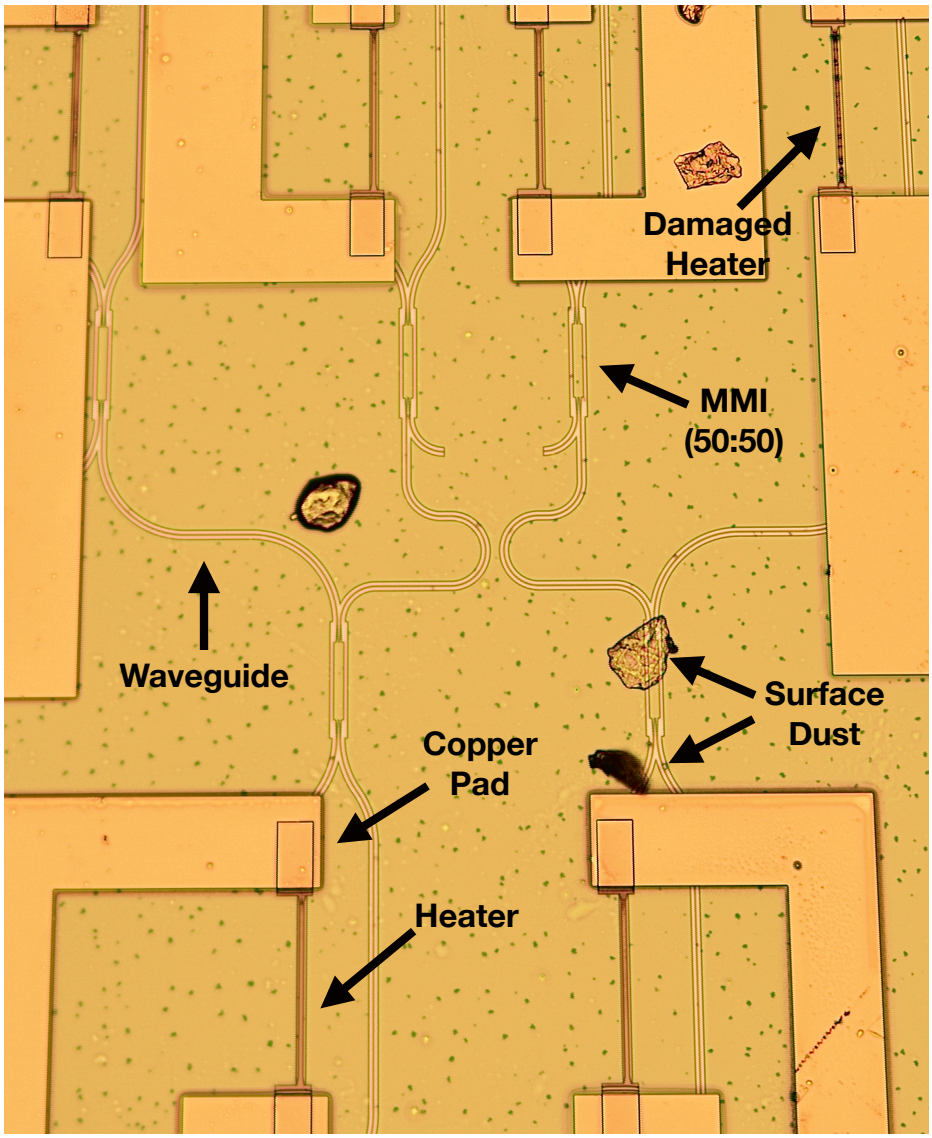

Figure 2.5: Microscope image of a silicon device used in this thesis 4D receiver, see chapter 5. The copper layer is visible directly above the optical layer. The pads are connected to an external PCB for device control.

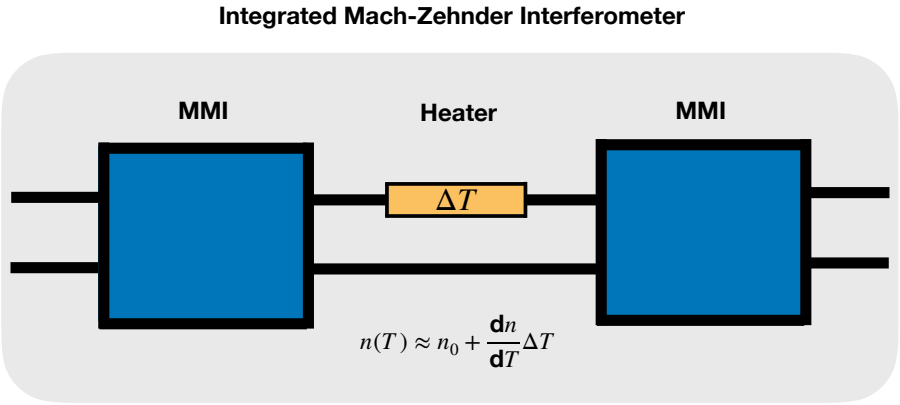

Figure 2.6: Schematic of an integrated MZI comprised of two MMI and a TO phase shifter.

through the integration of two multi-mode interferometers and a TO phase shifter on one arm, a schematic of which is shown in figure 2.6. The transformation matrix for this MZI can be calculated in terms of the optical phase shift ϕ through the matrix multiplication in the following way

$$\begin{aligned}\hat{U}_{\mathrm{MZI}}(\phi) &= \frac{1}{\sqrt{2}}\begin{pmatrix}1 & i\\ i & 1\end{pmatrix}\begin{pmatrix}e^{i\phi} & 0\\ 0 & 1\end{pmatrix}\frac{1}{\sqrt{2}}\begin{pmatrix}1 & i\\ i & 1\end{pmatrix} \\ &= ie^{i\phi}\begin{pmatrix}\sin(\phi/2) & \cos(\phi/2)\\ \cos(\phi/2) & -\sin(\phi/2)\end{pmatrix}\end{aligned} . \tag{2.75}$$

The MZI is an important state modification tool in linear-optic quantum information processing and is used widely throughout this thesis to prepare and measure path-encoded quantum states on chip. In principle, fabrication tolerances create errors on the above transformation matrix, though it has been shown that stacking multiple MZIs can result in increased accuracy [104].

The above transformation matrix can be used to create a classical interference pattern in the optical intensity at each output port. For example, light which enters the top port of the MZI $(1,0)^T$ leaves both ports with different amplitudes depending on the phase inside of the MZI $(1,0)^T \rightarrow ie^{i\phi}(\sin(\phi/2),\cos(\phi/2))^T$. The intensity of light leaving the top port thus becomes $\sin^2(\phi/2) = (1-cos\phi)/2$. The measurement of this interference pattern can be used to characterise the MZI phase inside the interferometer [105].

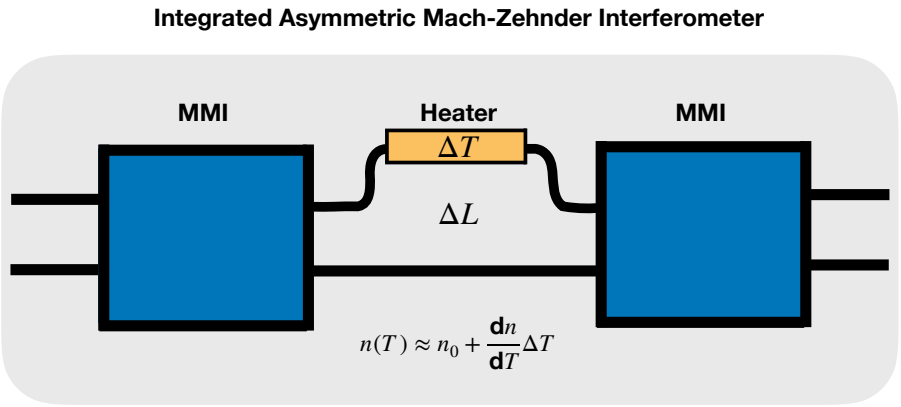

Figure 2.7: Schematic of an integrated AMZI comprised of two MMI and a TO phase shifter.

2.5.6 Asymmetric Mach-Zehnder Interferometer

An Asymmetric Mach-Zehnder Interferometer (AMZI) is an MZI where the length of each arm inside the interferometer are slightly different, such that light occupied in each arm travels a different distance ΔL. Figure 2.7 shows a schematic of this optical component. As a result, the light in each arm acquires a relative phase difference depending on the optical path and the colour of the light inside the interferometer. Therefore such a structure can be used such that different wavelengths of light leave different ports of the AMZI, and these components can be utilised as on-chip filters. The overall goal is that signal and idler photon pairs at wavelengths λ_s and λ_i can be spatially de-multiplexed with high probability. The free spectral range (FSR) $\Delta\lambda$ of such an interferometer is the difference in wavelength between two resonance peaks as is given by

$$\Delta\lambda = \frac{\lambda^2}{n_g \Delta L} \tag{2.76}$$

where n_g is the group velocity of the waveguide. Therefore the optical path length difference can be chosen such that the signal and idler photons leave at different ports. An example would be where the difference in wavelength $\Delta\lambda = 2(\lambda_s - \lambda_i)$, where here the FSR would be twice the size of the difference in wavelength of the single photons and so one photon would constructively interfere while the other destructively interferes. The exact implementation of this filtering can be seen in section 3.6.

2.5.7 Micro-ring Resonators

A ring resonator is a ring-like waveguide structure which is partially coupled to another nearby waveguide. The exact geometry of the ring may vary but is typically either circular or resembles a race track. In this section we specifically talk about microring resonator structures (those with μ scale length) and fabricated in the silicon architecture. In this discussion, there are two main types of resonator, a single-bus structure which is coupled to only a single waveguide, and a double-bus structure which couples to two waveguides simultaneously. For the interest of this thesis, we will deal primarily with the single-bus structure, and later (see chapter 3) we will discuss the implications of this structure in terms of non-linear effects and single-photon sources.

Figure 2.8 shows a simple schematic of a single-bus resonator. Here the light enters the lower left waveguide and propagates to the right. Since the microring structure is close in distance to the adjacently placed waveguide, there is an interaction region (highlighted grey) where the mode of light couples evanescently between the two structures [106]. This has a similar effect to a directional coupler which is discussed in section 2.5.3 [101, 102]. By tuning the interaction length and separation distance, one can tune the effective coupling between the two structures and influence the overall resonance effect. Since part of the light in the bus-coupled waveguide enters the ring, one might expect that the cavity field would interfere at the interaction region after completing a full cycle inside the ring. Naturally, this would mean that constructive interference would occur when the field inside the cavity forms an integer number of 2π phase drifts per cycle. Since the phase difference is dependent on both the path difference and wavelength, we expect to see a tunable FSR depending on the cavity size.

Figure 2.8 highlights the interaction region and defines the transmission τ and reflection r parameters. From this figure it is possible to directly infer the coupled equations:

$$E_{\text{out}} = \tau E_{\text{in}} - r\alpha e^{i\phi} E_{\text{C}} \tag{2.77}$$

and

$$E_{\text{C}} = -rE_{\text{in}} + \tau\alpha e^{i\phi} E_{\text{C}}, \tag{2.78}$$

where E is the amplitude of the electric field and subscript C refers to the cavity amplitude. Here τ and r are defined as the transmission and reflection coefficients as shown in figure 2.8 and α is the loss factor defined as the fractional loss per

round-trip inside the cavity. Formally α is defined in terms of the loss parameter β where $\alpha^2 = e^{-\beta L}$. In addition, note that since r and τ are defined as the reflection and transmission coefficients for the electric field, their relationship is such that

$$|r|^2 + |\tau|^2 = 1. \tag{2.79}$$

The ratio of the input and output fields, i.e. the portion of light which leaves the resonator, can be calculated by combining equations 2.78, 2.77 and 2.79 to get the following result

$$\frac{E_{\text{Out}}}{E_{\text{In}}} = e^{(\phi+\pi)} \frac{a - \tau e^{i\phi}}{1 - \tau a e^{i\phi}}. \tag{2.80}$$

In order to obtain a useful metric to characterise the microrings, one should calculate the absolute-square of this function, which tells us the ratio of field intensities as opposed to their amplitudes. Since for a complex number $|z|^2 = z^* z$ and $(z_1/z_2)^* = (z_1^*/z_2^*)$ it follows that the output transmission T_{Out} becomes

$$\begin{aligned} T_{\text{Out}} \equiv \left|\frac{E_{\text{Out}}}{E_{\text{In}}}\right|^2 &= \frac{(\alpha - \tau e^{i\phi})(\alpha - \tau e^{-i\phi})}{(1 - \tau\alpha e^{i\phi})(1 - \tau\alpha e^{-i\phi})} \\ &= \frac{\alpha^2 + \tau^2 - 2\alpha\tau\cos\phi}{1 + (\tau\alpha)^2 - 2\alpha\tau\cos\phi}. \end{aligned} \tag{2.81}$$

The field enhancement inside the cavity may be calculated in a very similar way giving

$$\frac{E_{\text{C}}}{E_{\text{In}}} = \frac{-r}{1 - \tau\alpha e^{i\phi}} \tag{2.82}$$

which follows that

$$T_{\text{Cavity}} = \left|\frac{E_{\text{C}}}{E_{\text{In}}}\right|^2 = \frac{1 - \tau^2}{1 + (\tau\alpha)^2 - 2\alpha\tau\cos\phi}. \tag{2.83}$$

Hence the two important parameters which describe the effects of the microring are the cycle loss factor α and the transmission coefficient τ. By looking again at equation 2.81, it is clear that the output field must be a minimum on resonance where $\alpha = \tau$, since in this case the equation reads

$$\frac{2\tau^2(1 - \cos\phi)}{1 + \tau^4 - 2\tau^2\cos\phi} \tag{2.84}$$

which becomes zero when ϕ is a positive integer multiple of 2π. In addition, this must be the best possible resonance condition since T_{Out} is strictly positive. From here it is natural to define three operating regions based on the relative values of α and τ

- Under-coupling region: where light is lost inside the cavity faster than it is gained, $\alpha < \tau$.
- Critical-coupling region: The loss matches the coupling ($\alpha = \tau$).
- Over-coupling region: More light is coupled into the resonator than is lost, $\alpha > \tau$.

The relative effects of these three regions are explored numerically in figure 2.10. Here the transmission (left y-axis) represents T_{Out} and the enhancement (right y-axis) represents T_{Cavity}. It can be seen from the figure 2.10**c** that the critical-coupling region also matches that of greatest field-enhancement. The significance of the enhancement will be explored in the next chapter within the context of integrated single-photon sources.

In the case of a double-bus microring resonator, the same analysis can be applied, except this time with two coupling regions described by an additional parameter τ', representing the coupling coefficient to the bus waveguide. In this case the transmission intensity factor is given by the following relationship

$$T'_{\text{Out}} = \frac{\tau'^2\alpha^2 - 2\tau'\tau\cos\phi + \tau^2}{1 - 2\tau'\tau\cos\phi + (\tau'\tau\alpha)^2}. \tag{2.85}$$

In this case light which leaves the bus waveguide acts as additional losses inside the resonator cavity. The coupling to the bus waveguide is described by the following relation

$$T'_{\text{Drop}} = \frac{(1-\tau'^2)(1-\tau^2)\alpha}{1 - 2\tau'\tau\cos\phi + (\tau'\tau\alpha)^2}. \tag{2.86}$$

Figure 2.9 shows the numerical simulation of such a double-bus microring resonator by using the standard component library in Lumerical Mode software. Here one can see that the resonance position now shows maximum coupling to the bus waveguide (bottom left output) which limits the enhancement. The off-resonance position (ϕ out of phase) gives maximum transmission through the input waveguide.

2.5.8 Crossers

Waveguide crossers are integrated optical components that allow the overlap of two separate waveguide structures with minimal or no optical effect on the output of each waveguide. In other words, the transformation matrix should apply a swap to the two optical modes which is written

$$\hat{U}_{\text{Swap}} = \begin{pmatrix} 0 & 1 \\ 1 & 0 \end{pmatrix}. \tag{2.87}$$

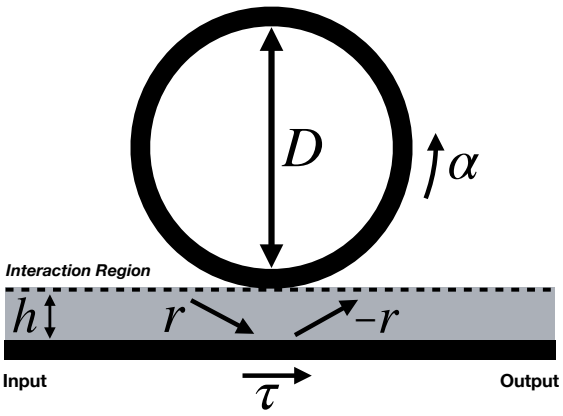

Figure 2.8: A schematic showing the general idea behind a micro-ring resonator. Light entering the top left waveguide becomes coupled to the ring structure, which can be tuned by controlling the lengths h and d. In addition, local heating can tune the optical path-length difference and tune the resulting resonances one sees.

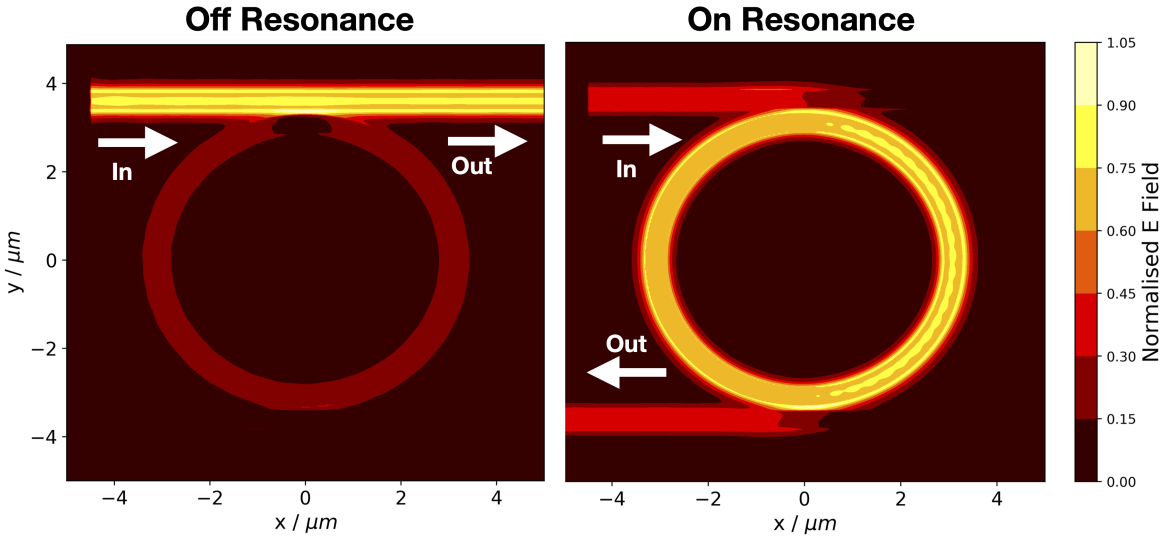

Figure 2.9: FDTD simulation of a standard (double bus) microring structure. Here $\approx 1550nm$ light is incidence from the top left channel of the resonator. Light in the waveguide interferes inside the microring structure and depending on the wavelength can be maximally coupler to either the top right waveguide or bottom left waveguide as shown in the two diagrams. Here the 'off resonance' position was at $\lambda = 1550nm$ and the 'on resonance' position was at $\lambda = 1558nm$.

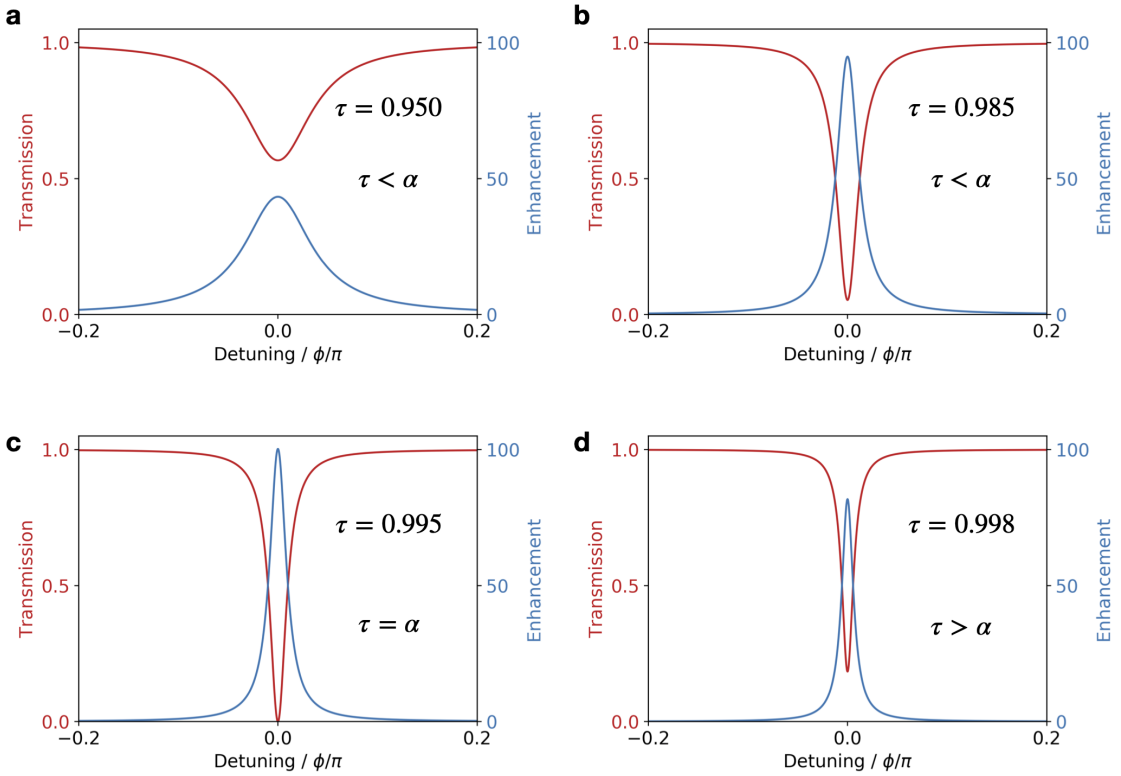

Figure 2.10: Single-Bus MRR E Field Intensity Transmission and Enhancement. Figures **a-d** show the predicted transmission (red) and enhancement (blue) intensities, as a function of the detuning parameter $\phi(L, \lambda)$ whose arguments are the ring circumference L and wavelength λ. In each figure, the optical transmission intensity, T_{Out}, and cavity enhancement, T_{Cavity}, are calculated by using equations 2.81 and 2.83, respectfully. The value of the loss parameter is $\alpha = 0.995$ and the transmission factor τ is specified in each plot, along with the coupling region. In both the over-coupled (**a,b**) and under-coupled (**d**) scenarios, the characteristic transmission dip is limited in visibility (does not reach zero). At the critical coupling, the field intensity inside the ring is maximum.

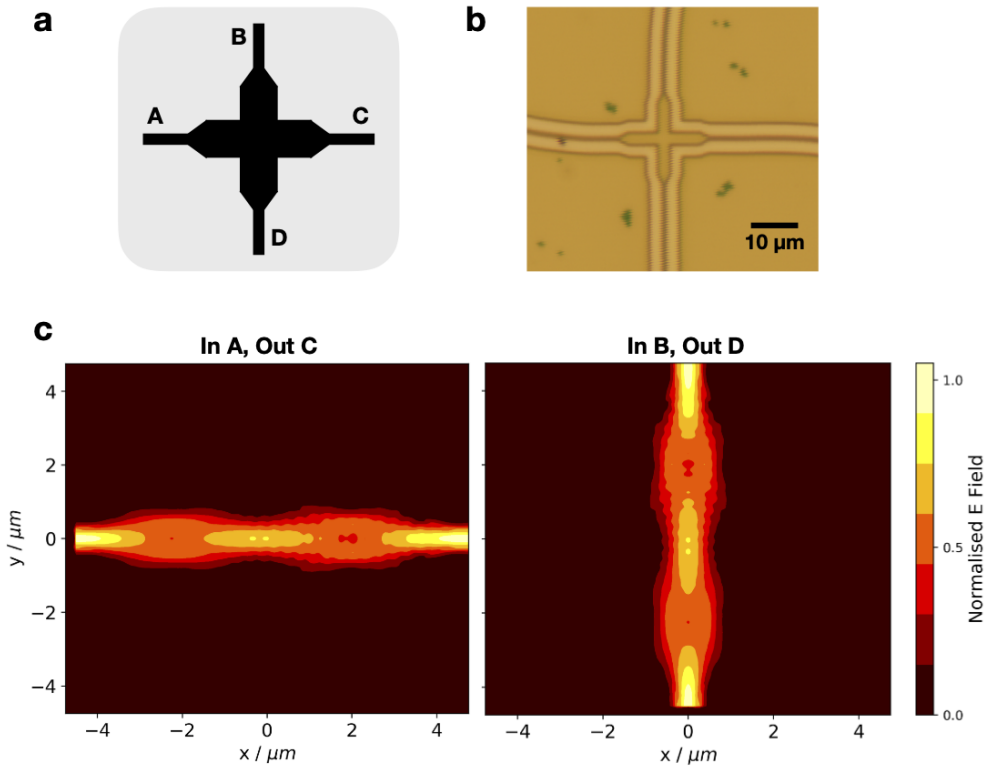

Figure 2.11: Waveguide crosser. **a** Diagram representation of waveguide crosser design. Waveguide tapers are designed to reduce losses and waveguide crossing section design to minimize mode overlap. **b** Optical microscope image of a waveguide crosser on-chip (4D receiver). **c** FDTD simulation using Lumerical software. The left image shows a Gaussian mode profile entering from waveguide A (see diagram in **a**), and right image shows light entering port B. In each case the light passes through the interaction region without loss.

Since the general approach used in this thesis is to encode quantum information simultaneously in multiple different waveguides, it is often convenient (and for some experiments completely necessary) to restructure the physical waveguide layout such that multiple pairs of modes can be interfered. This exact operation can be achieved by placing two waveguides adjacent to one another, each with a taper. The result is minimal overlap between the two fields. Figure 2.11**a** shows a schematic for such a crosser, whilst figure 2.11**b** shows a numerical simulation of a standard crosser component from the Lumerical optical library.

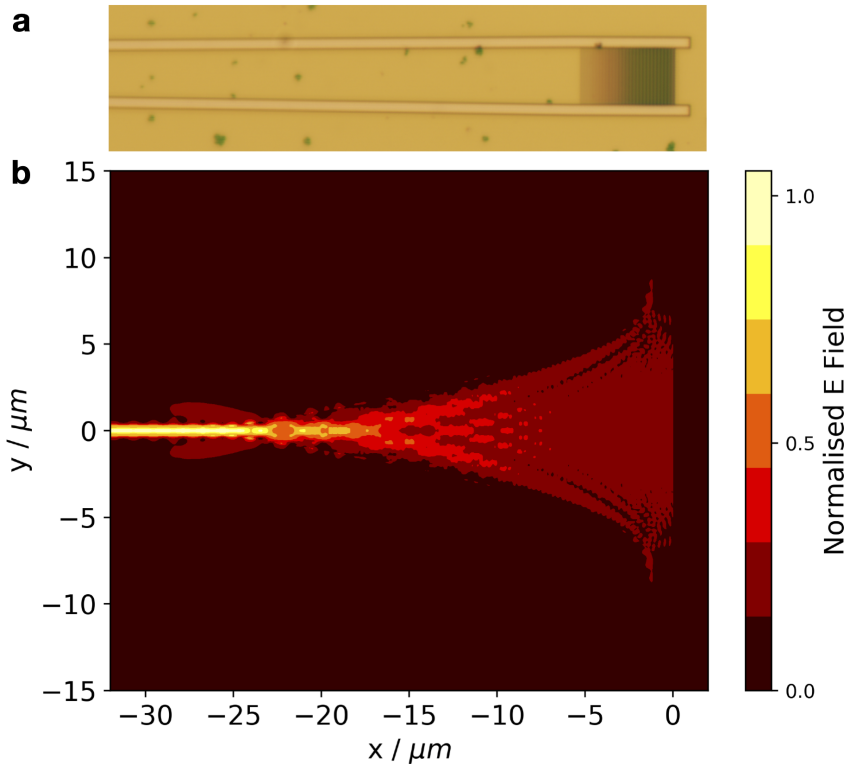

Figure 2.12: Grating coupler simulation. **a** Optical microscope image of grating coupler into tapered waveguide. **b** 2D FDTD simulation of grating coupler, where the contours show the normalised electric field.

2.5.9 Chip to Fibre Coupling - Grating Couplers

Throughout the experiments in this thesis, it is often necessary to couple light in or out the integrated chips. For example, pulsed lasers couple from fibre to chip and single photons couple from chip to fibre. One of the difficulties of this is that the core of a single mode fibre is roughly an order of magnitude larger than the integrated silicon waveguides, $\approx 8\mu m$ vs $0.5\mu m$. Efficient coupling, however, is necessary since single photon states are sensitive to losses and cannot be amplified due to the no-cloning theorem. In this thesis, grating couplers are used on chip in order to guide the light in or out of the chip, where the silicon waveguides taper in width to match the fibre width. Periodically etched gratings on the chip cause destructive interference that transmits coupled light at a tangential angle θ away from the chip, where θ depends on the wavelength of light inside the chip. The efficiency of the gratings depends on the design, where in our specific case a mixture of highly efficient ($\approx$ 1 dB) gratings are used on the primary device and $\approx$ 3 dB gratings are used on receiver devices. Figure 2.12 **a** shows an image of the standard design, whilst **b** shows the simulation of a standard grating coupler utilising Lumerical software.

In addition to these single mode grating couplers, two integrated waveguides can be brought perpendicular to one another and the gratings can be superimposed at 90 degrees. In this configuration, the gratings are referred to as two-dimensional, where one of the modes coupled horizontally polarised light and the other vertical. The 2D approach, see section 3.1.1.4, are used in this thesis for quantum demonstration where path encoded qubits $|0/1\rangle$ are converted to polarisation encodings $|H/V\rangle$ for chip-to-chip transmission.

CHAPTER 3

DEVICE DESIGN, CHARACTERISATION AND PERFORMANCE

Chapter 2 introduces the reader to the motivations of quantum information processing with photons. In addition, ideal integrated photonic components are described which are, in principle, able to encode quantum information in single photons on chip. The goal of this chapter is to expand on those findings, and to comment on the proximity between these ideal devices and current state-of-the-art integrated silicon photonic components. Moreover, we benchmark multiple integrated single photon sources on chip based on a micro-ring resonator design. We show that the properties of these resonator sources are sufficient to perform multi-photon, and therefore multi-qubit, operations on a photonic chip. We acknowledge Jianwei Wang for his work on photonic chip design, Yunhong Ding for component design and chip fabrication and Imad Faruque for his experimental expertise on the topic of heralded single photon indistinguishability measurements (PIM). Unless stated otherwise, in the following work within this chapter, I am responsible for building the experiment setup, programming and calibrating the devices, designing the experiments, data collection and data analysis.

3.1 Device Specifications and Performance

This thesis contains experiments across three integrated silicon devices comprised of one transmitter circuit and two receiver circuits. In this section, the main transmitter device is introduced and characterised. This transmitter is manufactured in the silicon-

on-insulator (silicon waveguides on silica substrate) platform. All of the single device measurements in this thesis were achieved through the calibration and reconfiguration of the main transmitter circuit, which is referred to interchangeably as Alice or Transmitter Device throughout this thesis. In this chapter, the transmitter circuit was used as the primary device for all on-chip single photon generation experiments. As a result, this chapter focuses only on the design of the main transmitter device, which was designed to achieve a large range of quantum optics experiments in a single device. This chapter discusses the design and performance of each of its components, and aims to summarise the general design of the device shown in figure 3.1. In many of the experiments performed in this thesis, only a fraction of the total components are utilized at any one time, and hence in many scenarios, simplified schematics will be given in order to aid the reader and add clarity in each case. The specific design and functionality of the chip will be expanded on and discussed in-depth in the later chapters of this thesis in the context of their implementations.

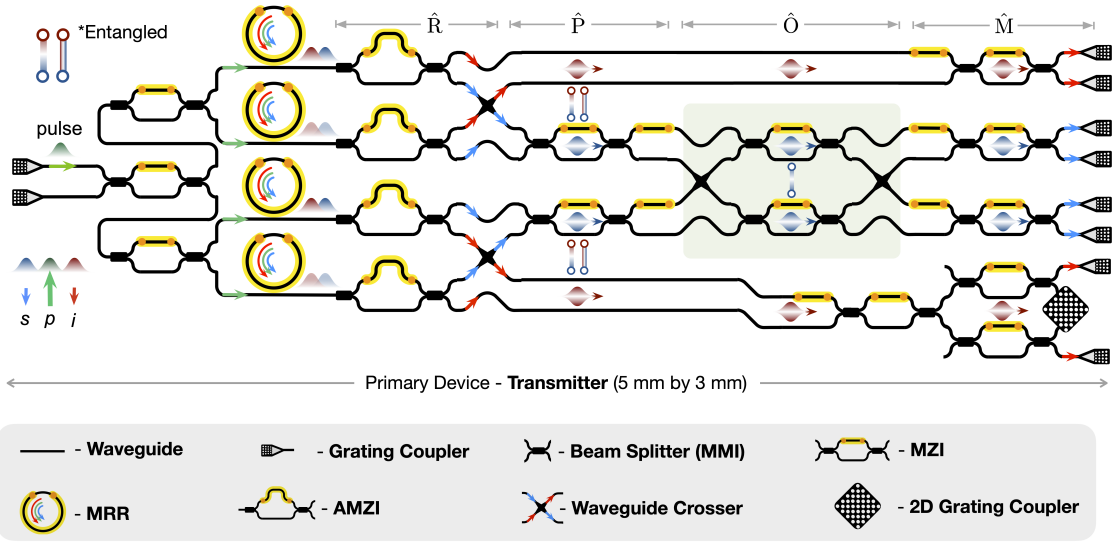

Figure 3.1: Schematic of the Transmitter chip (Alice) used during these experiments. The chip is designed to be highly reconfigurable and able to perform a large range of quantum optic demonstrations. Red and Blue arrows show (in general) where the photons (created in the rings by SFWM) are configured in the chip. Blue, green and red pulses represent signal, pump and idler frequencies, respectively. Arrow labels at the top of the diagram represent the core design of each section - $\hat{R}$ rotation, $\hat{P}$ preparation unitary, $\hat{O}$ operator, and $\hat{M}$ measurement. Red and blue vertical bars represent where photons may be entangled or separated on chip, depending on the configuration. The grey oval below the schematic shows the list of basic components used in the design of Alice. Here black lines represent optical waveguides (silicon core, glass cladding) and the yellow highlighted regions represent heaters and electronic control. On each of the heaters, two orange dots represent the electrical contact points that allow current to pass through the heaters. Each component is discussed in more detail in the previous chapter, section 2.5. For an analysis on the non-linear enhancement of the MRR structures and their use as single-photon sources, see section 3.3

.

3.1.1 Device Design

In each of the following sections key experimental parameters are measured and compared against their expected values. The verification of these key parameters, such as group index and filter FSR, is crucial for the calibration of quantum optic experiments on chip.

3.1.1.1 Optical Coupling & Group Index

In all of the integrated silicon devices in this thesis, the standard strip waveguide geometry is 450 nm×250 nm. These dimensions are also used in order to simulate the characteristic waveguide modes in section 2.5.2, and are therefore expected to be well-aligned with the measured results. Due to the roughness on the sidewalls due to fabrication tolerances, we use light which is polarised in the fundamental TE_0 mode at $\lambda_p = 1550\ nm$. This polarisation choice gives a mode profile concentrated at the centre of the waveguide cross-section, see the numerical simulation in figure 2.2. This configuration should therefore obtain a significantly higher optical transmission where the optical losses due to scattering at the waveguide sidewalls are minimised. In practice, this is optimised by utilising a polarisation controller at the input of the chip, where the correct polarisation setting is found to maximise the coupling efficiency through the optical circuits. This can be easily measured by placing a fibre-coupled optical power meter at one of the chip output ports and manually maximising the measured power. Along this polarisation, coupling through chip test structures comprising (≈ 1 cm) straight waveguides and 2 grating couplers achieved a minimum optical loss of around −4 dB. This is measured by an optically coupled 24 channel fibre array with a CW laser at λ_p with an average input power of 0 dBm= 1 mW.

In order to experimentally determine the group index of the integrated waveguides, a test structure comprised of a single-bus coupled microring resonator was fabricated. By measuring the microring FSR, one may easily infer the group index. The FSR_λ of an MMR as measured at wavelength λ is given by

$$FSR_\lambda \equiv \Delta\lambda = \frac{\lambda^2}{n_g L}, \tag{3.1}$$

where n_g is the group index of the waveguide and L is the perimeter of the MMR. As a result, the group index can be determined by inferring the FSR from the measured optical spectrum as can be seen in figure 3.2. The transmission of the microring was taken by coupling a CW laser (around $\lambda = 1.55\mu m$) to the input port of the test MMR and measuring the optical transmission (optical power as measured in dBm) through the bus-coupled waveguide. The characteristic dips in optical intensity are caused by

the resonance condition inside the microring cavity, as described in greater detail in section 2.5.7. The test structure is designed with a radius $R = 200\mu m$ and the group index is estimated in the following way

$$n_g = \frac{\lambda^2}{2\pi R \Delta\lambda}, \tag{3.2}$$

where we have used $\Delta\lambda = \lambda_{\mathrm{res},n+1} - \lambda_{\mathrm{res},n}$ and $L = 2\pi R$ in order to perform the calculations in Fig. 3.2b. As predicted from the strip waveguide with geometry 450 nm×250 nm, the measured group index is in good agreement with the simulated value 4.31.

3.1.1.2 Micro-ring Resonators

Each of the four identical MRRs in the transmitter device are designed with a radius of $R = 27.68\ \mu m$ and corresponding FSR of 400 GHz. This FSR was chosen to match off the shelf lab equipment from the telecommunication industry, with a channel spacing that is compatible with the international telecommunication union (ITU) standardisation.

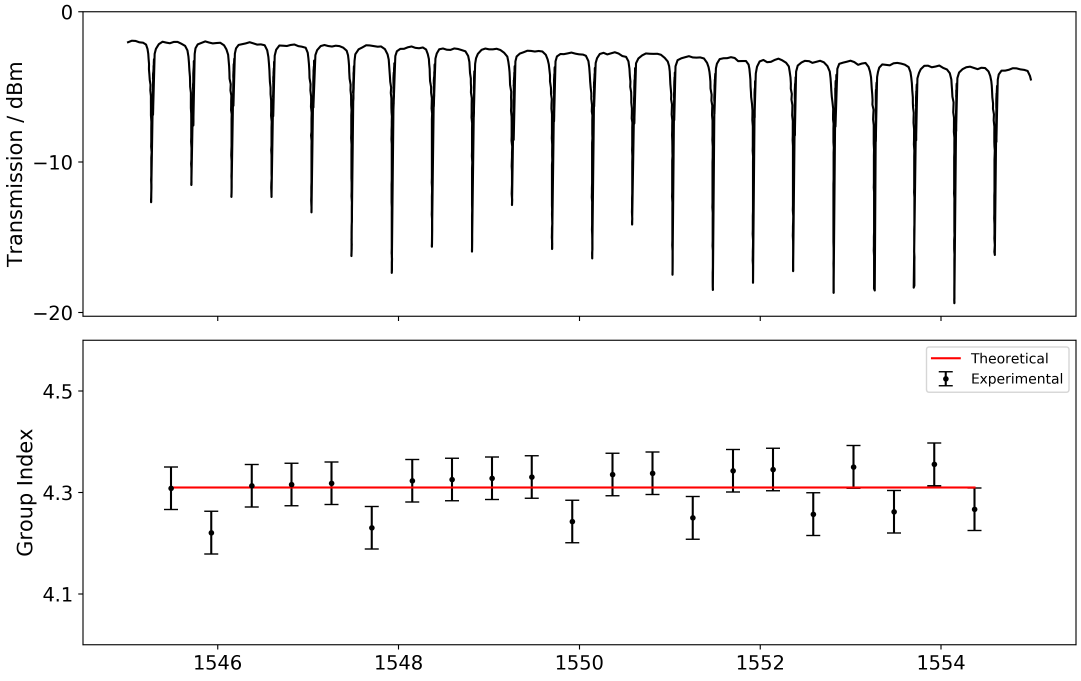

Figure 3.2: Measured optical transmission spectrum (Top figure) of test SOI MRR structures with R=200um at 1550nm. The lower figure shows the calculated group index values and standard deviation error bars of the SOI waveguides used in this thesis and are extracted from the top figure using equation 3.2. The resulting average 4.30 ± 0.04 is in agreement with the predicted value (4.31 - red line) estimated using Lumerical Mode Software and the nominal structure parameters.

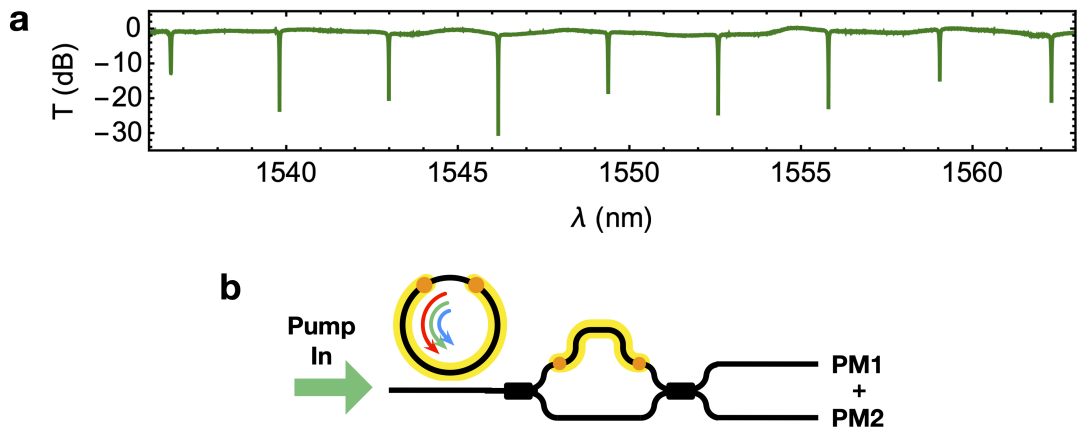

Figure 3.3: Optical Spectrum of MRR1 (top MRR). **a** Transmission spectrum of MMR1 situated at the top left of the transmitter chip. In order to achieve this, a CW laser was coupled to the chip via one of the input grating couplers. **b** shows how light leaving the ring is further spectrally filtered by an AMZI. PM1 and PM2 each represent two optical power meters at the output of each of the two waveguides. The optical power is then measured as a function of pump wavelength and the resulting spectrum in **a** is achieved by summing together the two spectra PM1 + PM2.

In order to measure the FSR channel spacing, a CW laser was coupled to the input waveguides in the chip and light was steered via MZI switches to the MRR. Figure 3.3b shows a simplified schematic and how the corresponding MRR spectrum is further split by an AMZI directly attached to the bus-coupled waveguide. Two optical power meters, PM1 & PM2, are fibre-coupled to the output waveguides and their readings (when measured in a linear scale) are added together to effectively erase the AMZI spectral contribution. The resulting spectrum should therefore directly correspond to the optical resonances inside the microring cavity, as shown in fig 3.3a over a $\approx 30nm$ range, and as described mathematically in section 2.5.7. The measured FSR were $\Delta\lambda = 3.21 \pm 0.03\ nm$ or alternatively in frequency $\Delta\nu = 400.9 \pm 1.5$ GHz, within one standard deviation of the target FSR.

3.1.1.3 On-Chip Filters - AMZI

The main transmitter device features four integrated MRR, each coupled into one arm of an unbalanced interferometer. These identical AMZIs are designed to spectrally filter the single photons produced inside the MRR cavities. For this reason they are designed to have broader bandwidth than the four MRR, as to effectively filter as many of the single photons as possible. For an introduction to AMZI and their spectral effects see section 2.5.6. Optical phase shifters on one arms of each AMZI allows the

centre of the interference fringes to be well aligned with each other and the MRR resonances. When well calibrated, the photon pairs that are produced inside the MRR cavity and subsequently coupled into the bus waveguide enter the interferometer in the same spatial mode (bunched) and leave in opposite spatial modes.

The four identical AMZI featured in the device are designed with two unequal arms corresponding to a path length difference equal to $\Delta L = 217.372\mu m$. The definition of FSR provided in equation 3.1 holds true for the AMZI, and so the theoretical design gives $\Delta\nu$ = 320GHz. As a result, the ratio of FSRs between the MRR sources and AMZI filters is expected to be approximately $\Delta\nu_{\mathrm{MRR}}/\Delta\nu_{\mathrm{AMZI}}$ = 400/320 = 5/4. The measurement FSR from the optical transmission spectrum (see figure 3.6) obtains a value of 320 ± 2GHz giving a measured FSR ratio of $\Delta\nu_{\mathrm{MRR}}/\Delta\nu_{\mathrm{AMZI}} = 1.25 \pm 0.02$, which is in direct agreement of the theoretical prediction. As a result, the optical alignment is such that for every 5 resonances (4 FSR) of the MRR, there will be 6 (5 FSR) AMZI resonances.

When aligned together using the thermal phase shifters, every 5th MRR resonance will be well-aligned with every 6th AMZI resonance. This means that every 6th MRR resonance will be anti-correlated with the corresponding AMZI resonance, and will optimally filter photons generated at those frequencies. Therefore, side-band MRR channels (λ_s, λ_i) were chosen at ± 3 resonances away from the pump in order to collect signal and idler photons. These channels are then further filtered off-chip in order to remove any photons present in the pump. After this filtering, the remaining single photons are connected to off-chip single photon detectors. Aligned MRR and AMZI channels are shown in 3.6 in order to see how this works in practice. Here the chosen signal, pump and idler channels, labeled left to right, are highlighted in white. In this figure, the signal resonance of the MRR is well aligned with the red (top) port of the AMZI and the idler resonance (6 MRR FSR away) is well aligned with the blue (bottom) port of the AMZI. These are used as the main channels used in the following experiments.

3.1.1.4 Sub-wavelength Grating Couplers

Sub-wavelength gratings formed from silicon waveguide structures can couple external light into supported optical modes of silicon waveguides. This method proves a convenient approach to transmitting and receiving photonic states between integrated photonic architectures and single-mode with low loss. Such coupling techniques are crucial for the near-term and long-term success of integrated quantum photonics.

For example, the primary goal of this thesis is to provide progress towards fully

integrated and scalable quantum photonic technologies. During the early demonstrations of such technologies, single photon quantum states were generated and prepared in bulk optics and coupled to passive devices whereby some quantum operation would be performed. The single photons would then be coupled off-chip and measured by stand-alone single photon detectors. In this work, and compared to early demonstrations, significant process has been made in generating and preparing single photon states on-device and in developing increasingly useful and programmable circuits in silicon.

Despite the fast progress, we retain a semi-integrated platform whereby strong pump fields are generated by off-chip lasers and coupled on-device with low loss. Perhaps more crucially, due to the lack of integrated single-photon detectors, single photons generated inside the device must be effectively coupled to single mode fibres and sent remotely to efficient single-photon detectors. As a result, the efficient coupling of photon states is crucial for the work in this thesis. Moreover, even for fully integrated architecture's whereby lasing, single photon generation filtering and detectors are integrated into a single device, quantum communication protocols will inevitably rely on the ability to transmit quantum particles between chips with high efficiency.

In our devices, we utilise sub-wavelength GCs designed and optimised by Y. Ding et al [107]. In order to increase coupling efficiency, an apodized crystal structure is formed in silicon which mode matches a single mode fibre and a $100nm^2$ (aluminium) mirror reflects light from below the lower cladding, able to increase the coupling efficiency. The optimal coupling wavelength λ from such a structure may be calculated in terms of the effective index n_{eff}, upper cladding index n_0 (air) and length of the scattering unit l_i by the following relationship

$$\lambda = l_i(n_{\text{eff}} - n_0 \sin\theta), \tag{3.3}$$

where θ represents the angle between the surface normal (to the chip) and the single mode fibre. In our experiments the optimal angle is found to be 15° in order to maximise coupling at $\lambda = 1550nm$. In addition, the profile of the coupled mode can be tuned by optimising the photonics scattering unit parameters (n_{eff}, l_i), which are predicted to give Gaussian output profiles in our experiments. The width of the crystal structure, as shown in fig 3.4, is approximately 345 nm which gives a total insertion loss per coupler (TE polarised) of approximately 0.8 dB at $\lambda = 1550nm$.

In addition to the 1D grating structures discussed so far, the the transmitter device features the inclusion of a 2D grating coupler structure. These structures are formed by the superposition of two 1D gratings at right angles with one another. The resulting structure is able to efficiently couple both horizontal and vertical polarisation's to

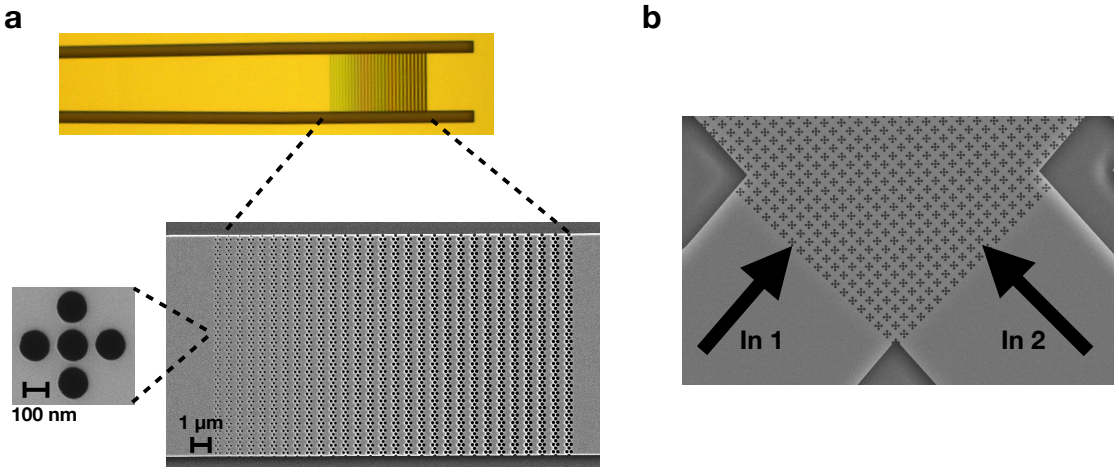

Figure 3.4: Images of the integrated grating couplers. **a**, optical image (top) and SEM (bottom) image of the single mode grating couplers optimised for $\lambda = 1550nm$ at an angle 15°. **b**, SEM image of a 2D grating coupler. Credit: the SEM images were taken at the Technical University of Denmark directly after fabrication by Dr Yunhong Ding.

a single mode fibre. These are used throughout this thesis in order to exchange information encoding between path and polarisation in order to remotely connect different integrated devices. As a result, the qubits $|0\rangle$ ($|1\rangle$) mode couples to the fibre with a $|H\rangle$ ($|V\rangle$) polarisation, and therefore an arbitrary path encoded qubit $|\psi\rangle$ evolves as

$$\begin{aligned} |\psi\rangle &= \alpha|0\rangle + \beta|1\rangle \\ &\rightarrow \alpha|H\rangle + \beta|V\rangle, \end{aligned} \tag{3.4}$$

where $|\alpha|^2 + |\beta|^2 = 1$. The converted qubit can then be transformed back to path encoding on a receiver device through an identical 2D grating coupler, a technique that has been experimentally demonstrated with single photons [108]. Scanning electron microscope (SEM) images of the 2D grating design can be seen in figure 3.4b.

3.1.2 Device Fabrication

The integrated silicon devices discussed within this thesis were all fabricated by Dr Yunhong Ding from the Technical University of Denmark (DTU). This section discusses some of the fabrication techniques and processes that were used in order to develop these devices. This section is included for completeness and is taken in part from the authors published works within the following reference [109].

In on-chip quantum experiments, decreasing optical losses, in particular coupling loss and insertion loss of quantum optical components, is critical. For this purpose, we

achieve ultra-high efficiency grating couplers by preparing a sophisticated Silicon-on-Insulator (SOI) platform with bonded Al mirror [107]. It starts from a commercial SOI wafer with top Silicon thickness of 250 nm and a buried oxide layer of 3 μm. Firstly, 1.6 μm thick SiO_2, which is an optimum thick SiO_2 for fully-etched grating coupler with Al mirror [107], is deposited by the plasma-enhanced chemical vapour deposition (PECVD) process on the SOI wafer. After that, the Al mirror is deposited by electron-beam (ebeam) evaporator, and followed by another thin layer of SiO_2 deposition with thickness of 1 μm. The wafer is flip-bonded to another Silicon carrier wafer by Benzocyclobutene (BCB) bonding process. The final Al-introduced SOI wafer is consequently achieved by removing the substrate and buried oxide (BOX) layers of the original SOI wafer. The Silicon photonic circuit with fully-etched apodized grating couplers using a photonic crystal [110] are fabricated by standard ebeam lithography (EBL) followed by Inductively Coupled Plasma (ICP) etching and ebeam resist stripping. After the photonic circuit part is fabricated, 1.3 μm thick SiO_2 is deposited by PECVD, followed by chemical mechanical polishing (CMP) process to planarize the surface with approximately 300 nm sacrifice, resulting in a final top SiO_2-cladding layer of 1 μm. The micro-heaters are patterned afterwards by standard ultraviolet (UV) lithography process followed by 100 nm titanium (Ti) deposition and liftoff process. The conducting wires and electrode pads are obtained by a second UV lithography followed by Au/Ti deposition and lift-off process.

Our fabrication platform enables a propagation loss of ~2 dB/cm measured by the cut-back method for the standard fully-etched Silicon waveguide with a geometry of 450 nm×250 nm. Figure 3.5a shows the characterisation of 1d SGCs. Thanks to the the Al-mirror, a peak coupling efficiency of -0.8 dB at 1555 nm, with 1 dB bandwidth of 40 nm is achieved. The 2×2 multimode interferometers (MMIs) are developed for 50:50 beamsplitters. In order to characterise the thermal tunability of the Ti heater and splitting ratio, insertion loss of the 2×2 MMI structures, we implemented an AMZI filter with a Ti micro-heaters applied on one arm as phase-shifters. Note that this AMZI is only used for testing the performance of MMIs and phase-shifters, which have a different FSR to the ones in Fig. 3.1A and section 3.1.1. In this situation, applying a heating power to the Ti micro-heater results in a change of the refractive index in the Silicon waveguide, inducing a phase shift and thus transmission shift. As shown in Fig. 3.5b, 14.5 mW heating power results in a transmission shift of more than one FSR. The resistance of the Ti heaters is measured to be around 500 Ω. Such efficient Ti heaters enable us to efficiently fully reconfigure the quantum circuit to prepare, operate and measure different quantum states, and also precisely align the four MRRs

to obtain indistinguishable single photon generation. Moreover, the transmission presented in the inset of Fig. 3.5b is less than 0.1 dB, indicating a insertion loss less than 0.05 dB for each 2×2 MMI. The high extinction ratio in Fig. 3.5b also confirms the highly balanced splitting ratio in the MMIs.

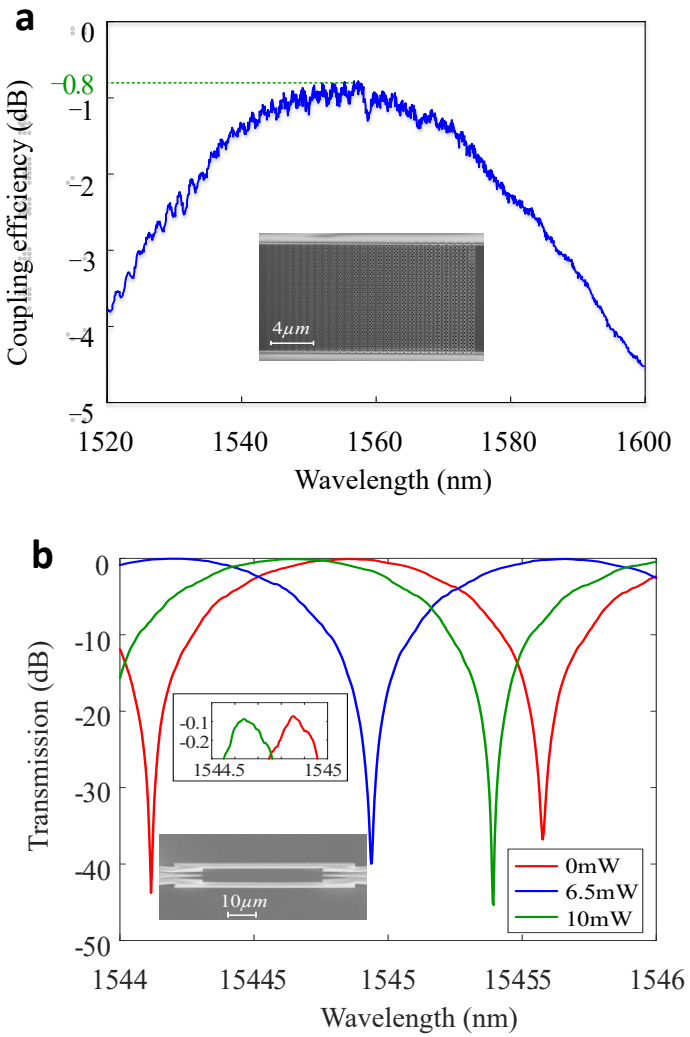

Figure 3.5: Characterisations of the integrated optical components. **a,** measured spectrum for a fully etched 1d-dimensional grating coupler on the Silicon-on-Insulator platform with Al mirror. **b,** measured spectrum for a thermal-tunable AMZI used in the Silicon circuits. The scanning electron microscope (SEM) images of the fabricated grating coupler with one-dimensional photonic crystal and 2×2 MMI are presented in each figure. Credit: the SEM images were taken at the Technical University of Denmark directly after fabrication by Dr Yunhong Ding.

3.1.3 Tunability and Alignment

The overall chip performance at any quantum information task depends largely on the accurate calibration of active components. This maximises the transmission of photons along the correct optical paths in order to prepare quantum states with high accuracy. The method for device characterisation was as follows. First, a CW laser at 0 dBm is coupled to the chip through one of the 16 available optical ports. In many cases, the laser is coupled directly to one of the optical ports of the component to be calibrated. A current vs voltage curve is recorded over the voltage range of $(0,4)$ V and an order 4 non-linear curve fit model fits the data giving $I(V) \equiv f(V)$, and is saved to a calibration file. Next, the optical power at each output port is recorded as a function of heater power, which gives an interference pattern for each MZI and AMZI. Here the heater power is also a function of voltage $P(V) = VI(V) = Vf(V)$. Finally, the interference fringes are fit with a sinusoidal function that matches the MZI fringe predicted in section 2.5.5. From the best fit parameters, the optical phase can be extracted as a function of heater voltage. Once the calibration is complete, the specified parameter is the desired optical phase shift that matches the unitary transformation required by the experiment, see figures 4.1, 4.4 and 5.3 for details on these phase settings. Once the calibration is complete, optical alignment can be achieved through the correct phase settings, an example of which is shown in figure 3.6 where the chip is configured such that an AMZI and MRR are both well aligned with the signal and idler channels of an off-chip filter.

This configuration is of particular interest for single photon measurements, where the role of the on-chip filtering is to separate signal and idler photons, and the off-chip filters allow pump suppression. The off-chip pump suppression is approximately 100 dB from the pump channel relative to the signal and idler channels. An additional off-chip filter is used on the input of the chip in order to suppress optical noise in the signal and idler channels that may lead to false single photon counts. The number of spurious pump photons that are transmitted through the filter can be easily estimated by assuming that each photon is centred at $\lambda = 1550nm$, having energy $hc/\lambda \approx 1.33 \times 10^{-18}\ J$ giving of the order of 10^{14} photons per second. After the filtering this reduces the number of leaked photons to around 10^4, similar to the number of dark counts seen on the single photon detectors and becomes undetectable once the chip losses and detection efficiency is taken into account.

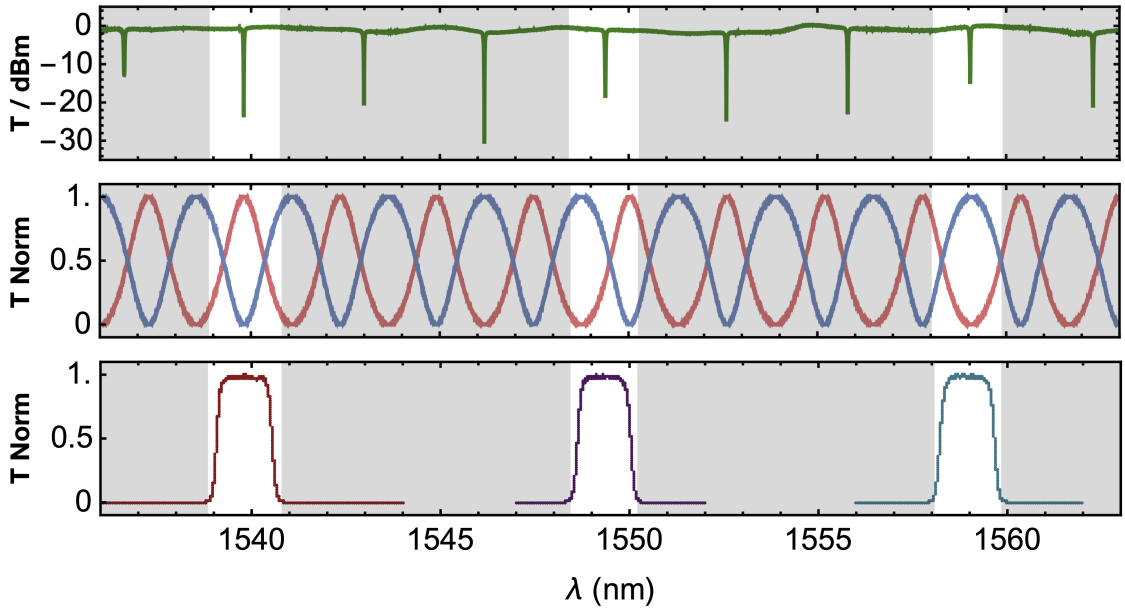

Figure 3.6: On-device Filtering and Programmability. The top figure shows the resonances of one of the microring resonators. The spectrum analysis was taken in the same way as shown in section 3.1.1.2 and fig 3.3. The middle figure shows the normalised transmission spectra of the AMZI where the blue (red) curve represents the optical power measured from the top (bottom) port. The bottom figure shows the normalised transmission spectra of the off-chip WDM filters which are fixed. The integrated heaters on each AMZI and MRR can shift the optical spectra in order to align each of the channels. The greyed sections are used to guide the eye to the fact that each of the channels, referred to from left to right as signal ($\lambda_s \approx 1539nm$), pump ($\lambda_p \approx 1549nm$) and idler ($\lambda_i \approx 1558nm$) are well aligned with each other. This means that single photons that are emitted from the sources are filtered on-chip and later 'cleaned' (removing pump photons) off-chip by the WDMs.

3.2 Practical photon pair sources on the SOI platform

3.2.1 Ideal Sources

An ideal single photon source is one which emits an on-demand stream of identical and pure single photon states on-chip. The ultimate goal is to construct devices that contain large numbers (many millions) of ideal sources such that N identical and pure single photons are controlled in M spatial modes. By utilizing active optical components arbitrary unitary transformations can be conducted on those M modes through well-known schemes [6, 111, 112]. By constructing gates between successive photons one can build complex photonic states on-chip for quantum applications in

communications and computing [66, 113].

In this section we explore why the requirement for highly pure photonic states arises from the need for high visibility quantum interference. As described in section 2.4, the ability to deterministically interfere single photons depends on a large range of quantum information phenomena which are the building blocks of quantum technologies such as quantum entanglement generation required in communications and computations. We have seen in these earlier sections how ideal Fock states, when applied to linear optics and path encoding, may result in entanglement generation and secure communication protocols - both rudimentary exercises for any advanced quantum device. The natural question arises then, how is it possible to produce these pure single-photon states. Alternatively, as we will see in greater details in this chapter, with the lack of ideal single photon sources, under what condition can we approximate single Fock states in integrated photonics.

3.2.2 Approximating Single Photons via SFWM

In section 2.2.3 we describe SFWM in the context of silicon waveguides. Due to silicons strong $\chi^{(3)}$ nonlinearity and absence of the $\chi^{(2)}$ nonlinearity, we therefore describe the effective Hamiltonian and unitary transformation of spontaneous four-wave mixing through the nonlinear waveguides of interaction length L. Here we explain this result in the context of single photon sources, how the presence of SFWM in silicon waveguides gives the tensor product of many two-mode squeezed states and how the number of squeezers depends directly on the factorability of the JSA $f_{\text{SFWM}}(\omega_s, \omega_i)$.

In silicon quantum photonics, photon-pairs are emitted by nonlinear sources due to spontaneous four-wave mixing. The interaction Hamiltonian and corresponding unitary transformation of this procedure is described in more detail in section 2.2.3. The resulting quantum state which arises from the interaction is the tensor product of various two-mode squeezed states, as can be seen in the following way. Take the unitary transformation $\hat{U}_{\text{SFWM}}$[1]

$$\hat{U}_{\text{SFWM}} = \exp\left[-\frac{i}{\hbar}\left(A \int \mathrm{d}\omega_s \mathrm{d}\omega_i f_{\text{SFWM}}(\omega_s, \omega_i) \hat{a}_s^\dagger(\omega_s) \hat{a}_i^\dagger(\omega_i) + \text{h.c.} \right) \right], \tag{3.5}$$

where $f_{\text{SFWM}}(\omega_s, \omega_i)$ is the joint-spectral amplitude (JSA) as described in equation B.10 which describes the energy and momentum conservation properties of the FWM process. The spectral purity of the resulting state depends directly on the separability of the JSA. In general, it is possible to take the spectral decomposition

[1] See derivation in appendix B.

according to the singular value decomposition theorem [114]

$$-\frac{i}{\hbar}A f_{\mathrm{SFWM}}(\omega_s,\omega_i)=\sum_k a_k g_k^*(\omega_s)h_k^*(\omega_i), \tag{3.6}$$

where g_k and h_k each form a complete set of orthonormal functions and a_k represents some complex amplitude. Notice that the set a_k is not necessarily normalised, and will be dependent on many factors such as pumping strength which contributes to the amplitude A and phase matching which contributed to f_{SFWM}. By making the substitution, the resulting transformation can be seen as

$$\begin{aligned}\hat{U}_{\mathrm{SFWM}} &= \exp\left[\sum_k a_k \hat{A}_k^\dagger(\omega_s)\hat{B}_k^\dagger(\omega_i)+\mathrm{h.c.}\right]\\ &= \otimes_k \exp\left[a_k \hat{A}_k^\dagger(\omega_s)\hat{B}_k^\dagger(\omega_i)+\mathrm{h.c.}\right]\\ &= \otimes_k \hat{S}_k^{ab}(-a_k),\end{aligned} \tag{3.7}$$

which represents the tensor product of the k^{th} state $\otimes_k$ of the twin-beam squeezers $\hat{S}_k^{ab}(-a_k)$ in the k^{th} spectral mode, and where the operators $\hat{A}_k^\dagger$, $\hat{B}_k^\dagger$ are defined as

$$\begin{aligned}\hat{A}_k^\dagger &= \int \mathrm{d}\omega_s g_k^*(\omega_s)\hat{a}_s^\dagger\\ \hat{B}_k^\dagger &= \int \mathrm{d}\omega_i h_k^*(\omega_i)\hat{a}_i^\dagger.\end{aligned} \tag{3.8}$$

As a result, for each spectral mode with non-negligible amplitude a_k, the resulting state $|\Psi\rangle$ picks up a contribution $|\zeta_k\rangle$ where $|\Psi\rangle = \otimes_k |\zeta_k\rangle$ [115]. In each case the squeezer contributions may be written as a superposition of single photons in the Fock basis as

$$|\zeta_k\rangle = \sqrt{1-|a_k|^2}\sum_{n=0}^{\infty} a_k^n |n,n\rangle_{s,i}\,. \tag{3.9}$$

Rather unfortunately, the state that is generated by the SFWM transformation is far more complex than the desired single Fock state. In addition, as we have seen numerous times in chapter 2, pure Fock states are often required for many quantum information protocols and are the backbone of quantum information. Despite this disadvantage, however, one could still recover the desired pure state $|1,1\rangle$ by simply projecting onto the subspace spanned by the bi-photons Fock state $\hat{A} = |1,1\rangle\langle 1,1|$. Practically, this could be achieved by introducing single photon detectors that could effectively count the number of photons in each mode. These type of detectors are referred to as number-resolving, and is a significant challenge in quantum photonic technologies [116]. There are essentially two main approaches to achieving the resolution of photon number, inherent number resolving detectors that can directly measure

photon number [116–121], and pseudo number resolving systems that multiplex many single photon detectors to indirectly verify the photon number [122–126]. In recent work, a vast amount of progress has been made towards these ideal number resolving detectors [127] however, optimised standard (not number resolving) detectors remain higher efficiency [128] and are commercially available at telecomm wavelengths. In addition, the multiplexed schemes have the significant trade-off that they require large quantities of high efficiency single photon detectors which makes their application unrealistic for large-scale quantum technology experiments today. Once available, however, these technologies could allow the post-selection of pure states from highly squeezed states in order to generate pure single photons for quantum applications.

Another unfortunate property of the above squeezed state is that single photons are emitted into different spectral modes, where the fraction of photons in any particular mode is determined by the JSA. As we will see in sections 3.2.4.2 and 3.2.4.1, the shape of the JSA determines the extent to which the produced single photons can interfere with one another. This can be intuitively explained by the fact that only identical single photon terms experience quantum interference, and the distinguishable photons do not. This issue can be solved if the JSA is shaped such that photons are only emitted in a single spectral mode. In general, however, it turns out to be enough that the spectra of the produced signal and idler beams are uncorrelated with one another, i.e. that they are not entangled in the frequency domain [129, 130]. A standard approach for achieving this is to spectrally filter the produced broadband single photon spectra, although this introduces significant losses and limits the heralding efficiency [57]. This low heralding efficiency then limits the multiphoton terms that are required to scale the number of qubits that are encoded in single photon states. Another approach is to spectrally shape the JSA through the use of resonators [98, 131, 132], pulse pumping modifications [133] or through multi-mode SFWM [130]. In this thesis, microring resonator structures are utilised in silicon which have been shown to have an approximately pure JSA, with simulations estimating 92% purity.

The remaining significant issue is the control of multi-photon terms in ones experiment. The single photon detectors used in this thesis are commercial systems by the company 'Photon Spot', which obtain high ($\approx 90\%$) efficiency detection at $1550nm$. However, due to the scarcity of the resource, no photon number resolving implementations are utilised in the experiments throughout this thesis. Instead, single bi-photon states are approximated by tuning the squeezing parameter (by controlling the pumping strength) such that the probabilities of producing high photon numbers becomes negligible. For example, equation 3.9 describes a state which may produce n photon pairs, $\{ |1,1\rangle, |2,2\rangle \dots |n,n\rangle \}$, with relative probabilities $|x|^{2n}$, where in general x is

the squeezer strength[2]. For low squeezing strength then, it quickly becomes apparent that high order terms become negligible. An interesting property of equation 3.9 is that the squeezer strength, and therefore probability of emitting photon pairs, of each spectral mode depends directly on the spectral decomposition ($\{a_k\}$) of the JSA. There is therefore an interesting link between the spectra of the single photons and their counting statistics [115]. As a result, the approach to generating single photons throughout this thesis is to prepare micro-resonator enhanced SWFM which approximately produces twin-mode squeezers in a single spectral mode. Coincidence counts are then measured between the produced signal and idler photons such that the presence of one of the photons determines, with high probability depending on loss, a single photon in the opposite spectral mode.

The drawback then, is that the closer one gets to approximating the single photon-pair case, the lower the probability of producing single photons. This once again violates one of the conditions for an ideal single photon source - that is, one which emits deterministic single photons. This gives rise to the frustrating trade-off, the higher the squeezing strength, the higher probability one has on generating photons but the less knowledge one has on the number of produced photons. Thankfully, there are proposed solutions to this problem, the most promising of which is that of the multiplexed single photon source [134–138]. The solution proposes that many sources, each with low squeezing strength, may be combined in such a way that *at least one* source will produce a photon in any time interval. When combined with high efficiency detection, optical delay lines, fast switching and fast electrical feed-forward, one may indeed create a highly pure near-deterministic single photon source. Though the technological challenges in doing so may be far out of reach for today's standards.

In order to assess the effects of multipair emission, one can compute the probabilities $P(n_s, n_i)$ of producing n_s, n_i signal and idler pairs relative to the single pair case. The vacuum probability $P(0,0)$, single pair probability $P(1,1)$, multi-pair probability $P(>1,>1)$ and multipair vs single pair ratio ($P(>1,>1)/P(1,1)$) are given by

$$\begin{aligned} P(0,0) &= 1-|x|^2 \\ P(1,1) &= (1-|x|^2)|x|^2 \\ P(>1,>1) &= 1-P_{00}-P_{11} \\ &= |x|^4, \\ \frac{P(>1,>1)}{P(1,1)} &= \frac{|x|^2}{1-|x|^2}. \end{aligned} \tag{3.10}$$

[2]See section 2.2.2.3 for an introduction to squeezed states.

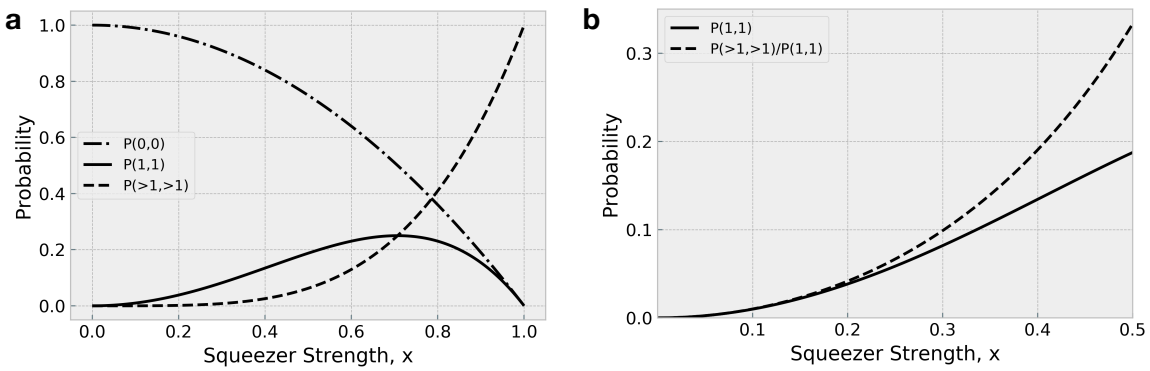

Figure 3.7: N Photon-pair Probabilities. $P(0,0)$, $P(1,1)$ and $P(>1,>1)$ represent the probability of producing 0, 1 and more than 1 photon pairs, as plotted against squeezer strength x. Here one sees the natural trade-off between success probability and number purity. **a** shows the calculated probabilities for n photon pairs, whilst **b** highlights the ratio of these probabilities against $P(1,1)$.

In attempt to summarise the above conclusions, figure 3.7a shows the relative probabilities of producing n photon pairs from a twin-mode squeezed state. Figure 3.7b shows the ratio of probabilities of producing a single pair, vs more than one pair. Our aim should be to work in the region of maximum squeezing, given that the probability of multiple pair producing is of a few % compared with single pairs. The ideal scenario is then to choose squeezing strength in the range $x \in (0.1, 0.2)$ which gives a signal to noise ratio of approximately 1-4%.

3.2.3 Coincidence Measurements

The majority of quantum experiments in this thesis rely heavily on the ability to effectively generate and measure single photons. As described in section 3.2.2, the unitary transformation giving rise to four-wave mixing generates a state described by multi-mode twin-beam squeezed states, which through the simultaneous detection of photon pairs may arbitrarily approximate single photons in the low squeezing regime. This makes SFWM sources an ideal candidate for heralded single photon sources. Since we rely heavily on the coincidence detection between the produced photon pairs, it is of utmost importance we understand what is meant by a simultaneous detection.

Consider the following experiment, where one sends a pulsed laser (producing trails of identical pulses, centred at $\lambda = 1550nm$) through a non-linear waveguide producing single-mode twin-beam squeezed states at time intervals $\Delta = \tau$. Since the generated single photons are non-degenerate and distinguishable in frequency, we can spatially separate (demultiplex) the photons and send the two channels to separate detectors D1 and D2. In the standard approach, the stream of produced single photons

are detected at each detector, producing small currents which are measured and processed using an external time tagger. The role of the time tagger is to accurately count and record the time of each single photon measurement. Due to the physical (superconducting) mechanism of the single photon detectors, once a photon is detected the detector temporarily breaks down. This means that there is a small time window at which the detector is not operational and unable to detect more photons. This is referred to as dead-time and can be reduced to a few nanoseconds in today's commercial hardware. In principle this places an upper limit on the pulse repetition rate of ones laser, such that photon detection's are not systematically missed. However, in practice, when operating in the lower squeezing regime, one can in principle operate at larger repetition rates since the probability of consecutive pulse coincidences reduces rapidly. In order to determine the coincidences, one typically calculates the histogram produced by counting the pairs of photons and their associated time intervals.

In this experiment, single photons should be produced only at time intervals which are multiples of τ. One therefore expects to see a histogram which gives exactly zero counts outside of these intervals and peaks at each interval. In reality, noises in ones experiment tend to influence this picture. For example, ones pulse width gives a distribution around each peak, and dark counts caused by external sources of photons give unpredictable coincidences. In a practical experiment, one should integrate around each peak to calculate the true coincidences, and dark counts can be minimised or even time-averaged and subtracted from the peaks. The natural question arises, how are the sizes of the peaks related to the experiment parameters.

In the ideal case, where no losses are present and the detection efficiency is unity, it is expected that every produced photon pair is measured as a coincidence detection event. In the case of perfectly short pulses, the time interval between these individual detection events should measure zero. Again, in practice, experimental factors such as detector timing jitter (detector timing error) and time-tagging finite time-resolution may in principle effect these conclusions. However, with today's technologies these factors are manageable. For example, state-of-the-art time-taggers have a timing resolution on the order of a few picoseconds, comparable to the optical pulse-width in our experiments. Detector timing jitter, however, tends to be larger (tens of picoseconds) which acts to broaden the coincidence peaks one measures in time. The crucial factor is that these specifications are far smaller than the temporal repetition rate of ones laser, such that integrating over the coincidence peaks truly corresponds to photons produced within each pulse. The maximum repetition rate used in this thesis is 500 MHz ($2n$ sec), well within the timing errors of lab equipment. Therefore in actuality, we expect single photon pairs to produce coincidence measurements within tens of picoseconds of one

another[3].

In this perfect transmission case, we expect the ratio of peak intensities to be directly related to the probabilities of producing photon pairs. For instance, all photon pairs generated within a single pulse should contribute to the centre peak around $\Delta t = 0$, however, side peaks will be generated by correlations between consecutive pulses. If the probability of generating at least one photon pair per pulse is P_{CC}, then the $\Delta t = 0$ peak is proportional to P_{CC}. In contrast, the side-peaks at integer time intervals $m\tau$ is related to P_{CC}^2, since photons must've been produced at time t_0 and $t_1 = t_0 + \tau$. Hence the ratio of coincidence counts at time intervals $0, \tau$ should be related by $\mathrm{CC}(\Delta t = \tau)/\mathrm{CC}(\Delta t = 0) = P_{\mathrm{CC}}$. The coincidence count probability, in the limit of zero losses, can be easily computed by summing the absolute value squared of the squeezed state amplitudes

$$\begin{aligned} \frac{\mathrm{CC}(\Delta t = \tau)}{\mathrm{CC}(\Delta t = 0)} &= P_{\mathrm{CC}} \\ &= 1 - P_{0,0} \\ &= 1 - (\sqrt{1-x^2})^2 \\ &= x^2 \end{aligned} \tag{3.11}$$

where $P_{0,0}$ represents the vacuum probability of the squeezed state. Here we see, that in the presence of perfect losses, the coincidence measurement is an ideal measure of the squeezing parameter. One therefore expects to see minimal side peaks for any experiment with low squeezing.

In light of this calculation, one ought to be naturally dubious as to how imperfect detection efficiencies and losses should effect this approximation. In order to incorporate losses in this calculation, one should replace the probability of generating a coincidence detection with the probability of measuring a coincidence detection in the presence of losses. Here we can combine the terms 'loss' and detection efficiency into one parameter $\eta = (\text{loss} \times \text{det. eff.})$ which determines the overall detection probability for a single photon. In this picture, the probability that a coincidence measurement occurs is equal to the sum of the probabilities that $n \geq 1$ photon pairs is produced each multiplied by the probability that *at least* one signal and idler photon is detected. For n simultaneous single photons, the probability that at least one is measured is given by

$$P_d(n) = 1 - \underbrace{(1-\eta)^n}_{\text{no detection}} . \tag{3.12}$$

[3]Of course, there may be an actual optical delay, such as different length fibres. This will result in a systematic shift of the centre peak, which may be accounted for in ones software.

The overall probability is the sum that at least one signal and idler photon are detected

$$\begin{aligned} P_{\mathrm{CC,d}}(\Delta t=0) &= \sum_{n\geq 1}(1-x^2)x^{2n}P_{d,s}(n)P_{d,i}(n) \\ &= \sum_{n\geq 1}(1-x^2)x^{2n}\big(1-(1-\eta_s)^n\big)\big(1-(1-\eta_i)^n\big), \end{aligned} \tag{3.13}$$

where $\eta_{s,i}(n)$ represents the signal or idler detection probability. For the sake of simplicity, in the following analysis we treat these values as being identical $\eta=\eta_s=\eta_i$, though a general analysis is straightforward under the same approach. Here I define the parameter $a=1-\eta$ as the probability that photon is not detected, and rewrite the probability as

$$\begin{aligned} P_{\mathrm{CC,d}}(\Delta t=0) &= \sum_{n\geq 1}(1-x^2)x^{2n}\big(1-a^n\big)^2 \\ &= (1-x^2)\Big[\sum_{n\geq 1}(x^2)^n-2\sum_{n\geq 1}(ax^2)^n+\sum_{n\geq 1}(a^2x^2)^n\Big]. \end{aligned} \tag{3.14}$$

Note that $|a|\leq 1$, $|x|\leq 1$ and hence $|ax|\leq 1$, hence the three infinite series all converge in the cases where $|a|\neq 1$ *and* $|x|\neq 1$. By substituting the general expression

$$\sum_{n\geq 1}^{\infty}\alpha^n=\frac{\alpha}{1-\alpha}, \tag{3.15}$$

and factorising the expression, one arrives at the following probability

$$P_{\mathrm{CC,d}}(\Delta t=0)=\frac{(1-a)^2(1+ax^2)}{(1-ax^2)(1-a^2x^2)}x^2, \tag{3.16}$$

which has the desired limits that no photons are detected with infinite losses $P_{\mathrm{CC,d}}(\Delta t=0)=0$ as $a\to 1$, and we recover the ideal case where there are no losses $P_{\mathrm{CC,d}}(\Delta t=0)=x^2$ as $a\to 0$.

Now we turn our attention to $P_{\mathrm{CC,d}}(\Delta t=\tau$, the probability that we detect at least one photon from consecutive pulses. Note that this is not simply the squared of the $\Delta t=0$ probability, since we need only detect one photon from each pulse,

$$\begin{aligned} P_{\mathrm{CC,d}}(\Delta t=\tau) &= \Big((1-x^2)\sum_{n\geq 1}x^{2n}(1-a^n)\Big)^2 \\ &= (1-x^2)^2\Big(\frac{x^2}{1-x^2}-\frac{ax^2}{1-ax^2}\Big)^2 \\ &= \frac{(1-a)^2}{(1-ax^2)^2}x^4. \end{aligned} \tag{3.17}$$

The ratio of coincidence counts in the presence of losses can then be written as the ratio of the detection probabilities

$$\begin{aligned} \frac{\mathrm{CC}(\Delta t=\tau)}{\mathrm{CC}(\Delta t=0)} &= \frac{P_{\mathrm{CC,d}}(\Delta t=\tau)}{P_{\mathrm{CC,d}}(\Delta t=0)} \\ &= \frac{(1-a^2x^2)x^2}{(1+ax^2)(1-ax^2)}, \end{aligned} \tag{3.18}$$

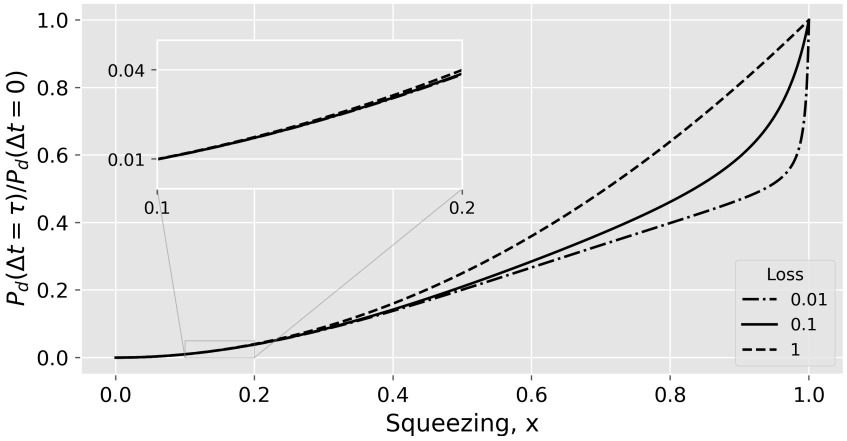

Figure 3.8: Ratio of coincidence counts at time intervals $\Delta t = \tau$ and $\Delta t = 0$ as a function of squeezing parameter, x. Different line styles correspond to different heralding efficiencies (equivalent to loss) as shown in the legend. The zoomed inset shows that at low squeezing (where we operate in our experiments) the measured coincidence ratios are independent of losses and approximate the lossless case.

which returns the lossless value x^2 with an additional squeezing dependent loss parameter $L(x,\eta)$

$$L(x,\eta) = \frac{\left(1-(1-\eta)^2x^2\right)}{\left(1+(1-\eta)x^2\right)\left(1-(1-\eta)x^2\right)}. \tag{3.19}$$

Figure 3.8 shows the calculated fraction plotted for different losses and across the squeezing range. Here it can be seen that for imperfect (i.e. not number resolving detectors) the limiting ratio is found to be 1 for high squeezing. For low squeezing values, the ratio becomes independent of losses, as can be seen from the inset image. We can therefore justify the approximation that the ratio scales as x^2 for low squeezing and moderate losses.

3.2.4 Quantum Interference

The previous section describes how the SFWM effect generates a range of squeezed states in separate spectral modes. We go on to show that since each mode is a two-mode squeezed state, the single photon pair state $|1,1\rangle$ may be arbitrarily approximated by looking at coincidence counts across the signal and idler channels. The key takeaway message is that this fundamentally creates a trade-off between success probability and purity, but that hope is not lost since significant hardware improvements may one-day lead to high-purity near-deterministic sources.

You may have realised, however, that during the previous discussions, I avoided the fact that one inevitably ends up with multiple squeezed states, each representing a different spectral mode. And that, in principle, for an unfactorable JSA, one may end up with arbitrarily many squeezed states. In order to assess the collateral damage this may cause, in this section we explore the effect this has on two types of quantum interference phenomena. Consider first the two-photon interference experiment introduced with reference to ideal single photon states in section 2.4.2.

3.2.4.1 Effect of Spectral Purity on Two-photon Interference

In this section we describe the effects of spectral separability (purity) on the ability to produce two-photon interference measurements on our device. A popular approach to create this kind of interference is described in the background chapter 2.4.2 and experimentally shown in reference [94]. The premise of this measurement is that a superposition of photon-pair states are generated by two photon pair sources. A phase is applied to one arm, which picks up a double phase due to the two-photon state passing through the waveguide. The two-photon superposition is then incident on a 50:50 beamsplitter which deterministically bunches, or anti-bunches the photons dependent on the phase. Note that one should see a doubling in the frequency of the produced interference pattern due to the double phase. Such an interference has been coined time-reversed HOM interference, since anti-bunched photons on the output arise from a superposition of bunched photons on the input port. This is a further interesting result, since the two-photon states that interfere with one another are actually non-degenerate, as described by the four-wave mixing.

The goal in this section is to turn our attention to the JSA of the produced photonic state. Here the key assumption is that it is possible to produce significantly low squeezing, such that a coincidence pair detection in time interval Δt must arise only from a single source. A secondary assumption is that it is possible to construct two identical sources, which produce the same photon-pair state. Under these assumptions, we may discard all high order photon number terms as described in section 3.2.2, and project the squeezed states onto a superposition state of the following form

$$\begin{aligned} |\Psi\rangle \propto \Big(& \int_{\lambda_s,\lambda_i} \mathrm{d}\lambda_s \mathrm{d}\lambda_i f(\lambda_s,\lambda_i) \hat{\lambda}^{\dagger}_{s,0} \hat{\lambda}^{\dagger}_{i,0} \\ & + \int_{\lambda'_s,\lambda'_i} \mathrm{d}\lambda'_s \mathrm{d}\lambda'_i f'(\lambda'_s,\lambda'_i) \hat{\lambda}'^{\dagger}_{s,1} \hat{\lambda}'^{\dagger}_{i,1} \Big) |\mathrm{vac}\rangle \,, \end{aligned} \tag{3.20}$$

where $\lambda_{s,i}$ represent the wavelength of the signal and idler photon, $f(\lambda_s,\lambda_i)$ represents the spectral correlations described by the JSA and where $\hat{\lambda}^{\dagger}_{s,0}$ represents the creation operator of a signal photon in the 0 (top) spatial mode. If we now enforce the

assumption that the spectral correlations are identical between the two sources, then we may combine the integrals

$$|\Psi\rangle \propto \int_{\lambda_s,\lambda_i} \mathrm{d}\lambda_s \mathrm{d}\lambda_i f(\lambda_s,\lambda_i)\left(\hat{\lambda}^\dagger_{s,0}\hat{\lambda}^\dagger_{i,0} + \hat{\lambda}^\dagger_{s,1}\hat{\lambda}^\dagger_{i,1}\right)|\mathrm{vac}\rangle\,, \tag{3.21}$$

At this point, one can propagate the state through the linear optic components described in the process

$$\begin{aligned} &\hat{\lambda}_{x,0} \rightarrow e^{i\phi}\hat{\lambda}_{x,0} \\ &\hat{\lambda}_{x,0} \rightarrow (\hat{\lambda}_{x,0} + \hat{\lambda}_{x,1})/\sqrt{2} \\ &\hat{\lambda}_{x,1} \rightarrow (\hat{\lambda}_{x,0} - \hat{\lambda}x,1)/\sqrt{2} \end{aligned} \tag{3.22}$$

giving the final state

$$\begin{aligned} |\Psi\rangle \propto \int_{\lambda_s,\lambda_i} \mathrm{d}\lambda_s \mathrm{d}\lambda_i f(\lambda_s,\lambda_i)\Big(&\left(\hat{\lambda}^\dagger_{s,0}\hat{\lambda}^\dagger_{i,0} + \hat{\lambda}^\dagger_{s,1}\hat{\lambda}^\dagger_{i,1}\right)\left(1+e^{2i\phi}\right)/2 \\ &+\left(\hat{\lambda}^\dagger_{s,0}\hat{\lambda}^\dagger_{i,1} + \hat{\lambda}^\dagger_{s,1}\hat{\lambda}^\dagger_{i,0}\right)\left(1-e^{2i\phi}\right)/2\Big)|\mathrm{vac}\rangle\,, \end{aligned} \tag{3.23}$$

which gives perfectly anti-correlated interference between bunching terms and anti-bunching terms. Hence, if we project the state onto the $\hat{\lambda}^\dagger_{s,0}\hat{\lambda}_{i,1}$ modes by filtering the signal (idler) resonance on the top (bottom) waveguide, the resulting interference pattern will evolve as $1-e^{2i\phi}$.

The key message here is that perfect two-photon interference can occur with JSA's which are not spectrally pure. One only has to build identical sources with low squeezing to produce the above interference. This explains the results from simple waveguide sources in various platforms which have achieved high visibility two photon interference. In the following section, we will see that these assumptions break down when considering multi-photon terms, for example when projecting onto states where each source emits exactly one photon-pair.

3.2.4.2 Effect of Spectral Purity on Heralded Two-photon Interference

By applying the same analysis to the heralded MZI fringe, as outlined in section 2.4.3, one finds that perfect quantum interference may only be achieved under two conditions. Firstly, the joint spectral amplitudes must be equivalent between the two sources. And secondly, each JSA must be spectrally pure such that $f(\lambda_{s,i}) = f_s(\lambda_s)f_i(_i)$. By considering the case where each source emits a single photon pair, one may write the following state

$$|\Psi\rangle \propto \int_{\lambda_s,\lambda_i,\lambda'_s,\lambda'_i} \mathrm{d}\lambda_s \mathrm{d}\lambda_i \mathrm{d}\lambda'_s \mathrm{d}\lambda'_i f(\lambda_s,\lambda_i) g(\lambda'_s,\lambda'_i)\hat{\lambda}^\dagger_{s,\uparrow,0}\hat{\lambda'}^\dagger_{s,\uparrow,1}\hat{\lambda}^\dagger_{i,\downarrow,2}\hat{\lambda'}^\dagger_{i,\downarrow,3}|\mathrm{vac}\rangle\,, \tag{3.24}$$

where λ_x (λ'_x) represents the wavelength of the signal or idler photon from the first (second) source, f and g are the two JSA and where $\hat{\lambda}^\dagger_{s,a}$ represents the creation operator of the signal photon in spatial mode a. If $f = A(\lambda_s)B(\lambda_i)$ and $g = C(\lambda_s)D(\lambda_i)$ are each separable, then the state becomes

$$
\begin{aligned}
|\Psi\rangle \propto & \int_{\lambda_i} A(\lambda_i)\hat{\lambda}^\dagger_{i,2}\mathrm{d}\lambda_i \\
& \times \int_{\lambda'_i} B(\lambda'_{i,3})\hat{\lambda'}^\dagger_i d\lambda'_i \\
& \times \int_{\lambda_s,\lambda'_s} C(\lambda_s)D(\lambda'_s)\hat{\lambda}^\dagger_{s,0}\hat{\lambda'}^\dagger_{s,1}\mathrm{d}\lambda_s\mathrm{d}\lambda'_s\,|\mathrm{vac}\rangle\,.
\end{aligned} \tag{3.25}
$$

When the MZI is configured as the identity $\hat{I}$, we measure maximal four-fold coincidence counts across the four detectors at output modes $\{0,1,2,3\}$. At the minimum configuration, when projecting modes $\{0,1\}$ onto $\hat{\sigma}_x$, we see the following destructive interference if $C(\lambda_s) = D(\lambda_s)$

$$
\begin{aligned}
\hat{\sigma}_{x,0,1}|\Psi\rangle \propto & \int_{\lambda_i} A(\lambda_i)\hat{\lambda}^\dagger_{i,2}\mathrm{d}\lambda_i \int_{\lambda'_i} B(\lambda'_i)\hat{\lambda'}^\dagger_{i,3}\mathrm{d}\lambda'_i \\
& \times \int_{\lambda_s,\lambda'_s\geq\lambda_s} C(\lambda_s)D(\lambda'_s)\Big[\hat{\lambda}^\dagger_{s,0}\hat{\lambda'}^\dagger_{s,0} \\
& \qquad + \hat{\lambda'}^\dagger_{s,0}\hat{\lambda}^\dagger_{s,0} \\
& \qquad - \hat{\lambda}^\dagger_{s,1}\hat{\lambda'}^\dagger_{s,1} \\
& \qquad - \hat{\lambda'}^\dagger_{s,1}\hat{\lambda}^\dagger_{s,1}\Big]\mathrm{d}\lambda_s\mathrm{d}\lambda'_s\,|\mathrm{vac}\rangle\,,
\end{aligned} \tag{3.26}
$$

where we have used the reordering of terms within the integral to conclude the interference. The outcome is such that no terms are found simultaneously in the $\{0,1\}$ modes. As a result, it is possible to obtain perfect quantum interference in the case where two pure and identical biphoton states interfere.

Finally consider the case where the joint spectra from each source is identical, however the signal and idler photons from each source are completely correlated (i.e. single source produces $\approx \lambda_s\lambda_i + \lambda'_s\lambda'_i + \lambda''_s\lambda''_i + \ldots$). In this case, multiphoton terms (from different sources) where $\lambda_s = \lambda'_s$ still experience quantum interference, however the orthogonal terms (for d dimensions) in the total state dominate with a ratio given by $\lim_{d\to\infty} d/d^2 = 0$. In addition, the perfectly correlated signal and idler photons break the spectral symmetry seen in the previous two cases. For example consider the two orthogonal terms

$$
\frac{1}{2}\mathrm{d}\lambda_s\mathrm{d}\lambda_i\mathrm{d}\lambda'_s\mathrm{d}\lambda'_i f(\lambda_s,\lambda_i)f(\lambda'_s,\lambda'_i)(\hat{\lambda}^\dagger_{s,\uparrow,0} + \hat{\lambda}^\dagger_{s,\uparrow,1})(\hat{\lambda'}^\dagger_{s,\uparrow,0} - \hat{\lambda'}^\dagger_{s,\uparrow,1})\hat{\lambda}^\dagger_{i,\downarrow,0}\hat{\lambda'}^\dagger_{i,\downarrow,1}, \tag{3.27}
$$

and

$$\frac{1}{2}\mathrm{d}\lambda_s'\mathrm{d}\lambda_i'\mathrm{d}\lambda_s\mathrm{d}\lambda_i f(\lambda_s',\lambda_i')f(\lambda_s,\lambda_i)(\hat{\lambda'}^{\dagger}_{s,\uparrow,0}+\hat{\lambda'}^{\dagger}_{s,\uparrow,1})(\hat{\lambda}^{\dagger}_{s,\uparrow,0}-\hat{\lambda}^{\dagger}_{s,\uparrow,1})\hat{\lambda'}^{\dagger}_{i,\downarrow,0}\hat{\lambda}^{\dagger}_{i,\downarrow,1}. \tag{3.28}$$

Here the idler photons prevent factorisation of these terms and hence also prevent the quantum interference between signal photons. In addition, since these orthogonal frequency terms completely dominate the total wavefunction, the overall state will see no interference. This case results in a heralded MZI interference fringe with a visibility of 33% (where $v = (cc_{\max} - cc_{\min})/(cc_{\max} + cc_{\min})$).

3.2.4.3 Spectral Purity of Waveguides vs MRR Sources

The above sections explain how, in general, SFWM single photon sources give rise to multimode twin-beam squeezed states on chip. In order for these states to correctly approximate single photons, we require low squeezing where the probability that photons are generated becomes low. Furthermore, the ability to interfere such single photons requires high spectral purity as expanded on in the previous section. It is therefore of vital importance that both of these parameters can be controlled in experiment. Thankfully the photon number purity, as described by the squeezing, can be controlled simply by reducing pumping power. In addition, heralded second-order correlation function measurements can directly infer the number purity of single photon states [139–141]. These measurements will set an effective upper limit in the pumping strength one can use in quantum information experiments. The natural drawback is the trade-off between number purity and generation probability.

The trickier parameter to deal with is that of the spectral purity, which typically has much stronger drawbacks. In the majority of integrated quantum information experiments, long cm-scale waveguides are used in order to produce single photons. These waveguides utilize long interaction lengths in order to increase the SFWM. The result is typically broadband twin-beam squeezers, emitting in many spectral modes. The natural approach is to filter the spectral properties such that the single photons are collected in one single mode. This has been shown with high success, although there is a major drawback that the single photon heralded efficiency is greatly impacted. Further more, there is a natural degradation in the heralding efficiency due to the long waveguides and their associated losses.

An alternative approach is that of integrated MRRs, which have been shown to have naturally high spectral purities. For simple resonator designs, calculations estimate spectral purities of approximately 92%. Since this purity is intrinsic, there is no hit on the heralding efficiency and so this is greatly advantageous compared with waveguide sources. In addition, the resonant enhancement factor, see section 2.5.7, naturally

boosts the SWFM for low pumping powers and effectively decouples the SFWM contribution from surrounding waveguides. Furthermore, multiple MRR sources can be tuned and overlapped to create either distinguishable or identical photons depending on the application. The main drawback to this approach is the inherent (but small) drop in heralding efficiency one sees as a function of the resonator coupling parameters. At critical coupling, one sees a 50% drop in the single photon heralding efficiency. Moreover, exciting research has suggested that improved resonator designs along with better pumping strategies may improve ones spectral purities close to ideal [132, 133]. For these reasons, it was decided to include four MRR single photon sources within the primary device.

3.3 Single Photon Characterisation & Quantum Interference Experiments

In the previous section, we investigate the mathematics that describes single photon sources in silicon. The goal in the following section is to perform characterisation measurements and experiments which benchmark this chips performance and to comment about what this means for future quantum experiments to be performed. Ultimately, we would like to benchmark the extent to which identical single photons may be created on this chip, and how well they may interfere with one another.

3.3.1 Locking of Micro-ring Sources

Indistinguishable single-photons are generated in this device by precisely tuning each of the MRR resonances simultaneously. When each of the four resonances are perfectly overlapped, the produced photon spectra are in the least distinguishable configuration with one another. This is desired for any quantum information experiment where single photons should interfere. However, since the MRR resonances have extremely small FWHM, it can in principle be difficult to maintain good overlap between each of the four single photon sources. In addition, since many single photon experiments require low squeezing, and thus demand high integration times, it is paramount that the overlapping of sources become procedural.

The approach to source overlapping and stabilisation is the following. Since the fault tolerances of the fabrication process are low, the four MRR FSR are built with near identical values. As a result, one can simultaneously match all of the resonance channels between different rings by only keeping track of a single channel at a time. If this were not true, measurements would have to be performed across multiple

resonances of each ring and the maximal overlap inferred via a more complicated method. In our case, however, the successful overlapping of the centre idler channels of each MRR will also see good agreement between every other pair of local channels, including the pump and signal. In practice, the cavity resonances are exceptionally sensitive to external temperature fluctuations and require continual monitoring and stabilising. To minimise this effect, a thermistor is used to measure the surrounding temperature and a temperature controller stabilises the overall device at 22 degrees Celsius. This locally minimises the relative frequency shift of overlapped resonances caused by temperature drift in the external environment, however, small-scale temperature changes can still causes the MRR resonances to drift locally with respect to each-other. This can be counteracted by utilizing a CW seed laser at fixed operational frequency. This seed laser probes each of the MRR in turn, and the voltages across each MRR is scanned as to measure the voltage required to achieve peak resonance. At peak resonance, the coupled light to the bus waveguide is minimised, which results in minimal coupling to the output fibres. As a result, the critical voltage can be found trivially by monitoring optical power. During each stabilisation, and for each ring, an array of coupling values (optical powers) are measured and recorded. The transmission as a function of voltage can be fitted with a Lorentzian shape, as predicted in section 2.5.7 and shown in fig. 3.9**b**. The centre dip voltage is extracted from the fitting parameters and is the value applied to the ring for the next single photon measurements.

Figure 3.9a reports the experimental setup for locking the MRRs. In practice, each of the four MRR sources are simultaneously probed. The chip is configured in such a way where the optical power measured at certain outputs corresponds only to light from a particular ring. In this way, the voltages may be simultaneously scanned and optimised. Figure 3.9c shows the calculated critical voltages over a time period of 20 hours in the lab. For maximal overlap, each of the sources take a much different average value, though the trends in each value are similar due to the similar temperature changes. Notice that at around 15 hours a large systematic drift in value is found, and corresponds to the air-conditioning change over the evening in the lab.

3.3.2 Coincidence Counts and MRR Gain

During discussions up until this point, we have been able to quantify the expected number of photon pairs and coincidence measurements based on a single squeezing parameter. However, in our experiments, we do not have direct access to this parameter, and it should be estimated in order to suitably draw conclusions. In these experiments,

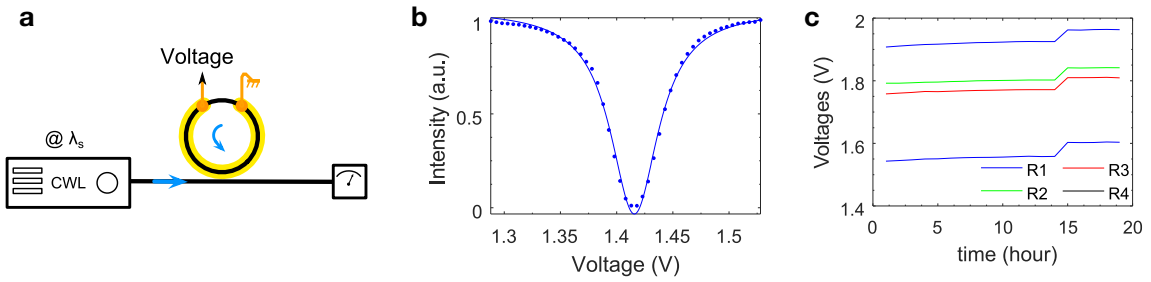

Figure 3.9: Single photon source automatic alignment. **a,** Schematic detailing how a fixed CW probe laser is able to lock each MRR at a particular resonance by evaluating the critical voltage at which the measured optical power is minimised. **b,** Experimental result of a particular minimisation, the optical powers are fit with a Lorentzian shape and non-linear fitting algorithm. **c,** the measured critical voltages over a 20 hour period.

the actual control parameters is the pumping strength measured in mW. In very broad terms, we expect that the squeezing strength should vary linearly with respect to the pump power, since the SFWM Hiltonian gains a 2× contribution of the pump field operator each with similar amplitudes. Since we have calculated that the coincidence probability roughly grows as the square of the squeezing parameter, we expect that the number of measured coincidences will also grow as the square of the pumping strength. In general the photon pair flux, f, does indeed grow proportionally to the square of the power [142]

$$f \propto \gamma^2 P^2, \tag{3.29}$$

where the proportionality constant is given by $\gamma = 2\pi n_2/\lambda A_{\text{eff}}$ and is the effective non-linearity of the silicon waveguide with effective area A_{eff} at wavelength λ and intrinsic non-linearity n_2. Figure 3.10a shows the two fold coincidence counts measured from a single ring at various pumping strengths. In order to minimise changes in the alignment the optical power was fixed at average power of 1mW and the coupled signal was attenuated before entering the chip in each case.

In order to quantify how the gain profile of the MRR structure will effect the brightness of photons created inside the rings, a second experiment was carried out. In this experiment coincidence counts are again measured from a single source, however this time the power is kept constant and the wavelength of a CW pump is swept across the MRR pump resonance. Due to the enhancement factor derived in section 3.1.1.2, we expect to see a further boost to the generated single photons as the wavelength matches the resonant condition. The expected shape is proportional to the square of equation 2.83 and the results can be seen in figure 3.10b. The method to derive the

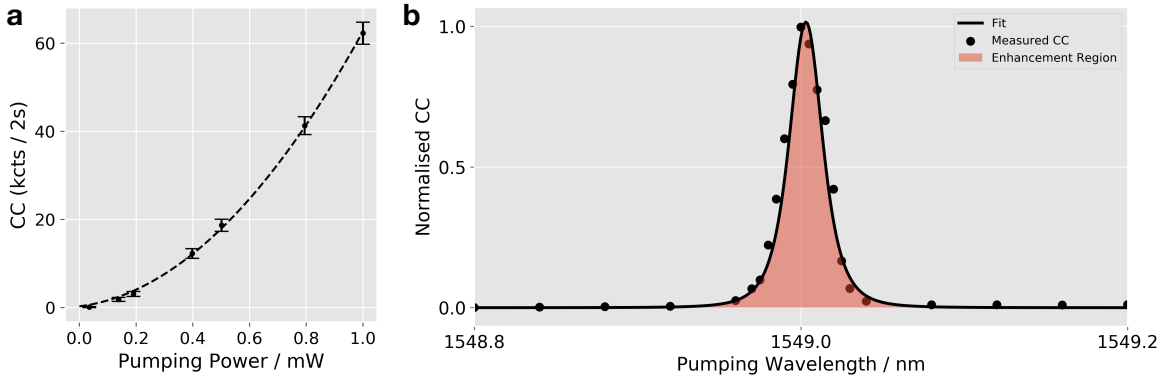

Figure 3.10: Source characterisation. **a,** the measured coincidence counts in a two second integration window as a function of pump power. Measurements were made with fixed pumping and utilizing a variable optical attenuator to reduce the optical power coupled to the chip. Error bars are estimated using poissonian count statistics, although the sizes of the error bars are plotted 10× larger to make them more visible. **b,** the measured gain profile of MRR1 as a function of wavelength. This curve quantifies how the MRR enhancement effects the SFWM inside the cavity.

fitting was as follows. First the transmission spectrum of the MRR ring is measured and is fit with a nonlinear model fit in python using equation 2.81, $T_{\text{Out}}(\tau, \alpha, \phi)$. The fitting parameters τ and α which describe the self-coupling coefficient and loss parameter are kept and recorded. Then the two-fold coincidence counts are normalised and fit with the following shape $AT^2_{\text{Cavity}}(\tau, \alpha, \phi)$ for some scaling parameter A.

3.3.3 Probing Photon Number Purity

In this section we assess the number purity of the heralded single photon sources as a function of power. The goal here is to learn the optimal pumping strength that is required to achieve a good balance between high pair probability but low multipair emission. We have seen in section 3.2.3 that the squeezing can be inferred directly by measuring the coincidences to accidentals ratio which arises in the time-tagging histogram from pulsed SFWM sources. Figure 3.11a shows a working example of this histogram at an external average pumping power of 1 mW with a pulse repetition rate of 500 MHz. Here the regular (at n integer intervals) $\pm 2n$ nanosecond peaks can be seen in the inset for each case. A 2 ns coincidence window is defined around each peak in order to infer the coincidences, where the counts inside each window are summed. Due to the low numbers of counts with non-zero delay, each of these peaks are averaged in order to determine the ratio $P_d(\Delta t = \tau)/P_d(\Delta t = 0)$. Here the measured ratio was found to be $P_d(\Delta t = \tau)/P_d(\Delta t = 0) = 0.0134$, which estimates the on-chip squeezing strength (via equation 3.18) as $x = 0.116$ according to the method

outlined in section 3.2.3.

Figure 3.11b shows an alternative method for calculating the multiphoton terms as a function of pumping power. The heralded second-order correlation function $g^{(2)}(0)$ splits the single photons between two detectors via a 50:50 beam splitter. The $g^{(2)}(0)$ computes the correlation between the two detectors at a zero time delay in order to estimate the multi-photon terms [140]. The data in figure 3.11b was taken by Imad Faruque on the same chip used within this thesis, but is included here for completeness.

Finally, figure 3.11c shows the purity of one of the single photons from the two-mode squeezed state as a function of squeezing. The state of the signal and idler photon for a pure two-mode squeezed state is given by the reduced density matrix

$$\rho_{s/i} = (1-x^2)\sum_n x^{2n} |n\rangle \langle n|_{s/i}\,, \tag{3.30}$$

where the single photon purity is given by $\mathrm{Tr}(\rho_{s/i}^2)$ and numerically evaluates as

$$\begin{aligned} \mathrm{Tr}(\rho_{s/i}^2) &= (1-x^2)^2 \sum_{n=0}^{\infty} x^{4n} \\ &= \frac{1-x^2}{1+x^2}. \end{aligned} \tag{3.31}$$

The measured squeezing of $x = 0.12$ gives a single photon state purity of 0.972 and is highlighted in the inset figure along with the general purity verses squeezing curve.

3.3.4 Time-reversed HOM Interference

The goal in this section is to show the ability to interfere two-photon states on chip with high visibility. It is clear from section 3.2.4.1 that we expect the spectral overlap of the MRRs and the squeezing parameter to play a crucial role in the ability to perform two photon interference. In this experiment, the aim is to interfere a superposition of signal and idler pairs on a fixed MZI with internal phase set to $\pi/2$ such that the MZI resembles a 50:50 beamsplitter. By adding a complex phase to one of the arms in the superposition, one expects to see interference in the number of anti-bunched coincidence counts measured at the output of the MZI. A schematic of the chip configuration is shown in figure 3.12a.

By simultaneously and coherently pumping two near-identical and overlapped MRRs the generated state is approximately the superposition of two twin-mode squeezed states

$$|\psi\rangle = \sqrt{1-x_1^2}\sum_n x_1^n |n,n\rangle \otimes \sqrt{1-x_2^2}\sum_m x_2^m |m,m\rangle\,. \tag{3.32}$$

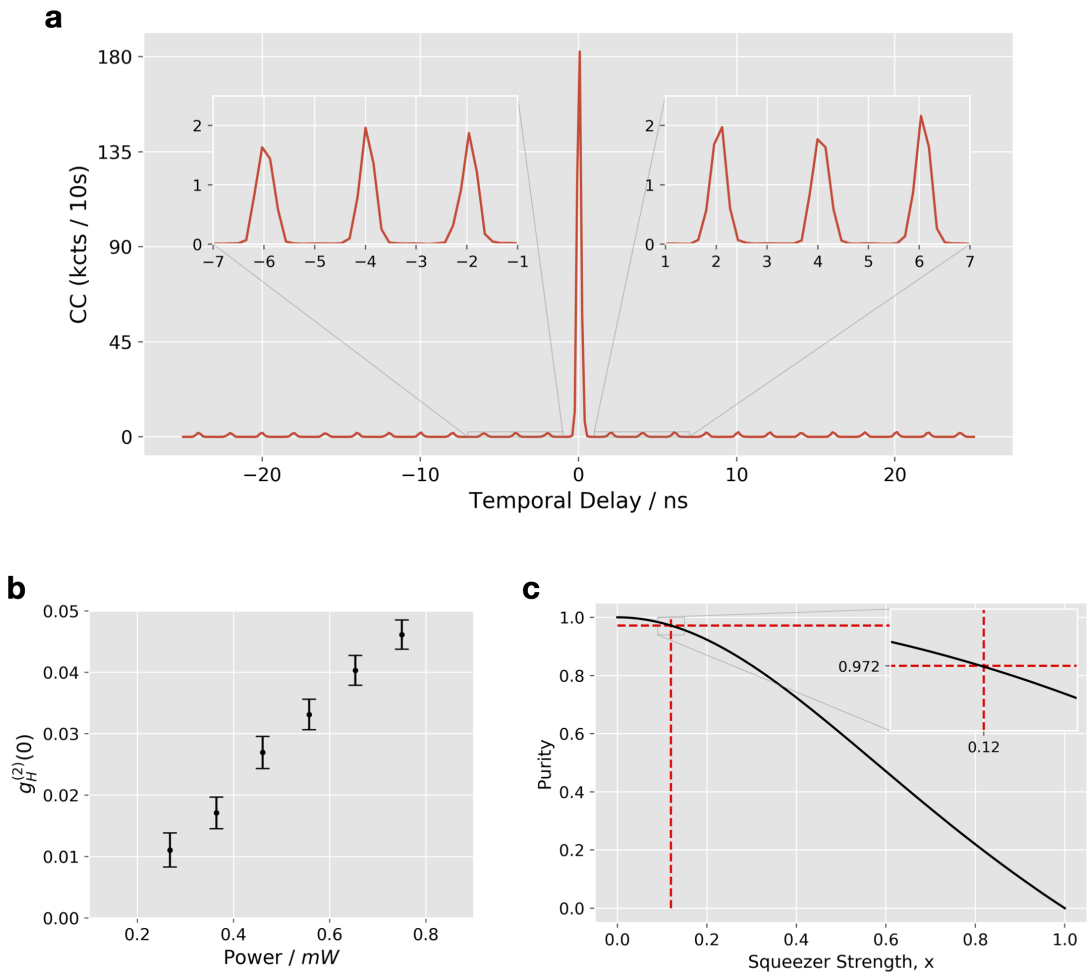

Figure 3.11: **Photon Number Purity. a,** two detector histogram of events caused by pumping a single photon pair source. The sharp peak at $\Delta t = 0$ is due to the simultaneous arrival of photon pairs from the same photon source. Simultaneous peaks at $2ns$intervals are due to finite squeezing, and hence correlations between counts in different pulses. **b,** shows the measured heralded second-order correlation functions $g^{(2)}(0)$ at a range of pumping strengths. This measurement gives us information about how many multi-photon terms we can expect from the single photon sources. **c** shows the theoretical number purity as related to the squeezing parameter of a spectrally pure photon source. Red dashed lines along with inset zoomed image highlights the estimated operational parameters in our experiment.

Under the single photon pair approximation, the only significant terms are those which correspond to at most a single pair. Here we assume that by controlling the relative pumping strength between each MRR, we can match the two squeezing parameters such that $x_1 = x_2$,

$$|\psi\rangle \approx (1-x^2)\Big(|0,0;0,0\rangle + x\,|1,1;0,0\rangle + x\,|0,0;1,1\rangle + O(x^2)\Big), \tag{3.33}$$

where $|1,1;0,0\rangle$ ($|1,1;0,0\rangle$) represents a photon pair produced from the top (bottom) MRR.

From here, it is clear that in the event of sufficiently small squeezing, and followed by the post-selection of two-photon states one can perform the following renormalisation

$$|\psi\rangle \rightarrow \frac{1}{\sqrt{2}}(\hat{s}_0^\dagger \hat{i}_0^\dagger + \hat{s}_1^\dagger \hat{i}_1^\dagger)|\text{vac}\rangle\,. \tag{3.34}$$

which is the desired form that was derived in section 2.4.2. Under the condition that the above initial state is generated with high fidelity, the rest of the experiment follows the method outlined in section 2.4.2. Due to equation 2.68, we expect the measurable two-photon anti-bunching terms to interfere with a double phase, oscillating twice over a 2π range. The resulting state evolution is of the form

$$\cos\phi\,|\text{Bunched}\rangle + \sin\phi\,|\text{Anti-bunched}\rangle \tag{3.35}$$

where the probability that an antibunched photon state is measured depends on the applied phase-shift ϕ as $P_{\text{AB}} = |\langle\psi|\text{Anti-bunched}\rangle|^2 = \sin^2\phi \equiv (1-\cos 2\phi)/2$, and therefore picks up a double phase when compared with the classical fringe.

This double phase arises from the fact that part of the superposition containing two photons passes through the phase shifter, since the squeezed state produces only photon pairs. Since each photon accumulates the phaseshift then the resulting state picks up a double phaseshift due to the tensor product of the two states. In order to visualise this, the interference pattern of the classical fringe was also measured during this experiment. Since there is no superposition, the beam may only pass through either the top or bottom waveguide and so we should see only a single interference fringe over the 2π range.

Figure 3.12b shows the experimental results, where a clear doubling in the oscillation frequency is seen in the quantum measurements (black) compared with the classical measurements (blue). The quantum coincidence counts were obtained by counting the two photon coincidences between the two spatial modes over period of 10 seconds per measurement. The coincidence detection was repeated for phase values in

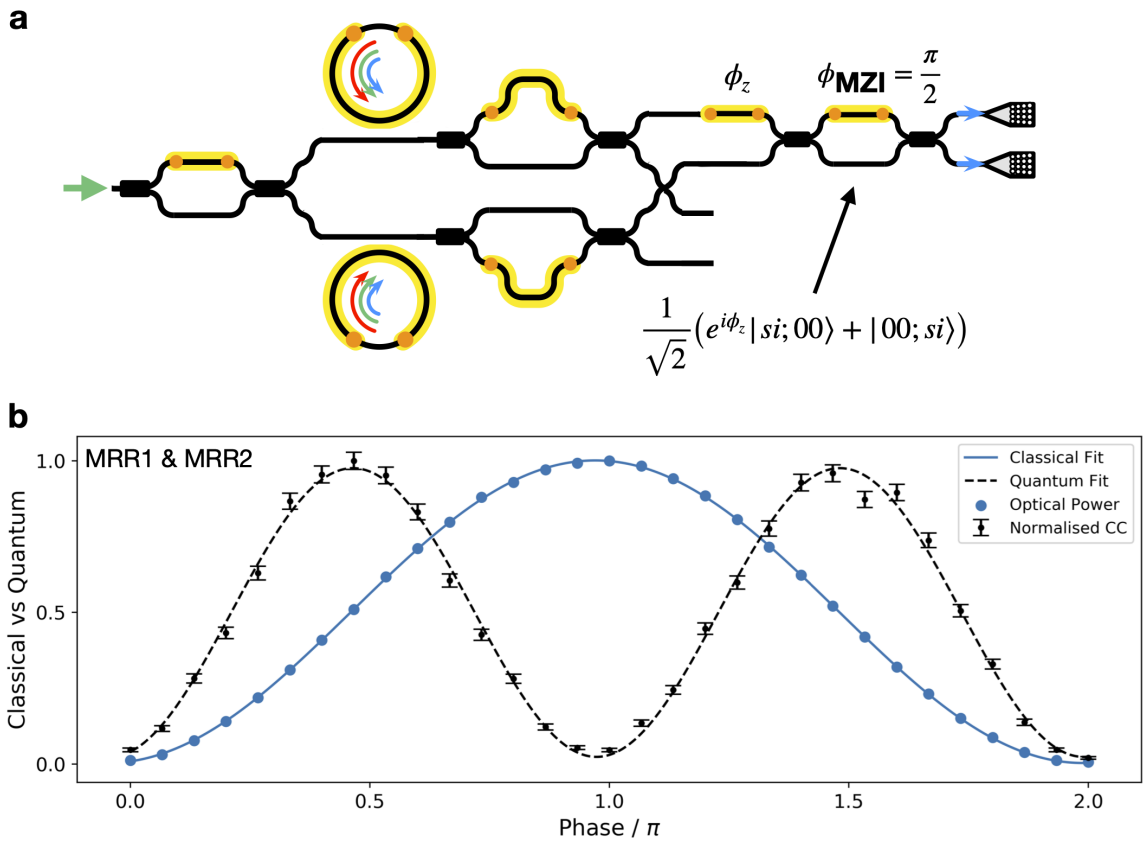

Figure 3.12: Time Reversed Hong-Ou-Mandel. **a,** chip schematic showing how the interference occurs. The coherent pumping of two separate sources generates an equal probability of producing a photon pair from either arm. By guiding the photons with the two AMZI, a noon-like state is created involving the signal and idler photons. This state is then interfered on a MZI with a $\pi/2$ phase shift between each arm of the interferometer. **b,** resulting two photon interference fringe. The blue dots represent the measured normalised optical power and the black dots represent the normalised antibunching coincidence counts. The solid blue line and dashed black line represent the classical and quantum fit, respectfully.

the range $(0, 2\pi)$ in increments of $\pi/15$. The resulting list of coincidence counts were then normalised to see the relative change in probability of each measurement, as can be seen in the figure. In addition, the pump optical power was recorded during each measurement and subsequently normalised. This experiment was repeated between rings 1&2 (shown in the figure) and rings 3&4, where the measured visibility $V \equiv 1 - P_{\text{min}}/P_{\text{max}}$ in each case was 0.97 ± 0.02 and 0.99 ± 0.08, respectfully. Each visibility is obtained from the best sinusoidal fit parameters and the error in visibility was estimated through a Monte-Carlo simulation on the Poissonian counting statistics.

3.3.5 Heralded Quantum Interference - Spectral Purity Measurement

In this section we outline the method and results of the photon indistinguishability measurements performed. These results lay the foundation for the multi-photon experiments in this thesis and will outline our expectations going forward with respect to multiphoton interference.

Perhaps the most classic indistinguishability measurement is the HOM fringe, whereby similar photons are incident on a single beam splitter. A relative delay in the photon arrival time introduces an asymmetry, allowing otherwise similar photons to be easily distinguished in time. In this case, all quantum interference's are removed and one sees only classical correlations between the counting statistics of the photon arrivals. However, when the photons are perfectly overlapped, one sees an interference due to the indistinguishable photons, and thus the photons tend to bunch at one output port of the beam splitter, rather than half of the time leaving from different ports (or anti-bunching). This is an ideal test, since strictly pure and identical photons will produce exactly zero coincidences between the photon detectors at each port of the beam splitter. In contrast, perfectly dissimilar photons will see no change in the statistics when their arrival times overlap. The details of the standard HOM experiment are shown in section 2.4.1

In contrast to the HOM experiment, where similar photons are distinguished by introducing an optical delay, we here interfere heralded single photons on a MZI as outlined in section 2.4.3. This measurement has been shown in section 3.2.4.2 to depend directly on the separability of the JSA of each single photon source. Specifically, 100% interference may only occur in the low squeezing limit and where each single photon source emits in only a single spectral mode. In reality, these conditions lead to two distinct sources of error. The first of which is the probability that simultaneous pairs of photons are heralded from each source, but from different spectral modes. Clearly these orthogonal photon states will not interfere with one another and will reduce the fringe visibility. The second source of error are multiphoton terms, where there is a non-zero chance that a source will produce multiple pairs of photons. Here the multiphoton terms will not fully interfere with single photon terms from the other source and hence will also degrade the visibility interference fringe.

Figure 3.13a shows the simplified schematic of the setup used during the photon indistinguishability measurements. For each pair of single photon sources, a subset of the chip was used in order to resemble the schematic. In each case, a femtosecond pulsed laser at $\lambda = 1550nm$ was used to pump two sources. The pump laser is coupled

to the chip and enters the top port of a MZI, as highlighted by a green pulse to the left of the schematic. The pulse is then split equally between the two MZI outputs by adjusting the internal phase-shifter such that the relative phase is $\phi = \pi/2$. The equally split pump then propagates through the MRR sources which are precisely tuned such that the pump resonances match the centre of the pump wavelength. Here the coupled light inside the MRR is maximised, which results in an enhancement factor inside the MRR cavity as explained and quantified in figure 2.10 and quantified in section 2.5.7. Single photons at signal and idler frequencies are then probabilistically and spontaneously produced inside the MRR cavity and subsequently released into the bus-coupled waveguide with 50% probability. The resulting photons are then spectrally filtered on chip by the AMZI and deterministically (with high probability) leave the interferometer from different waveguides.

Single photons then pass through the linear optic circuits and are coupled to four high-efficiency grating couplers. The single photons are coupled to separate single mode fibres through a fibre-array that maintains fixed pitch between each fibre core. The single-mode fibres feed back to four superconducting nano-wire single photon detectors with approximately 90% detection efficiency. The electrical outputs of each detector are sent to a time-tagger which is able to accurately and precisely record the arrival time of single photons across multiple channels. The time-tags are processed to show the four-fold coincidence counts, that is the number of events at which four photons arrive simultaneously at each detector. Due to the design of the schematic, a four-fold coincidence event can occur only when at least one photon-pair is emitted from each source. This is because photon pairs from each ring are spectrally filtered on chip. The idler photons are collected along their own waveguides and measured in detectors D1 and D4, corresponding to i1 and i2. The remaining two signal photons are guided along separate waveguides and both meet simultaneously at each port of a MZI. The four channels are labeled in fig 3.13a as i_1, s_1, s_2, i_2 and blue/red pulses show where the photons are guided in each part of the circuit. Here the subscript $\{1,2\}$ relates directly to the source of the single photons, either S1 or S2.

The number of four-fold coincidences one measures depends on the propagation of single photons through the linear-optics which are rotated by a single phaseshifter, see section 2.5.4. When the phase difference between each arm of the MZI is zero, the MZI matrix acts as the identity, causing no interference in the measured single photons. As a result, here we expect to see maximal four-fold counts limited only by the probability of detecting a 2-fold coincidence from each ring simultaneously $P_d^2(\Delta t = 0)$. Similarly, when the phase different equals π, the matrix resembles a swap, and so again there is maximum coincidence counts and no interference. When the phase difference is

equal to $\pi/2$ or $3\pi/2$, the resulting MZI matrix resembles a beamsplitter. Classically we would expect a 50% drop in the measured four-fold coincidence counts at the configuration. However, since the photons are well-overlapped and near-identical (and approximately pure) we expect these terms to interfere with one another as in the HOM experiment. The calculated visibility, here defined as [143]

$$V_{\mathrm{MZI}} = \frac{(\mathrm{CC}_{4F})_{\max} - (\mathrm{CC}_{4F})_{\min}}{(\mathrm{CC}_{4F})_{\max} + (\mathrm{CC}_{4F})_{\min}} \tag{3.36}$$

ranges from a maximum value of 1 (maximal interference) and minimum value of 1/3 (classical limit).

In an effort to deduce the true indistinguishability of each source, the design includes two switches SN1 and SN2. By tuning each switch the signal photons can be measured or not measured in the final outcome. Notice that when one of the arms is blocked by the switch, the fourfold coincidence counts may only arise due to multipair terms from the other source. For example, if single photons are produced by S1 and S2 but SN1 is turned off, only the signal photons from S2 will enter the MZI. In this case, when the MZI acts as an identity or a swap, there should be no fourfold coincidences. Alternately, when the MZI acts as a beamsplitter, there can be fourfold coincidences only when S2 emitted more than one photon pair. For high squeezing, these terms are not negligible and are $\pi/2$ out of phase with the interference fringe. Figure 3.13b shows an example measurement. Here the black dots represent the MZI interference pattern caused by measuring the four-fold coincidences as a function of MZI phase. The black fitted line is achieved via a mathematical model (explained below) whereby a indistinguishable fringe is merged with partial distinguishability. The blue and red points are the multipair emission from each ring respectively, measured by individually erasing the signal photons from one of the arms at a time. The asymmetry in the interference pattern can be accounted for by considering imperfect MMI couplers [144]. The inferred raw visibility by interfering sources 1 and 2 was 70%, which rose to 91% after the multipair corrections as can be seen in fig 3.14b.

3.3.5.1 Imperfect MZI

In this section, I introduce a model of the heralded quantum interference by including an imperfect MZI. This model is then used to fit both the raw and corrected fringes. The requirement for such a model arises, as can be seen from the fringes in figures 3.14b and 3.13b. In each case, the expected sinusoidal interference pattern is substantially altered to include one large peak and two diminished ones. Upon inspection the diminished peaks correspond to the events where single photons are to be deterministically swapped inside the circuit. This suggests that the ideal model, where

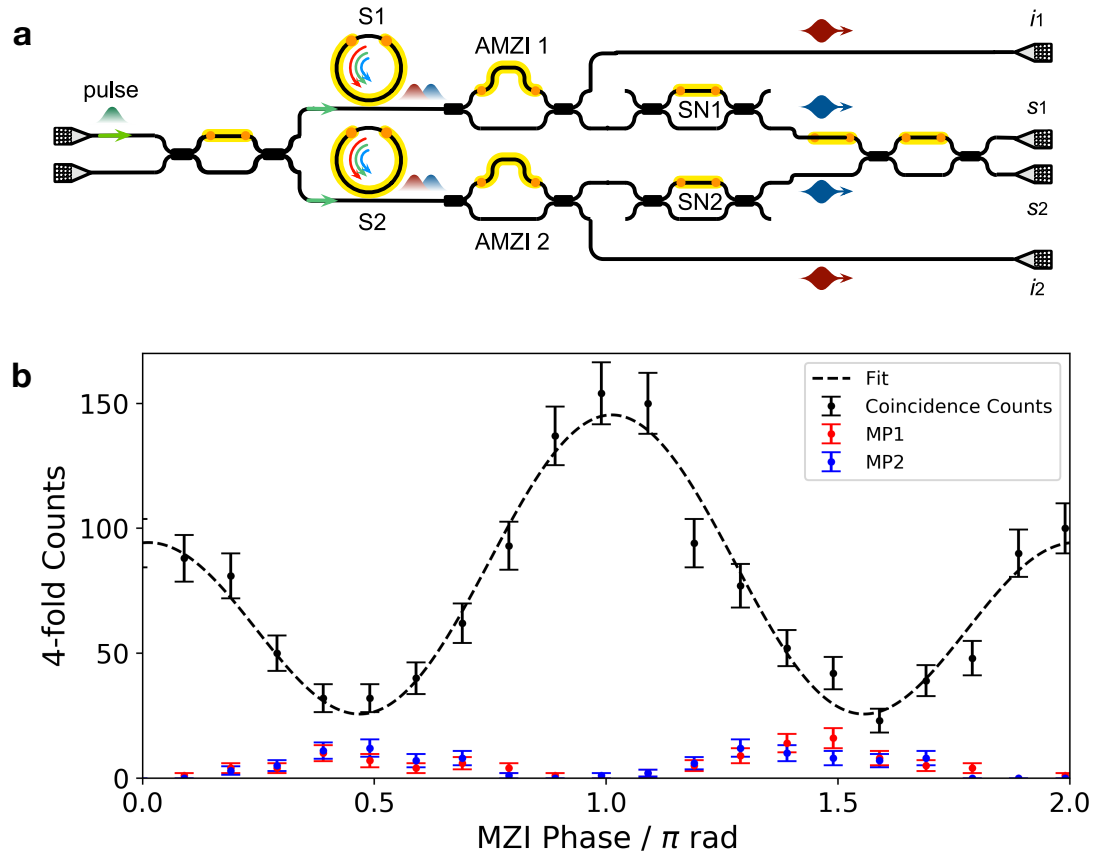

Figure 3.13: **Photon Indistinguishability Measurement: a**, simplified chip schematic. Schematic outlining how the photon indistinguishability measurements were carried out on the device. Green, blue, red pulses represent pump, signal and idler frequencies, respectfully. **b**, black data points represent raw four-fold coincidence events as part of a PIM measurement. Red and blue points represent the estimated multi-pair contributions from source 1 and 2. The black dashed line represents the fit to the raw data.

MZI are constructed from perfect MMI is likely false. Consider instead that each MZI is constructed from two imperfect MMI couplers such that they have variable beamsplitter ratios

$$U_{\mathrm{MMI}}(\theta) = \begin{pmatrix} \cos\theta & \sin\theta \\ -\sin\theta & \cos\theta \end{pmatrix},$$

which has a reflection coefficient giving by $\eta = \cos^2\theta$. The standard MMI is now the special case where $\theta = \pi/4$. The total MZI will evolve any input state under the following matrix

$$U_{\mathrm{MZI}}(\phi,\theta_1,\theta_2) = \begin{pmatrix} \cos\theta_1 & \sin\theta_1 \\ -\sin\theta_1 & \cos\theta_1 \end{pmatrix} \begin{pmatrix} e^{i\phi} & 0 \\ 0 & 1 \end{pmatrix} \begin{pmatrix} \cos\theta_2 & \sin\theta_2 \\ -\sin\theta_2 & \cos\theta_2 \end{pmatrix},$$

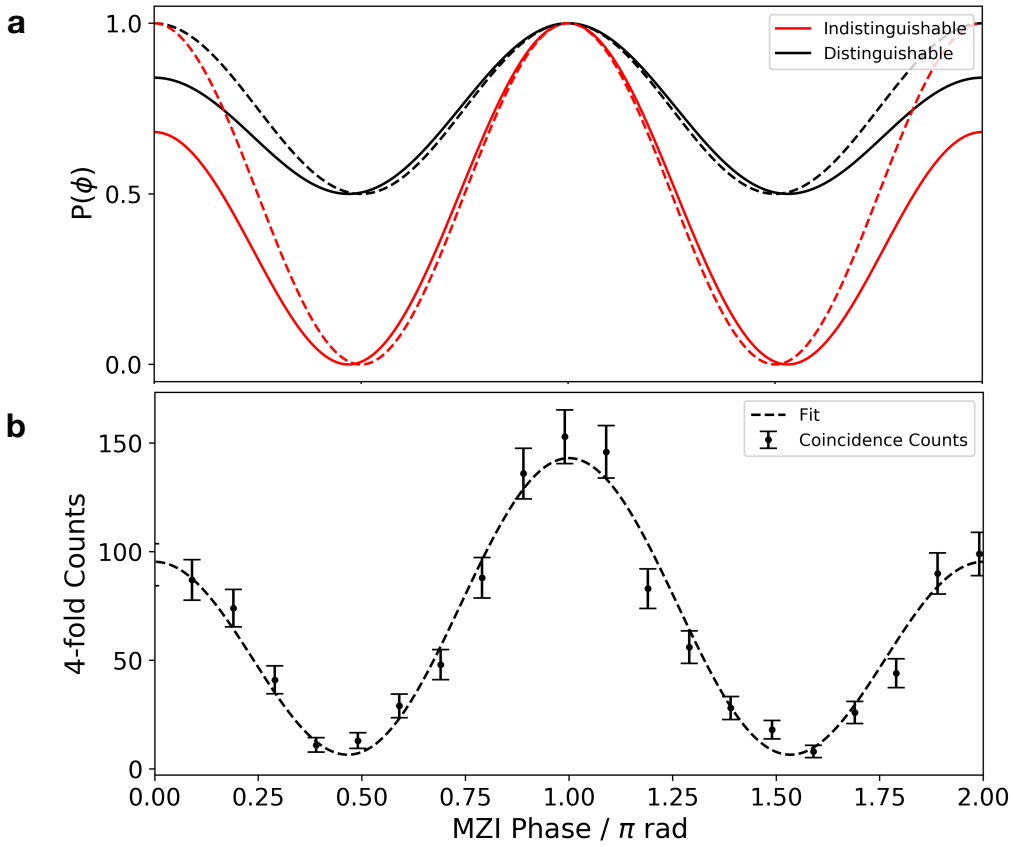

Figure 3.14: PIM Results. **a**, antibunching probability against MZI phase for a heralded HOM fringe. Red curves represent the case where the heralded single photons are pure and indistinguishable. The black curves represent perfectly distinguishable photons. In each case, a dashed line represents the expected results produced by a perfect MZI ($\alpha_1 = \alpha_2 = \pi/4$) and the solid lines represent unbalanced MMI with $\alpha_1 = \alpha_2 = \pi/4 + 0.15$. In each case the visibility as defined in equation 3.36 is unchanged from the ideal values, however the fringe itself becomes distorted. **b**, experimental result showing the 4-fold coincidence counts vs MZI phase, with background correction applied. The fit visibility is 91%.

which equates to the following

$$\begin{pmatrix} e^{i\phi}\cos\theta_1\cos\theta_2 - \sin\theta_1\sin\theta_2 & e^{i\phi}\cos\theta_1\sin\theta_2 + \sin\theta_1\cos\theta_2 \\ -e^{i\phi}\sin\theta_1\cos\theta_2 - \cos\theta_1\sin\theta_2 & -e^{i\phi}\sin\theta_1\sin\theta_2 + \cos\theta_1\cos\theta_2 \end{pmatrix} \equiv \begin{pmatrix} A & B \\ C & D \end{pmatrix}.$$

Now that we have shown the transformation matrix for the unbalanced MZI, we consider the effect on quantum interference in two cases. The first case is where the single photons are emitted in the same spectral mode, and the second, orthogonal modes. When the identical signal photons $\hat{s}^\dagger_{t(b)}$ are incident on the top (bottom) port of the MZI, we have the following

$$\hat{U}_{\mathrm{MZI}}(\phi,\theta_1,\theta_2)\hat{s}^\dagger_t\hat{s}^\dagger_b|\mathrm{vac}\rangle = (A\hat{s}^\dagger_t + B\hat{s}^\dagger_b)(C\hat{s}^\dagger_t + D\hat{s}^\dagger_b)|\mathrm{vac}\rangle\,. \tag{3.37}$$

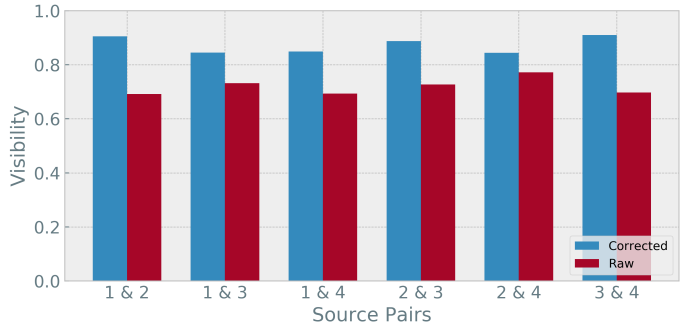

Figure 3.15: Pairwise PIM Measurement. Showing the raw (red) and corrected (blue) visibilities of the heralded HOM experiment.

Here the interesting parameter is the antibunching probability, which is inferred by the four-fold measurement in this experiment and evaluates to $|AD+BC|^2$. After some algebra, the resulting expression for the antibunching probability is given by

$$P_{\text{antibunch}} = (2\cos^2\theta_1 - 1)(2\cos^2\theta_2 - 1) - 4\cos\phi\sin\theta_1\cos\theta_1\sin\theta_2\cos\theta_2. \tag{3.38}$$

In the case where the photons are distinguishable, one can also distinguish two antibunching cases, as a result the antibunching probability becomes $P_{\text{antibunching}} = |AD|^2 + |BC|^2$, which evaluates as the following

$$\begin{aligned} P_{\text{antibunching}} = &(\cos^2\theta_1\cos^2\theta_2 + \sin^2\theta_1\sin^2\theta_2 - 2\cos\phi\sin\theta_1\cos\theta_1\sin\theta_2\cos\theta_2)^2 \\ &+(\sin^2\theta_1\cos^2\theta_2 + \cos^2\theta_1\sin^2\theta_2 + 2\cos\phi\sin\theta_1\cos\theta_1\sin\theta_2\cos\theta_2)^2. \end{aligned} \tag{3.39}$$

Figure 3.14a shows how small variations from the ideal MZI parameters $\theta_1 = \theta_2 = \pi/4$ effect the antibunching probability. Here the black (red) lines show the distinguishable (indistinguishable) models. In each case, the dashed line represents the perfect MZI and the solid lines show small deviations of aproximately 10% from the ideal values. Most notable is that we see zero effect on the maximum (corresponding to identity) or minimum ($\phi = \pm\pi/2$) coincidence counts. This means that we do not expect small changes in the MMI to effect the measured visibility. However these fluctuations prevent the full swapping of photons and thus lower the maximum counts in those cases. Another artifact of these imperfect splitting ratios is the slight change in minima positions. In general the minima is found slightly outside of the estimated ranges predicted by the calibration. Good agreement between the model and data can be found in the raw counts (fig 3.13b) and the corrected counts (fig 3.14b). In these measurements the optimal fit predicted MMI with splitting ratios 65:35.

In order to fully benchmark the indistinguishability of each of the single photon sources on this chip, these measurements were repeated between each pairwise combinations of MRRs. The raw and corrected measurements in each case are summarised

in figure 3.15. In each of the cases, the corrected visibilities are in rough agreement with the expected 92%.

3.4 Discussion

This thesis chapter outlines and assesses the conditions for ideal single photon sources in silicon. The ultimate goal is to produce multiple pure single photons on chip, each with high success probability. The additional goal is then to build precise linear-optical elements which can manipulate these pure single photons to achieve arbitrarily good quantum interference. As the reader will see in the following chapters of this thesis, the ability to construct high quality quantum bits (both Qubits and Qudits) using silicon photons, depends largely on how well we can achieve these above goals.

When looking into the details, what one finds is that spontaneous sources in silicon relying on the four-wave mixing process actually produce quantum states which are many tensor products of twin-beam squeezers. This essentially gives rise to multi-mode twin-beam squeezed states where the squeezing parameters in each case are decided by the Schmidt-decomposition, i.e. how willing the state is to emit photons in a particular spectral mode. We find that single photons may be arbitrarily approximated by reducing the squeezing strength and shaping the JSA to produce photons in a single optical mode. Reducing the squeezing is as easy as reducing ones pumping power, which introduces a trade-off between generation probability and number purity. Shaping the spectral JSA so that photons are emitted in only a single spectral mode is found to be problematic [145–147], although multiple solutions have been proposed [130, 148].

In this chapter, we show that historical experiments (such as the reverse HOM experiment, see section 2.4.2) which post-select onto two-fold coincidences tend to be uneffected by the spectral purity, but are effected by the number purity. This is consistent with the findings of high visibility bi-photon interference experiments previously demonstrated [12, 61, 94, 108]. It is shown that the interference condition here is actually that the single photon spectra is identical between the sources, but not that they are pure. However, in order to build more complex quantum states on-chip one is required to scale the number of simultaneous photons generated in the device. Interfering many photons (or even heralded single photons) as it turns out requires the spectral separability of the JSA. These mathematical observations are then explored experimentally on the same device, giving very high two-photon interference visibility, whilst the heralded single photon visibility remains significantly lower.

The heralded single photon indistinguishability measurements are able to assess the overall quality of ones photon sources. Importantly, the two major contributions which tend to degrade the interference (spectral purity and number purity) can be decoupled by utilizing optical switches. After correcting for the multi-pair emission, it was found that the average quantum visibility (heralded) was $87.3 \pm 4.5\%$. This is slightly lower (on average) than the estimated 92%. The likely cause for this is is due to the optical pump width. For example, a broad pump results in a four-wave mixing interaction between the pump and straight waveguides, since a higher fraction of light bypasses the MRR resonance. As the width of the pump reduces, this problem is avoided, but theoretical predictions of MRR purity are based on flat pumping profiles. Of course, as the pumping profile becomes comparable in width to the MRR linewidth, the pump is certainly not flat, which will have an effect on the SFWM inside the cavity.

In this work, high purity multiphoton interference was shown between multiple integrated micro-ring resonator sources with multi-pair correction for the first time [109]. In the remaining chapter we take these results and apply them to some important quantum information experiments.

CHAPTER 4

SINGLE-CHIP QUANTUM INFORMATION PROCESSING EXPERIMENTS

In this chapter we explore the ability to encode multiple qubits in multiphoton states that are generated by up to four microring resonator single photon sources in silicon. In the previous chapter it was shown that multiple approximately pure bi-photon states can reliably interfere with one another, achieving $\approx 90\%$ interference visibility. Quantum interference is at the heart of many of the fundamental quantum information experiments such as quantum teleportation, entanglement swapping and multiphoton entanglement. The aim is to benchmark each of these quantum information protocols with one programmable four-qubit photonic device, where the final state fidelity serves as a quantifier for each experiment.

We begin by first introducing a single bi-photon state that can be encoded into two single qubits consisting of orthogonal signal and idler photon states. Superpositions of these bi-photon states can generate maximally entangled photon pairs encoded in the path degree of freedom. The fidelity of the generated entanglement serves as a combined benchmark for the similarity between each pair of MRR as well as the fidelity of the single qubit unitary transformations. Next the focus shifts towards encoding two identical qubits composed of heralded single photons of near identical colour. When encoded in this form, the identical qubits can reliably interfere with one another and a range of measurement induced non-linear operations are performed on chip. Specifically it is shown how two separable states can become entangled through a two-qubit logic gate with 50% probability. Finally we demonstrate four-photon multi-qubit experiments combining qubits that are encoded by photons from different MRR's.

Quantum experiments are achieved on these multiphoton states through the precise control of high fidelity single qubit unitary transformations, two-qubit operations and local qubit projectors in one device. The main results of this chapter are published in the following work [109] and some subsections of this chapter are based on that text.

4.1 Local Measurements On Single Qubits Generated from Pure Bi-photon States

This section provides the reader with essential experimental information in order to understand the quantum information demonstrations in the following two chapters. We discuss the approach to encoding and measuring single qubits in terms of a few linear-optic parameters. At the end of this section we discuss how these methods combine to produce a bi-photon entangled state on chip.

4.1.1 Experimental Setup and Device Design

The Silicon device used throughout this chapter[1] is a four-qubit, eight spatial-mode device that integrates four MRR single photon sources, each capable of emitting photon pairs. The qubits on this chip are constructed directly from these produced photon pairs at low squeezing. In order to reduce noise, single qubits are detected by measuring heralded single photons, whereas the simultaneous arrival of two single photons may also be prepared and measured as two qubit states. In order to generate higher numbers of qubits, we require that multiple single photon sources will emit photon pairs in the same pump pulse. The number of active qubits can be controlled per experiment by limiting the number of single photon sources that are in use. Each MRR single photon source is turned on when its pump resonance overlaps with the coupled pumping field and is turned off when the resonance is detuned. Linear optical components comprised by MMI, phase-shifters and waveguide crossers all enable the preparation and measurement of qubit states on chip. For each of the experiments in this chapter, and externally coupled pulsed laser centered at $\approx 1550nm$ is used. A 50 MHz laser repetition rate is used for the two-photon experiments that follow, while for the four-photon experiments a 500 MHz repetition rate is used.

The fundamental building block for quantum information processing and many applications of quantum information are the single qubit gates and two-qubit gates.

[1] A simplified device schematic will be given for each experiment in this chapter, however, refer to the schematic in fig. 3.1 as a reference of the full chip design.

In the following sections it is shown how simple thermally controlled optical interferometers can be constructed to easily perform deterministic single qubit unitary transformation and projections. Here we draw a distinction between the transformation of a state under a local unitary transformation and the change of basis which occurs by measuring the same state in another measurement setting.

4.1.2 Single-qubit Preparation and Projection

The devices in this thesis are designed to enable the preparation of arbitrary single-qubit states and to perform arbitrary single-qubit projective measurements across four qubits encoded in path. These operations and projections are broken down into the components $\hat{U}_{\text{Phase}}(\phi)$, which controls the relative photon phase across adjacent modes, and $\hat{U}_{\text{MZI}}(\theta)$, which controls the relative probability amplitude of measuring a photon in the $|0\rangle$ or $|1\rangle$ mode. As this section outlines, an ordered combination of these effects allows for full local unitary rotations $\hat{U} = \hat{U}_{\text{Phase}}(\phi)\hat{U}_{\text{MZI}}(\theta)$ [108]. The parameters θ and ϕ are relative phase shifts between the two optical paths, where a phase shift can be applied to either the $|0\rangle$ (top) or $|1\rangle$ (bottom) mode. Unitaries with optical phase shifts on the top (bottom) mode will be represented as $\hat{U}_t(\phi,\theta)$ ($\hat{U}_b(\phi,\theta)$). In the following approach we describe the case where the phase shift is on the bottom mode, but the alternate approach is explained in appendix A.

A quantitative assessment of these unitary operations can be given by summarising the linear optical transformations on each of the modes caused by each component as follows

$$\hat{U}_{\text{Phase}}(\theta) = \begin{pmatrix} 1 & 0 \\ 0 & e^{i\theta} \end{pmatrix}, \tag{4.1}$$

$$\hat{U}_{\text{MMI}} = \frac{1}{\sqrt{2}} \begin{pmatrix} i & 1 \\ 1 & i \end{pmatrix}, \tag{4.2}$$

$$\hat{U}_{\text{MZI}}(\theta) = \hat{U}_{\text{MMI}}\hat{U}_{\text{Phase}}\hat{U}_{\text{MMI}} = e^{i(\theta+\pi)/2} \begin{pmatrix} \sin(\theta/2) & \cos(\theta/2) \\ \cos(\theta/2) & -\sin(\theta/2) \end{pmatrix}. \tag{4.3}$$

Therefore the total unitary is written as

$$\begin{aligned} \hat{U}_b(\phi,\theta) &= \hat{U}_{\text{Phase}}(\phi)\hat{U}_{\text{MZI}}(\theta) \\ &= e^{i(\theta+\pi)/2} \begin{pmatrix} \sin(\theta/2) & \cos(\theta/2) \\ e^{i\phi}\cos(\theta/2) & -e^{i\phi}\sin(\theta/2) \end{pmatrix}. \end{aligned} \tag{4.4}$$

As a result, the general mapping of computational basis states as a function of the two phases θ and ϕ is written as

$$\hat{U}_b(\phi,\theta)|0\rangle = e^{i(\theta+\pi)/2}\big(\sin(\theta/2)|0\rangle + e^{i\phi}\cos(\theta/2)|1\rangle\big), \tag{4.5a}$$

$$\hat{U}_b(\phi,\theta)|1\rangle = e^{i(\theta+\pi)/2}\big(\cos(\theta/2)|0\rangle - e^{i\phi}\sin(\theta/2)|1\rangle\big). \tag{4.5b}$$

Hence the magnitude of the $\{0,1\}$ superposition states can be easily controlled by the parameter θ and the relative phase of the $\{0,1\}$ states can be controlled via the external phase ϕ. These bases therefore form an arbitrary orthonormal basis set, spanning the entire two dimensional space, under the conditions that each of the states are orthonormal with one another, i.e.

$$\big(\sin(\theta/2)|0\rangle + e^{i\phi}\cos(\theta/2)|1\rangle\big)^\dagger\big(\cos(\theta/2)|0\rangle - e^{i\phi}\sin(\theta/2)|1\rangle\big) = 0 \tag{4.6a}$$

$$\big(\cos(\theta/2)|0\rangle - e^{i\phi}\sin(\theta/2)|1\rangle\big)^\dagger\big(\sin(\theta/2)|0\rangle + e^{i\phi}\cos(\theta/2)|1\rangle\big) = 0 \tag{4.6b}$$

$$\big(\cos(\theta/2)|0\rangle - e^{i\phi}\sin(\theta/2)|1\rangle\big)^\dagger\big(\cos(\theta/2)|0\rangle - e^{i\phi}\sin(\theta/2)|1\rangle\big) = 1 \tag{4.6c}$$

$$\big(\sin(\theta/2)|0\rangle + e^{i\phi}\cos(\theta/2)|1\rangle\big)^\dagger\big(\sin(\theta/2)|0\rangle + e^{i\phi}\cos(\theta/2)|1\rangle\big) = 1, \tag{4.6d}$$

which is to say that $\hat{U}_b(\phi,\theta)$ is unitary such that $\hat{U}_b^\dagger(\phi,\theta)\hat{U}_b(\phi,\theta) = \mathbb{1}$, since this would imply that for $i,j \in \{0,1\}$

$$\begin{aligned}\big(\hat{U}_b(\phi,\theta)|i\rangle\big)^\dagger\hat{U}_b(\phi,\theta)|j\rangle &= \langle i|\hat{U}_b^\dagger(\phi,\theta)\hat{U}_b(\phi,\theta)|j\rangle \\ &= \delta_{i,j}.\end{aligned} \tag{4.7}$$

To test the condition, we can directly calculate $\hat{U}_b^\dagger(\phi,\theta)\hat{U}_b(\phi,\theta)$, applying $\hat{A}^\dagger = \hat{A}^{T*}$

$$\begin{aligned}\hat{U}_b^\dagger(\phi,\theta)\hat{U}_b(\phi,\theta) &= \begin{pmatrix}\sin\theta/2 & e^{-i\phi}\cos\theta/2\\ \cos\theta/2 & -e^{-i\phi}\sin\theta/2\end{pmatrix}\begin{pmatrix}\sin(\theta/2) & \cos(\theta/2)\\ e^{i\phi}\cos(\theta/2) & -e^{i\phi}\sin(\theta/2)\end{pmatrix} \\ &= \begin{pmatrix}1 & 0\\ 0 & 1\end{pmatrix},\end{aligned} \tag{4.8}$$

where the global phases immediately cancel.

For projective measurements, where arbitrary qubits are rotated back into the computational basis to be accurately measured, one can simply perform the adjoint transformation $\hat{U}_b^\dagger(\phi,\theta)$. By performing this projection back in to the computational basis, one can infer the statistical likelihood of particular eigenvalues only by measuring photon detection events in each mode. By utilizing this method one can infer the measured eigenvalues, as can be seen in the following approach

$$\hat{U}_b^\dagger(\phi,\theta)\big(\sin(\theta/2)|0\rangle + e^{i\phi}\cos(\theta/2)|1\rangle\big) = \hat{U}_b^\dagger(\phi,\theta)\hat{U}_b|0\rangle = |0\rangle, \tag{4.9a}$$

$$\hat{U}_b^\dagger\big(\cos(\theta/2)|0\rangle - e^{i\phi}\sin(\theta/2)|1\rangle\big) = \hat{U}_b^\dagger\hat{U}_b|1\rangle = |1\rangle. \tag{4.9b}$$

By utilizing the mathematical identity $(\hat{A}\hat{B})^\dagger = \hat{B}^\dagger\hat{A}^\dagger$, evaluating $\hat{U}_b^\dagger$ becomes straightforward under the following approach

$$\begin{aligned}\hat{U}_b^\dagger(\phi,\theta) &= \left(\hat{U}_{\text{Phase}}(\phi)\hat{U}_{\text{MZI}}(\theta)\right)^\dagger \\ &= \hat{U}_{\text{MZI}}^\dagger(\theta)\hat{U}_{\text{Phase}}^\dagger(\phi) \\ &= e^{-i(\theta+\pi)}\hat{U}_{\text{MZI}}(\theta)\hat{U}_{\text{Phase}}(-\phi).\end{aligned} \tag{4.10}$$

Hence the ability to project any qubit system back into the computational basis can be efficiently achieved by reversing the physical operation order $\hat{U}_{\text{Phase}} \leftrightarrow \hat{U}_{\text{MZI}}$ and also reversing the sign of the phase applied to the $|1\rangle$ mode, $\hat{U}_{\text{Phase}}(\phi) \rightarrow \hat{U}_{\text{Phase}}(-\phi)$. Figure 4.1 summarises the linear-optic integrated circuit diagrams for producing $\hat{U}_b(\phi,\theta)$ and $\hat{U}_b^\dagger(\phi,\theta)$ as well as the cases where the local phase shift is applied to the top mode $\hat{U}_t(\phi,\theta)$ and $\hat{U}_t^\dagger(\phi,\theta)$. A list of common projectors used in this thesis are given in fig 4.1c along with the phases required in order to set them. For example, the Hadamard transformation is often used in order to project into the eigenstates of the $\hat{\sigma}_x$ operator and can also be produced by setting $\hat{U}_b^\dagger(0,\pi/2)$.

4.1.3 Tomography and Coincidence Counts

In each of the experiments that follow, we operate under the assumption that it is possible to create well-defined qubits on our device with high purity. In this picture, up to four qubits are created simultaneously where no more than 1 photon can occupy each qubit at one time. Under this assumption, an abstraction layer is formed under which one can create well-defined logical states via the precise control of on-chip linear optic networks. In each of the experiments, the goal is to perform some state evolution task in the logical bases and then to gauge how closely to the ideal scenario the experiment was able to achieve. In general, a good measure of this closeness is the state fidelity which can be numerically computed between the desired pure state $|\psi\rangle$[2] and the measured state ρ as

$$F(|\psi\rangle, \rho) = \langle\psi|\,\rho\,|\psi\rangle\,. \tag{4.11}$$

In the best case scenario, where $\rho = |\psi\rangle\langle\psi|$, the fidelity is 1. In the worst case scenario, the fidelity equals exactly zero when the measured state is orthogonal to the desired state. As the measured state ρ becomes mixed, this also degrades the fidelity, where in the worst case (maximally mixed states), the computed fidelity drops by a factor of 1/2 for qubit states[3].

[2]This is the special case where the target state is pure, which for our purposes is adequate. The general expression is given in background section 2.1.7 equation 2.24.

[3]In general, for d dimensional states the fidelity drops by a factor of $1/d$.

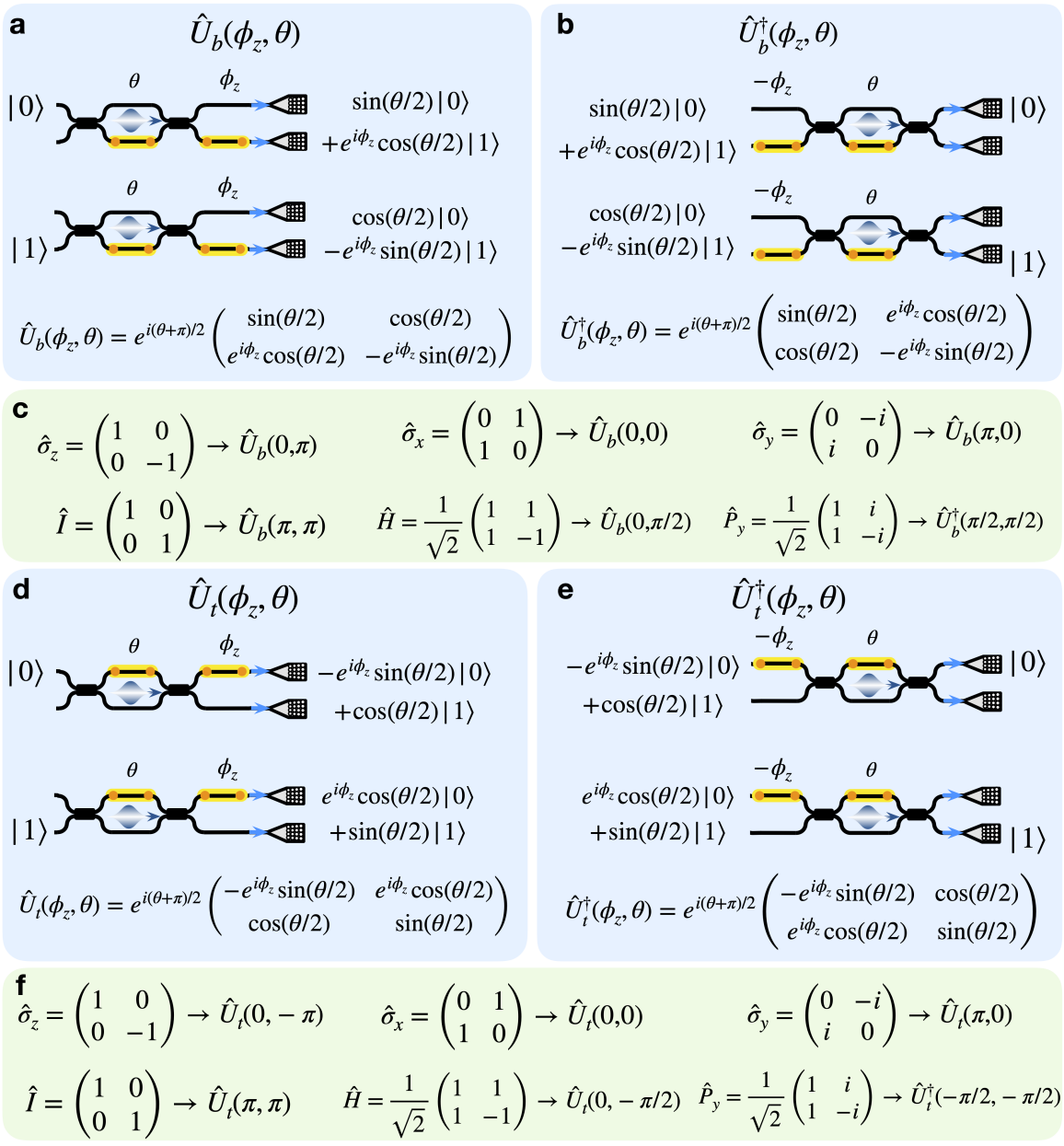

Figure 4.1: Linear-optic circuit diagrams for the calculated **a** $\hat{U}_b(\phi,\theta)$ unitary transformation and its Hermitian conjugate **b** $\hat{U}_b^\dagger(\phi,\theta)$ the projector. Here the two active phases θ and ϕ are on the bottom waveguide corresponding to a logical $|1\rangle$ state. **d** and **e** show the differences caused by the two phases being placed on the logical zero. On the left $\hat{U}_b(\phi,\theta)$ shows in general how the two phases change the input $|0\rangle$ or $|1\rangle$ state. The diagrams on the right show how these operations may be reversed to move back to the computational basis. **c & f,** examples of how some of the popular transformations are constructed on chip. $\hat{\sigma}_x$, $\hat{\sigma}_y$, $\hat{\sigma}_z$ are the three Pauli matrices, $\hat{I}$ is the identity matrix, $\hat{H}$ is the Hadamard matrix (useful for projecting into the $\hat{\sigma}_x$ eigenstates) and $\hat{P}_y$ represents the projection into each of the $\hat{\sigma}_y$ eigenstates.

Before the fidelity can be computed, one is required to first estimate the on-chip state[4]. The standard approach is to perform maximum likelihood tomographic processes which is achieved by sampling the on-chip state many times. In general, over-complete tomography of n qubits requires the measurement of the generated state in 3^n global product bases, $\otimes_{\forall x_i}\hat{\sigma}_{x_i}$ where $x_i \in \{x,y,z\}$ [149]. In practice this is achieved by sampling the prepared state many times in each basis and comparing the coincidence count-rate in each outcome to infer the relative probabilities.

As an example, consider the simplest case, the heralded single qubit. In this scenario, idler photons are used as a trigger in order to prepare a secondary qubit formed by the signal photon. If the generated single photons originated from the top MRR, a coincidence detection will occur in the output modes according to the state $|T\rangle|0\rangle$. Here $|T\rangle$ refers to the heralding photon which triggers the qubit initially prepared in the zero mode. In principle, any qubit can be prepared by operating on the initial state with a general unitary transformation $|T\rangle \otimes \hat{U}(\phi,\theta)|0\rangle$

$$\begin{aligned} |T\rangle \otimes |\psi\rangle &= |T\rangle \otimes \hat{U}(\phi,\theta)|0\rangle \\ &= |T\rangle \otimes \left(\sin\theta/2\,|0\rangle + e^{i\phi}\cos\theta/2\,|1\rangle\right). \end{aligned} \tag{4.12}$$

For the single qubit, three individual bases measurements are required, $\langle\hat{\sigma}_x\rangle$, $\langle\hat{\sigma}_y\rangle$, $\langle\hat{\sigma}_z\rangle$. With each of the Pauli operators written in their eigenbases, these evaluate as the following

$$\langle\psi|\hat{\sigma}_x|\psi\rangle = \langle\psi|\hat{P}_+|\psi\rangle - \langle\psi|\hat{P}_-|\psi\rangle = p_+ - p_-, \tag{4.13}$$

$$\langle\psi|\hat{\sigma}_y|\psi\rangle = \langle\psi|\hat{P}_{+i}|\psi\rangle - \langle\psi|\hat{P}_{-i}|\psi\rangle = p_{+i} - p_{-i}, \tag{4.14}$$

$$\langle\psi|\hat{\sigma}_z|\psi\rangle = \langle\psi|\hat{P}_0|\psi\rangle - \langle\psi|\hat{P}_1|\psi\rangle = p_0 - p_1, \tag{4.15}$$

where p_x represents the probability of measuring eigenvalue associated with the state $|x\rangle$, where $|x\rangle \in \{|0\rangle, |1\rangle, |+\rangle, |1\rangle, |+i\rangle, |-i\rangle\}$. Therefore two probabilities need to be measured for each of the three Pauli operators, giving six total measurements. These measurements can be estimated from the normalised coincidence counts between the trigger and $|0\rangle$ mode, $\mathrm{C}_{T,0}$, and the trigger and $|1\rangle$ mode, $\mathrm{C}_{T,1}$. For example, the probability of measuring the three positive eigenvalues, corresponding to $\hat{P}_0$, $\hat{P}_+$ and $\hat{P}_{+i}$, can be estimated via

$$p_{\mathrm{pos}} = \frac{\mathrm{C}_{T,0}}{\mathrm{C}_{T,0}+\mathrm{C}_{T,1}}, \tag{4.16}$$

and the remaining negative eigenvalues

$$p_{\mathrm{neg}} = \frac{\mathrm{C}_{T,1}}{\mathrm{C}_{T,0}+\mathrm{C}_{T,1}}. \tag{4.17}$$

[4]This is the primary method for determining state fidelity in this thesis. An alternative is to decompose the state into local observables that can each be measured.

In the standard approach, three single photon detectors are connected to output modes $|T\rangle$, $|0\rangle$ and $|1\rangle$, where the coincidence counts $C_{T,0}$ and $C_{T,1}$ can be trivially measured. However, for n qubits this approach requires at least $2 \times n$ detectors, which become resource intensive for large n. An alternative approach is to use only one detector per qubit (two including the trigger), and collect coincidence counts corresponding to $C_{T,0}$. The remaining $C_{T,1}$ coincidence counts can be estimated by applying a mode swap on chip, which is equivalent to operating an additional $\hat{\sigma}_x$. With this swap applied, the measured $C'_{T,0}$ estimate the $C_{T,1}$ measurements. Hence there is a trade-off between the number of measurement settings and the number of detectors.

In the three detector approach, each of the three expectation values are calculated from the coincidence detection's provided the correct projectors are applied to the two spatial modes. In this method, each of the expectation values are calculated via the following expression

$$\langle\psi|\hat{\sigma}_i|\psi\rangle = \frac{C_{T,0} - C_{T,1}}{C_{T,0} + C_{T,1}}. \tag{4.18}$$

For each of the $\hat{\sigma}_i$ bases, the correct projector phases are summarised in table 4.1.

Operator	$\hat{U}_b^\dagger(\phi,\theta)$	$\hat{U}_t^\dagger(\phi,\theta)$
$\hat{\sigma}_x$	$\hat{U}_b^\dagger(0,\pi/2)$	$\hat{U}_t^\dagger(0,-\pi/2)$
$\hat{\sigma}_y$	$\hat{U}_b^\dagger(\pi/2,\pi/2)$	$\hat{U}_t^\dagger(-\pi/2,-\pi/2)$
$\hat{\sigma}_z$	$\hat{U}_b^\dagger(0,\pi)$	$\hat{U}_t^\dagger(0,-\pi)$

Table 4.1: Projector phases for the three Pauli operators.

In the case where only two detectors are used, between the trigger and zero mode, additional measurement settings are required. In general, for N qubits and N detectors, the number of global measurement settings is 6^N compared with 3^N for $2N$ detectors. For a single qubit, this doubles the number of measurement settings to six. Here we require that coincidence counts between the trigger and zero mode can infer each of the eigenvector probabilities. The measurement settings for each of the six projectors are given in table 4.2 For N qubits, the same procedure should be followed, with measurements for each permutation of the above measurement settings.

4.1.4 Re-calibration of Single-photon Detector Efficiencies

The previous section outlines how the normalised coincidence counts across different spatial modes may infer the relative probabilities corresponding to different eigenvectors. As these measurements directly relate to the observed outcome probabilities, their

Projector	$\hat{U}_b^\dagger(\phi,\theta)$	$\hat{U}_t^\dagger(\phi,\theta)$
$\hat{P}_+$	$\hat{U}_b^\dagger(0,\pi/2)$	$\hat{U}_t^\dagger(0,-\pi/2)$
$\hat{P}_-$	$\hat{U}_b^\dagger(\pi,\pi/2)$	$\hat{U}_t^\dagger(\pi,-\pi/2)$
$\hat{P}_{+i}$	$\hat{U}_b^\dagger(\pi/2,\pi/2)$	$\hat{U}_t^\dagger(-\pi/2,-\pi/2)$
$\hat{P}_{-i}$	$\hat{U}_b^\dagger(-\pi/2,\pi/2)$	$\hat{U}_t^\dagger(\pi/2,-\pi/2)$
$\hat{P}_0$	$\hat{U}_b^\dagger(0,\pi)$	$\hat{U}_t^\dagger(0,-\pi)$
$\hat{P}_1$	$\hat{U}_b^\dagger(0,0)$	$\hat{U}_t^\dagger(0,0)$

Table 4.2: Projector phases for the six Pauli eigenvectors.

faithful measurement is crucial to any quantum information demonstration. However, in order for the normalised counts to give a true estimate of these relative probabilities, we have to ensure that measurements corresponding to different eigenvalues have equal detection efficiencies. For example, for any target state $|\psi\rangle = \sum_i \alpha_i |\phi_i\rangle$ on our device, the ideal outcome probabilities $|\alpha_i|^2$ are actually subject to relative losses between the different spatial modes $p_i = |\alpha_i|^2 L_i$, where L_i is the relative detection efficiency corresponding to the i^{th} vector. In other words, since single photons in our device travel different optical paths and are subsequently coupled to different optical fibres, the relative detection efficiency of photons in the $|0\rangle$ and $|1\rangle$ modes of each qubit will vary. As a result, when utilising a detector at each output port these efficiencies are not all equal $L_i \neq L_j$ and should be accounted for in order for the state tomography to better represent the on-chip fidelity.

One solution is to collect photons only belonging to a single eigenstate, say $|0000\rangle$ (having a fixed heralding efficiency) and then use the four on-device projectors to rotate the measured basis accordingly, as described in the previous section and summarised in table 4.2. For example, rather than directly measuring coincidence counts corresponding to the eigenvector $|1111\rangle$ one could continue to measure $|0000\rangle$ but apply the transformation $\hat{\sigma}_x^{\otimes 4}$ along all of the qubits. In this scenario, the photons corresponding to different eigenvectors travel along the same optical path and therefore experience the same transmission efficiencies. As a result, and providing the setup is temporally stable, the relative coincidence counts between each projector would give an accurate description of the quantum mechanical probabilities of measuring that state. One drawback of this method is that the number of global measurement settings required to perform a single n-qubit basis measurement scales as 2^N. In comparison, a single basis measurement can be performed with just a single global measurement setting with sufficient detectors across all output modes. As an example, for the experiments performed within this thesis, this approach gives a $2\times$ increase in measurement settings for teleportation, $4\times$ increase for entanglement swapping &

Bell projections and a 16× increase in GHZ measurements.

An alternative approach is to keep track of the heralding efficiency's (they may vary each time the coupling between chip and fibre array changes) and correct the measured coincidence counts in the following manner. Let the detection probability of a photon in the $|0\rangle$ ($|1\rangle$) mode of the i^{th} qubit be written as $\eta_{i,0}$ ($\eta_{i,1}$). In this case the measured four-fold counts C_{meas} may be written in terms of the on-device four-fold counts C_{true} as

$$C_{\text{meas},ijkl} = \eta_{1,i}\eta_{2,j}\eta_{3,k}\eta_{4,l}C_{\text{true},ijkl}. \tag{4.19}$$

In order to balance the losses across each of the measurements, we can manually correct the counts by normalising them relative to the $|0000\rangle$ modes

$$\frac{C_{\text{meas},ijkl}}{C_{\text{meas},0000}} = \frac{\eta_{1,i}\eta_{2,j}\eta_{3,k}\eta_{4,l}}{\eta_{1,0}\eta_{2,0}\eta_{3,0}\eta_{4,0}}\frac{C_{\text{true},ijkl}}{C_{\text{true},0000}} \tag{4.20}$$

and so the desired corrected quantity, $C_{\text{corr},ijkl} \equiv C_{\text{true},ijkl}/C_{\text{true},0000}$, can be measured in terms of the measured quantities $C'_{\text{meas},ijkl} \equiv C_{\text{meas},ijkl}/C_{\text{meas},0000}$ the ratio of heralding efficiency's by applying the correction factor $K_{i,j,k,l}$ to the measured results in the following way

$$K_{i,j,k,l} \equiv \frac{\eta_{1,0}\eta_{2,0}\eta_{3,0}\eta_{4,0}}{\eta_{1,i}\eta_{2,j}\eta_{3,k}\eta_{4,l}}, \tag{4.21}$$

where

$$C_{\text{corr},ijkl} = K_{i,j,k,l}C'_{\text{meas},ijkl}. \tag{4.22}$$

As a result, each of the corrected coincidence counts can be obtained through just four relative detection parameters L_i, where $L_i = \eta_{i,0}/\eta_{i,1}$. See table 4.3 for a summary of which correction factors apply to each of the 16 mode combinations. These four heralding efficiency ratios can be measured by comparing two fold coincidence counts from a single sources across both modes of each qubit. For example, in the regime where a single source is pumped, the single photons produced per second inside the device is the probability of generating a photon per pulse p (at a given pumping strength) multiplied by the repetition rate R, such that $R \times p$ photon pairs are emitted per second on average. The coincidence count-rate across any two given spatial modes $\{i,j\}$ is then given by $C_{i,j} = \eta_i\eta_j Rp$. The four correction ratios $\{L_i\}$ can then be calculated by using an ancillary channel to compare the two-fold counts produced from the same source when swapping the path of single photons between the zero and one mode of a particular qubit, as can be seen from the following

$$\frac{C_{0,\text{ancilla}}}{C_{1,\text{ancilla}}} = \frac{\eta_0}{\eta_1}. \tag{4.23}$$

This process can then be repeated to calculate the (up to four, one for each qubit) relative heralding efficiencies for each qubit.

Qubit Modes (i,j,k,l)	Correction Factor, $K_{i,j,k,l}$
0,0,0,0	1
0,0,0,1	L_4
0,0,1,0	L_3
0,0,1,1	L_3L_4
0,1,0,0	L_2
0,1,0,1	L_2L_4
0,1,1,0	L_2L_3
0,1,1,1	$L_2L_3L_4$
1,0,0,0	L_1
1,0,0,1	L_1L_4
1,0,1,0	L_1L_3
1,0,1,1	$L_1L_3L_4$
1,1,0,0	L_1L_2
1,1,0,1	$L_1L_2L_4$
1,1,1,0	$L_1L_2L_3$
1,1,1,1	$L_1L_2L_3L_4$

Table 4.3: Measurement correction factors for the four-qubit (four photon) coincidence counts.

4.1.5 Two-Photon Entanglement

In this section, we combine the results so far to show that two photon entangled states can be prepared and measured with high fidelity on chip. The successful implementation of this experiment requires two identical single photon sources, single qubit unitary transformations and local projective measurements. In the following subsection, it is shown how the similarity between the two sources directly affects the ability to perform quantum interference on chip. Moreover, it is shown how this interference forms the coherence's of the entangled state density matrix. The subsequent subsection shows the results of generating all four Bell states on chip through the proposed on-chip bi-photon generation. For background information see section 2.3.1, and for the experimental configuration see figure 4.2a.

4.1.5.1 State Generation

Generating Bell pairs in our device relies on the ability to interfere two photons generated within in one of two MRR sources with high visibility. Without this quantum

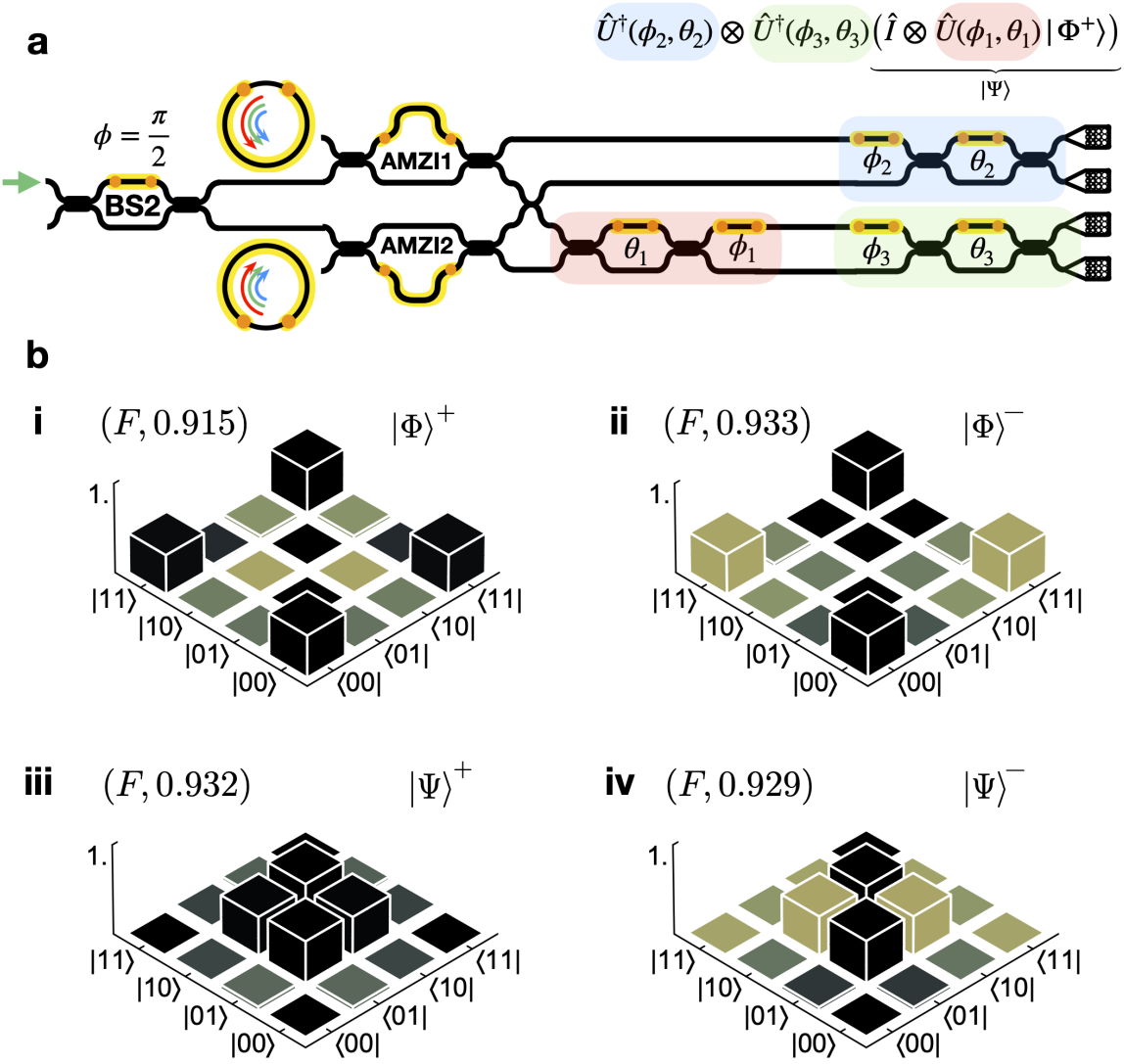

Figure 4.2: **Two-photon Entangled States on Chip. a,** simplified schematic of the two-photon entanglement chip configuration. The role of each part of the chip is highlighted as coloured regions and their associated mathematical contribution to the state evolution are highlighted in the upper right of the figure. **bi-iv,** Reconstructed density matrices of the four Bell states generated on-chip. Each of the density matrices were numerically estimated by collecting 36 normalised 2-photon coincidence detection measurements between two single photon detectors. These normalised counts estimate the probability of measuring each eigenvector that together allow the reconstruction of the density matrix for the measured state. The fidelity of each state is shown above each reconstructed density matrix.

interference, the photons are found in a maximally mixed state as the coherence terms of the density matrix vanish. This can be seen directly from the density matrix of the $|\Phi^+\rangle = (|0,0\rangle + |1,1\rangle)/\sqrt{2}$ state, where

$$\rho_{\Phi^+} = \frac{1}{2}\big(|0,0\rangle\langle 0,0| + |0,0\rangle\langle 1,1| + |1,1\rangle\langle 0,0| + |1,1\rangle\langle 1,1|\big). \tag{4.24}$$

The diagonal matrix components, $|0,0\rangle\langle 0,0|$ and $|1,1\rangle\langle 1,1|$, can be measured directly in the computational basis. However, the remaining off-diagonal elements, referred to as the coherence terms, are actually obtained from measurements along the $\hat{\sigma}_x \otimes \hat{\sigma}_x$ and $\hat{\sigma}_y \otimes \hat{\sigma}_y$ directions, where

$$\frac{1}{2}\big(|0,0\rangle\langle 1,1| + |1,1\rangle\langle 0,0|\big) = \frac{1}{4}\big(\hat{\sigma}_x \otimes \hat{\sigma}_x - \hat{\sigma}_y \otimes \hat{\sigma}_y\big). \tag{4.25}$$

In this section it is shown how a superposition of identical bi-photon states can encode the $|\Phi^+\rangle$ state, where the coherence terms of this state relies on the quantum interference between the bi-photon superposition.

When attempting to generate the Bell state $|\Phi\rangle^+$, two sources are pumped in the low photon number regime. In the cases where only two photons are detected, the measured photons must arise from the same source with high probability. In this scenario, the full state can be written as a superposition of bi-photon states in different spatial modes with frequency ω as

$$\begin{aligned} |\Psi\rangle = N\Big(&\int_{\omega_s,\omega_i} \mathrm{d}\omega_s \mathrm{d}\omega_i f(\omega_s,\omega_i)\hat{a}^\dagger_{\omega_s,A,0}\hat{a}^\dagger_{\omega_i,B,0} \\ &+ \int_{\omega'_s,\omega'_i} \mathrm{d}\omega'_s \mathrm{d}\omega'_i f'(\omega'_s,\omega'_i)\hat{a}^\dagger_{\omega'_s,A,1}\hat{a}^\dagger_{\omega'_i,B,1}\Big)|\mathrm{vac}\rangle\,, \end{aligned} \tag{4.26}$$

where the subscripts $\{A,B\}$ reference the two qubits and 0/1 reference the qubit modes. After the single photons pass through the integrated AMZI, they give rise to classical correlations in the 00 and 11 mode, corresponding to $|00\rangle\langle 00|$ and $|11\rangle\langle 11|$ terms in the reconstructed density matrix. Note that, here it is explicitly assumed that one may balance these contributions by altering the overall relative pumping strength provided to each source. In order to show that the generated state has the correct quantum properties, however, it is necessary to show the following

$$\begin{aligned} |\Phi^+\rangle &= (|00\rangle + |11\rangle)/\sqrt{2} \\ &= (|{+}{+}\rangle + |{-}{-}\rangle)/\sqrt{2} \\ &= \hat{H}\otimes\hat{H}(|00\rangle + |11\rangle)/\sqrt{2}. \end{aligned} \tag{4.27}$$

The condition for our state to show the correct interference relies primarily on the

ability to tune the spectrum of the single photons such that $f(\omega_s,\omega_i) = f'(\omega_s,\omega_i)$, requiring only that we are able to generate identical single photon sources. Once the photons are projected into the local eigenvectors of the bases $(\hat{\sigma}_x \otimes \hat{\sigma}_x)_{A,B}$,

(4.28)
$$(\hat{H}\otimes\hat{H})_{A,B}|\Psi\rangle = \frac{1}{2N}\Big(\int_{\omega_s,\omega_s} \mathrm{d}\omega_s \mathrm{d}\omega_i f(\omega_s,\omega_i)(\hat{a}^\dagger_{\omega_s,A,0}+\hat{a}^\dagger_{\omega_s,A,1})(\hat{a}^\dagger_{\omega_i,B,0}+\hat{a}^\dagger_{\omega_i,B1}) + \int_{\omega'_s,\omega'_i} \mathrm{d}\omega'_s \mathrm{d}\omega'_i f(\omega'_s,\omega'_i)(\hat{a}^\dagger_{\omega'_s,A,0}-\hat{a}^\dagger_{\omega'_s,A,1})(\hat{a}^\dagger_{\omega'_i,B,0}-\hat{a}^\dagger_{\omega'_i,B,1})\Big)|\mathrm{vac}\rangle\,.$$

The amount of quantum interference can now be seen by comparing the integrand for various values of ω_s,ω_i. In instances where $\omega = \omega'$, the state may be factorised in a clear way, giving a contribution to the total state

(4.29)
$$f(\omega_s,\omega_i)\big(\hat{a}^\dagger_{\omega_s,A,0}\hat{a}^\dagger_{\omega_i,B,0}+\hat{a}^\dagger_{\omega_s,A,1}\hat{a}^\dagger_{\omega_i,B,1}\big).$$

In addition, due to the fact that $f = f'$ each integral in the general expression is symmetric around the case $\omega = \omega'$. For example, for every contribution to the overall state

(4.30)
$$\begin{aligned}&\mathrm{d}\omega_i \mathrm{d}\omega_s f(\omega_s,\omega_i)(\hat{a}^\dagger_{\omega_s,A,0}+\hat{a}^\dagger_{\omega_s,A,1})(\hat{a}^\dagger_{\omega_i,B,0}+\hat{a}^\dagger_{\omega_i,B,1})\\ &+\mathrm{d}\omega'_i \mathrm{d}\omega'_s f(\omega'_s,\omega'_i)(\hat{a}^\dagger_{\omega'_s,A,0}-\hat{a}^\dagger_{\omega'_s,A,1})(\hat{a}^\dagger_{\omega'_i,B,0}-\hat{a}^\dagger_{\omega'_i,B,1}),\end{aligned}$$

there is a symmetric contribution

(4.31)
$$\begin{aligned}&\mathrm{d}\omega'_i \mathrm{d}\omega'_s f(\omega'_s,\omega'_i)\big(\hat{a}^\dagger_{\omega'_s,A,0}+\hat{a}^\dagger_{\omega'_s,A,1}\big)(\hat{a}^\dagger_{\omega'_i,B,0}+\hat{a}^\dagger_{\omega'_i,B,1}\big)\\ &+\mathrm{d}\omega_i \mathrm{d}\omega_s f(\omega_s,\omega_i)\big(\hat{a}^\dagger_{\omega_s,A,0}-\hat{a}^\dagger_{\omega_s,A,1}\big)(\hat{a}^\dagger_{\omega_i,B,0}-\hat{a}^\dagger_{\omega_i,B,1}\big),\end{aligned}$$

which provides the quantum interference. Summing these terms together one arrives at

(4.32)
$$\begin{aligned}&2\mathrm{d}\omega'_i \mathrm{d}\omega'_s f(\omega'_s,\omega'_i)\big(\hat{a}^\dagger_{\omega'_s,A,0}\hat{a}^\dagger_{\omega'_i,B,0}+\hat{a}^\dagger_{\omega'_s,A,1}\hat{a}^\dagger_{\omega'_i,B,1}\big)\\ &+2\mathrm{d}\omega_i \mathrm{d}\omega_s f(\omega_s,\omega_i)\big(\hat{a}^\dagger_{\omega_s,A,0}\hat{a}^\dagger_{\omega_i,B,0}+\hat{a}^\dagger_{\omega_s,A,1}\hat{a}^\dagger_{\omega_i,B,1}\big),\end{aligned}$$

exploiting this symmetry for all values of ω_i,ω_s the full quantum state may be written as

(4.33)
$$\frac{1}{\sqrt{2}}\int_{\omega_s,\omega_s} \mathrm{d}\omega_s \mathrm{d}\omega_i f(\omega_s,\omega_i)\big(\hat{a}^\dagger_{\omega_s,A,0}\hat{a}^\dagger_{\omega_i,B,0}+\hat{a}^\dagger_{\omega_s,A,1}\hat{a}^\dagger_{\omega_i,B,1}\big)|\mathrm{vac}\rangle\,.$$

The key point here is that no assumption is placed on the correlation functions $f(\omega_s,\omega_i)$ except for the fact we can generate an identical bi photon state from each source. This is analogous in our experiment to the overlapping of MRR resonances and predicts high fidelity two-qubit entangled states generated in our device. The main source of noise in this experiment is due to the multi-photon terms which can be controlled by reducing the pump power.

4.1.5.2 Experiment

In order to prepare and measure two-qubit Bell pairs on-chip, MRR1 and MRR2 are coherently and equally pumped[5] using a 50 MHz pulsed laser centered at approximately $\lambda = 1550nm$. In order to balance the squeezing in each ring, one can add a slight offset ϵ to the MZI value $\theta_{\text{MZI}} = \pi/2 + \epsilon$. If four single photon detectors are used (one at each output channel), the coincidence histograms can be used to estimate the squeezing strength of each MRR and determine ϵ experimentally. The method for estimating the squeezing strengths in the presence of losses is outlined in section 3.2.3. Essentially the goal would be to compare the squeezing in each ring and by locally offsetting BS2 one may arrive at equal values.

The generated state (explained in more detail above, see section 4.1.5.1) via the coherent pumping of each MRR followed by AMZI spectral filtering is the $|\Phi+\rangle$ state. In order to obtain each of the four bell states, local operations can be applied to one of the qubits in the following way

$$\begin{aligned} |\Phi^-\rangle &= \hat{\sigma}_z |\Phi^+\rangle, \\ |\Psi^+\rangle &= \hat{\sigma}_x |\Phi^+\rangle, \\ |\Psi^-\rangle &= \hat{\sigma}_y |\Phi^+\rangle, \end{aligned} \tag{4.34}$$

which relies on the ability to reproduce each the Pauli operations on chip with high fidelity. Figure 4.1c explains how these operators are performed on chip and details the target values of each optical phase. The chip schematic, shown in figure 4.2a, highlights the position of this local unitary in pink.

In order to perform the tomography on each of the generated states, each state is projected into different eigenbases. In principle, in order to perform the tomography for the two qubit Bell pair, $|\Phi^+\rangle$, the nine projectors $\hat{\sigma}_i \hat{\sigma}_j$ where $i, j \in \{x, y, z\}$ should each be measured. By simultaneously connecting four single photon detectors to each of the four output modes, one can estimate the expectation values $\langle \Phi^+ | \hat{\sigma}_i \hat{\sigma}_j | \Phi^+ \rangle$ directly from the normalised coincidence counts. However, for this experiment two detectors were used in order to infer the coincidence counts between each of the channels. This means the projector bases should be correctly rotated such that each of the coincidence counts $\text{CC}_{0,0}$ can infer each of the 36 probabilities implied by the 9 measurement bases - since each measurement setting $\hat{\sigma}_i \otimes \hat{\sigma}_j$ corresponds to four projectors $P_{00}, P_{01}, P_{10}, P_{11}$. As an example, the calculated ideal and measured probabilities of each of the 36 measurements for the $|\Phi^+\rangle$ state are given in table 4.3. Each of the reconstructed density matrices are shown in fig 4.2b along with the measured fidelities. In addition,

[5] Here the pump is split via an MZI with internal relative phase-shift set to $\theta = \pi/2$, which produces a 50:50 beam splitter on chip.

Ideal Probabilities:

	$\|0\rangle\langle 0\|_A$	$\|1\rangle\langle 1\|_A$	$\|+\rangle\langle +\|_A$	$\|-\rangle\langle -\|_A$	$\|+i\rangle\langle +i\|_A$	$\|-i\rangle\langle -i\|_A$
$\|0\rangle\langle 0\|_B$	0.5	0	0.25	0.25	0.25	0.25
$\|1\rangle\langle 1\|_B$	0	0.5	0.25	0.25	0.25	0.25
$\|+\rangle\langle +\|_B$	0.25	0.25	0.5	0	0.25	0.25
$\|-\rangle\langle -\|_B$	0.25	0.25	0	0.5	0.25	0.25
$\|+i\rangle\langle +i\|_B$	0.25	0.25	0.25	0.25	0	0.5
$\|-i\rangle\langle -i\|_B$	0.25	0.25	0.25	0.25	0.5	0

Measured Probabilities:

	$\|0\rangle\langle 0\|_A$	$\|1\rangle\langle 1\|_A$	$\|+\rangle\langle +\|_A$	$\|-\rangle\langle -\|_A$	$\|+i\rangle\langle +i\|_A$	$\|-i\rangle\langle -i\|_A$
$\|0\rangle\langle 0\|_B$	0.49	0.02	0.26	0.22	0.23	0.24
$\|1\rangle\langle 1\|_B$	0.02	0.47	0.32	0.21	0.27	0.26
$\|+\rangle\langle +\|_B$	0.24	0.2	0.46	0.02	0.25	0.22
$\|-\rangle\langle -\|_B$	0.27	0.29	0.05	0.46	0.23	0.3
$\|+i\rangle\langle +i\|_B$	0.27	0.31	0.36	0.26	0.02	0.52
$\|-i\rangle\langle -i\|_B$	0.21	0.2	0.19	0.19	0.45	0.01

Figure 4.3: Calculated ideal probabilities (top) vs measured probabilities (bottom) for the 36 coincidence counts measured for the $|\Phi^+\rangle$ state.

Monte-Carlo simulations with 5000 iterations were performed on the tomographic reconstruction and fidelity errors were calculated via standard error in the mean. The results for the $|\Phi^+\rangle$, $|\Phi^-\rangle$, $|\Psi^+\rangle$ and $|\Psi^-\rangle$ states are 0.915 ± 0.003, 0.933 ± 0.002, 0.932 ± 0.002 and 0.929 ± 0.002, respectfully.

4.2 Linear-optic Multi-qubit Operations

In this section we explore linear-optic interferometer circuits that can produce two-qubit interactions. In particular it is shown that measurement induced non-linearities are sufficient for both entangling separable qubits through fusion operations, as well as analysing Bell states through on-device Bell measurements.

4.2.1 Two Qubit Operations

We have seen in the previous section that applying logical qubit abstractions to the photon states produced on chip enables high fidelity quantum states to be generated and measured on-chip. In section 4.1.2, single qubit unitary transformations (allowing qubit state preparation) and projector circuits were shown and mathematically evaluated. These operators were then utilised experimentally in section 4.1.5.2 to prepare and measure two-qubit entangled states. Through this approach, probabilistic Bell states were prepared and measured with high fidelity via the operation of local

unitaries and projective measurements. However, for this demonstration, two qubit states were actually composed from orthogonal (signal and idler) photonic states, where qubit A (B) contained a signal (idler) photon. In this approach multi-qubit interactions are limited due to the inability to directly interfere the non-degenerate signal and idler photons by utilizing linear-optical components. Such multi-qubit constructions would require precise and controllable non-linear interactions between adjacent qubits. In contrast, two-qubit interactions are possible with linear-optics alone, but require the assumption that they are formed from identical pure single photons. A plausible approach is that of heralded pure single photons, which chapter 3 analytically evaluates.

Through the already proposed single qubit architectures, arbitrary separable states can be prepared via heralded single photons. Consider the case where N bi-photons are simultaneously prepared among N sources, where each source emits exactly one pair. In this scenario, N pure qubits can be constructed from the N identical signal photons, where the idlers are used as heralding triggers. By constructing dual-rails, the initial state is $\otimes^N|0\rangle$. Through the use of general single qubit unitary transformations any separable N qubit state can be generated $\otimes^N\hat{U}(\phi_i,\theta_i)|0\rangle$. However, the generation of entanglement or quantum correlations between qubits requires the multi-qubit interactions. Figure 4.4a shows a heralded two-qubit (four-photon) schematic, incorporating 2 MRR single photon sources, arbitrary single qubit preparation (green), single qubit projectors (pink) and a two-qubit gate (blue). Here, the extra two modes (T_A, T_B) are the heralding idler channels. The remaining two signal photons construct the two qubits composed of $\{0_A,1_A\}$ and $\{0_B,1_B\}$. The general two-qubit interaction can be mathematically expressed by calculating the linear optical transformation obtained by mapping the input states $\{|0\rangle_A, |1\rangle_A, |0\rangle_B, |1\rangle_B\}$ to the output. This can be achieved by first decomposing the transformation into three time-ordered transformations

$$\hat{O}_{A,B}(\theta_1,\theta_2) \equiv \hat{O}_{\text{Swap}}\big(\hat{U}_{\text{t,MZI}}(\theta_1)\otimes\hat{U}_{\text{b,MZI}}(\theta_2)\big)\hat{O}_{\text{Swap}}, \tag{4.35}$$

where $\hat{O}_{\text{Swap}}$ simply relabels the modes $1_A \leftrightarrow 0_B$ and can be interpreted from the schematic in figure 4.4a. By evaluating the orthogonal state mappings in terms of the MZI transformations as follows

$$\hat{O}_{A,B}(\theta_1,\theta_2)|0\rangle_A = e^{i(\theta_1+\pi)/2}\big(-\sin\theta_1/2\,|0\rangle_A + \cos\theta_1/2\,|0\rangle_B\big), \tag{4.36a}$$

$$\hat{O}_{A,B}(\theta_1,\theta_2)|1\rangle_A = e^{i(\theta_2+\pi)/2}\big(\sin\theta_2/2\,|1\rangle_A + \cos\theta_2/2\,|1\rangle_B\big), \tag{4.36b}$$

$$\hat{O}_{A,B}(\theta_1,\theta_2)|0\rangle_B = e^{i(\theta_1+\pi)/2}\big(\cos\theta_1/2\,|1\rangle_A + \sin\theta_1/2\,|1\rangle_B\big), \tag{4.36c}$$

$$\hat{O}_{A,B}(\theta_1,\theta_2)|1\rangle_B = e^{i(\theta_2+\pi)/2}\big(\cos\theta_2/2\,|1\rangle_A - \sin\theta_2/2\,|1\rangle_B\big), \tag{4.36d}$$

which has the important characteristic that each of the input states map to states of both qubits. From these mappings, it is possible to construct the full matrix representation where the two qubits are represented by a four-dimensional vector given by $|0\rangle_A \rightarrow (1,0,0,0)^T$, $|1\rangle_A \rightarrow (0,1,0,0)^T$, $|0\rangle_B \rightarrow (0,0,1,0)^T$ and $|1\rangle_B \rightarrow (0,0,0,1)^T$. In this case, the full matrix can be written

$$\hat{O}_{A,B}(\theta_1,\theta_2) = e^{i\pi/2}\begin{pmatrix} -e^{i\frac{\theta_1}{2}}\sin\frac{\theta_1}{2} & 0 & e^{i\frac{\theta_1}{2}}\cos\frac{\theta_1}{2} & 0 \\ 0 & e^{i\frac{\theta_2}{2}}\sin\frac{\theta_2}{2} & 0 & e^{i\frac{\theta_2}{2}}\cos\frac{\theta_2}{2} \\ e^{i\frac{\theta_1}{2}}\cos\frac{\theta_1}{2} & 0 & e^{i\frac{\theta_1}{2}}\sin\frac{\theta_1}{2} & 0 \\ 0 & e^{i\frac{\theta_2}{2}}\cos\frac{\theta_2}{2} & 0 & -e^{i\frac{\theta_2}{2}}\sin\frac{\theta_2}{2} \end{pmatrix}, \tag{4.37}$$

and fulfills the unitary condition for general θ_1 and θ_2 since

(4.38)

$$\begin{aligned} \hat{O}^{\dagger}_{A,B}(\theta_1,\theta_2)\hat{O}_{A,B}(\theta_1,\theta_2) = &\begin{pmatrix} -e^{-i\frac{\theta_1}{2}}\sin\frac{\theta_1}{2} & 0 & e^{-i\frac{\theta_1}{2}}\cos\frac{\theta_1}{2} & 0 \\ 0 & e^{-i\frac{\theta_2}{2}}\sin\frac{\theta_2}{2} & 0 & e^{-i\frac{\theta_2}{2}}\cos\frac{\theta_2}{2} \\ e^{-i\frac{\theta_1}{2}}\cos\frac{\theta_1}{2} & 0 & e^{-i\frac{\theta_1}{2}}\sin\frac{\theta_1}{2} & 0 \\ 0 & e^{-i\frac{\theta_2}{2}}\cos\frac{\theta_2}{2} & 0 & -e^{-i\frac{\theta_2}{2}}\sin\frac{\theta_2}{2} \end{pmatrix} \\ &\times\begin{pmatrix} -e^{i\frac{\theta_1}{2}}\sin\frac{\theta_1}{2} & 0 & e^{i\frac{\theta_1}{2}}\cos\frac{\theta_1}{2} & 0 \\ 0 & e^{i\frac{\theta_2}{2}}\sin\frac{\theta_2}{2} & 0 & e^{i\frac{\theta_2}{2}}\cos\frac{\theta_2}{2} \\ e^{i\frac{\theta_1}{2}}\cos\frac{\theta_1}{2} & 0 & e^{i\frac{\theta_1}{2}}\sin\frac{\theta_1}{2} & 0 \\ 0 & e^{i\frac{\theta_2}{2}}\cos\frac{\theta_2}{2} & 0 & -e^{i\frac{\theta_2}{2}}\sin\frac{\theta_2}{2} \end{pmatrix} \\ =&\hat{I}_{A,B} \end{aligned}$$

The derived two-qubit operation was designed in order to achieve the two well-known multi-qubit interactions, fusion entangling gates and Bell measurements. Entangling gates are required in order to produce large entangled states required by quantum communications and computations [11, 150–153]. In addition, Bell projections are required by many quantum information protocols such as quantum teleportation and entanglement swapping [58, 86, 154–156]. From this motivation, three important operations, $\hat{O}_I$, $\hat{O}_{\text{Bell}}$, $\hat{O}_{\text{Fusion}}$ are defined, along with the required phases to produce them from the general interaction. These are each summarised in figure 4.4. The following sections 4.2.2 and 4.2.3 give analytical and experimental insights into the inner workings of these interactions.

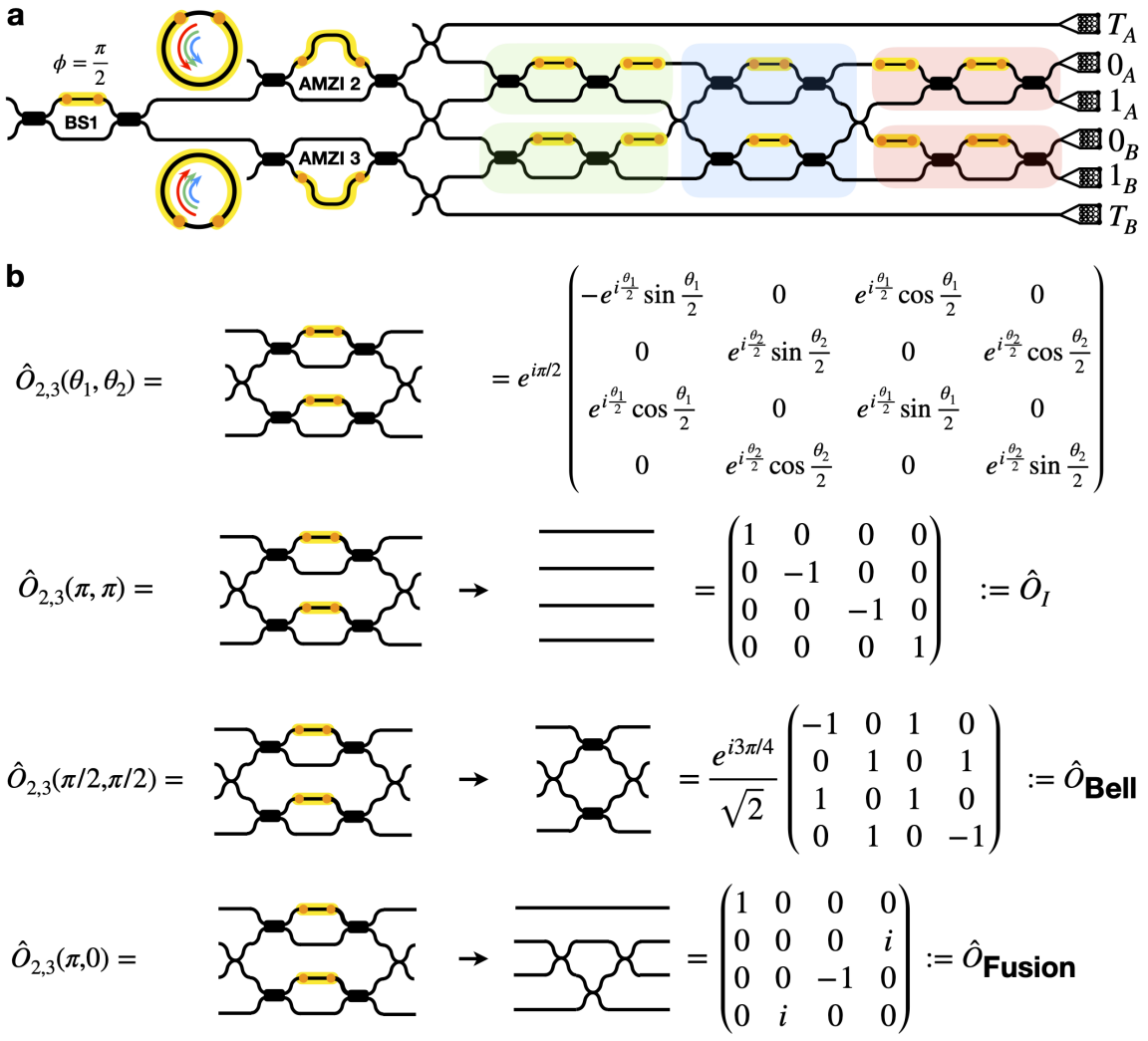

Figure 4.4: Two Qubit Operators. **a,** device schematic for the heralded two qubit experiments. Idler photons generated in the two MRR are sent to the upper most or lower most waveguides. The remaining four waveguides construct two heralded qubits. Green and pink boxes highlight the single qubit unitary transformations and the single qubit projectors, respectively. The blue box represents the controllable two qubit operator. **b,** the general form of the two qubit operator is given in terms of two phases θ_1, θ_2. Below the general form, three main examples are given.

4.2.2 Bell Entangling Operation

4.2.2.1 Theory

In this section, we are interested in evaluating the special case where the two-qubit unitary transformation becomes $\hat{0}_{\text{Bell}} \equiv \hat{0}_{A,B}(\pi/2, \pi/2)$, giving

$$\hat{O}_{\text{Bell}} = \frac{e^{i3\pi/4}}{\sqrt{2}} \begin{pmatrix} -1 & 0 & 1 & 0 \\ 0 & 1 & 0 & 1 \\ 1 & 0 & 1 & 0 \\ 0 & 1 & 0 & -1 \end{pmatrix}. \tag{4.39}$$

A key motivation for constructing such a unitary stems from the need to find two-qubit operators able to entangle two pure separable qubits. A secondary motivator is the complete reverse operation, i.e. ones that can project entangled states back onto separable states to be measured in the computational bases, thus performing a Bell measurement. As we will see in practice within this section, by first concentrating on the former motivation, an entangling operation, the reverse operation can be found trivially by taking the adjoint operator. For instance, suppose we are able to entangle one of the separable and pure two-qubit states $|\psi\rangle \in \{\,|0,0\rangle, |0,1\rangle, |1,0\rangle, |1,1\rangle\,\}$ such that $\hat{O}_{\text{Bell}}|\psi\rangle = |\Psi\rangle$ is one of the four maximally entangled Bell states. Since the general transformation $\hat{O}_{A,B}(\theta_1, \theta_2)$ is unitary, the reverse operation can be achieved by performing the adjoint transformation

$$\begin{aligned} \hat{O}^{\dagger}_{\text{Bell}}|\Psi\rangle &= \hat{O}^{\dagger}_{\text{Bell}}\hat{O}_{\text{Bell}}|\psi\rangle \\ &= |\psi\rangle\,. \end{aligned} \tag{4.40}$$

The exact form of $\hat{O}_{\text{Bell}}$ can be found by considering the general transformation $\hat{O}_{A,B}(\theta_1, \theta_2)$ acting on each of the two-qubit computational basis states $|\psi\rangle$ in the following way. First consider the evolution of the $|0,0\rangle$ pure state which can be written in terms of the signal photon creation operator $\hat{S}^{\dagger}_{i,j}$ in the j^{th} mode of the i^{th} qubit as

$$\begin{aligned} \hat{O}_{A,B}(\theta_1,\theta_2)|0,0\rangle &= \hat{O}_{A,B}(\theta_1,\theta_2)\hat{S}^{\dagger}_{A,0}\hat{S}^{\dagger}_{B,0}|\text{vac}\rangle \\ &= -\big(-e^{i\theta_1/2}\sin(\theta_1/2)\hat{S}^{\dagger}_{A,0} + e^{i\theta_1/2}\cos(\theta_1/2)\hat{S}^{\dagger}_{B,0}\big) \\ &\quad \times \big(e^{i\theta_1/2}\cos(\theta_1/2)\hat{S}^{\dagger}_{A,0} + e^{i\theta_1/2}\sin(\theta_1/2)\hat{S}^{\dagger}_{B,0}\big)|\text{vac}\rangle \\ &= -e^{i\theta_1}\big[\frac{1}{2}(\hat{S}^{\dagger 2}_{A,0} + \hat{S}^{\dagger 2}_{B,0})\sin\theta_1 + \hat{S}^{\dagger}_{A,0}\hat{S}^{\dagger}_{B,0}\cos\theta_1\big]|\text{vac}\rangle\,, \end{aligned} \tag{4.41}$$

and is obtained from the mappings outlined in equation 4.37. In this scenario, the identical signal photons either bunch at the output port ($\hat{S}^{\dagger 2}_{A,0}$, $\hat{S}^{\dagger 2}_{B,0}$) thus destroying

the two-qubit encoding, or produce the two-qubit state $|0,0\rangle$. The probability of each event depends only on θ_1, giving maximum bunching at phases $\pm\pi/2$.

The $|0,1\rangle$ state evolves in the following way

$$
\begin{aligned}
\hat{O}_{A,B}(\theta_1,\theta_2)|0,1\rangle &= \hat{O}_{A,B}(\theta_1,\theta_2)\hat{S}^{\dagger}_{A,0}\hat{S}^{\dagger}_{B,1}|\text{vac}\rangle \\
&= -\big(-e^{i\theta_1/2}\sin(\theta_1/2)\hat{S}^{\dagger}_{A,0} + e^{i\theta_1/2}\cos(\theta_1/2)\hat{S}^{\dagger}_{B,0}\big) \\
&\qquad \times \big(e^{i\theta_2/2}\cos(\theta_2/2)\hat{S}^{\dagger}_{A,1} + e^{i\theta_2/2}\sin(\theta_2/2)\hat{S}^{\dagger}_{B,1}\big)|\text{vac}\rangle \\
&= -e^{i(\theta_1+\theta_2)/2}\Big[-\sin(\theta_1/2)\cos(\theta_2/2)\hat{S}^{\dagger}_{A,0}\hat{S}^{\dagger}_{A,1} \\
&\qquad -\sin(\theta_2/2)\cos(\theta_1/2)\hat{S}^{\dagger}_{B,0}\hat{S}^{\dagger}_{B,1} \\
&\qquad +\sin(\theta_1/2)\sin(\theta_2/2)\hat{S}^{\dagger}_{A,0}\hat{S}^{\dagger}_{B,1} \\
&\qquad +\cos(\theta_1/2)\cos(\theta_2/2)\hat{S}^{\dagger}_{A,1}\hat{S}^{\dagger}_{B,0}\Big]|\text{vac}\rangle\,.
\end{aligned}
\tag{4.42}
$$

In this scenario we end up with four terms, two of which describe photons in the same qubit but opposite modes[6] and two in which the photons end up in the opposite mode of different qubits. By post-selecting away the former two terms, we are left with entangled photons when $\sin(\theta_1/2)\sin(\theta_2/2) = \pm\cos(\theta_1/2)\cos(\theta_2/2)$, occurring when $\theta_1,\theta_2 = \pm\pi/2$. In the specific case where $\theta_1 = \theta_2 = \pi/2$, the two qubits are found in the state $|\Psi^+\rangle$ with 50% probability.

A similar analysis can be applied to the $|1,0\rangle$ state, as follows

$$
\begin{aligned}
\hat{O}_{A,B}(\theta_1,\theta_2)|1,0\rangle &= \hat{O}_{A,B}(\theta_1,\theta_2)\hat{S}^{\dagger}_{A,1}\hat{S}^{\dagger}_{B,0}|\text{vac}\rangle \\
&= -\big(e^{i\theta_2/2}\sin(\theta_2/2)\hat{S}^{\dagger}_{A,1} + e^{i\theta_2/2}\cos(\theta_2/2)\hat{S}^{\dagger}_{B,1}\big) \\
&\qquad \times \big(e^{i\theta_1/2}\cos(\theta_1/2)\hat{S}^{\dagger}_{A,0} + e^{i\theta_1/2}\sin(\theta_1/2)\hat{S}^{\dagger}_{B,0}\big)|\text{vac}\rangle \\
&= -e^{i(\theta_1+\theta_2)/2}\Big[\sin(\theta_1/2)\cos(\theta_2/2)\hat{S}^{\dagger}_{B,0}\hat{S}^{\dagger}_{B,1} \\
&\qquad +\sin(\theta_2/2)\cos(\theta_1/2)\hat{S}^{\dagger}_{A,0}\hat{S}^{\dagger}_{A,1} \\
&\qquad +\sin(\theta_1/2)\sin(\theta_2/2)\hat{S}^{\dagger}_{A,1}\hat{S}^{\dagger}_{B,0} \\
&\qquad +\cos(\theta_1/2)\cos(\theta_2/2)\hat{S}^{\dagger}_{A,0}\hat{S}^{\dagger}_{B,1}\Big]|\text{vac}\rangle\,,
\end{aligned}
\tag{4.43}
$$

which also gives rise to the $|\Psi^+\rangle$ state where $\theta_1 = \theta_2 = \pi/2$. Finally, for completeness,

[6] Coincidences are only measured between different qubit modes, hence these states are not measured.

we see that the evolution of the $|1,1\rangle$ state

$$\begin{aligned}\hat{O}_{A,B}(\theta_1,\theta_2)|1,1\rangle &= \hat{O}_{A,B}(\theta_1,\theta_2)\hat{S}^{\dagger}_{A,1}\hat{S}^{\dagger}_{B,1}|\text{vac}\rangle \\ &= -\left(e^{i\theta_2/2}\sin(\theta_2/2)\hat{S}^{\dagger}_{A,1}+e^{i\theta_2/2}\cos(\theta_2/2)\hat{S}^{\dagger}_{B,1}\right) \\ &\qquad \times\left(e^{i\theta_2/2}\cos(\theta_2/2)\hat{S}^{\dagger}_{A,1}-e^{i\theta_2/2}\sin(\theta_2/2)\hat{S}^{\dagger}_{B,1}\right)|\text{vac}\rangle \\ &= -e^{i\theta_2}\left(\frac{1}{2}(\hat{S}^{\dagger 2}_{A,1}+\hat{S}^{\dagger 2}_{B,1})\sin\theta_2-\hat{S}^{\dagger}_{A,1}\hat{S}^{\dagger}_{B,1}\cos\theta_2\right)|\text{vac}\rangle\,,\end{aligned} \tag{4.44}$$

which gives maximum bunching terms where $\theta_2 = \pm\pi/2$, or the $|1,1\rangle$ state where $\theta_2 = 0,\pi$.

By choosing the specific values $\theta_1 = \theta_2 = \pi/2$ one arrives at the matrix shown in equation 4.39. The physical schematic for this unitary is shown in figure 4.4b. This particular configuration is intuitively interesting due to the fact that identical photons prepared in likewise logical modes will bunch, destroying the encoded qubits. This is similar to the way polarisation encoded qubits also bunch on a physical beam splitter and is akin to the HOM type interference introduced in section 2.4.1.

4.2.2.2 Experiment

In order to test the above analysis, a two qubit entangling experiment was performed. Equation 4.43 predicts that $\hat{O}_{\text{Bell}}$ is able to entangle the initially separable two qubit state $|1,0\rangle$ with 50% probability. In this section, this prediction is tested and experimentally verified. Figure 4.4a shows the device schematic comprised of two MRR single photon sources, that are designed to produce heralded two qubit states. Measurements of these two qubits are achieved by counting the four-photon coincidence counts across the relevant spatial modes. For example, a measurement in the computation bases $|0,0\rangle\langle 0,0|$ is achieved by computing the normalised coincidence counts across channels T_A, 0_A, 0_B and T_B. It can be seen from the device schematic that by setting the single qubit unitaries to identity, the prepared dual-rail two qubit state is $|1,0\rangle$. When the two qubit unitary phases are set to π such that $\hat{O}_I = \hat{O}_{A,B}(\pi,\pi)$, the state remains unchanged by the transformation, since $|1,0\rangle \rightarrow (-1)^2|1,0\rangle$. In this scenario, the initial pure state can be measured and estimated by performing an over complete tomography of the two qubits by measuring the 9 product bases, as outlined in section 4.1.3. The difference in this situation is that two photon coincidence counts are replaced by the four photon (heralded two photon) coincidence counts. The reconstructed density matrix is shown in figure 4.5 (left) and the measured fidelity is 0.99 ± 0.07. The high fidelity measurement here are owed to the lack of quantum interference required and low multi-photon terms. In order to entangle the two photons, the two qubit operator is set to $\hat{O}_{\text{Bell}}$. Here the same tomography process achieved the predicted $|\Psi^+\rangle$ state with

0.851 ± 0.040 fidelity. Here the error is estimated through a Monte-Carlo simulation with 10^4 tomography simulations. The standard error in the mean of these results is shown.

In the following, we will see that the extent to which the single photons prepared in likewise logical modes bunch can be seen by creating an interference pattern achieved by locally rotating one of the qubits. More specifically, the fringe is seen by preparing the initial state $|1,0\rangle$ and rotating the second qubit through an MZI to produce the state $|1\rangle\left(\sin(\theta/2)|0\rangle + \cos(\theta/2)|1\rangle\right)$. Once passing through $\hat{O}_{\text{Bell}}$ the state becomes

(4.45)

$$\begin{aligned}
\hat{O}_{\text{Bell}}|1\rangle\left(\sin(\theta/2)|0\rangle + \cos(\theta/2)|1\rangle\right) = -\frac{i}{2}\Big[& \sin(\theta/2)\big(\hat{S}^\dagger_{A,1} + \hat{S}^\dagger_{B,1}\big)\big(\hat{S}^\dagger_{A,0} + \hat{S}^\dagger_{B,0}\big) \\
& + \cos(\theta/2)\big(\hat{S}^\dagger_{A,1} + \hat{S}^\dagger_{B,1}\big)\big(\hat{S}^\dagger_{A,1} - \hat{S}^\dagger_{B,1}\big)\Big]|\text{vac}\rangle \\
= -\frac{i}{2}\Big[& \sin(\theta/2)\underbrace{\big(\hat{S}^\dagger_{A,0}\hat{S}^\dagger_{A,1} + \hat{S}^\dagger_{B,0}\hat{S}^\dagger_{B,1}\big)}_{\text{Same Qubit}} \\
& + \sin(\theta/2)\underbrace{\big(\hat{S}^\dagger_{A,1}\hat{S}^\dagger_{B,0} + \hat{S}^\dagger_{A,0}\hat{S}^\dagger_{B,1}\big)}_{\text{Entangled}} \\
& + \cos(\theta/2)\underbrace{\big(\hat{S}^\dagger_{A,1}\hat{S}^\dagger_{A,1} - \hat{S}^\dagger_{B,1}\hat{S}^\dagger_{B,1}\big)}_{\text{Bunched}}.\Big]|\text{vac}\rangle
\end{aligned}$$

Hence there are three terms, the first of which produces photons in the same qubit which invalidates the spatial mode encoding and is not measured - leading to no measured four-fold coincidence events. The second term produces the entangled $|\Psi^+\rangle$ state, and the third produced bunched photon pairs which is also not measured. Hence the second term is the only one which adds a contribution to the four measured coincidence counts within the two qubits. Therefore by varying the phase θ one should see an interference pattern in the total number of four-fold counts measured across the two qubits. However, since the qubits are imperfect, i.e. they are constructed from single photons sampled by different multi-mode twin-beam squeezed states, one will in reality see background counts[7]. Figure 4.5c shows the result of this fringe featuring $80.5 \pm 3.2\%$ fidelity. The measured four-fold coincidence events are recorded from all pairs of heralded qubit output modes and the data is fitted with a sinusoidal fringe.

[7] Particularly corresponding to the $|1,1\rangle$ vector.

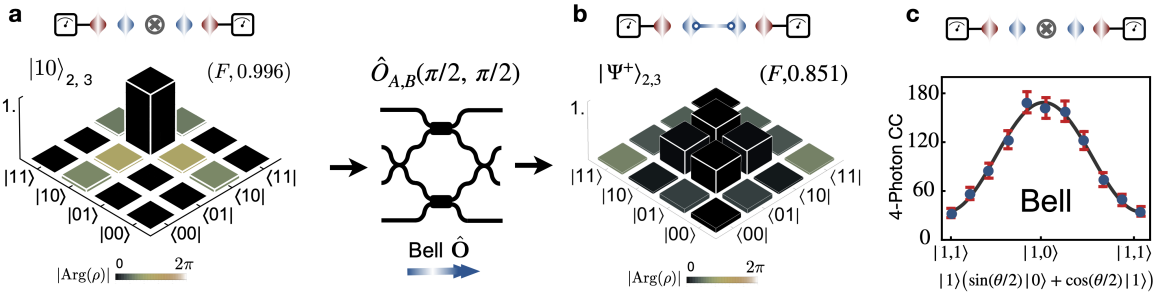

Figure 4.5: Heralded Bell state measurements. The initial state $|1,0\rangle$ (**a**) passes through $\hat{O}_{\mathrm{Bell}}$ and produces the $|\Psi^+\rangle$ state (**b**) with 50% probability. The heralded two qubit states are estimated via over-complete tomographic processes by measuring four-photon coincidence counts in 9 different product bases (36 measurements). The reconstructed density matrices and their fidelities are shown for the initial state (**a**) and final entangled state (**b**). Red and blue pulses above each density matrix show the chip configuration. **c**, the state $|1\rangle\left(\sin(\theta/2)|0\rangle + \cos(\theta/2)|1\rangle\right)$ is prepared and sent through $\hat{O}_{\mathrm{Bell}}$. The phase θ is then scanned over a range $0 \rightarrow \pi$. The total four photon coincidences are plotted against phase and fitted with a sinusoidal curve. The measured visibility of $80.5 \pm 3.2\%$ shows the suppressed four-fold coincidence counts caused by the bunching of identical single photons in likewise logical modes.

4.2.3 Fusion Entangling Operation

The next consideration is the $\hat{O}_{\mathrm{fusion}}$ operator, where figure 4.4b details the schematic design, general unitary phase values and matrix representation,

$$\hat{O}_{\mathrm{Bell}} = \begin{pmatrix} 1 & 0 & 0 & 0 \\ 0 & 0 & 0 & i \\ 0 & 0 & -1 & 0 \\ 0 & i & 0 & 0 \end{pmatrix}. \tag{4.46}$$

This operation is designed to act as a parity operator whereby opposite qubit modes are not measured and thus post-selected away. This is analogous to $\hat{O}_{\mathrm{Bell}}$ which removes likewise modes, instead of opposing modes. However, a key differentiating factor between the two operators is that each column of $\hat{O}_{\mathrm{Fusion}}$ contains only one non-zero value. As a result, this operator cannot be used to entangle initial states which are not superposition states. The general mapping of these states is

$$\begin{aligned} \hat{O}_{\mathrm{Fusion}}\{|0,0\rangle, |0,1\rangle, |1,0\rangle, |1,1\rangle\} \rightarrow \{&-\hat{S}^\dagger_{A,0}\hat{S}^\dagger_{B,0}|\mathrm{vac}\rangle, i\hat{S}^\dagger_{A,0}\hat{S}^\dagger_{A,1}|\mathrm{vac}\rangle, \\ &-i\hat{S}^\dagger_{B,0}\hat{S}^\dagger_{B,1}|\mathrm{vac}\rangle, -\hat{S}^\dagger_{A,1}\hat{S}^\dagger_{B,1}|\mathrm{vac}\rangle\}, \end{aligned} \tag{4.47}$$

which adds an equal global phase to the $|0,0\rangle$ and $|1,1\rangle$ states. The $|0,1\rangle$ and $|1,0\rangle$ states, however, do not contribute to any coincidence counts and are not measured. As a result, one might expect that the separable superposition state $|+,+\rangle$, which contains

a superposition of all of the qubit modes will give rise to the $|\Phi^+\rangle$ state. In order to see this effect, an experiment was performed which initially prepares the separable state

$$|+\rangle_A \otimes \left(\frac{|0\rangle_B + e^{i\phi}|1\rangle_B}{\sqrt{2}}\right), \tag{4.48}$$

which is achieved on the chip by operating on the $|1,0\rangle$ state with two single qubit unitaries[8]. The unitary phases must be set to the following values

$$\left(\hat{U}_{A_t}(0,\pi/2)\otimes\hat{U}_{B_b}(\phi,\pi/2)\right)|1,0\rangle_{A,B} = |+\rangle_A \otimes \left(\frac{|0\rangle_B + e^{i\phi}|1\rangle_B}{\sqrt{2}}\right), \tag{4.49}$$

where $\hat{U}_{A_t}$ ($\hat{U}_{B_b}$) takes into account the fact that the top (bottom) unitary has optical phase-shifters on the top (bottom) dual-rail mode.

As in the previous section, the two idler photons are prepared as heralded triggers, giving rise to four photon coincidence measurements. In order to see the fidelity of the prepared initial state, a tomography measurement must be made to estimate the produced density matrix ρ. To achieve this, the two qubit operator must be set to $\hat{O}_I$ which preserves the magnitudes of the vector amplitudes. However, we must also take into account the added π phase shifts applied to the $|1\rangle_A$ and $|0\rangle_B$ state vectors by the imperfect identity $\hat{O}_I$, as can be seen from the matrix representation in figure 4.4b. These phase shifts can be counteracted by applying a temporary π offset phase to the prepared initial state[9]. As a result, the phases cancel in the following way

(4.50)

$$\begin{aligned}\hat{O}_I\left(\hat{U}_{A_t}(\pi,\pi/2)\otimes\hat{U}_{B_b}(\phi+\pi,\pi/2)\right)|1,0\rangle_{A,B} &= \frac{\hat{O}_I}{2}\left[\left(-|0\rangle_A + |1\rangle_A\right)\otimes\left(|0\rangle_B - e^{i\phi}|1\rangle_B\right)\right] \\ &= |+\rangle_A \otimes \left(\frac{|0\rangle_B + e^{i\phi}|1\rangle_B}{\sqrt{2}}\right).\end{aligned}$$

By utilising these temporary phases, one can now take the full state tomography of the prepared two-qubit state. Figure 4.6a gives the reconstructed density matrix of the initial $|{+}{+}\rangle_{A,B}$ state, in the special case where $\phi = 0$. The measured state fidelity in this case was 0.966 ± 0.002.

Once the initial state tomography is performed, the temporary phase shifts are lifted and the initial state evolves under the unitary $\hat{O}_{\text{Fusion}}$. During this evolution, we expect the post-selection of opposite qubit modes, where the initial state $|\phi_0\rangle \equiv |+\rangle \otimes \left(|0\rangle + e^{i\phi}|1\rangle\right)/\sqrt{2}$ evolves as follows

$$\hat{O}_{\text{Fusion}}|\phi_0\rangle = \frac{1}{2}(-\hat{S}^\dagger_{A,0} + i\hat{S}^\dagger_{B,1})(\hat{S}^\dagger_{B,0} + ie^{i\phi}\hat{S}^\dagger_{A,1})|\text{vac}\rangle\,. \tag{4.51}$$

[8] The $|1,0\rangle$ state is the default initial state prepared by the four-photon coincidence counts measured from the two MRR.

[9] Here temporary means it is only applied during the tomography, but is later removed.

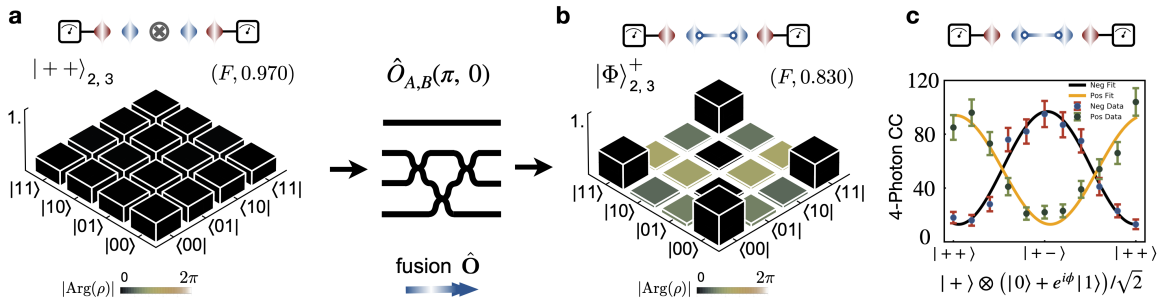

Figure 4.6: Entangling fusion operation measurements. Reconstructed density matrix of **a**, the initial $|+,+\rangle$ state and **b**, the maximally entangled $|\Phi^+\rangle$ state. **c** shows the effect of rotating the initial state around the $\hat{I} \otimes \hat{\sigma}_z$ axis by angle ϕ. The mathematical form of the initial state (incident on $\hat{O}_{\text{Fusion}}$) is shown on the x-axis of the figure. The resulting state is projected into the basis of eigenvectors of $\hat{\sigma}_x$, corresponding to the Hadamard gate. An interference pattern in the measured four-fold countrate is formed by plotting the positive eigenvalues (green) and negative eigenvalues (red) in this basis.

As can can be seen from equation 4.47, only terms which preserve the dual-rail qubit encoding lead to the measured four-fold coincidence events. As a result, the final measurable (and re-normalised) state becomes

$$|\Phi^{\phi}\rangle \equiv -\frac{1}{\sqrt{2}}\left(\hat{S}^{\dagger}_{A,0}\hat{S}^{\dagger}_{B,0} + e^{i\phi}\hat{S}^{\dagger}_{B,1}\hat{S}^{\dagger}_{A,1}\right)|\text{vac}\rangle\,, \tag{4.52}$$

which gives the Bell state $|\Phi^+\rangle$ ($|\Phi^-\rangle$) when $\phi = 0$ ($\phi = \pi$), and in general $\left(|00\rangle + e^{i\phi}|11\rangle\right)/\sqrt{2}$. In the case where $\phi = 0$ a full state tomography was taken of the four-photon heralded bell state. The reconstructed density matrix for this $|\Phi^+\rangle$ state is shown in figure 4.6b, and achieves a fidelity of 0.83 ± 0.03.

In order to see the full effect of the phase shift ϕ on the overall state, each qubit was projected into the eigenbasis of the $\hat{\sigma}_x$ operator. This is achieved by performing the Hadamard operation on each qubit. From here the four-photon coincidence counts are measured and normalised across the two qubits. The coherence's of the entangled state can be seen by sweeping over the phase shift ϕ over the 2π range and plotting the coincidence counts corresponding to the positive and negative eigenvalues. The eigenvalues of the $\hat{\sigma}_x$ operator are ± 1 for the $|\pm\rangle$ eigenvectors and, as a result, coincidence counts in the $|0,0\rangle$, $|1,1\rangle$ ($|0,1\rangle$, $|1,0\rangle$) modes correspond to positive (negative) eigenvalues. The interference fringes measured as a result of this phase change are shown in figure 4.6c. The exact shape of these fringes can be predicted by performing

a change of basis on the state $|\Phi^{\phi}\rangle$ as follows

$$
\begin{aligned}
|\Phi^{\phi}\rangle &= \frac{1}{\sqrt{2}}\big(|0,0\rangle + e^{i\phi}|1,1\rangle\big) \\
&= \frac{1}{2\sqrt{2}}\Big[\big(|+\rangle+|-\rangle\big)^{\otimes 2} + e^{i\phi}\big(|+\rangle-|-\rangle\big)^{\otimes 2}\Big] \\
&= \frac{1}{2\sqrt{2}}\Big[(1+e^{i\phi})\big(|+,+\rangle+|-,-\rangle\big)+(1-e^{i\phi})\big(|+,-\rangle+|-,+\rangle\big)\Big].
\end{aligned} \tag{4.53}
$$

Hence it is found that the positive eigenvalues evolve as $(1+e^{i\phi})$ and the negative eigenvalues as $(1-e^{i\phi})$. In full, the normalised coincidence count probabilities $P_{a,b}$ where $a,b \in \{+,-\}$ evolve as

$$
P_{+,+} = P_{-,-} = \Big|\frac{1+e^{i\phi}}{2\sqrt{2}}\Big|^2 = \frac{\cos^2(\phi/2)}{2}, \tag{4.54a}
$$

$$
P_{+,-} = P_{-,+} = \Big|\frac{1-e^{i\phi}}{2\sqrt{2}}\Big|^2 = \frac{\sin^2(\phi/2)}{2}, \tag{4.54b}
$$

which is directly reflected in the black and orange fit curves in figure 4.6c.

4.2.4 Bell-state Measurement

As is alluded to in the earlier sections of this chapter, the ability to perform a measurement that is able to unambiguously distinguish each of the four Bell states has many uses in quantum information theory - such as quantum teleportation, entanglement swapping and super-dense coding. The so-called joint (two qubit) measurement that is able to achieve this unambiguity is referred to as a Bell measurement. More precisely, this is achieved by the projection into the basis of Bell states given by $\{|\Phi^+\rangle, |\Phi^-\rangle, |\Psi^+\rangle, |\Psi^-\rangle\}$. This measurement can be thought of as the inverse operation of the entangling operation, one which maps the separable pure states $\{|00\rangle, |01\rangle, |10\rangle, |11\rangle\}$ to the Bell states $\{|\Phi^+\rangle, |\Phi^-\rangle, |\Psi^+\rangle, |\Psi^-\rangle\}$. This can be mathematically achieved by performing the Hamamard gate followed by a CNOT gate, $(\hat{U}_{\text{CNOT}})(\hat{U}_{\text{Had}} \otimes \hat{I})$. Since these gates are both unitary and Hermitian (and therefore self-inverse), reversing the order of operation performs a projective measurement from the Bell basis to the computational basis

$$
(\hat{U}_{\text{CNOT}})(\hat{U}_{\text{Had}} \otimes \hat{I})\{|\Phi^+\rangle, |\Phi^-\rangle, |\Psi^+\rangle, |\Psi^-\rangle\} \rightarrow \{|00\rangle, |01\rangle, |10\rangle, |11\rangle\}. \tag{4.55}
$$

Although a deterministic Bell state analysis is not possible with linear optics[10], a partial measurement able to unambiguously distinguish up to two of the four Bell states is possible. However, a full Bell state analysis in optics requires entanglement

[10] Since the deterministic CNOT gate is also not possible with only linear optics.

in additional degrees of freedom, where the hyper-entanglement assists the Bell analysis in one specific degree of freedom [157, 158]. For the single degree of freedom approach, several types of linear-optical Bell analysers are possible, for example, KLM CNOT type gates have been demonstrated with 1/16 probability [64, 159]. The previous demonstration of Bell measurements on a single integrated path encoded device managed a 1/9 probability with a scheme that scales for n control gates as $1/3^n$ [5, 160]. Recently, an on-chip fusion demonstration showed 1/2 probability [11], for detailed method see later section 4.2.3. In later sections of this thesis we show how this fusion entangling operation can also be utilised to achieve Bell measurements. Finally, bosonic Bell projectors can be achieved in photonic systems with 1/2 probability [58]. Each of the above demonstrations succeed with a given probability, $p < 1$, where the coincidence detection in a certain configuration post-selects the required result. The KLM CNOT gate and its Bell measurements have been reported in other material systems [4, 5], but these demonstrations all relied on multiphoton states generated by off-chip SPDC sources. In this thesis, demonstrations of the Bosonic Bell and Fusion projector are shown experimentally on-chip, each with higher success probability when compared with the KLM CNOT scheme. This section discusses the use of Bell measurements by utilising the $\hat{O}_{\text{Bell}}$ operator. A discussion of Bell measurements in the context of $\hat{O}_{\text{fusion}}$ is shown in section 4.4.1.3. The intuition for $\hat{O}_{\text{Bell}}$ as a Bell state analyser stems from the earlier analysis on Bell projections. Since $|0,0\rangle$ and $|1,1\rangle$ states are postselected away (due to the quantum interference of identical photons), they do not contribute to any measured effects. Moreover, since $|0,1\rangle$ and $|1,0\rangle$ states project the two qubits onto entangles states, we expect the Hermitian conjugate to perform the reverse operation. Since $\hat{O}_{\text{Bell}}$ has been shown to be Hermitian and unitary, it is its own inverse matrix, and should therefore transform these heralded entangled states back into separable states. In the following analysis, we consider the precise evolution of each of the Bell states under $\hat{O}_{\text{Bell}}$ and show how these states can be determined.

4.2.4.1 Perfect Qubits

First consider the evolution of the $|\Phi^{\pm}\rangle$ under the $\hat{O}_{\text{Bell}}$ operator. It is shown in section 4.2.2 that likewise logical modes bunch under the evolution of $\hat{O}_{\text{Bell}}$, and so we do not expect to be able to distinguish the $|\Phi^{\pm}\rangle$ states that contain a superposition of photons prepared in likewise modes. In the following analysis, we remain in a framework whereby heralded signal photons (through the simultaneous detection of two idler photon) give rise to two qubits, A and B. In this framework, and to keep the analysis

simple, it is first assumed that these on chip photon states have high spectral and number purity - that is to say that pure single photon states are emitted in pure spectral modes and are denoted by the creation operator $\hat{S}^\dagger$. Under these conditions, the on-device state may be written as

$$|\Phi^\pm\rangle_{A,B} = \frac{1}{\sqrt{2}}\left(\hat{S}^\dagger_{A,0}\hat{S}^\dagger_{B,0} \pm \hat{S}^\dagger_{A,1}\hat{S}^\dagger_{B,1}\right)|\text{vac}\rangle\,, \tag{4.56}$$

and evolves as

$$\begin{aligned}\hat{O}_{\text{Bell}}|\Phi^\pm\rangle_{A,B} &= \frac{-i}{2\sqrt{2}}\Big((-\hat{S}^\dagger_{A,0}+\hat{S}^\dagger_{B,0})(\hat{S}^\dagger_{A,0}-\hat{S}^\dagger_{B,0}) \pm (\hat{S}^\dagger_{A,1}+\hat{S}^\dagger_{B,1})(\hat{S}^\dagger_{A,1}-\hat{S}^\dagger_{B,1})\Big)|\text{vac}\rangle \\ &= \frac{i}{2\sqrt{2}}\left(\hat{S}^\dagger_{A,0}\hat{S}^\dagger_{A,0} - \hat{S}^\dagger_{B,0}\hat{S}^\dagger_{B,0} \mp \hat{S}^\dagger_{A,1}\hat{S}^\dagger_{A,1} \pm \hat{S}^\dagger_{B,1}\hat{S}^\dagger_{B,1}\right)|\text{vac}\rangle\,.\end{aligned} \tag{4.57}$$

giving a superposition of bunched states which do not contribute to the measured four-fold coincidence counts.

Next, the attention is turned to the evolution of the $|\Psi^\pm\rangle$ states,

$$|\Psi^\pm\rangle = \frac{1}{\sqrt{2}}(\hat{S}^\dagger_{A,0}\hat{S}^\dagger_{B,1} \pm \hat{S}^\dagger_{A,1}\hat{S}^\dagger_{B,0})|\text{vac}\rangle \tag{4.58}$$

Under the same transformation the states become

$$\begin{aligned}\hat{O}_{\text{Bell}}|\Psi^\pm\rangle &= \frac{-i}{2\sqrt{2}}\Big((-\hat{S}^\dagger_{A,0}+\hat{S}^\dagger_{B,0})(\hat{S}^\dagger_{A,1}-\hat{S}^\dagger_{B,1}) \pm (\hat{S}^\dagger_{A,1}+\hat{S}^\dagger_{B,1})(\hat{S}^\dagger_{A,0}+\hat{S}^\dagger_{B,0})\Big)|\text{vac}\rangle \\ &= \frac{-i}{2\sqrt{2}}\Big((\hat{S}^\dagger_{A,0}\hat{S}^\dagger_{A,1} + \hat{S}^\dagger_{B,0}\hat{S}^\dagger_{B,1})(-1\pm 1) \\ &\qquad +(\hat{S}^\dagger_{A,0}\hat{S}^\dagger_{B,1} + \hat{S}^\dagger_{A,1}\hat{S}^\dagger_{B,0})(1\pm 1)\Big)|\text{vac}\rangle\,.\end{aligned} \tag{4.59}$$

As a result, these two states can be distinguished by either measuring the simultaneous arrival of signal photons at different output ports. More specifically, the $|\Psi^+\rangle$ state may be measured from a simultaneous arrival at $\{T_A, 0_A, 1_B, T_B\}$ or $\{T_A, 1_A, 0_B, T_B\}$, i.e., the opposing modes of each qubit. Alternatively, the $|\Psi^-\rangle$ state may be measured by the simultaneous arrival at $\{T_A, 0_A, 1_A, T_B\}$ or $\{T_A, 0_B, 1_B, T_B\}$, i.e., the opposite mode of the *same* qubit. Note that since the Bell measurement is a destructive measurement, it is not crucial that the qubit encoding is broken for the $|\Psi^-\rangle$ state. The crucial message is that since the two $|\Phi^\pm\rangle$ states bunch, they should add minimal noise to the measurement. Therefore, if it is known that qubits A and B are prepared in one of the four Bell states (as true in the teleportation and entanglement swapping protocols), the states $|\Psi^\pm\rangle$ may be unambiguously determined by inferring the four-photon coincidence events corresponding to the correct modes. In later sections of this chapter, this measurement will be put into the context of quantum teleportation (section 4.3) and entanglement swapping (sec 4.3.2).

4.2.4.2 Distinguishable Qubits

In this section, the above analysis is applied to qubits that are prepared with spectrally distinguishable photons. Since the spectral purity of the MRR photon sources is less than unity ($P = \mathrm{Tr}(\rho_s^2) = \sum_k |\lambda_k|^4 \approx 0.92$), the probability that the two qubits are prepared within the same spectral mode is equivalent to the purity and approximately 92%[11]. Therefore for any tomographic process which collects many four-photon coincidence counts in order to estimate the true state characteristics, one can expect that around $1 - 0.92 = 8\%$ of the coincidence events will arise from spectrally distinguishable photons. In order to see what effects these distinguishable photons create, one should evolve these distinguishable states under the $\hat{O}_{\mathrm{Bell}}$ interaction. In the case that the supposed initial state is in one of the Bell pairs $|\Phi^{\pm}\rangle$, there will be additional photon counts corresponding to $\{T_A, 0_A, 0_B, T_B\}$ and $\{T_A, 1_A, 1_B, T_B\}$. These terms arise from the lack of interference between the distinguishable photons and their unequal superposition states. In this case, initial state is constructed from qubit A with the signal photon $\hat{S}_A^{\dagger}$ and qubit B with the signal photon $\hat{S'}_B^{\dagger}$

$$|\Phi^{\pm}\rangle'_{A,B} = \frac{1}{\sqrt{2}}\left(\hat{S}^{\dagger}_{A,0}\hat{S'}^{\dagger}_{B,0} \pm \hat{S}^{\dagger}_{A,1}\hat{S'}^{\dagger}_{B,1}\right)|\mathrm{vac}\rangle\,, \tag{4.60}$$

which evolves as

$$\begin{aligned}\hat{O}_{\mathrm{Bell}}|\Phi^{\pm}\rangle'_{A,B} &= \frac{-i}{2\sqrt{2}}\Big((-\hat{S}^{\dagger}_{A,0} + \hat{S}^{\dagger}_{B,0})(\hat{S'}^{\dagger}_{A,0} - \hat{S'}^{\dagger}_{B,0}) \pm (\hat{S}^{\dagger}_{A,1} + \hat{S}^{\dagger}_{B,1})(\hat{S'}^{\dagger}_{A,1} - \hat{S'}^{\dagger}_{B,1})\Big)|\mathrm{vac}\rangle \\ &= \frac{i}{2\sqrt{2}}\big(\hat{S}^{\dagger}_{A,0}\hat{S'}^{\dagger}_{A,0} - \hat{S}^{\dagger}_{B,0}\hat{S'}^{\dagger}_{B,0} \mp \hat{S}^{\dagger}_{A,1}\hat{S'}^{\dagger}_{A,1} \pm \hat{S}^{\dagger}_{B,1}\hat{S'}^{\dagger}_{B,1} \\ &\qquad \hat{S}^{\dagger}_{A,0}\hat{S'}^{\dagger}_{B,0} + \hat{S}^{\dagger}_{B,0}\hat{S'}^{\dagger}_{A,0} \mp \hat{S}^{\dagger}_{A,1}\hat{S'}^{\dagger}_{B,1} \pm \hat{S}^{\dagger}_{B,1}\hat{S'}^{\dagger}_{A,1}\big)|\mathrm{vac}\rangle\,.\end{aligned} \tag{4.61}$$

This gives rise to the additional four-fold coincidence terms as mentioned above. It is important to note that these terms will not affect the ability to distinguish the $|\Psi^{\pm}\rangle$ states or increase the noise in these measurements.

The more crucial effect is the evolution of the $|\Psi^{\pm}\rangle$ states, where distinguishable photons removes the ability to perform the unambiguous measurement. The state evolution of the

$$|\Psi^{\pm}\rangle'_{A,B} = \frac{1}{\sqrt{2}}\left(\hat{S}^{\dagger}_{A,0}\hat{S'}^{\dagger}_{B,1} \pm \hat{S}^{\dagger}_{A,1}\hat{S'}^{\dagger}_{B,0}\right)|\mathrm{vac}\rangle\,, \tag{4.62}$$

[11] This is because the probability that either ring emits single photons in the k^{th} mode is $|\lambda_k|^2$.

states are

(4.63)
$$\begin{aligned}\hat{O}_{\text{Bell}}|\Psi^{\pm}\rangle'_{A,B} &= \frac{-i}{2\sqrt{2}}\Big((-\hat{S}^{\dagger}_{A,0}+\hat{S}^{\dagger}_{B,0})(\hat{S}'^{\dagger}_{A,1}-\hat{S}'^{\dagger}_{B,1})\pm(\hat{S}^{\dagger}_{A,1}+\hat{S}^{\dagger}_{B,1})(\hat{S}'^{\dagger}_{A,0}-\hat{S}'^{\dagger}_{B,0})\Big)|\text{vac}\rangle \\ &= \frac{-i}{2\sqrt{2}}\Big(-\hat{S}^{\dagger}_{A,0}\hat{S}'^{\dagger}_{A,1}-\hat{S}^{\dagger}_{B,0}\hat{S}'^{\dagger}_{B,1}\pm\hat{S}'^{\dagger}_{A,0}\hat{S}^{\dagger}_{A,1}\mp\hat{S}'^{\dagger}_{B,0}\hat{S}'^{\dagger}_{B,1} \\ &\qquad +\hat{S}^{\dagger}_{A,0}\hat{S}'^{\dagger}_{B,1}+\hat{S}'^{\dagger}_{A,1}\hat{S}^{\dagger}_{B,0}\pm\hat{S}'^{\dagger}_{A,0}\hat{S}'^{\dagger}_{B,1}\mp\hat{S}^{\dagger}_{A,1}\hat{S}'^{\dagger}_{B,0}\Big)|\text{vac}\rangle\,.\end{aligned}$$

And so the distinguishable photons prevent the quantum interference as expected. This means that both of the $|\Psi^{\pm}\rangle$ states contribute to the $\{T_A,0_A,1_B,T_B\}$, $\{T_A,1_A,0_B,T_B\}$, $\{T_A,0_A,1_A,T_B\}$ and $\{T_A,0_B,1_B,T_B\}$ coincidences, and neither state can be distinguished. For each four-fold coincidence counts produced by distinguishable photons, the two-qubit state is projected onto the mixed state (with 50% purity)

(4.64)
$$\rho = \frac{1}{2}|\Psi^{+}\rangle\langle\Psi^{+}| + \frac{1}{2}|\Psi^{-}\rangle\langle\Psi^{-}|.$$

Since only 8% of the total coincidence counts arise from this mixture, the estimated experimental mixture caused by the impure single photons is

(4.65)
$$\rho_{\text{Bell}} = 0.96|\Psi^{+}\rangle\langle\Psi^{+}| + 0.04|\Psi^{-}\rangle\langle\Psi^{-}|,$$

which has an estimated state purity $\text{Tr}(\rho^2_{\text{Bell}}) = 92.3\%$. This mixture will act to moderately degrade the fidelity of any experiment involving Bell measurements.

4.3 Teleportation and Entanglement Swapping

In this section, the earlier results of this chapter are combined in order to perform the quantum teleportation and entanglement swapping protocols on chip. For an introduction to these protocols, see sections 2.3.2 and 2.3.3.

4.3.1 Quantum Teleportation of Single-qubit States

In the quantum teleportation protocol, a user, Alice, is able to transmit an arbitrary qubit to a receiver, Bob, without the need to transmit the physical system in which the quantum information is encoded. This theoretically works independent of the distance between the two users and the quantum state may even be unknown to both parties. This is inherently counter-intuitive, since if information is physical, as described by the laws of physics, it should be encoded in a given physical system whereby information can be extracted by performing measurements on that system. So a natural question

is, how can quantum information be transmitted without the transmission of the physical object itself? The answer lies in the use of pre-shared entanglement between the sender and receiver. Since this pre-shared entanglement is described by a single non-separable quantum state, measurements on the two system exhibit non-local correlations. That is to say that the information is encoded non-locally in space - so called spooky action at a distance. In fact, quantum teleportation is made possible precisely by the use of this pre-shared entanglement, which is able to transmit not only the probabilities of occupying the $|0\rangle$ or $|1\rangle$ state, but also the phase between them.

The specifics of the quantum teleportation protocol is initially outlined in section 2.3.2. In this section, all of the previous work in this chapter is combined in order to explain how to successfully perform the quantum teleportation of dual-rail photonic qubits on a chip. In this experiment, three qubits A, B & C are defined on the chip. The goal in this experiment is to encode a range of states in qubit A, and by performing a joint Bell measurement on qubits A & B, transmit these states to qubit C. Figure 4.7a shows the on-chip schematic for this experiment. Notice that here the three qubits are each encoded into photons produced from three MRR single photon sources. An additional channel, T_A shown in the schematic, is used as a heralded trigger for the initially prepared qubit. This trigger ensures that a photon pair is deterministically produced from the top MRR2. This heralded determinism is required so that the single qubit can be prepared correctly. Due to the schematic design, the heralded qubit A is initially prepared in the logical $|1\rangle_A$ state, where this state is then rotated under a unitary transformation in order to achieve the arbitrary prepared state. For the second (B) and third (C) qubits, it is allowed that they arise from either of the remaining two MRR sources. By allowing this condition, an initial superposition state is formed which entangles the two photons that encode the two qubits. This probabilistic entanglement generation between the two qubits is precisely the same method as explained in greater detail in section 4.1.5.2, requiring only two-photon coincidence detections which achieved high Bell pair state fidelity. Note that in this experiment, qubits A & B are both encoded in signal photons, whereas qubit C is encoded in the orthogonal idler photon. This means that the goal is to transfer the path encoded information in qubit A (signal photon) to qubit C (idler photon). This decision allows the implementation of the teleportation protocol requiring only four-photon coincidence events.

The chosen transmitted states are the six eigenvectors of the three Pauli matrices $\{|0\rangle, |1\rangle, |+\rangle, |-\rangle, |+i\rangle, |-i\rangle\}$. Each of these states are prepared in turn in qubit A and then verified on qubit C through a local quantum state tomography on that qubit.

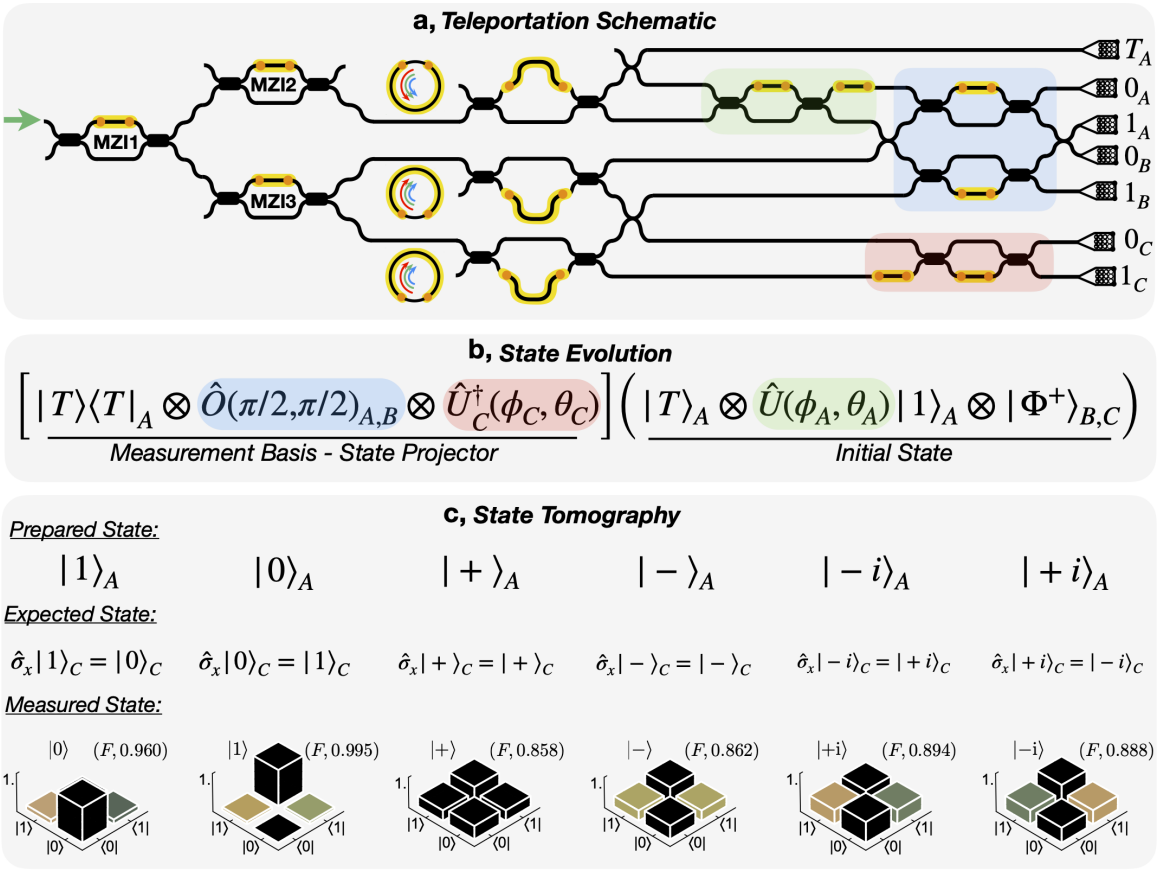

Figure 4.7: Teleportation experiment results. **a,** Teleportation schematic, comprised of three qubits. The schematic includes three MRR single photon sources where the first qubit is heralded from the top source. The second two qubits are in a superposition of single photons produced from the second (middle) and third (bottom) source and are initially entangled. The integration of three MZI (shown left) control the initial pumping, where the configuration is set such that all three sources are pumped. Each of the three MRR are well-overlapped to produce identical photon spectra. The device contains single qubit state preparation (green), Bell measurement (blue) and a single qubit projector (pink). To the right of the schematic, at each grating coupler, the qubit labels are shown. T_A refers to the heralding channel (trigger), the rest of the waveguide modes are required for the three qubits and are labelled corresponding to the qubits A, B, and C. The general state evolution is shown in **b**, where the green, blue and pink operators are highlighted as consistent with the schematic in **a**. The Bell measurement collapses qubits A and B onto the $|\Psi^+\rangle$ state. As a result, the measured third qubit is the prepared initial qubit with a $\hat{\sigma}_x$ rotation applied to the state. The list of prepared and expected qubits are shown in **c** along with the reconstructed state topographies and their measured fidelities which average $F_{\text{Mean}} = 0.91 \pm 0.04$.

The initial state

$$|\psi_0\rangle = |T\rangle_A \otimes |1\rangle_A \otimes |\Phi^+\rangle_{B,C} \tag{4.66}$$

is prepared on-chip by coherently pumping three MRR, a, b & c. Photons from sources b & c are prepared in the entangled state $|\Phi^+\rangle_{B,C}$ through the same process as outlined in section 4.1.5.2. A heralded single photon (signal channel) produced by source a prepares the $|1\rangle_A$ state, which is to be remotely transferred to qubit C through the teleportation scheme. As can be seen from the schematic in figure 4.7a and 4.7b, qubit A first evolves under a local rotation $\hat{U}_t(\phi_A,\theta_A)$, then qubits A and B are rotated under $\hat{O}_{\text{Bell},A,B}$, followed by a operation on qubit C, $\hat{U}_b(\phi_C,\theta_C)$. Each of these operations can be classified into one of two categories, where $\hat{U}_t(\phi_A,\theta_A)$ is required for state preparation and $\hat{O}_{\text{Bell},A,B}$, $\hat{U}_C^\dagger(\phi_C,\theta_C)$ are required for state measurements. These classifications allow the final state to be written as

$$\Big[\underbrace{|T\rangle\langle T|_A \otimes \hat{O}_{\text{Bell},A,B} \otimes \hat{U}_b^\dagger(\phi_C,\theta_C)}_{\text{Measurement}}\Big]\Big(\underbrace{|T\rangle_A \otimes \hat{U}_t(\phi_A,\theta_A)|1\rangle_A \otimes |\Phi^+\rangle_{B,C}}_{\text{Prepared State}}\Big). \tag{4.67}$$

Each of the six initial qubit states can be prepared via the following settings

$$\hat{U}_t(\phi_A,\theta_A)|1\rangle_A = e^{i\phi_A}\cos(\theta_A/2)|0\rangle_A + \sin(\theta_A/2)|1\rangle_A \equiv |\psi\rangle_A\,, \tag{4.68a}$$

$$\hat{U}_t(0,0)|1\rangle_A = |0\rangle_A\,, \tag{4.68b}$$

$$\hat{U}_t(0,\pi)|1\rangle_A = |1\rangle_A\,, \tag{4.68c}$$

$$\hat{U}_t(0,\pi/2)|1\rangle_A = |+\rangle_A\,, \tag{4.68d}$$

$$\hat{U}_t(\pi,\pi/2)|1\rangle_A = |-\rangle_A\,, \tag{4.68e}$$

$$\hat{U}_t(-\pi/2,\pi/2)|1\rangle_A = |+i\rangle_A\,, \tag{4.68f}$$

$$\hat{U}_t(\pi/2,\pi/2)|1\rangle_A = |-i\rangle_A\,. \tag{4.68g}$$

Once the initial states are prepared, they can be rewritten in the basis of Bell states for qubits A and B. This is achieved by performing the substitutions $|0,0\rangle_{A,B} = (|\Phi^+\rangle + |\Phi^-\rangle)_{A,B}/\sqrt{2}$, $|1,1\rangle_{A,B} = (|\Phi^+\rangle - |\Phi^-\rangle)_{A,B}/\sqrt{2}$, $|0,1\rangle_{A,B} = (|\Psi^+\rangle + |\Psi^-\rangle)_{A,B}/\sqrt{2}$ and $|1,0\rangle_{A,B} = (|\Psi^+\rangle + |\Psi^-\rangle)_{A,B}/\sqrt{2}$. The rewritten state is

$$|T\rangle_A \otimes \frac{1}{2}\big[\,|\Phi^+\rangle_{A,B}\otimes|\psi\rangle_C + |\Phi^-\rangle_{A,B}\otimes\hat{\sigma}_z|\psi\rangle_C + |\Psi^+\rangle_{A,B}\otimes\hat{\sigma}_x|\psi\rangle_C + |\Psi^-\rangle_{A,B}\otimes\hat{\sigma}_y|\psi\rangle_C)\big], \tag{4.69}$$

where qubits A and B are in a superposition of entangled states. The act of determining which entangled state the two qubits are in (Bell measurement, see section 4.2.2) projects qubit C onto one of the four states $\{\,|\psi\rangle_C, \hat{\sigma}_z\,|\psi\rangle_C, \hat{\sigma}_x\,|\psi\rangle_C, \hat{\sigma}_y\,|\psi\rangle_C\}$. Since the two qubit operator $\hat{O}_{\text{Bell}}$ has the power to successfully distinguish two of the

Bell pairs, $|\Psi^{\pm}\rangle$, the two resulting states at C are $\hat{\sigma}_x|\psi\rangle_C$ and $\hat{\sigma}_y|\psi\rangle_C$. To complete the teleportation protocol, it is normally required to rotate this qubit such that it is equal to the desired $|\psi\rangle_C$ state, however, due to the lack of fast-feedforward in this experiment, it was chosen to simply perform a tomography on the resulting state. As an example, a full state tomography was shown for the resulting state when measuring qubits A and B in the $|\Psi^+\rangle$ state. The process for this was as follows. First the qubit A was prepared in one of the six chosen states, as detailed in equation 4.68. Secondly, and as detailed in section 4.2.2, coincidence counts across the opposite modes of qubits A and B give a projection onto the state $|\Psi^+\rangle_{A,B}$. Therefore, the state at qubit C is projected onto $\hat{\sigma}_x|\psi\rangle_C$. For each of the prepared initial states, a full tomography of this resulting state was achieved by taking the four-photon coincidence events across modes $\{T_A, 0_A, 1_B, 0_C/1_C\}$ and $\{T_A, 0_A, 0_B, 0_C/1_C\}$, where '/' here indicates that both permutations are measured. The number of four-fold coincidence counts were doubled by adding these contributions together. Here the cases where $0_C/1_C$ is detected determines whether the measured eigenvalue was positive/negative. The local projector $\hat{U}_b(\phi_C, \theta_C)$ then determines the measurement bases of the final qubit. The normalised four-photon coincidence counts across each basis were calculated over an integration time of 20 minutes was recorded, which were used to estimate the probability of each measurement. The reconstructed density matrices are shown in figure 4.7c, and the prepared and expected states are shown. The fidelity of each of the measurements were $F_0 = 95.7 \pm 2.0, F_1 = 97.6 \pm 2.6, F_+ = 85.7 \pm 3.4, F_- = 86.3 \pm 3.9, F_{+i} = 89.3 \pm 4.0, F_{-i} = 88.9 \pm 4.4$. Each of the estimated errors were achieved by performing a Monte-Carlo simulation on the data, assuming poissonian counting statistics. The average measured fidelity $\approx 91\%$ is among the highest seen in any platform [63].

4.3.2 Entanglement Swapping (Teleportation of Entanglement)

Entanglement swapping, able to entangle particles that have never interacted with one another, is a powerful tool in quantum information science. Its uses apply to a range of quantum information technologies, such as quantum repeaters, the quantum internet, quantum secret-sharing and device-independent quantum cryptography [38, 44, 84, 85]. This section presents a novel on-chip entanglement swapping protocol in silicon photonics that builds on the previous sections of this thesis to deliver the first four-qubit and four-photon experiment. The four-qubits are encoded in four photons across eight spatial modes (four dual-rail qubits). Figure 4.8a shows the device schematic used for this experiment, where one photon is present in each of the defined qubit

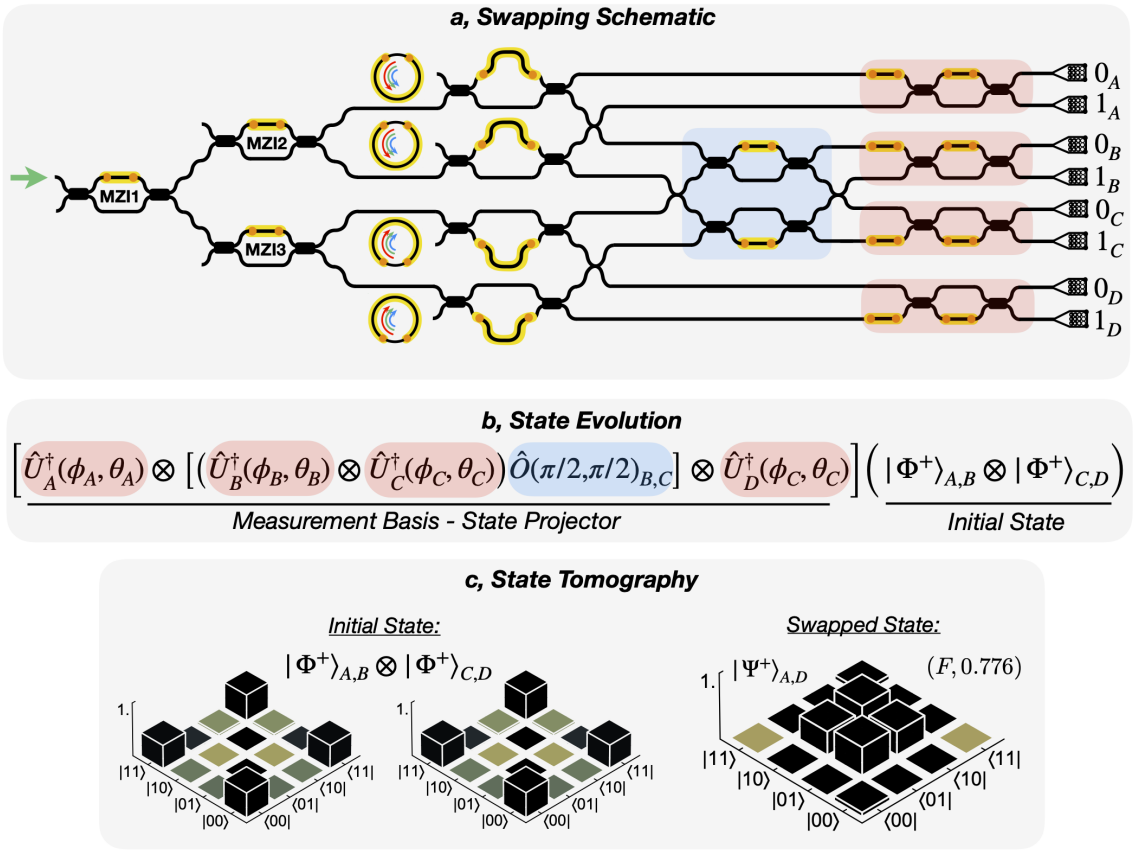

Figure 4.8: Entanglement swapping experiment. **a,** Chip schematic comprising four qubits and four MRR. Two Bell pairs are generated and incident on $\hat{O}_{\text{Bell}}$. The qubit definitions are given to the right of the grating couplers. The Bell measurement on qubits B and C projects qubits A and D onto an entangled state. **b,** shows the state evolution on chip, the coloured boxes match the chip schematic. **c,** topographies of the two initial Bell pairs (left) and the final swapped state (right).

spatial modes $0_x/1_x$, $x \in \{A,B,C,D\}$. The qubit definitions are presented to the right of the schematic at each of the eight grating couplers. Throughout this experiment, each of the four MRR are pumped equally and are well overlapped by utilising a CW seed laser as outlined in section 3.3.1. An array of MZI, {MZI1, MZI2, MZI3}, are each set to split the input pulsed laser (500MHz repetition rate) equally across each of the MRR resonances. By setting this pumping configuration, and by detecting four-photon coincidence events such that only one photon is measured per qubit $\{0_A/1_A, 0_B/1_B, 0_C/1_C, 0_D/1_D\}$, the initial state is

$$|\Psi^+\rangle_{A,B}\otimes|\Psi^+\rangle_{C,D}\,. \tag{4.70}$$

Here $\{0_A/1_A, 0_B/1_B, 0_C/1_C, 0_D/1_D\}$ refers to all 16 possible permutations of four-fold coincidence counts across the four qubits. This initial state can be precisely measured

by setting $\hat{O}_{B,C}(\theta_1,\theta_2) \rightarrow \hat{O}_I$ and adding a $\Delta\phi_z = \pi$ z-phase shift to the projectors of qubits B and C. This cancels the π phase shifts that are introduced by $\hat{O}_I$, see figure 4.4b. By rotating each of the qubit projectors, two two-qubit tomographies are measured of the Bell states $|\Phi^+\rangle_{A,B}$ and $|\Phi^+\rangle_{C,D}$, and can be seen in figure 4.8c (left). Each of these measurements takes on an identical approach (and is explained in greater detail) as in section 4.1.5.2.

The initial (bi-separable) initial state can be rewritten in the basis of Bell states, for qubits $\{A,D\}$ and $\{C,D\}$. To complete this change of basis, the following substitutions are made

$$|0,0\rangle_{A,D} = (|\Phi^+\rangle_{A,D} + |\Phi^-\rangle_{A,D})/\sqrt{2}, \tag{4.71a}$$

$$|1,1\rangle_{A,D} = (|\Phi^+\rangle_{A,D} - |\Phi^-\rangle_{A,D})/\sqrt{2}, \tag{4.71b}$$

$$|0,1\rangle_{A,D} = (|\Psi^+\rangle_{A,D} + |\Psi^-\rangle_{A,D})/\sqrt{2}, \tag{4.71c}$$

$$|1,0\rangle_{A,D} = (|\Psi^+\rangle_{A,D} + |\Psi^-\rangle_{A,D})/\sqrt{2}, \tag{4.71d}$$

$$|0,0\rangle_{B,C} = (|\Phi^+\rangle_{B,C} + |\Phi^-\rangle_{B,C})/\sqrt{2}, \tag{4.71e}$$

$$|1,1\rangle_{B,C} = (|\Phi^+\rangle_{B,C} - |\Phi^-\rangle_{B,C})/\sqrt{2}, \tag{4.71f}$$

$$|0,1\rangle_{B,C} = (|\Psi^+\rangle_{B,C} + |\Psi^-\rangle_{B,C})/\sqrt{2}, \tag{4.71g}$$

$$|1,0\rangle_{B,C} = (|\Psi^+\rangle_{B,C} + |\Psi^-\rangle_{B,C})/\sqrt{2}, \tag{4.71h}$$

which rewrites the initial state (equation 4.70) as

$$\frac{1}{2}\big[\,|\Phi^+\rangle_{A,D}\otimes|\Phi^+\rangle_{B,C} + |\Phi^-\rangle_{A,D}\otimes|\Phi^-\rangle_{B,C} + |\Psi^+\rangle_{A,D}\otimes|\Psi^+\rangle_{B,C} + |\Psi^-\rangle_{A,D}\otimes|\Psi^-\rangle_{B,C}\,\big]. \tag{4.72}$$

When written in this basis, one sees a superposition of swapped entangled states. By turning on $\hat{O}_{\text{Bell}}$ to perform the Bell measurement, qubits B & C are projected onto the $|\Psi^+\rangle_{B,C}$ when detecting four-photon coincidence events in the $\{0_A/1_A, 0_B, 1_C, 0_D/1_D\}$ or $\{0_A/1_A, 1_B, 0_C, 0_D/1_D\}$ channels. As in the teleportation experiment, these two configurations are summed together to increase the statistical significance. Again, here the '/' represents either the 0 mode or 1 mode in that qubit, where all combinations are valid and measured. The post-selection of this state on qubits B & C simultaneously projects the remaining qubits into the equivalent entangled state $|\Psi^+\rangle_{A,D}$, which completes the swapping.

The verification of this state is achieved via normalised four-photon coincidence counts in the following way. For this tomography, six superconducting single photon detectors are used, one at each of the following modes $\{0_A, 0_B, 1_B, 0_C, 1_C, 0_D\}$. An external time-tagger calculates the four-photon coincidence events $\{0_A, 0_B, 1_C, 0_D\}$ & $\{0_A, 1_B, 0_C, 0_D\}$. An integration time is chosen, and the returned values are the total number of four-fold events within that time window, one value corresponding to the

first set and another to the second. Provided the initial state is set correctly, each of these four-fold coincidences contribute to the measurement of the same eigenvalue $P_{+,+}$ and are summed together. In order to measure each global product basis $\hat{\sigma}_i \otimes \hat{\sigma}_j$ where $i,j \in \{x,y,z\}$, four offset phases are applied to each projector to complete the basis measurement. Each applied phase is defined in equation 4.26 and more details are given in section 4.1.3. Each of the 36 measurements combine to give the state tomography, the reconstructed density matrix of which is shown in figure 4.8c. The measured state fidelity for the entanglement swapping $\langle\Psi^+|\rho_{\text{meas}}|\Psi^+\rangle_{A,D}$ was 0.776 ± 0.018.

4.4 Genuine Multipartite GHZ Entangled States

In this section, genuine multipartite entangled states of up to four photons are prepared, measured and verified through entanglement witness operators as well as the multipartite concurrence. For these results eight superconducting single photon detectors are used, one at each of the qubit output modes which reduces the number of global measurement settings by a factor of 16. Due to the different detection efficiencies in each channel, when connecting eight detectors in this way, some post-processing is applied to the data, and is explained in section 4.1.4.

4.4.1 Generation of GHZ States

During this thesis, it has so far been shown how to generate high fidelity separable states on chip. Moreover, entangled qubits have been generated in two ways, firstly via the superposition of identical bi-photon states, and secondly through the interactions of near-identical heralded single photons and multi-qubit interactions. The production of both separable and two-qubit entangled states have been useful in some of the later experiments such as the verification of quantum teleportation and entanglement swapping on chip. These biseparable states[12] are extremely useful in many quantum information protocols, in fact, it is the superposition of biseparable states that directly allows the teleportation and entanglement swapping protocols - which are backbones in quantum information processing. However, genuine multipartite (n>2) entangled states that have no factorisation between any of the qubits are of use in many applications of quantum information such as quantum secret sharing and scalable quantum computing with photons [64, 65, 84, 156]. In this section, it is shown that two initially biseparable four-photon states may be multipartite entangled by applying $\hat{O}_{\text{Fusion}}$ to

[12]Multi-qubit states that are not fully separable but have one separable partition.

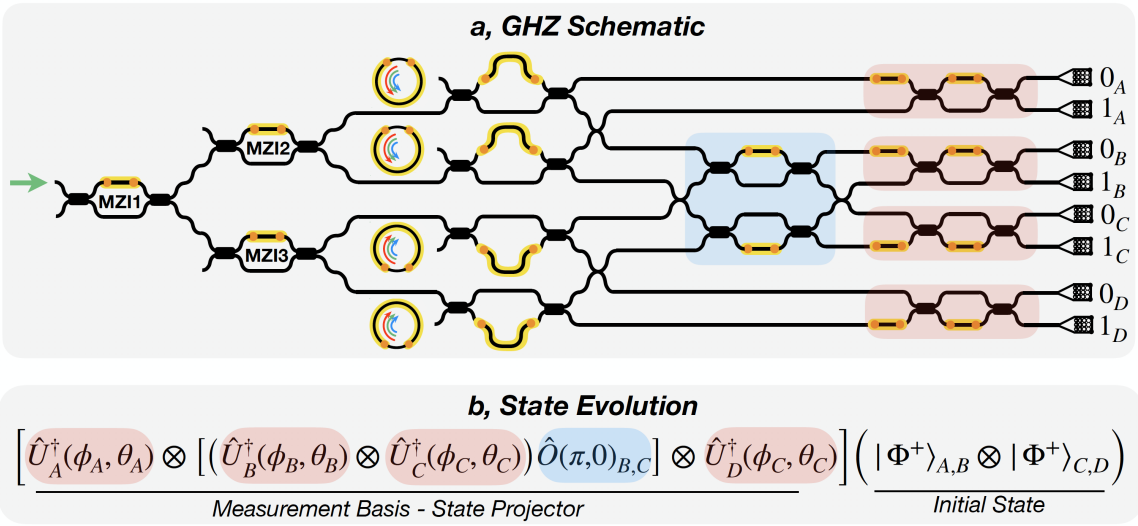

Figure 4.9: GHZ Chip schematic and state evolution. **a,** four-qubit GHZ chip schematic comprised of four MRR single photon sources. The detection of four photons across each of the encoded qubits (shown right) produces the initial bi-separable state $|\Phi^+\rangle_{A,B}\otimes|\Phi^+\rangle_{C,D}$. Once passed through the fusion operation, the biseparable state becomes multipartite entangled. **b** shows the general state evolution for the initial state and the measurement sections.

two of the unentangled qubits. In this experiment, the target states are the n-photon GHZ class of states, which are introduced in chapter 2 section 2.3.1. In addition to preparing the state, a quantitative measure of this multipartite entanglement is given, and the state fidelity is estimated.

Figure 4.9a shows the device schematic, which highlights the following experiments. In this layout, the four coherently pumped MRR produce high count-rate photon pairs. The chip is configured to equally pump each MRR and filter the signal and idler photons. In the case where four-photon coincidence events are detected across each qubit (and remaining in the low squeezing regime), the initial prepared state is a tensor product of Bell pairs $|\Phi^+\rangle_{A,B}\otimes|\Phi^+\rangle_{C,D}$. Note that qubits A & D are prepared using idler photons and qubits B & C are prepared via the corresponding and identical signal photons. Since these qubits (B & C) are formed from identical photons, one can utilise the two qubit operator to perform quantum interference measurements and entangling operations.

4.4.1.1 Four Photon GHZ

The four-photon GHZ entangled states are generated on-chip by applying the two-qubit entangling operator $\hat{O}_{\text{fusion}}$ (see section 4.2.3) onto the initially prepared biseparable states $|\Phi^+\rangle_{A,B}\otimes|\Phi^+\rangle_{C,D}$. This initial state is rotated under $\hat{O}_{\text{fusion}}$ which acts on the

signal $\hat{S}^\dagger$ and idler $\hat{i}^\dagger$ photons in the following way

(4.73)
$$\begin{aligned}&\left(\hat{I}_A \otimes \hat{O}_{\text{fusion,B,C}} \otimes \hat{I}_D\right)\left[\frac{\left(\hat{i}^\dagger_{A,0}\hat{S}^\dagger_{B,0} + \hat{i}^\dagger_{A,1}\hat{S}^\dagger_{B,1}\right)}{\sqrt{2}}\frac{\left(\hat{S}^\dagger_{C,0}\hat{i}^\dagger_{D,0} + \hat{S}^\dagger_{C,1}\hat{i}^\dagger_{D,1}\right)}{\sqrt{2}}\right]|\text{vac}\rangle \\ &= \frac{1}{2}\Big(\underbrace{-\hat{i}^\dagger_{A,0}\hat{S}^\dagger_{B,0}\hat{S}^\dagger_{C,0}\hat{i}^\dagger_{D,0}}_{\text{Measured}} \underbrace{-i\,\hat{i}^\dagger_{A,0}\hat{S}^\dagger_{B,0}\hat{S}^\dagger_{B,1}\hat{i}^\dagger_{D,1}}_{\text{Not Measured}} \underbrace{-i\,\hat{i}^\dagger_{A,1}\hat{S}^\dagger_{C,1}\hat{S}^\dagger_{C,0}\hat{i}^\dagger_{D,0}}_{\text{Not Measured}} \underbrace{-\hat{i}^\dagger_{A,1}\hat{S}^\dagger_{C,1}\hat{i}^\dagger_{B,1}\hat{S}^\dagger_{D,1}}_{\text{Measured}}\Big)|\text{vac}\rangle,\end{aligned}$$

where $\hat{i}^\dagger_{A,0}$ represents the creation operator for the idler photon in the 0^{th} mode of the A^{th} qubit. Hence the un-measured states do not contribute and are post-selected away from the final state. In this case, the measureable photon terms are prepared in the four-photon GHZ state when detecting only one photon in each of the qubit mode combinations $\{0_A/1_A, 0_B/1_B, 0_C/1_C, 0_D/1_D\}$. The detection of four-photon coincidence events thus results in the four-qubit entangled GHZ state, which after normalisation reads:

(4.74)
$$\begin{aligned}&\Rightarrow \frac{1}{\sqrt{2}}(\hat{i}^\dagger_{A,0}\hat{S}^\dagger_{B,0}\hat{S}^\dagger_{C,0}\hat{i}^\dagger_{D,0} + \hat{i}^\dagger_{A,1}\hat{S}^\dagger_{B,1}\hat{S}^\dagger_{C,1}\hat{i}^\dagger_{D,1})|\text{vac}\rangle \\ &\Rightarrow |\text{GHZ}\rangle_4 = \frac{\left(|0,0,0,0\rangle + |1,1,1,1\rangle\right)_{A_i,B_s,C_s,D_i}}{\sqrt{2}}.\end{aligned}$$

4.4.1.2 Three Photon GHZ

To create the three-photon GHZ entangled state, a local measurement is made of qubit D which projects the remaining qubits into the three qubit GHZ state. By choosing the $\hat{\sigma}_x$ basis, the four qubit GHZ state may be rewritten in the following way

(4.75)
$$\begin{aligned}|\text{GHZ}\rangle_4 &= \frac{1}{2}\left(|0,0,0\rangle_{A,B,C}(|+\rangle + |-\rangle)_D + |1,1,1\rangle_{A,B,C}(|+\rangle - |-\rangle)_D\right) \\ &= \frac{1}{2}\Big(\left(|0,0,0\rangle + |1,1,1\rangle\right)_{A,B,C}|+\rangle_D + \left(|0,0,0\rangle - |1,1,1\rangle\right)_{A,B,C}|-\rangle_D\Big)\end{aligned}$$

Hence the desired three photon GHZ state $|\text{GHZ}\rangle_3 = (|0,0,0\rangle + |1,1,1\rangle)/\sqrt{2}$ can be found with 50% probability when the fourth qubit is measured in the $|-\rangle$ eigenstate.

4.4.1.3 Two Photon GHZ, Entanglement Swapping

Likewise, when qubits B and C are measured in the $\hat{\sigma}_x$ basis, the two qubit entangled state can be post-selected in a similar manner. Applying a similar analysis to these

qubits one arrives at the following state

$$
\begin{aligned}
|\mathrm{GHZ}\rangle_4 = \frac{1}{2\sqrt{2}}\Big[& |0,0\rangle_{A,D}\left(|+\rangle+|-\rangle\right)_B\left(|+\rangle+|-\rangle\right)_C \\
& +|1,1\rangle_{A,D}\left(|+\rangle-|-\rangle\right)_B\left(|+\rangle-|-\rangle\right)_C\Big] \\
= \frac{1}{2\sqrt{2}}\Big[& \left(|0,0\rangle+|1,1\rangle\right)_{A,D}\left(|{+}{+}\rangle+|{-}{-}\rangle\right)_{B,C} \\
& +\left(|0,0\rangle-|1,1\rangle\right)_{A,D}\left(|{+}{-}\rangle+|{-}{+}\rangle\right)_{B,C}\Big],
\end{aligned}
\tag{4.76}
$$

which gives the desired $|\Phi^+\rangle_{A,D}$ state wherever the two $|+\rangle$ or two $|-\rangle$ eigenstates are measured. As a result, through the operator $\hat{O}_{\mathrm{fusion}}$ the remaining swapped states can be measured, since $\hat{O}_{\mathrm{Bell}}$ allows the swapping of the $|\Psi^{\pm}\rangle$ states. As an example, the $|\Phi^+\rangle$ state is measured via a full state tomography whereby qubits A & D are measured in the different Pauli bases and qubits B & C are projected into the eigenstates $|+,+\rangle$ or $|-,-\rangle$. Figure 4.10a shows the reconstructed density matrices of the initial biseparable state (left) and the swapped entangled state $|\Phi^+\rangle_{A,D}$ (right) by performing a full quantum state tomography. The measured fidelity of the swapped state was 0.737 ± 0.019.

4.4.2 Certification of GME by Entanglement Witness

In order to quantitatively certify genuine multipartite GHZ entanglement, a suitable entanglement witness was measured. A multipartite entanglement witness $\hat{W}$ is defined as an operator which when measured yields values greater than 0 for all biseparable states and values less than 0 for all genuine multipartite entangled states. Such an operator is trivial to construct, yet not always straightforward to evaluate. For example, suppose that the chip is configured as outlined in the previous section, such that the output of the four qubits is the desired four-photon GHZ state $|\mathrm{GHZ}\rangle_4$. The actual output of the chip will in-fact be some approximation of the ideal state, and in general will produce four-fold coincidence events which are found in a statistical mixture of states ρ_{meas}. The fidelity between the desired ideal state and the measured state is defined as $F_\rho = \langle \mathrm{GHZ}| \rho_{\mathrm{meas}} |\mathrm{GHZ}\rangle$, is a well established benchmark for device performance and has been used many times throughout this thesis. It is useful, then, to construct the measured witness in terms of this fidelity, such that only states that are close enough to the ideal state are truly multipartite entangled. A straightforward approach to achieve this is to define the witness operator $\hat{W}$ based on its expectation value when measured on the output of our device ρ_{meas}. The suitable expectation value should be written in terms of the maximum overlap between any bi-separable

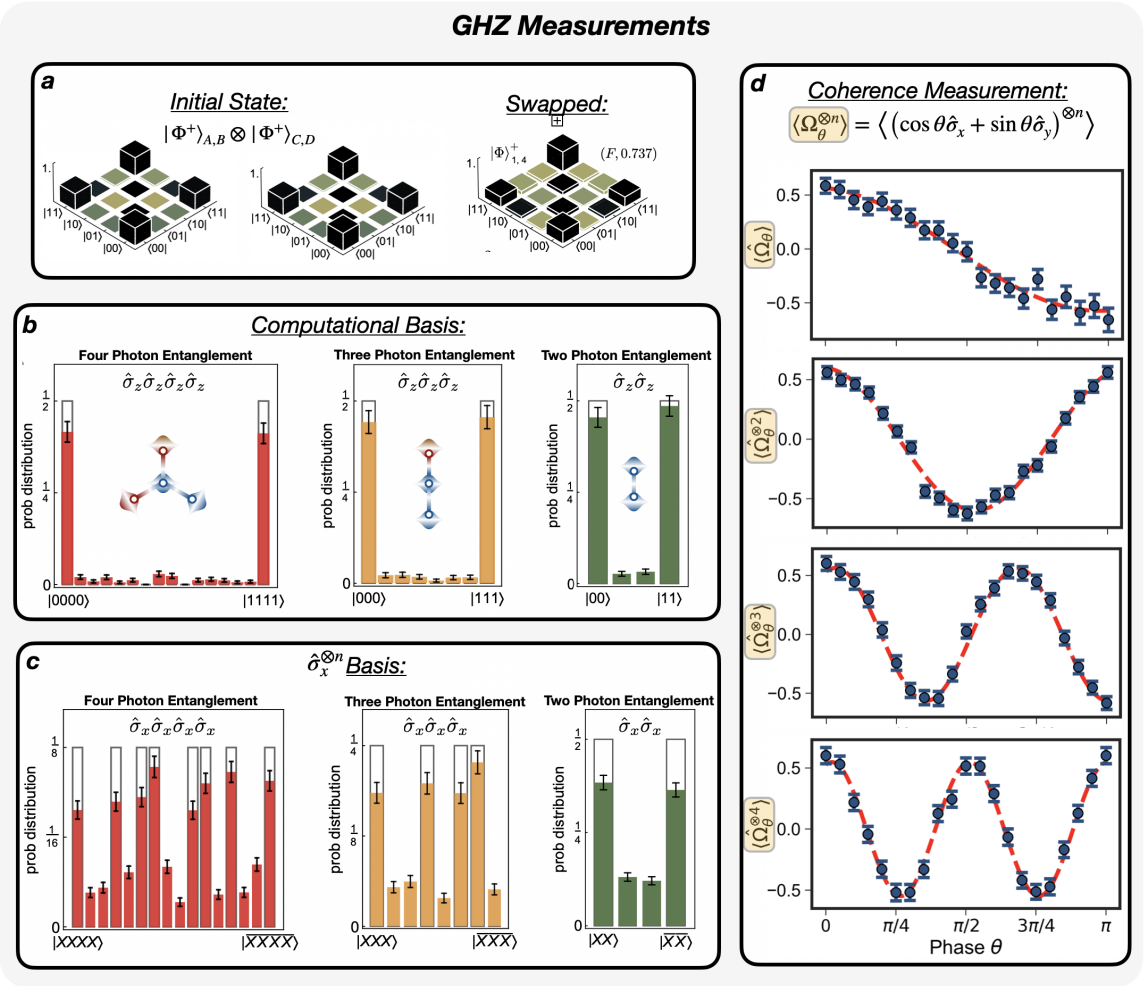

Figure 4.10: Measurements of n-photon GHZ state generation for $n = 2, 3, 4$. **c,** experimental data. **i,** measured initial state is the same as for the swapping exp (shown left), however, this time the swapped state is the $|\Phi^+\rangle_{A,D}$ state (shown right). **ii,** computational basis measurements of the n-photon entangled state comprised of n^2 measurements. **iii,** measurements of the n-photon entanglement in the $\hat{\sigma}_x^{\otimes n}$ basis. Here the grey boxes represent the ideal values, and the colored boxes represent the measured values. **iv,** coherence measurements of the four-photon entangled state. By measuring $\mathrm{Tr}(\rho_{\mathrm{meas}}\Omega_\theta^{\otimes n})$ (shown in fig) one measures an interference fringe which increases frequency with n. All error bars are estimated by assuming poissonian counting statistics in the four-photon coincidence measurements.

state $\phi \in B$ and the target state $|\mathrm{GHZ}\rangle_4$, which can be written as follows

$$F_\alpha \equiv \max_{\phi \in B} |\langle \phi | \mathrm{GHZ} \rangle_4|^2. \tag{4.77}$$

If the measured fidelity F_ρ is greater than the value of F_α, then it is closer to the desired GHZ state than any biseparable state, and is therefore said to be genuine multipartite entangled. The suitable witness is therefore in our case defined as

$$\hat{W} = \alpha \hat{I} - |\mathrm{GHZ}\rangle \langle \mathrm{GHZ}|, \tag{4.78}$$

where $\alpha \equiv F_\alpha = \max_{\phi \in B} |\langle \phi | \mathrm{GHZ} \rangle_4|^2$. The expectation value of this witness is therefore given as

$$\mathrm{Tr}\left(\rho_{\mathrm{meas}} \hat{W}\right) = F_\alpha - F_\rho, \tag{4.79}$$

which has the desired properties that yields a negative value for genuine multipartite entangled states and positive values for other states. By measuring this operator, one can use this value to estimate the confidence to which the four particles are entangled with one another. For states in the GHZ class that are considered in this thesis[13], the value of α can be mathematically evaluated as 1/2 [161, 162]. As a result, any measured state fidelity F_ρ greater than 1/2 certifies genuine multipartite entanglement of the four photon state.

The standard approach to estimating the on chip state fidelity within this thesis has been to first estimate the on chip density matrix through a full state tomography, and then to compute the overlap between the desired pure state and measured state. However, the full state tomography of the four-photon four qubit GHZ state requires a minimum of 81 global measurement settings (using eight detectors) and $81 \times 4^2 = 1,296$ measurements. In addition, the continuous use of eight high efficiency superconducting single photon detectors is an expensive resource. An alternative approach is to utilise only four detectors, but this approach requires the full 1296 measurement settings to be performed.

This can be avoided by finding a more efficient scheme to estimate the state fidelity, without the need to reconstruct the full density matrix. In practice, this is achieved by decomposing the four qubit GHZ state into so-called local measureable observables. Under this decomposition, the GHZ state fidelity can be estimated by locally rotating each qubit in a smaller number of measurements than the full tomography. This can be done efficiently for (n qubit) GHZ class states, which reduces the required global

[13] A witness operator can be constructed for different classes of entangled state.

measurement settings from exponential scaling (2^n, required by first computing the tomography) to the linear scaling $n+1$. The fidelity can be estimated by measuring the average of two expectation values in the following way [57]

$$F_{\mathrm{GHZ}} = \frac{\langle \hat{P} \rangle + \langle \hat{C} \rangle}{2} \tag{4.80}$$

where $\hat{P}$ is the population term given by

$$\hat{P}_n = |0\rangle\langle 0|^{\otimes n} + |1\rangle\langle 1|^{\otimes n}, \tag{4.81}$$

and $\hat{C}$ is the coherence term, given by

$$\hat{C}_n = \frac{1}{n}\sum_{k=0}^{n-1} (-1)^k \langle \hat{\Omega}_{k\pi/n}^{\otimes n} \rangle, \tag{4.82}$$

where

$$\hat{\Omega}_\theta = \cos\theta\hat{\sigma}_x + \sin\theta\hat{\sigma}_y. \tag{4.83}$$

In this experiment, the population term can be trivially computed via measurements in the computation basis. The results of which are shown in figure 4.10b (left). For the coherence term, however, n qubits must be each projected into the $\hat{\Omega}_\theta$ eigenbases. These $\hat{\Omega}_\theta$ terms require some further attention in order to determine the correct measurement settings for each of the single qubit projectors. In order to perform projective measurements in this basis, one is first required to find the correct eigenvectors, and then one can find the inverse transformation that allows $\hat{U}_{t/b}^\dagger$ to project these states back into the computation basis. The eigenvectors of this operator can be deduced through simple geometric arguments. Since $\hat{\Omega}_\theta$ is in fact a rotation around the Z axis of the Bloch sphere, generating a circle in the x-y plane. The origin of the rotation is simple, since at $\hat{\Omega}_0 = \hat{\sigma}_x$, whose eigenvectors are known as $|\pm\rangle$. At $\theta = \pi/2$ the operator becomes $\hat{\Omega}_{\pi/2} = \hat{\sigma}_y$, which has eigenvectors $|\pm i\rangle$. The expected general vectors are therefore $|\pm e^{i\theta}\rangle \equiv (|0\rangle \pm e^{i\phi}|1\rangle)/\sqrt{2}$, which has the correct condition that they are unbiased with the $\hat{\sigma}_z$ basis. Of course, one can more rigorously check this result by first solving the characteristic equation

$$|\cos\theta\hat{\sigma}_x + \sin\theta\hat{\sigma}_y - \lambda\hat{I}| = \begin{vmatrix} -\lambda & e^{-i\theta} \\ e^{i\theta} & -\lambda \end{vmatrix} = 0, \tag{4.84}$$

giving eigenvalues ± 1. The eigenvectors are found by solving the eigenvector equation

on the general vector $a|0\rangle + b|1\rangle$ in the following way

$$\begin{aligned} \begin{pmatrix} 0 & e^{-i\theta} \\ e^{i\theta} & 0 \end{pmatrix} \begin{pmatrix} a \\ b \end{pmatrix} &= \pm \begin{pmatrix} a \\ b \end{pmatrix}, \\ \begin{pmatrix} e^{-i\theta} b \\ e^{i\theta} a \end{pmatrix} &= \pm \begin{pmatrix} a \\ b \end{pmatrix}, \\ \implies b &= \pm e^{i\theta} a, \end{aligned} \tag{4.85}$$

giving the normalised vectors $|\pm e^{i\theta}\rangle$ as expected. From here, the correct projection can be found by computing the phases ϕ_x, θ_x which are able to rotate the states $|+e^{i\theta}\rangle$ into the computational basis via the projector $\hat{U}_x^\dagger(\phi_x, \theta_x)$, where $x \in \{A, B, C, D\}$. For qubits C and D, which each have their phase shifts positioned in the logical $|1\rangle$ modes, the general evolution is

$$\begin{aligned} \hat{U}_{b,x}^\dagger(\phi_x, \theta_x)|\pm e^{i\theta}\rangle &= \begin{pmatrix} \sin(\theta_x/2) & e^{i\phi_x}\cos(\theta_x/2) \\ \cos(\theta_x/2) & -e^{i\phi_x}\sin(\theta_x/2) \end{pmatrix} \frac{1}{\sqrt{2}} \begin{pmatrix} 1 \\ \pm e^{i\theta} \end{pmatrix} \\ &= \frac{1}{\sqrt{2}} \begin{pmatrix} \sin(\theta_x/2) \pm e^{i(\phi_x+\theta)}\cos(\theta_x/2) \\ \cos(\theta_x/2) \mp e^{i(\phi_x+\theta)}\sin(\theta_x/2) \end{pmatrix}. \end{aligned} \tag{4.86}$$

Hence, when $\theta_x = \pi/4$ and $\phi_x = -\theta$, the positive eigenvector is mapped to the $|0\rangle$ and the negative eigenvector is mapped to the $|1\rangle$ state. A similar analysis finds that for qubits A and B, which have their phaseshifters located on the $|0\rangle$ mode (see figure 4.1 for a summary), the correct phases are $\theta_x = -\pi/4$ and $\phi_x = \theta$. This can be seen from the following expressions

$$\begin{aligned} \hat{U}_{t,x}^\dagger(\phi_x, \theta_x)|\pm e^{i\theta}\rangle &= \begin{pmatrix} -e^{i\phi_x}\sin(\theta_x/2) & \cos(\theta_x/2) \\ e^{i\phi_x}\cos(\theta_x/2) & \sin(\theta_x/2) \end{pmatrix} \frac{1}{\sqrt{2}} \begin{pmatrix} 1 \\ \pm e^{i\theta} \end{pmatrix} \\ &= \frac{1}{\sqrt{2}} \begin{pmatrix} -e^{i\phi_x}\sin\theta_x/2 \pm e^{i\theta}\cos(\theta_x/2) \\ e^{i\phi_x}\cos(\theta_x/2) \pm e^{i\theta}\sin(\theta_x/2) \end{pmatrix}. \end{aligned} \tag{4.87}$$

Each of the four qubits are projected into the $\hat{\Omega}_\theta$ basis, and the expectation value was calculated for the phases $\theta = \{0, \pi/4, \pi/2, 3\pi/4\}$. From these measurements the coherence term $\hat{C}_4$ can be constructed. When combined with the population term, these measurements gave a fidelity of 0.735 ± 0.017. The error here was calculated by applying a Monte-Carlo simulation to the poissonian counting statistics. This fidelity gives a witness value of $\langle \hat{W}_{\mathrm{GHZ}} \rangle = 1/2 - F_{\mathrm{meas}} = -0.235 \pm 0.017$, which certifies the genuine multipartite entanglement of the system by more than 13 standard deviations. This measurement was then repeated for the three photon GHZ, which is post-selected in the way outlined in section 4.4.1.2. The three photons are measured

in the $\hat{\Omega}_\theta$ basis for $\theta = \{0, \pi/3, 2\pi/3\}$. The population measurements are each shown in figure 4.10b (middle). The 16 individual measurements for the coherence terms, where $\theta = 0$ in each case $\langle \hat{\Omega}_0^{\otimes n} \rangle$, are shown for the n-photon GHZ states in figure 4.10c which is equivalent to the basis $\hat{\sigma}_x^{\otimes n}$. By combining all of the results, the measured fidelity for the three-photon state was 0.683 ± 0.014, giving a witness value of -0.183 ± 0.014, again certifying the multipartite entanglement by a large margin ($\approx 13\sigma$). The following subsection derives the interference pattern achieved by measuring the $\langle \hat{\Omega}_0^{\otimes n} \rangle$ operator over a range $0 \leq \theta \leq \pi$, of which can be seen in figure 4.10d.

4.4.2.1 Coherence Measurements

In this section, the above results are expanded on and the general expression for the n-photon coherence measurements is given. Specifically, the relative probability of each of the 16 four-fold combinations are calculated and the expectation value of the measurements are numerically calculated as a function of θ. It has so far been shown that for n qubit GHZ target states, the fidelity can be measured with only $n+1$ global measurement settings. These $n+1$ global settings are comprised of a single measurement in the computational basis, which are required to estimate the population term described in the previous section. This measurement is enough to assess the classical correlations one expects from the GHZ state, which can be reproduced even from qubits that are prepared by completely distinguishable photon states.

The remaining n global measurement settings each form the so-called coherence terms which arise due to the quantum coherence's of the state (the non-diagonal elements of the density matrix). It is these terms which distinguish the prepared GHZ states from the statistical mixture of states $\rho_{\text{mixed}} = (|0000\rangle\langle 0000| + |1111\rangle\langle 1111|)/2$. For example, this mixture would give rise to identical population (computational basis) measurement as with the target GHZ state, however, there would be a zero contribution from the coherence terms. As a result, the classical threshold for the GHZ state is set at 50% fidelity. In order to see the expectation value of the $\hat{\Omega}_\theta$ operator directly, the explicit calculation is performed on the mixed state ρ_{mixed}, in this case the expectation value is

$$\langle \hat{\Omega}_\theta^{\otimes 4} \rangle_{\text{mixed}} = \text{Tr}\left(\rho_{\text{mixed}} \hat{\Omega}_\theta^{\otimes 4}\right). \tag{4.88}$$

Since ρ_{mixed} has only two diagonal non-zero values, only the following two inner products remain once taking the trace, therefore

$$\text{Tr}\left(\rho_{\text{mixed}} \hat{\Omega}_\theta^{\otimes 4}\right) = \frac{1}{2}\left[\langle 0000|\hat{\Omega}_\theta^{\otimes 4}|0000\rangle + \langle 1111|\hat{\Omega}_\theta^{\otimes 4}|1111\rangle\right] \tag{4.89}$$

But since $\hat{\Omega}_\theta^{\otimes 4} = \left(e^{i\theta}|0\rangle\langle 1| + e^{-i\theta}|1\rangle\langle 0|\right)^{\otimes 4}$ and contains zero diagonal elements, it can be seen that the trace is zero for all values of θ. Therefore the coherence terms of this mixed state are zero, and the total fidelity is 50%. Hence the measured coherence values arise from the off-diagonal elements of the density matrix, and the expectation value equals 1/2 for the GHZ state.

In order to derive the relative probabilities of each of the four-qubit $2^4 = 16$ coincidence channels, the GHZ state can be rewritten in the basis of eigenstates for the $\hat{\Omega}_\theta^{\otimes 4}$ operator. The eigenvectors of these operators have been shown to be $|\pm e^{i\theta}\rangle = (|0\rangle \pm e^{i\theta}|1\rangle)/\sqrt{2}$. The change of basis can be completed by performing the following basis substitutions

$$\begin{aligned} |0\rangle &= \frac{1}{\sqrt{2}}\left(|+e^{i\theta}\rangle + |-e^{i\theta}\rangle\right), \\ |1\rangle &= \frac{e^{-i\theta}}{\sqrt{2}}\left(|+e^{i\theta}\rangle - |-e^{i\theta}\rangle\right). \end{aligned} \tag{4.90}$$

By performing these substitutions, the four qubit GHZ state may be written as follows

$$\begin{aligned} |\mathrm{GHZ}\rangle_4 = \frac{1}{4\sqrt{2}}\Big[&\Big(|+e^{i\theta}\rangle_{A,B,C,D}^{\otimes 4} + |+e^{i\theta}\rangle_{A,C}^{\otimes 2}\otimes|-e^{i\theta}\rangle_{B,D}^{\otimes 2} + |+e^{i\theta}\rangle_{A,D}^{\otimes 2}\otimes|-e^{i\theta}\rangle_{B,C}^{\otimes 2} \\ &+|+e^{i\theta}\rangle_{B,C}^{\otimes 2}\otimes|-e^{i\theta}\rangle_{A,D}^{\otimes 2} + |+e^{i\theta}\rangle_{B,D}^{\otimes 2}\otimes|-e^{i\theta}\rangle_{A,C}^{\otimes 2} \\ &+|+e^{i\theta}\rangle_{C,D}^{\otimes 2}\otimes|-e^{i\theta}\rangle_{A,B}^{\otimes 2} + |-e^{i\theta}\rangle_{A,B,C,D}^{\otimes 4}\Big)\left(1+e^{-4i\theta}\right) \\ &+\Big(|+e^{i\theta}\rangle_A\otimes|-e^{i\theta}\rangle_{B,C,D}^{\otimes 3} + |+e^{i\theta}\rangle_B\otimes|-e^{i\theta}\rangle_{A,C,D}^{\otimes 3} \\ &+|+e^{i\theta}\rangle_C\otimes|-e^{i\theta}\rangle_{A,B,D}^{\otimes 3} + |+e^{i\theta}\rangle_D\otimes|-e^{i\theta}\rangle_{A,B,C}^{\otimes 3} \\ &+|+e^{i\theta}\rangle_{A,B,C}^{\otimes 3}\otimes|-e^{i\theta}\rangle_D + |+e^{i\theta}\rangle_{A,B,D}^{\otimes 3}\otimes|-e^{i\theta}\rangle_C \\ &+|+e^{i\theta}\rangle_{A,C,D}^{\otimes 3}\otimes|-e^{i\theta}\rangle_B + |+e^{i\theta}\rangle_{B,C,D}^{\otimes 3}\otimes|-e^{i\theta}\rangle_A\Big)\left(1-e^{-4i\theta}\right)\Big]. \end{aligned} \tag{4.91}$$

When written in this way, one can see that all of the eigenvectors associated with a positive eigenvalue ($\lambda = 1$) gain a θ dependent term $\left(1+e^{-4i\theta}\right)$. This eigenvalue belongs to all of the vectors with an even number of qubits that contain a $|-e^{i\theta}\rangle$ term, of which there are eight. Each of the eight remaining vectors with a negative associated eigenvalue ($\lambda = -1$) gain a corresponding interference fringe proportional to $\left(1-e^{-4i\theta}\right)$. The probability that any individual positive eigenvector is measured is equal to

$$\begin{aligned} \left|\frac{1+e^{-4i\theta}}{4\sqrt{2}}\right|^2 &= \frac{1}{8}\cos^2(2\theta) \\ &= \frac{1+\cos(4\theta)}{16}, \end{aligned} \tag{4.92}$$

and a similar calculation for the negative eigenvectors gives $\big(1-\cos(4\theta)\big)/16$. These eigenvector probabilities are confirmed experimentally in figure 4.11 (bottom), which lists the measured positive (blue) and negative (yellow) eigenvalue probabilities as a function of θ. Here the positive and negative contributions are added together and should (for an ideal measurement) read $\big(1+\cos(4\theta)\big)/2$ and $\big(1-\cos(4\theta)\big)/2$, respectfully.

From these results the expectation value of the $\hat{\Omega}_\theta$ measurement can be calculated in terms of the eigenvalues λ_k and the associated probability P_k in the following way

$$\begin{aligned}\langle\hat{\Omega}_\theta\rangle = \sum_k \lambda_k P_k &= 8\times\frac{1+\cos(4\theta)}{16} - 8\times\frac{1-\cos(4\theta)}{16}\\ &= \cos(4\theta).\end{aligned} \tag{4.93}$$

Hence, by projecting each of the four qubits into the basis of eigenvectors of $\hat{\Omega}_\theta$ one should see an interference pattern of frequency $\pi/2$ when varying theta. A similar analysis applied to three photon GHZ states (two photon GHZ state), the result is $\langle\hat{\Omega}_\theta^{\otimes 3}\rangle = \cos(3\theta)$, ($\langle\hat{\Omega}_\theta^{\otimes 2}\rangle = \cos(2\theta)$). This can be seen from the fringes of varying frequency in figures 4.10d and 4.11. As a result, one can verify the effective number of entangled qubits by looking at the interference fringes recorded by the expectation value of this basis. In each of the figures, the additional $n = 1$ fringe is shown by tracing out all other qubits and projecting a single qubit into the $\hat{\Omega}_\theta$ basis. Here clear and well-defined periods match the expected results over a measured range $0 \le \theta \le \pi$.

4.4.3 Quantifying GME with Two Bases Measurements

Optimal methods for the quantification of entanglement has been a central topic in quantum information theory for several decades now [163, 164]. Concurrence has become a well-established measure of bipartite entanglement, where the entropy of one of the systems determines the amount of entanglement [165]. This gives a relationship between the fundamentals of thermodynamics and quantum information theory [164]. For a pure quantum state $|\psi\rangle$, the concurrence is defined as

$$C(|\psi\rangle) = \sqrt{2\big(1-\mathrm{Tr}(\rho_A^2)\big)}, \tag{4.94}$$

where $\rho_A = \mathrm{Tr}_B(\rho)$ is the reduced density matrix of $\rho = |\psi\rangle\langle\psi|$.

The concurrence can be generalised for mixed states by the convex roof construction

$$C(\rho) = \inf_{\{p_i,|\psi_i\rangle\}} \sum_i p_i C(|\psi_i\rangle), \tag{4.95}$$

where the infimum is taken over all possible pure state decomposition's of ρ. For separable states, the concurrence gives a value of 0, while for maximally entangled

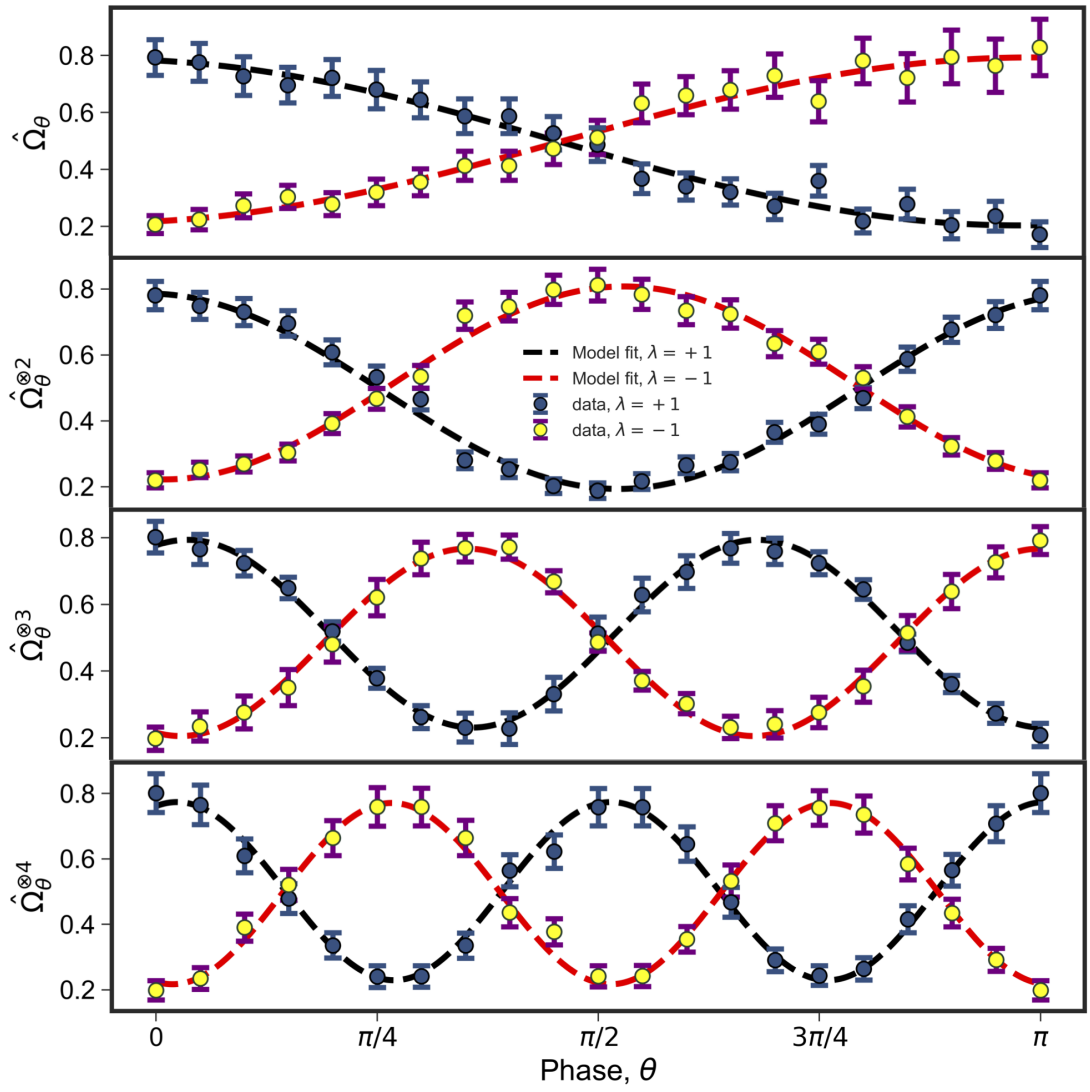

Figure 4.11: The inferred probability of measuring the positive (blue) and negative (red) eigenvalues of the $\hat{\Omega}_\theta^{\otimes n}$ operator. The key feature is the n-fold increase in interference frequency, which corresponds to the n photon entangled state. Here the optimal minimum and maximum values are $0, 1$, where the slightly reduced visibility arises from the reduced coherence terms of the generated density matrix.

states such as a Bell state, it reaches its maximum value of 1. Intermediate values of concurrence quantify the amount of entanglement present in a given bipartite state.

The genuine multipartite entanglement concurrence (GME-concurrence) is a measure of multipartite entanglement that is obtained by extending the regular notion of concurrence in the following manner. For example, for pure multipartite states a similar measure can be obtained by looking at all possible bipartitions of a multipartite state and calculating its concurrence [166]. In this manner, the GME-concurrence can be defined as

$$C_{\mathrm{GME}} \equiv \min_{\gamma_i \in \gamma} \sqrt{2[1 - \mathrm{Tr}(\rho^2_{A_{\gamma_i}})]} \tag{4.96}$$

where $\gamma = \{\gamma_i\}$ represents the set of all possible bipartitions $\{A_i|B_i\}$ of $\{1,2,...,n\}$. The C_{GME} can be generalised for mixed multipartite states by making a convex roof construction in a manner similar to above. A serious consideration in large-scale quantum information experiments, however, is the resources required to obtain such measurements, where topographical processes, for example, require exponential bases measurements for n-partite d-dimensional systems. Considering this, and to much surprise, it was shown in recent work how the GME-concurrence can be efficiently lower-bounded from measurements in just two global product bases, drastically reducing the number of measurements required for estimating it [167, 168]. Moreover, these measurements make no assumption on the state itself and can be completely arbitrary.

In the following, the GME-concurrence is measured for the three- and four-qubit GHZ states as measured in the previous sections. In each case, we will give the exact formula for explicitly calculating the GME-concurrence, which verifies true GME for positive values greater than 0. The two required measurement bases for the following calculations are the $\hat{\sigma}_z^{\otimes n} = \{0,1\}^{\otimes n}$ and $\hat{\sigma}_x^{\otimes n} = \{+,-\}^{\otimes n}$, the results of which are shown for n-partite systems in figures 4.10b and 4.10c, respectfully.

4.4.3.1 Three Photons Example

The GME-concurrence for a tripartite qubit GHZ state can be lower bounded by the following expression that involves measurements in two global product bases, $\hat{\sigma}_x^{\otimes 3}$ and $\hat{\sigma}_z^{\otimes 3}$ [168]:

$$\begin{aligned} C_{GME} \geq C_{3,2} - 4\Big(&\sqrt{\langle 001|\,\rho\,|001\rangle\,\langle 110|\,\rho\,|110\rangle} + \sqrt{\langle 010|\,\rho\,|010\rangle\,\langle 101|\,\rho\,|101\rangle} \\ &+ \sqrt{\langle 011|\,\rho\,|011\rangle\,\langle 100|\,\rho\,|100\rangle}\Big), \end{aligned} \tag{4.97}$$

where the term $C_{3,2}$ is obtained in the following way from diagonal measurements in the first mutually unbiased basis $\hat{\sigma}_x^{\otimes n} = \{+,-\}^{\otimes n}$:

$$
\begin{aligned}
C_{3,2} = {} & \langle+++|\rho|+++\rangle + \langle+--|\rho|+--\rangle + \langle-+-|\rho|-+-\rangle + \langle--+|\rho|--+\rangle \\
& - \langle++-|\rho|++-\rangle - \langle+-+|\rho|+-+\rangle - \langle-++|\rho|-++\rangle - \langle---|\rho|---\rangle .
\end{aligned} \tag{4.98}
$$

This lower bound can be directly evaluated by measuring four-fold coincidence counts and tracing out qubit four in the way described in section 4.4.1.2). By calculating these 14 diagonal density matrix elements, a value of $C_{GME} \geq 0.390 \pm 0.040$ was obtained, which certifies the multipartite entangled with $n = 3$ by at least 9 standard deviations. Here the statistical significance was calculated via a Monte Carlo simulation of the experiment assuming Poissonian statistics.

4.4.3.2 Four Photons Example

The calculation for four photons proceeds in a manner similar to above. The GME-concurrence for a four particle qubit GHZ state can be lower bounded by the expression

$$
\begin{aligned}
C_{GME} \geq C_{4,2} - 4\Big(& \sqrt{\langle 0001|\rho|0001\rangle \langle 1110|\rho|1110\rangle} + \sqrt{\langle 0010|\rho|0010\rangle \langle 1101|\rho|1101\rangle} \\
& + \sqrt{\langle 0011|\rho|0011\rangle \langle 1100|\rho|1100\rangle} + \sqrt{\langle 0100|\rho|0100\rangle \langle 1011|\rho|1011\rangle} \\
& + \sqrt{\langle 0101|\rho|0101\rangle \langle 1010|\rho|1010\rangle} + \sqrt{\langle 0110|\rho|0110\rangle \langle 1001|\rho|1001\rangle} \\
& + \sqrt{\langle 0111|\rho|0111\rangle \langle 1000|\rho|1000\rangle}\Big),
\end{aligned} \tag{4.99}
$$

where the term $C_{4,2}$ is obtained in the following way from diagonal measurements in the first mutually unbiased basis $\hat{\sigma}_x = \{+,-\}$:

$$
\begin{aligned}
C_{4,2} = {} & \langle++++|\rho|++++\rangle + \langle++--|\rho|++--\rangle + \langle+-+-|\rho|+-+-\rangle + \langle+--+|\rho|+--+\rangle \\
& + \langle-++-|\rho|-++-\rangle + \langle-+-+|\rho|-+-+\rangle + \langle--++|\rho|--++\rangle + \langle----|\rho|----\rangle \\
& - \langle+++-|\rho|+++-\rangle - \langle++-+|\rho|++-+\rangle - \langle+-++|\rho|+-++\rangle - \langle+---|\rho|+---\rangle \\
& - \langle-+++|\rho|-+++\rangle - \langle-+--|\rho|-+--\rangle - \langle--+-|\rho|--+-\rangle - \langle---+|\rho|---+\rangle .
\end{aligned} \tag{4.100}
$$

By measuring four-fold coincidence counts in the $\hat{\sigma}_z = \{0,1\}$ (see figure 4.10b middle) and $\hat{\sigma}_x = \{+,-\}$ (see figure 4.10c middle) bases and calculating the 30 diagonal density matrix elements above, a value of $C_{GME} \geq 0.192 \pm 0.039$ was obtained, which certifies that we are multipartite entangled with $n = 4$ by at least 4 standard deviations.

4.4.3.3 Bounding State Fidelity with Concurrence

The state fidelity F_{GHZ} can also be lower bounded by a similar approach [166]. For three qubits it turns out that

$$F_{\mathrm{GHZ}} \geq \frac{1}{2}C_{3,2} - \Big(\sqrt{\langle 001|\rho|001\rangle\langle 110|\rho|110\rangle} + \sqrt{\langle 010|\rho|010\rangle\langle 101|\rho|101\rangle} + \sqrt{\langle 011|\rho|011\rangle\langle 100|\rho|100\rangle}\Big) + \frac{1}{2}(\langle 000|\rho|000\rangle + \langle 111|\rho|111\rangle), \tag{4.101}$$

as well as for four qubits

$$\begin{aligned} F_{\mathrm{GHZ}} \geq \frac{1}{2}C_{4,2} - \Big(&\sqrt{\langle 0001|\rho|0001\rangle\langle 1110|\rho|1110\rangle} + \sqrt{\langle 0010|\rho|0010\rangle\langle 1101|\rho|1101\rangle} \\ &+ \sqrt{\langle 0011|\rho|0011\rangle\langle 1100|\rho|1100\rangle} + \sqrt{\langle 0100|\rho|0100\rangle\langle 1011|\rho|1011\rangle} \\ &+ \sqrt{\langle 0101|\rho|0101\rangle\langle 1010|\rho|1010\rangle} + \sqrt{\langle 0110|\rho|0110\rangle\langle 1001|\rho|1001\rangle} \\ &+ \sqrt{\langle 0111|\rho|0111\rangle\langle 1000|\rho|1000\rangle}\Big) + \frac{1}{2}(\langle 0000|\rho|0000\rangle + \langle 1111|\rho|1111\rangle). \end{aligned} \tag{4.102}$$

The bounded fidelities for the three-qubit and four-qubit states were 0.693 ± 0.020 and 0.593 ± 0.019, respectfully.

4.5 Discussion

The motivation within this chapter has been to utilise near-identical bi-photon wavepackets that can be generated and interfered with high visibility, to allow the generation of high fidelity photonic qubits on a chip. Though previous work has assessed the performance of two photon states on a chip [4, 12, 13, 61, 94, 108, 169], there remains significant work in characterising multiphoton qubits on chip. For example, some of the earlier demonstrations of multiphoton states arose from off-chip sources and were later coupled on chip [5]. Many of the demonstrations within this chapter such as on-chip teleportation, entanglement swapping and multiphoton entanglement are the first of their kind. For example, quantum teleportation has not yet been achieved with integrated single photon sources [5] and to the best of my knowledge entanglement swapping has not previously been demonstrated in any integrated photonics platform. A theoretical proposal to create on-chip path encoded 3-GHZ states was released just a few years ago [97], though its practical implementation is not ideal since it requires degenerate four-wave mixing compared with the non-degenerate

case, and the outcome probability is slightly reduced (1/4) compared with this scheme (1/2). Moreover, their approach does not intuitively scale to four-photon states or beyond. During the publication of the results summarised in this chapter [109], a similar approach to generating GHZ states was shown but implemented single photon generation within waveguides, attaining lower spectral purity and therefore obtaining lower state fidelities [11]. In addition, the reconfigurability of this device enables the testing of many quantum information protocols including Bell measurements. The 91% average fidelity quantum teleportation shown in this thesis is among the highest obtained in any platform [63], which shows how silicon quantum photonics has become a compelling platform for quantum information processing with photons.

The multiqubit demonstrations throughout this chapter (see summary in table 4.4) are also fundamental to the field of linear optic quantum computers, where the most scalable proposals so far either utilise quantum teleportation as a major resource [64], or graph states such as the three partite GHZ [69, 170]. The former case relies on the bosonic Bell operation within section 4.2.2 and the latter on the fusion operation within section 4.2.3. In both schemes probabilistic gate success (50% in both cases) is enough to provide polynomial scaling of resources for LOQC [64, 69]. In this case, the heralded Bell entangled state generation parts of this chapter form a good benchmark for current technologies for theorists. The hope is that alongside experimental progress and technological advances, simultaneously theoretical innovations will lower the LOQC resource requirements and close the gap between theory and experiment. In the following sections of this discussion we assess some of the most prominent and current experimental challenges, as well as share ideas towards what future progress might look like, and highlight areas of future work.

4.5.1 Experimental Challenges and Scalability

In this section we briefly explore some of the main challenges within the current implementations shown in this chapter and aim to provide insights in how some of the key issues may be mitigated in future demonstrations.

4.5.1.1 The Link Between Entanglement and Purity in Heralded Single Photon Sources

The first point to address is the limitations within the single photon sources on chip. In recent work, significant progress has been made towards developing near-ideal integrated parametric single photon sources [98, 130]. Due to their near optimal interference of identical single photons, current sources such as those introduced

#	Quantum State	Fidelity	Quantifier
1	$\|\Phi\rangle^{+}_{\text{Bell}}$ (Bell entangled, qubits 3,4)	0.915 ± 0.003	QST [9]
2	$\|\Phi\rangle^{-}_{\text{Bell}}$ (Bell entangled, qubits 3,4)	0.933 ± 0.002	QST [9]
3	$\|\Psi\rangle^{+}_{\text{Bell}}$ (Bell entangled, qubits 3,4)	0.932 ± 0.002	QST [9]
4	$\|\Psi\rangle^{-}_{\text{Bell}}$ (Bell entangled, qubits 3,4)	0.929 ± 0.002	QST [9]
5	$\|10\rangle$ (separated, qubits 2,3)	0.964 ± 0.072	QST [9]
6	$\|{+}{+}\rangle$ (separated, qubits 2,3)	0.966 ± 0.002	QST [9]
7	$\|\Psi\rangle^{+}_{\text{Bell}}$ (heralded Bell , qubits 2,3)	0.851 ± 0.040	QST [9]
8	$\|\Phi\rangle^{+}_{\text{Bell}}$ (heralded Bell , qubits 2,3)	0.830 ± 0.032	QST [9]
9	$\|0\rangle$ (teleportation, qubit 2 $\Rightarrow$ 4)	0.957 ± 0.020	QST [3]
10	$\|1\rangle$ (teleportation, qubit 2 $\Rightarrow$ 4)	0.976 ± 0.026	QST [3]
11	$\|+\rangle$ (teleportation, qubit 2 $\Rightarrow$ 4)	0.857 ± 0.034	QST [3]
12	$\|-\rangle$ (teleportation, qubit 2 $\Rightarrow$ 4)	0.863 ± 0.039	QST [3]
13	$\|+i\rangle$ (teleportation, qubit 2 $\Rightarrow$ 4)	0.893 ± 0.040	QST [3]
14	$\|-i\rangle$ (teleportation, qubit 2 $\Rightarrow$ 4)	0.889 ± 0.044	QST [3]
15	$\|\Psi\rangle^{+}_{\text{Bell}}$ (swapping, qubits 1,4)	0.776 ± 0.019	QST [9]
16	$\|\Phi\rangle^{+}_{\text{Bell}}$ (swapping, qubits 1,4)	0.737 ± 0.019	QST [9]
17	$\|\Phi\rangle^{4}_{\text{GHZ}}$ (GHZ entangled, qubits 1,2,3,4)	0.683 ± 0.014	EW [5]
18	$\|\Phi\rangle^{3}_{\text{GHZ}}$ (GHZ entangled, qubits 1,2,3)	0.735 ± 0.017	EW [4]
19	$\|\Phi\rangle^{2}_{\text{GHZ}} = \|\Phi\rangle^{+}_{\text{Bell}}$ (qubits 1,4)	0.786 ± 0.019	EW [3]
20	$\|\Phi\rangle^{4}_{\text{GHZ}}$ (GHZ entangled, qubits 1,2,3,4)	0.593 ± 0.019	TBM [2]
21	$\|\Phi\rangle^{3}_{\text{GHZ}}$ (GHZ entangled, qubits 1,2,3)	0.693 ± 0.020	TBM [2]

Table 4.4: Measured fidelities for each of the prepared multiqubit states. For each state, the verification methods are given where, QST: quantum state tomography; EW: entanglement witness; TBM: two-basis measurement. In each case, [*] represents the required number of global measurement settings. In each measurement setting, 2^n n-fold coincidence events are recorded in the experiment, where n is the number of qubits. The Bell states for the qubits 1, 2 are not listed, but similar fidelities were observed as the qubits 3, 4, see section 4.1.5.2 for those fidelities. Note that the "heralded Bell" (no.7 & 8) refers to the probabilistic generation of qubits 2, 3 entangled states in the presence of joint clicks in photons 1 & 4. For the 4-photon and 3-photon GHZ states, an EW was measured by 5 measurement settings (no.17) and by 4 measurements (no.18), respectively, and we also implemented TBM by 2 measurements (no.20 & 21). The latter gains an efficient verification of GME with a slight reduction of fidelity due to the inaccuracy of fewer measurements. For the 2-photon entangled state $|\Phi\rangle^{2}_{\text{GHZ}} = |\Phi\rangle^{+}_{\text{Bell}}$, the full QST requires 9 global measurement settings (no.16) while TBM only requires 2 measurement setting (no.22). For larger GHZ entangled states, TBM provides a much efficient approach for GME verification. Up to eight SPSNDs are used to collect the data. All the error bars are calculated via a Monte Carlo simulation of the experiment assuming Poissonian statistics of photons.

within this thesis are adequate for small-scale photonic demonstrations for the first time, allowing the demonstration of high fidelity multi-photon operations on chip. However, demonstrations requiring multi-particle ($n > 2$) interference between many integrated sources will require increasingly optimised spectral purities. The reason for this can be seen from the following, suppose a pure bi-photon state $|\psi\rangle$ is generated of the form

$$|\psi\rangle = \int \mathrm{d}\omega_s \mathrm{d}\omega_i f(\omega_s,\omega_i)\hat{a}_s^\dagger(\omega_s)\hat{a}_i^\dagger(\omega_i)|\mathrm{vac}\rangle \tag{4.103}$$

where the joint spectral amplitude function $f(\omega_s,\omega_i)$ describes the spectral correlations between the signal and idler photons. Depending on the shape of f the photons are either entangled in the frequency domain or fully separable. In the case where the state is separable then each photon is found in a pure quantum state, and when they're entangled each photons density matrix is mixed. In the limiting case where the photons are fully correlated, the resulting reduced density matrix would give the maximally mixed identity operator on the Hilbert space $\rho_x = \hat{I}_x = \int \mathrm{d}\omega_x |\omega_x\rangle\langle\omega_x|$, where x denotes either the signal or idler photon, $x \in \{s,i\}$. One way to quantify this mixture is to measure the purity of the reduced density matrix for each photon, i.e. $P = \mathrm{Tr}(\rho_x^2)$ where ρ_x is obtained from the reduced trace $\mathrm{Tr}_{s/i}(\rho) = \rho_{i/s}$[14]. The measured purity will range from 0 to 1, where 0 is obtained when ρ is maximally entangled resulting in a reduced density matrix ρ_x that is maximally mixed, and 1 corresponds to the opposite case where ρ is separable and ρ_x is pure. This is a very similar (but numerically reversed) approach compared with the concurrence measure of entanglement as outlined in section 4.4.3[15].

By considering the spectral decomposition of the JSA $f(\omega_s,\omega_i) = \sum_k a_k g_k(\omega_s) \otimes h_k(\omega_i)$ which rewrites the bi-photon state as

$$\begin{aligned} |\psi\rangle &= \sum_k \int \mathrm{d}\omega_s \mathrm{d}\omega_i a_k g_k(\omega_s) \otimes h_k(\omega_i)\hat{a}_s^\dagger(\omega_s)\hat{a}_i^\dagger(\omega_i)|\mathrm{vac}\rangle \\ &= \sum_k a_k \Big(\int \mathrm{d}\omega_s g_k(\omega_s)\hat{a}_s^\dagger(\omega_s) \otimes \int \mathrm{d}\omega_i h_k(\omega_i)\hat{a}_i^\dagger(\omega_i) \Big)|\mathrm{vac}\rangle \\ &\equiv \sum_k a_k |g_k\rangle \otimes |h_k\rangle \end{aligned} \tag{4.104}$$

the reduced density matrices of the signal and idler photons can be written as

$$\begin{aligned} \rho_s &= \sum_k |a_k|^2 |g_k\rangle\langle g_k| \\ \rho_i &= \sum_k |a_k|^2 |h_k\rangle\langle h_k| \end{aligned} \tag{4.105}$$

[14] Here the '/' means 'or', i.e. tracing out the idler photon yields ρ_s.

[15] The concurrence is also a function of the purity of the reduce density matrix $\mathrm{Tr}(\rho_x^2)$.

where each photon has the same purity equal to $P_i = P_s = \sum_k |a_k|^4$ and is approximately 92% for our sources [98, 109]. Coincidentally though, the purity of the two reduced density matrices is the same as the probability that two photons from identical sources are found in the same spectral mode. This is to say that the purity of a heralded single photon is a good measure of the probability that they will interfere, since they only interfere when in identical photon state. Since the spectral purity of our sources is high, we see good visibility interference and high quality multi-qubit interactions that directly rely on this interference. However, the probability that n heralded photons from n identical sources are simultaneously in the same spectral mode evolves as

$$\begin{aligned} p(n \text{ photons in identical spectral mode}) &= \mathrm{Tr}\rho_s^n \\ &= \sum_k |a_k|^{2n} \end{aligned} \tag{4.106}$$

which significantly reduces for high n and its maximum value is the purity of the single photon state for $n \geq 2$. Despite this pessimistic viewpoint, theoretical work estimates that scalable quantum photonic architectures can be achieved with only a few photon interactions [69]. Therefore, further work must be done to improve the spectral purity by multiple significant figures. A likely approach to achieve this was outlined in reference [132] which proves that, in principle, advanced micro-resonators could achieve 0.999 spectral purity with few modifications. This above approach should be investigated to assess the ability to produce high quality photonic qubits on-chip.

4.5.1.2 Performance Limits of Probabilistic Single Photon Sources

All of the photonic demonstrations in this thesis take a 'repeat until success' approach. For example, multiphoton coincidence counts arise from multiple squeezed vacuum states, where the correct terms are post-selected at their detection but only happen a small percentage of the time. By integrating over large periods of time the correct state is post-selected a significant number of times to achieve the desired statistical significance. Equation 3.16 derives the probability p_{cc} that a signal and idler pair are detected as a 2-fold coincidence event, where multiphoton terms from each source are not discriminated, i.e. two pairs also constitutes as a click. The significant issue with this approach is that the probability that n pairs are simultaneously detected by different sources drops exponentially with n as p_{cc}^n. The way to combat this issue is through the multiplexing of sources, where each source is made up of m individual sources. Since each source is made up of a large amount of squeezed states the probability that at least one contains a photon pair that leads to a coincidence count is

$1-(1-p_{cc})^m$, which tends to unity as m becomes large even if the individual probability is small. These heralded photon states could then in principle be rerouted within the circuit if ultra-fast detection and switching were available. In fact, both high efficiency on-chip detection and high extinction ratio, high-speed all-optical switching could be possible within the next few years by leveraging on-chip resonators [171–173].

It is worth noting that despite the current lack of these technologies, there is still scope for progress with current techniques over the next few years. One key area of interest is that of boson sampling, the act of passing n photons through an m channel interferometer and computing the output counting statistics. It turns out this computation is classically very challenging and much progress has been made towards these demonstrations [174–181]. Along with recent development in high dimensional states on chip [12], another avenue for improvement will be the demonstration of multipartite high dimensional entanglement on chip, able to generate exponentially larger Hilbert spaces.

In order to test the limits of current technologies, we can create a simple simulation based on a few parameters. First, suppose we can tolerate a signal to noise ratio of 1/10, where 1/10 of the single photons contain multi-photon terms. The squeezing parameter $x_{0.1}$ at which this occurs can be calculated from equation 3.10 and evaluates as approximately $x_{0.1} \approx 0.3$. Suppose that the optimal coupling efficiency achievable with current technology is around $\eta = -6$ dB per channel, which is feasible with passive devices, state-of-the-art grating couplers and SNSPDs. Combine these parameters with gigahertz pumping rates, $R = 10^9$ Hz, and the expected number of n-fold events per second evaluates as $p_{cc}^n(\eta, x_{0.1}) \times R$, giving on average a single 10-fold event per minute. In order to check the feasibility of this experiment we must also estimate the number of individual detection events that occur per second, and see if they fall within the limits of current technology. Current state of the art time taggers can count approximately 10^8 detection events per second, where the simultaneous arrival of n photons must be post-processed from the recorded counts. The singles can be estimated per channel as a function of the squeezing strength x in a similar manner to equation 3.16. We need only the probability that n signal and idler pairs are produced $(1-x^2)x^{2n}$ as well as the probability that at least one photon gets measured $1-(1-\eta)^n$. Let a be the probability a photon is not detected $(1-\eta)$, then the singles probability is the sum over these terms

$$\begin{aligned} p_s &= (1-x^2)\sum_{n\geq 1} x^{2n}(1-a^n) \\ &= \left(1-\frac{(1-x^2)a}{1-ax^2}\right)x^2 \end{aligned} \quad . \tag{4.107}$$

The total number of singles is then $s \times 2 \times p_s \times R$ for s sources and R repetition rate. For a 10 photon experiment with the same channel loss and squeezing as above, the equation predicts approximately 24 million singles events per second. This is approaching the limit of what modern time taggers can handle but is certainly within current experimental scope. Based on the current technologies that are demonstrated within this chapter, it is reasonable to believe that a practical multiphoton experimental limit is approximately 10 photons, matching those of state-of-the-art off-chip experiments [57, 178]. Based on these calculations it is likely that this demonstration could be achieved on chip in the near future.

CHAPTER 5

CHIP-TO-CHIP QUANTUM COMMUNICATIONS WITH SINGLE PHOTONS IN SILICON

So far in this thesis we have explored several key areas of quantum information science with photons. Chapter 3 explores non-linear photonic states on chip, and assesses their approximation as single photon sources in the low squeezing regime. The particular focus was on the current state-of-the-art silicon photonics components and their performance. The main aim was to assess the visibility of on-chip quantum interference in a few different forms, one of the fundamental mechanisms of quantum information science. Chapter 4, however, explores how well these approximate single photon states can produce qubits, and what are their limitations. We explore linear-optic schemes able to perform single qubit measurements as well as explore the operation of key multi-qubit operations with 50% operational probability. In contrast with those previous chapters, the main aim of this section is to assess the ability to perform chip-to-chip quantum information measurements by utilising the same silicon photonic technologies and components. Here we develop two main methods, the first of which transports single qubit states with high fidelity between two chips via a path-polarisation interconnect, see section 5.1. Secondly, bi-photons are encoded in high dimensional qudit states and subsequently transmitted between chips by utilising advanced fibres and active phase stabilisation, see section 5.2. In the first approach, a path-polarisation interconnect is able to convert between the on-chip path encoding to a polarisation encoding inside the connected fibre. By utilising this method a single mode fibre is capable of coherently transferring a single qubit between chips, where the on-chip encoding is in optical path and the interconnect encoding is

in polarisation. In the second (high-dimensional approach) the > 2 optical modes can no longer map to orthogonal polarisation states, and therefore a different approach is required to complete the transfer. The approach presented in section 5.2 takes inspiration from reference [182] where qubits are transported in path encodings across a multi-core fibre. For each transport method a range of experiments are designed and verified between the transmitter and receiver circuits. In each case, all single photon generation takes place in a transmitter circuit and two different receiver circuits are designed to perform projective measurements on the transmitted photon state. These experiments should provide the reader with an appreciation for the potential of silicon quantum photonics technologies in the field of quantum communication applications, where the aim of this chapter is to demonstrate several proof of principle experiments that may become a key aspect of future communication protocols.

5.1 Chip-to-chip Entanglement Distribution and Quantum Teleportation via Path-to-Polarisation Interconnect

5.1.1 Motivation

In the previous chapter, state-of-the-art on-chip quantum information experiments show that silicon photonics is both a viable and a compelling platform for future advanced quantum information applications. In particular, high-quality identical qubits and high fidelity multi-qubit projections together allowed the demonstration of some of the highest fidelity teleportation seen in any platform [63]. This is an exciting result for the fields of quantum information processing, however, for communication applications chip-to-chip demonstrations are required. The goal of the following experiments within this chapter is to prove the feasibility of this chip-to-chip quantum state transfer for use in potential communication applications. The prediction is that, when combined with highly coherent chip-to-chip qubit transfer, the measured teleportation fidelity will remain significantly high such that it may be useful in many applications of quantum science [108]. On the other hand, a significant drawback of the proposed chip-to-chip schemes in this section are the relatively high coupling losses, which must be aggressively addressed in future work in quantum technologies.

In this section two main experiments are conducted. The first experiment is referred to as 'chip-to-chip entanglement distribution' and aims to demonstrate that two single photons can remain entangled across two separate silicon chips connected

only by a single mode fibre. In order to conduct this experiment, two non-degenerate single photons are initially generated on a transmitter circuit through the method outlined in section 4.1.5.2. Under this method, the two photons (one at signal frequency and the other at idler frequency) can be prepared in each of the four maximally entangled Bell pair states with high fidelity through the utility of an integrated single qubit unitary transformation and multiple single-qubit projector circuits.

In section 4.1.5.1 of this thesis, it was shown that each of these Bell pairs can be prepared and measured with high fidelities of above 90% on a single device. Here this experiment should be repeated, however, in this case the idler photon is transferred to a receiver circuit and two photon coincidence events are recorded between the two chips in an array of measurement settings in order to reconstruct the two-photon density matrix between the two chips. Here the single photons are transferred to the receiver device via a path-to-polarisation interconnect that comprises an integrated 2D grating coupler design, see section 3.1.1.4 for details.

The second experiment discussed within this section, is a 'chip-to-chip quantum teleportation' experiment. The details of the quantum teleportation protocol are initially explained in section 2.3.2 and an initial single-device experiment is reported in section 4.3 of this thesis. Here we repeat the findings of that experiment, but here we aim to transmit the teleported state to a secondary receiver chip where its density matrix is reconstructed through quantum state tomography. The desired outcome is that an initially prepared qubit on the transmitter device can be remotely transferred to the secondary device through the quantum teleportation protocol.

5.1.2 Results

5.1.2.1 Entanglement Distribution

As an introductory proof-of-concept experiment, two entangled signal and idler photons are prepared in one of the four Bell states through the method outlined in section 4.1.5.2 of this thesis. In contrast to that section (where both photons are measured on one chip), the goal here is to measure entangled qubits between two separate devices in a similar fashion to the work by Wang *et al.* explored in reference [108][1]. In this work, the authors were able to initially demonstrate a two photon Bell state on a single transmitter, and later transfer one of the photons to another device such that one

[1]In the stated reference, the authors explore chip-to-chip entanglement distribution through the verification of a Bell test. However, in this demonstration we will go beyond this result to fully reconstruct the two-photon density matrices between the two devices. In addition, we will show this result for each of the four Bell states compared with the single state achieved in the aforementioned reference.

photon on each chip remain entangled. This entanglement distribution experiment was verified by the authors through a Bell measurement [183] and quantum interference fringes between the two chips.

Since the two entangled photons are originally created and encoded on a single chip, a highly coherent qubit transfer link must be utilised in order to successfully achieve the chip-to-chip entangled state, see section 3.1.1.4. The probabilistic generation of Bell states encoded in optical path has become a useful benchmark throughout this thesis due in part to its low resource demands, requiring the alignment of only two sources, two SNSPDs detectors (measuring two-fold coincidence events) and only single qubit unitary and projector circuits. In addition to the low resources required, the measured joint probabilities of Alice and Bob's measurement outcomes given their choice of measurement setting is a good figure of merit for the preserved coherence between the two qubits.

The specific goal in the experiment is to prepare each of the four maximally entangled Bell states on the transmitted device, and in each case to send the photon which encodes qubit C to the receiver device (see figure 5.1a for labeled qubit modes). Qubit B is then measured on the transmitter (Alice) and the third qubit is measured on the receiver (Bob). Here measured means that the measurement settings are chosen and set on those particular devices, before being sent to off-chip SNSPDs for coincidence detection. In this scenario Alice's measurement settings are denoted X, while Bob's is denoted Y.

Figure 5.1a shows the chip schematic for this experiment, where each of the output modes are labeled corresponding to the qubit logical modes. Note that the final qubit (subscript C/R) may be measured on a single device, in which photons are collected from output modes $0_C/1_C$ or from the receiver device, where photons are collected from output modes $0_R/1_R$. Two switches formed by two individual MZIs control whether the photons are measured on which device. In order to first demonstrate the entanglement distribution experiment, only the lower two rings are pumped (equally and coherently) to produce the initial entangled state, which is successfully detected when only two photons arrive at the qubit output modes B and C. When in this configuration, the general state evolution is shown in figure 5.1b labeled as 'Entanglement Distribution'. Each of the projectors, highlighted pink on the schematic, are set such that Alice and Bob each measure one of the Pauli operators $X, Y \in \{\hat{\sigma}_x, \hat{\sigma}_y, \hat{\sigma}_z\}$. The chip projector phases that Alice and Bob each need to set per measurement are summarised in figure 4.1 and explained in section 4.1.2. As outlined in section 4.1.3, by measuring the normalised coincidence counts across the two chips (across four mode permutations), one may estimate the joint probability functions and reconstruct the two qubit density

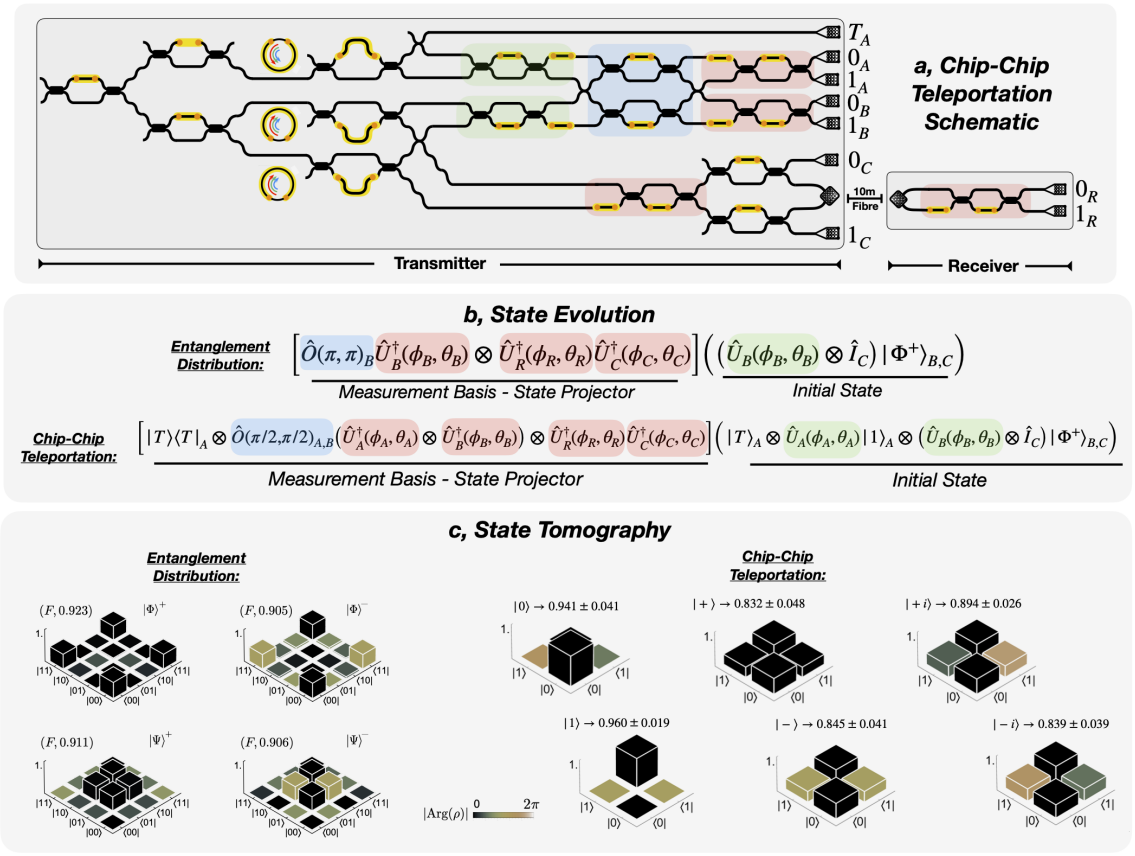

Figure 5.1: Chip-to-chip quantum teleportation experiment. **a**, teleportation and entanglement distribution schematic featuring the transmitter and receiver design. Here the transmitter circuit is almost identical to the earlier single-chip design, but comprises an additional path-polarisation converter design for qubit C. **b**, state evolution of the two qubit entangled state (top) or three qubit teleportation scheme (bottom). **c**, reconstructed density matrices of (left) all four Bell states measured between two chips (right) the six measured chip-to-chip teleported states. The fidelities of each result compared with the expected result is shown to the top of each density matrix. Errors in each case are calculated via Monte-Carlo simulation assuming poissonian counting statistics.

matrix as ρ_{meas}.

The fidelity between the target Bell state and ρ_{meas} is a good quantifier for the coherence between the two chips, since a statistical mixture will give optimal population terms but zero coherence terms (see sec 4.4 for more info) giving $F = 0.5$ and a perfectly coherent Bell state transfer will give $F = 1$. The single-chip measured fidelities do not reach the fidelity limit $F = 1$, however, and one is thus limited by about 93% state fidelity on average (see sec 4.2). As a result, fidelities that are measured above 90% result in approximately zero chip-to-chip decoherence when compared with the single device results. The measured reconstructed density matrices for the four Bell states are shown in figure 5.1c and are labeled 'Entanglement Distribution'. The measured chip-to-chip state fidelities are summarised in table 5.1 and present an average measured fidelity of 0.911 ± 0.019. Remarkably, on average, these fidelities fall just within the single sigma significance of the average single chip measured fidelities which gave 0.937 on average. As a result, the chip-to-chip distribution of entanglement gave very little decoherence when compared with the single chip result - owing to the high quality path-polarisation interconnect, see section 3.1.1.4.

The main caveat with this approach was the additional transmission losses endured by the two-dimensional grating couplers that form the path-polarisation interconnect - see section 2.5.9 and 3.1.1.4 for details. The estimated additional single photon losses caused by the switch to the two-dimensional couplers was approximately -5 dB per coupler. This value was measured by comparing the difference in maximum optical power between port 0_C (1D grating) and directly from the transmitter two-dimensional coupler. In addition, the total transmission through the receiver chip was approximately -14 dBm with input power 0 dBm, which suggests that the total chip-to-chip coupling decreases by 19 dB by transitioning to the multi-device setup[2]. As a result, the measured coincidence two-photon counts between the two chips are suppressed by almost two orders of magnitude when compared with the single chip demonstrations, since the single photon that encodes qubit C is transmitted through the multi-device setup.

5.1.2.2 Chip-to-Chip Quantum Teleportation

For the teleportation experiment, qubits B and C are once again prepared in the $|\Phi^+\rangle_{B,C}$ state and qubit A is prepared in one of the eigenvectors of the three Pauli matrices. The overall state evolution is almost identical to the one outlined in section 4.3 with the addition of the MZI switches to the second chip. The general state

[2]Here the extra -5dB losses arise from the switch to a two-dimensional grating coupler on the transmitter chip.

Expected State	Measured Fidelity
$\|\Phi^+\rangle$	0.923 ± 0.027
$\|\Phi^-\rangle$	0.905 ± 0.015
$\|\Psi^+\rangle$	0.911 ± 0.019
$\|\Psi^-\rangle$	0.906 ± 0.014

Table 5.1: Summary of the chip-to-chip entanglement distribution state fidelities between each of the target (expected) states and the reconstructed density matrices.

evolution for this experiment is shown in figure 5.1b. When the switches are turned on (and the optical phase shift is set to π), each optical path picks up the same global phase from the MZI and so the net effect is not measurable to the transported qubit. In this chip-to-chip configuration, the projector $\hat{U}_C^\dagger$ is configured to the identity. Instead, the projector $\hat{U}_R^\dagger$ projects the qubit onto each eigenbases in order to construct the measured density matrix via the quantum state tomography. The chip projector phases that Alice and Bob each need to set per measurement are summarised in figure 4.1 and explained in section 4.1.2.

The projection onto the teleported state occurs (see sections 4.39 & 4.3) only when heralding the simultaneous arrival of single photon detection events in the following optical mode permutations $\{T_A, 0_A, 1_B, 0_R/1_R\}$ and $\{T_A, 1_A, 0_B, 0_R/1_R\}$. In each case, four-fold coincidence counts are measured in order to infer the relative probabilities of detection in the $0_R/1_R$ optical modes, where the "/" means that both measurements are valid and are necessary to reconstruct the density matrix. As in the case of the single device experiment, for any prepared qubit $|\psi\rangle_A$ the reconstructed state is in fact $\hat{\sigma}_x|\psi\rangle_A$ due to the chosen Bell state projection. The reconstructed density matrices are shown in figure 5.1c and are represented as the six single qubit density matrices shown right. For each target state, the measured fidelity and errors are summarised in table 5.2. When compared with the single device results, the average fidelity was found to be 0.885 ± 0.036, compared with 0.906 ± 0.034 achieved on a single device. Again, these results fall within a few percent and are indistinguishable within one standard deviation of statistical significance.

In order to put these results into more context, and to further quantify their significance, a good figure of merit is the comparison between the average teleportation fidelity and the classical limit. More specifically, the 'classical limit' here means the fidelity at which one could cheat the teleportation by guessing the input state[3] $|\psi\rangle$ based on a quantum measurement in some basis, and then remotely prepare the

[3] i.e. the state to be teleported to the receiver.

Expected State	Measured Fidelity
$\|0\rangle$	0.941 ± 0.041
$\|1\rangle$	0.959 ± 0.019
$\|+\rangle$	0.832 ± 0.048
$\|-\rangle$	0.845 ± 0.041
$\|+i\rangle$	0.894 ± 0.026
$\|-i\rangle$	0.839 ± 0.039

Table 5.2: Summary of the chip-to-chip quantum teleportation state fidelities between each of the target (expected) states and the reconstructed density matrices.

guessed state on the receiver. Since the qubit is encoded in a single quantum particle, any attempt to perform the cheating collapses the state (via measurement) into the measured eigenvalue. Therefore an infinite ensemble of identical $|\psi\rangle$ states is required to perform a perfect cheating protocol.

The optimal average fidelity based on the single-shot cheating approach is 2/3, and is limited by the optimal information one can learn from a single quantum measurement of a qubit state [184]. For a single qubit, the classical limit is also equivalent to the cloning limit due to the no-cloning theorem [185] which states that a single quantum system cannot be accurately measured or reproduced. Quantum teleportation is able to defy this 2/3 limit through the simultaneous destruction and remote preparation of the original quantum state itself, and can in principle reach unity fidelity. As a result, any teleportation result able to remotely reproduce a single qubit state with higher than 2/3 fidelity must truly be quantum and cannot be reproduced classically.

The following compares the average number of standard deviations (estimated through Monte-Carlo simulations) above the classical limit that these experiments were able to achieve. For the single chip results, on average the teleported states violated the classical limit with 7σ significance. The minimum measured violation was the minus state with approximately 5σ. As for the chip-to-chip results, the average violation was 6 standard deviations, with the minimum individual state violation of 3.5σ. These results show that the reconstructed states were remotely prepared via the destructive Bell state measurements firmly above the limit that can be achieved classically or via optimal cloning. Therefore the on-chip quantum teleportation scheme developed in this thesis is a fundamentally useful quantum resource, which outperforms the optimal classical schemes with high statistical significance.

5.2 High Dimensional Entanglement Distribution

5.2.1 Motivation

Qubits that are composed from single photons in linear optical circuits are a great platform for high fidelity quantum information processing. This fact combined with light-speed travel makes photons an ideal candidate for long-range quantum information carriers in communications. In light of the previous experiments in this thesis, a substantial goal for ongoing research in this field is to produce and control increasingly complex quantum photonic systems on a chip. A natural approach to categorise the size of available quantum states on a chip is to compare the size of the available Hilbert space one is able to control, which grows exponentially for n photons in d dimensions as d^n. This essentially gives two key avenues for near-term improvements in on-chip complexity. For integrated photonic systems in particular, the ability to arbitrarily increase n is a challenging problem due to the current reliance on parametric single photon sources, since the ability to simultaneously produce n photons scales poorly with n. This forms the main short-term bottle-neck for on-chip quantum information processing with photons, though I remain optimistic that this bottleneck will be removed in the long-term - and will require improvements in many key areas as discussed in section 3.2.1. For short-term demonstrations, however, scaling the number of local dimensions d is far more ideal. The main challenge for this approach is to control smaller numbers of high quality single photons through large linear optic networks, and has been demonstrated in silicon with high success [12, 182] and in many other platforms [53, 186–190].

Short-term innovations, in particular, should focus on the engineering of high speed electronics, increased number of integrated components, suitable external control and integration of large numbers of single photon detectors. The miniaturisation and specialised electronic hardware will be a key milestone in delivering near-term complexity breakthroughs. The route to achieving high dimensional entangled states in integrated photonics has been partially mapped out and verified by utilising two key approaches [12, 187]. The key advantage of reference [12] is the use of path encoding that allows highly coherent and high fidelity measurements, showing two photon states in up to 15 dimensions. A drawback to this approach is the inevitable increase in on-chip complexity and device footprint for large d. Reference [187] is able to avoid this large footprint by utilising frequency encoding, but the results require off-chip ultra-fast electronics and their results obtain significantly lower overall fidelities compared with the former approach. As we will see in the following sections of this

thesis, it is crucial that these measured fidelities remain very high (typically at least 90%) in order to benefit from states which cannot be achieved by multiplexing smaller dimensional systems.

On the theoretical side, a growing body of work shows the potential use-cases of high dimensional states, such as high dimensional quantum teleportation [191] and hyper-entangled deterministic bell state analysis [158]. A particular area of interest is that of quantum communications, where high dimensional systems have been shown to simultaneously aid in higher noise tolerances and increase information density [41]. Increasing the physical encoding of quantum information into many dimensions may be a practical approach to dealing with low key-rates in QKD, for example [192]. In recent work, high dimensional QKD was achieved in silicon photonics by utilizing weak coherent pulses [182]. This approach opens the door to more advanced QKD systems built using silicon photonics, where utilising high-dimensional chip-scale multi-party networks would be the ultimate goal. The key bottle-neck with this approach however is the lack of phase stability between the two chips.

The chip-to-chip quantum teleportation results in this thesis avoided this issue due to the phase stability of the path-polarisation conversion technique that transferred the single qubit, since the superposition states travel along the same optical fibre. The transfer of high dimensional systems encoded in path between chips, however, will require a different approach. The verified approach in reference [182] is to connect the two devices via a multi-core fibre, which minimises the relative phase drift between optical paths since the single photons travel along very similar optical paths. Although, despite the use of advanced fibres, the authors still report phase instability in their system. Another key drawback with the above implementation is the limitation of weak coherent pulses, which are useful in many QKD protocols, but in general carry many high-order photon number terms and limit the applications of the technology.

In the following experiments in this thesis, the idea of chip-to-chip high dimensional entanglement generation and verification is explored. The ultimate goal is to certify that high dimensional entangled states may be reliably transferred between integrated silicon devices with high coherence. The idea is that this approach may soon be applied to devices of increasing complexity and open the door to many near-term quantum information protocols.

5.2.2 High Dimensional State Preparation

As mentioned in the previous section, recent experimental work outlines a novel scheme to produce arbitrary d-dimensional entangled states encoded in optical paths

on-chip. In general, the scheme shows that these entangled states are achieved via the coherent superposition of bi-photon states that are spatially de-multiplexed on-chip. In fact, the generated state has complexities which are set aside in the demonstration, but in the context of this thesis should be mentioned. The aforementioned scheme generates photonic states from the preparation of d multi-mode twin-beam squeezed states, where the entanglement generation arises upon the post-selection of bi-photon states in the scenario where the vacuum substantially dominates.

The mathematical analysis in this section begins under the direct assumption that these bi-photons can be efficiently post-selected from the initial multi-mode squeezed state. This assumption avoids the difficulty and complexity of evaluating the large tensor product of squeezed states written in the Fock basis, see section 3.2.1 for more information. In the following, we operate under the condition where only terms with order $O(1)$ in photon-number will be post-selected in the low squeezing regime, see appendix B.2 for details of this approximation. This assumption relies on the fact that the amount of squeezing is easily controlled (through pumping strength) and measured where high order terms are approximately negligible. It is through this guiding principle which forms an abstraction layer, moving from complex photonic states to simple Fock states that can be more easily mathematically manipulated. In light of the previous chapter, this assumption is particularly accurate when one is required only to count bi-photons and not the simultaneous arrival of $n > 2$ photons, as is the case in this proposed experiment.

In this proposal, bi-photon high dimensional qudit states are generated on chip via the coherent pumping of up to four MRR sources. Each of the sources are well spectrally overlapped and are locked to a centre wavelength (at the pump resonance) of approximately $1549.3nm$. A CW pump laser at the pumping wavelength is fixed and its optical power is split evenly between each of the four sources via the control of three MZI. When written in the Fock basis, the generated state is the tensor product of n multi-mode twin-beam squeezed states, where n is the number of MRR sources pumped. In the low pumping regime, where the squeezing inside each MRR is sufficiently low, the probability of producing bi-photon states dominates and the probabilities of higher order photon-pair states is diminished. In the cases where a two-photon coincidence event occurs (one for each the signal and idler photon)[4], the vacuum term is post-selected away (see section B.2) and the resulting state is the high dimensional entangled state with high fidelity. The above statement holds precisely when the produced bi-photon states are identical, as elaborated in the case of Bell pairs in section 3.2.4.1 and verified experimentally with high ($> 90\%$) fidelity several

[4]Achieved via off-chip filters, see section 3.2.3 on counting single photon coincidence events.

times in the thesis, see sections 3.3.4 and 4.1.5.2. The aim, then, is to produce the maximally entangled states $|\psi_d\rangle$ in three and four dimensions, $d = 3,4$, where

$$|\psi_d\rangle = \frac{1}{\sqrt{d}} \sum_{k=0}^{d-1} |i,i\rangle_{A,B}\,, \tag{5.1}$$

and where d in this specific proposal is equivalent to the number of equally and coherently pumped identical MRR sources. The full state, however, is approximately the superposition of d bi-photons, which in the case that $d = 4$ may be written in terms of the creation operator $\hat{a}^{\dagger}_{\lambda,q,m}$ of single photons at wavelength $\lambda \in \{\lambda_s, \lambda_i\}$, qudit $q \in \{A,B\}$ and spatial mode $m \in \{0,1,2,3\}$

$$\begin{aligned}\frac{1}{2}\Bigg[&\int_{\lambda_s,\lambda_i} f(\lambda_s,\lambda_i)\hat{a}^{\dagger}_{\lambda_s,A,0}\hat{a}^{\dagger}_{\lambda_i,B,0}\mathrm{d}\lambda_s\mathrm{d}\lambda_i + \int_{\lambda_s,\lambda_i} f'(\lambda_s,\lambda_i)\hat{a}^{\dagger}_{\lambda_s,A,1}\hat{a}^{\dagger}_{\lambda_i,B,1}\mathrm{d}\lambda_s\mathrm{d}\lambda_i \\ &+ \int_{\lambda_s,\lambda_i} f''(\lambda_s,\lambda_i)\hat{a}^{\dagger}_{\lambda_s,A,2}\hat{a}^{\dagger}_{\lambda_i,B,2}\mathrm{d}\lambda_s\mathrm{d}\lambda_i + \int_{\lambda_s,\lambda_i} f'''(\lambda_s,\lambda_i)\hat{a}^{\dagger}_{\lambda_s,A,3}\hat{a}^{\dagger}_{\lambda_i,B,3}\mathrm{d}\lambda_s\mathrm{d}\lambda_i\Bigg]|\mathrm{vac}\rangle\,,\end{aligned} \tag{5.2}$$

where each of the functions $\{f, f', f'', f'''\}$ describe the spectral correlations between single photons that are produced within the twin-beam. However, each of the four MRR single photon sources are designed (and experimentally overlapped) to be identical, and hence in the special-case where each of the MRR are identical and pumped equally, each of the correlation functions are equal and state can be efficiently factorised as

$$\int_{\lambda_s,\lambda_i} \mathrm{d}\lambda_s\mathrm{d}\lambda_i f(\lambda_s,\lambda_i)\big(\hat{a}^{\dagger}_{\lambda_s,A,0}\hat{a}^{\dagger}_{\lambda_i,B,0} + \hat{a}^{\dagger}_{\lambda_s,A,1}\hat{a}^{\dagger}_{\lambda_i,B,1} + \hat{a}^{\dagger}_{\lambda_s,A,2}\hat{a}^{\dagger}_{\lambda_i,B,2} + \hat{a}^{\dagger}_{\lambda_s,A,3}\hat{a}^{\dagger}_{\lambda_i,B,3}\big)|\mathrm{vac}\rangle\,. \tag{5.3}$$

Once factorised in this way, the shape of the spectral function becomes irrelevant to the joint statistics achieved by counting the pairs of signal-idler coincidence events across different combinations of spatial modes. This can be seen trivially in the computational basis, since each integrand gives rise to counting statistics that perfectly match the target state $|\psi_4\rangle$ encoded in path. As a result, in this experiment, one expects an upper limit of fidelity in line with previous bi-photon experiments such as the time-reversed HOM and Bell state measurements. In fact, one should expect that the measured fidelity of this high dimensional state is upper bounded by these former results. This is expected since here we require that each of four MRR simultaneously produce joint spectra that are identical to one another, where in previous bi-photon experiments only two of the MRR were required to be identical.

A suitable lower bound for the expected fidelity should be that of the previous four-photon experiments which not only required identical joint spectra across the four MRR but also required single-mode behaviour, which is not required in this experiment.

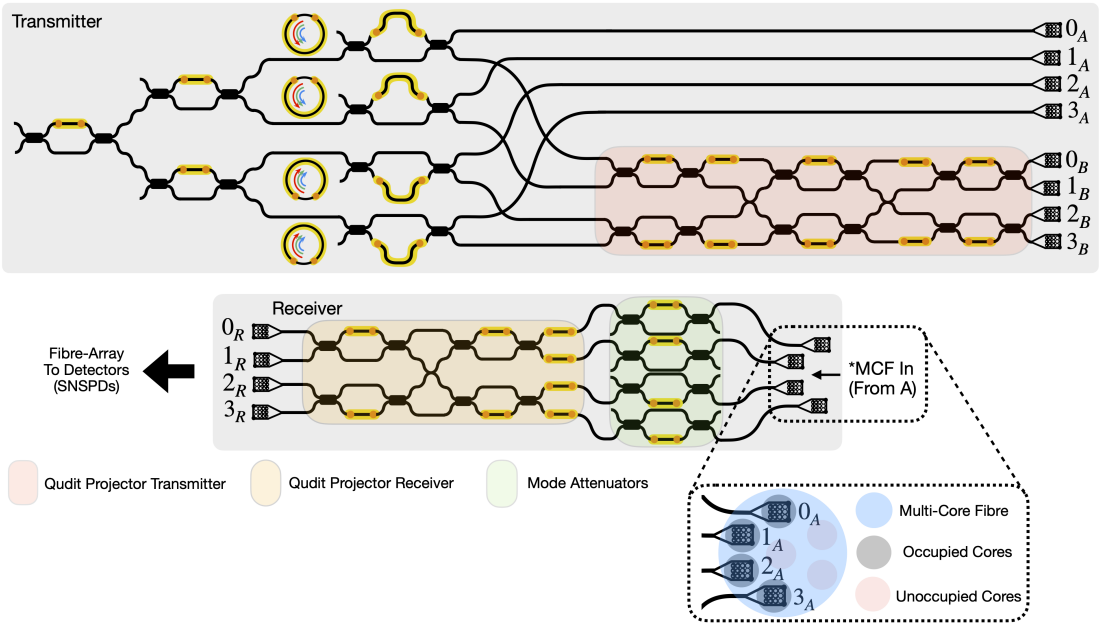

Figure 5.2: High dimensional entanglement setup. Transmitter device, comprised of four MRR single photon sources split across eight spatial modes which form two qudits of up to four dimensions. The transmitter device contains one high dimensional state analyser circuit highlighted in pink. Qudit A couples initially to a VGA, and then to a multi-core fibre. The receiver chip, shown below, is designed with four grating couplers spaced to perfectly match four of the cores of the 7-core fibre. Inset image shows how this works in practice and highlights the utilized optical modes. Each of the numbered optical modes match the transmitter output modes for clarity. The receiver is designed with four MZI attenuators to balance the signal in each of the modes, required due to uneven losses across the different spatial modes. The remainder of the circuit forms a high-dimensional state analyser, with a similar design to the transmitter device and is highlighted in yellow. Output modes 0_A and 0_R are connected to off-chip SNSPDs and detect two-photon coincidence events in a given time-window.

In light of this prediction, the optimal expected fidelities should approximately lie in the range $80-95\%$. Due to the counting of only bi-photons, for this experiment a CW pump configuration was chosen to optimise the number of coincidence events at low pumping.

5.2.3 High-dimensional Device Design

Figure 5.2 shows the multi-device schematic comprised of a 2 ququart (4D) transmitter chip design and a single ququart receiver circuit. Each qudit is encoded in single photons produced by one of four integrated MRR single photon sources. Qudit A (top) is encoded by the signal photon and qubit B (bottom) is encoded by the idler photon,

each simultaneously produced by the SFWM process inside the MRR sources. The transmitter is designed to produce two entangled photons of up to four dimensions. Qudit B (labeled in the figure) houses an additional measurement stage, whilst qudit A is transferred directly to the secondary receiver device via a fibre-array and multi-core fibre.

The inclusion of a 7-core fibre (see figure 5.2 inset image) allows four of the cores to be perfectly aligned with the four on-chip grating couplers for chip-to-chip state transfer. Since photons in different spatial modes travel along the same fibre, passive phase stabilisation between each of the eigenvectors is maximised. Measurements of qudit A are made on the receiver circuit where the output labels are measured. All eight output modes of the transmitter chip are initially coupled to separate single-mode fibres through an 8 channel fibre array (angle from chip normal is 15 degrees), where the four top modes are additionally coupled to the multi-core fibre.

For each of the following experiments, two SNSPDs are coupled to the output modes 0_R and 0_B, and the projective measurements in different bases are obtained by the local qudit projector circuits highlighted in pink and yellow on the schematics. For a mathematical justification of the receiver design in the context of 4D qudit projections, see section 5.2.4. Additional spatial mode attenuators are provided on each optical path of the receiver device, so that each channel gains a similar optical transmission. Additional off-chip $\approx 30cm$ delay-lines are utilized between devices in order to temporally overlap the single-photon states between each optical path of qudit A. The inset image of figure 5.2 shows the alignment of the multi-core fibre, where four cores of a seven-core fibre are utilised to transfer the qudit state. Four of the fibre cores are well aligned with the on-chip grating couplers, enabling efficient path-path state transfer. The specific state generation and evolution will be discussed in the following sections.

5.2.4 High-dimensional Projectors

The previous section shows how high dimensional entangled states can be generated on device via the coherent superposition of identical single photons in many optical modes. Though the above approach specifically targets four-dimensional systems, the general scheme may be arbitrarily expanded for d-dimensional systems via the multiplexing of many identical sources and linear optic circuits. The focus during this section is the necessary linear-optic requirements that measuring these four-dimensional entangled states entails.

Universal linear-optic circuits able to perform arbitrary transformations on d

optical modes have been shown and experimentally verified [6]. The largest drawback of these schemes is the relatively large resource requirements, where high numbers of active components are required. The approach in this experiment is to provide circuits that are able to perform arbitrary projective measurements on four-dimensions, but that are not necessarily universal in their approach. This resource decision is particularly crucial in this experiment, since the chip-to-chip coupling efficiency should be kept as high as possible, and where the introduction of each linear optic component on-chip is estimated to produce approximately 0.5 dB of optical loss. The approach of the receiver circuit design utilised in this experiment is based on the similar scheme shown in reference [12] and equivalent to reference [182].

The design of the 4-dimensional receiver shown in figure 5.3a can be intuitively justified, since it is comprised of block-diagonal forms of the two-dimensional projectors circuits. Here block-diagonal refers to the optical matrix transformation, since operations on modes 1&2 do not affect 3 or 4, for example. When combined with the swapping of waveguide modes via the integrated waveguide crossers, the circuit should allow for the projection of all combinations of complex superposition amplitudes, i.e. all possible 4-dimensional qudit eigenstates. For example, take the arbitrary normalised eigenvector composed of four complex amplitudes, $|\psi\rangle = (\alpha, \beta, \gamma, \delta)^T$. In order to perform a measurement of this vector, the projector phases should be set such that $U_4^\dagger |\psi\rangle = (1,0,0,0)^T$. The receiver circuit could project in this way by first considering the qubit subspaces $(\alpha, \beta)_a^T$, $(\gamma, \delta)_b^T$ and then forming the mapping $(\alpha, \beta)_a^T \rightarrow (\cos\theta, 0)_b^T$ and $(\gamma, \delta)_b^T \rightarrow (\sin\theta, 0)_b^T$. Here the $\cos\theta$, $\sin\theta$ correspond to the fact that the subspaces are not each normalised, since they actually belong to part of the four-dimensional space and are therefore together normalised, i.e. such that $(\sin\theta, 0, \cos\theta, 0)^T$ is correctly normalised. From here, the projection into the computational basis could be achieved by swapping the waveguide modes and performing one final 2-mode projection.

In order to show that this argument truly holds, a more accurate analysis must be derived. The full transformation matrix that describes $\hat{U}_4^\dagger$ can be derived by looking at the on-chip state evolution for an arbitrary heater configuration. Figure 5.3a shows the circuit schematic in terms of the device components. Each of the components can be decomposed into a set of four time-ordered state evolutions whose time ordering is given in figure 5.3a and explicitly shown in figure 5.3b. Each of the block-diagonal solutions are taken from the previous work on 2-mode projectors that are summarised in figure 4.1. The four matrices are multiplied together to give the general projector which is shown in figure 5.3c.

The goal now is to show that this general transformation matrix can be configured to project the eigenvector $|\psi\rangle$ into the computational basis. A natural way to show this

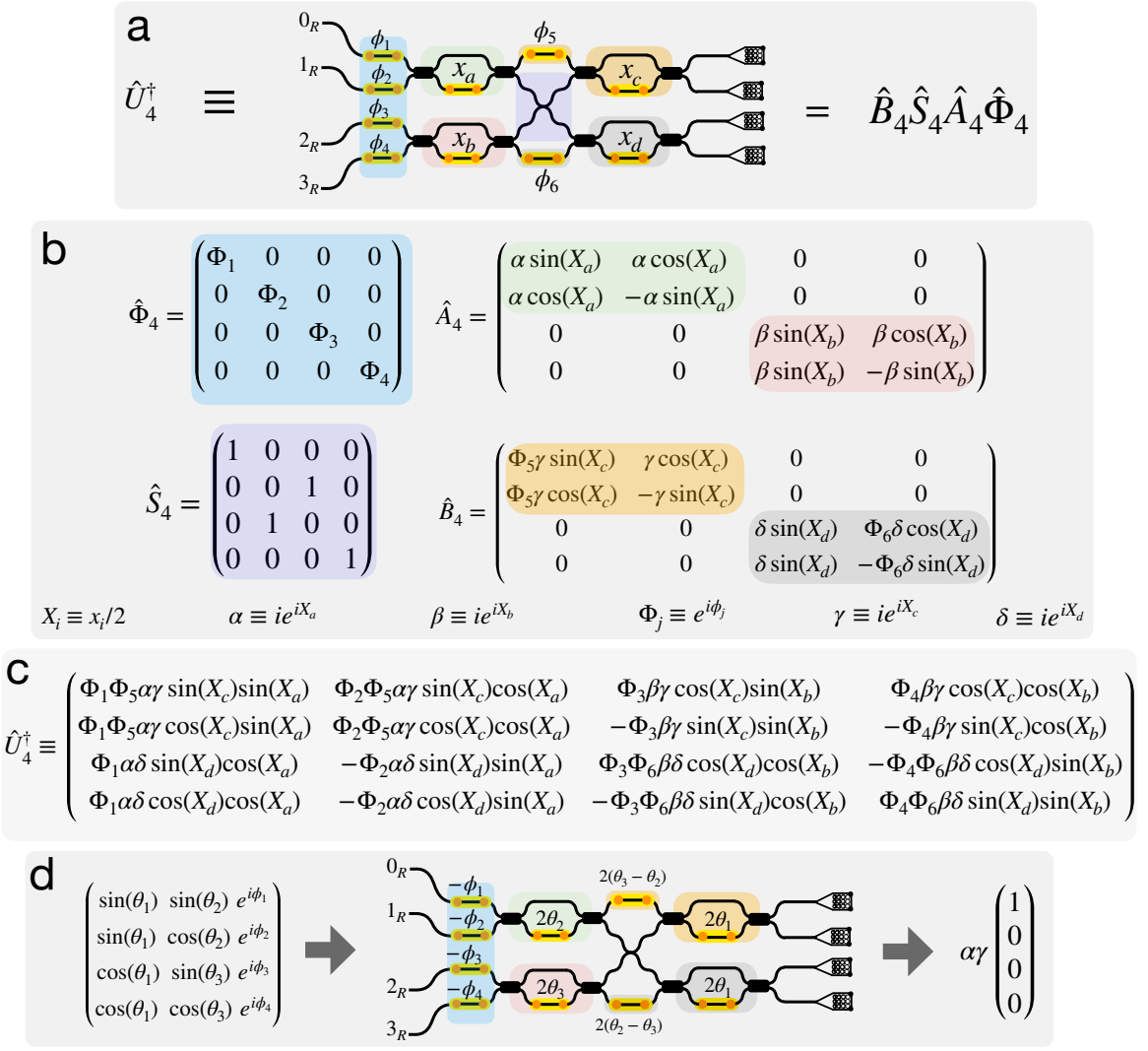

Figure 5.3: Four-dimensional projector circuit. **a**, the on-chip linear-optical components and schematic, which can be decomposed into four evolution matrices. Each of the labels correspond to the applied optical phase shift in the corresponding phase shifter. **b**, each of the time-ordered state transformations where the colour encoding matches the chip components in **a**. Below each of the matrices, the variables are defined in terms of the on-chip phases. **c**, full general transformation matrix for the 4D projector circuit. **d**, the general four-dimensional state as defined left can be projected into the computational basis via the labeled phase settings.

is to write the eigenvector not in terms of independent amplitudes $|\psi\rangle = (\alpha, \beta, \gamma, \delta)^T$ but in terms of the real parameters $\{\theta_1, \theta_2, \theta_3, \phi_1, \phi_2, \phi_3, \phi_4\}$ which gives the general normalised state in terms of coupled parameters

$$|\psi\rangle \rightarrow \begin{pmatrix} \sin(\theta_1)\ \sin(\theta_2)\ e^{i\phi_1} \\ \sin(\theta_1)\ \cos(\theta_2)\ e^{i\phi_2} \\ \cos(\theta_1)\ \sin(\theta_3)\ e^{i\phi_3} \\ \cos(\theta_1)\ \cos(\theta_3)\ e^{i\phi_4} \end{pmatrix}. \tag{5.4}$$

When written in this form, the optimal phase values in order to project the eigenstate $|\psi\rangle$ into the computational basis (specifically the $(1,0,0,0)$ state) can be obtained by multiplying the matrix $\hat{U}_4^\dagger |\psi\rangle$. The optimal values[5] are found to be $\Phi_{1,2,3,4} = e^{-i\phi_{1,2,3,4}}$, $\Phi_5 = e^{2i(\theta_3 - \theta_2)}$, $\Phi_6 = e^{2i(\theta_2 - \theta_3)}$, $x_a = 2X_A = 2\theta_2$, $x_b = 2X_B = 2\theta_3$ and $x_c = 2X_C = x_d = 2X_D = 2\theta_1$. Figure 5.3d summarises these optimal values and maps them to the receiver schematic. Hence, in principle, any eigenvector can be mapped in this way. In practice, the projection of any particular state is achieved by first mapping the state to the parameters $\{\theta_1, \theta_2, \theta_3, \phi_1, \phi_2, \phi_3, \phi_4\}$, once this is achieved the chip configuration can immediately be found.

A protocol to efficiently achieve this mapping is the following. Suppose the desired eigenstate is $(\alpha, \beta, \gamma, \delta)^T$. First, find each of the complex phases $e^{i\phi_j}$, each of which can be obtained directly from the argument of the complex amplitudes $\{\alpha, \beta, \gamma, \delta\}$[6]. Since the complex arguments are now taken care of, the trigonometric parts of the expression, $\{\theta_i\}$, need only describe the absolute values of the state, and so their domain is limited to $(0, \pi/2)$. The remaining elements can now be determined by the following relations,

$$\begin{aligned} \theta_1 &= \arcsin\left(\sqrt{|\alpha|^2 + |\beta|^2}\right) \\ \theta_2 &= \arcsin\left(|\alpha| / \sin\theta_1\right) \\ \theta_3 &= \arcsin\left(|\gamma| / \cos\theta_1\right). \end{aligned} \tag{5.5}$$

By utilising the above method arbitrary four-dimensional bases can be measured on chip by projecting into each of the eigenvectors in turn, where the associated measurement probability that the generated state is found in the measured eigenvector $p = \langle\psi|\,\rho\,|\psi\rangle$ are estimated from the normalised coincidence counts in that configuration.

An alternative approach is to simultaneously measure the relative probabilities of multiple eigenvectors. This can be achieved by finding the set of eigenvectors

[5] See figure 5.3 for definitions

[6] Take the arctan of the ratio of imaginary and real components, i.e. $\arctan(\mathrm{Im}\alpha/\mathrm{Re}\alpha)$

$\{|\psi_1\rangle, |\psi_2\rangle, |\psi_3\rangle, |\psi_4\rangle\}$, who form an orthonormal basis set

$$\hat{M} \equiv \left(|\psi_1\rangle, |\psi_2\rangle, |\psi_3\rangle, |\psi_4\rangle\right), \tag{5.6}$$

which can be mapped to the other optical ports such that $\hat{U}_4^\dagger \hat{M}$ yields the identity on four dimensions $\hat{I}_4$ up to some local phases. Such four states should be constructed similarly via the same seven real parameters $\{\theta_1, \theta_2, \theta_3, \phi_1, \phi_2, \phi_3, \phi_4\}$, such that the resulting four vectors form a complete set of orthonormal basis vectors in four dimensions. The found general orthonormal vectors $|\psi_{1/2/3/4}\rangle$ form the basis $\hat{M}$, where each of the four orthonormal vectors are defined as follows

$$\begin{aligned}
|\psi_1\rangle &\equiv \begin{pmatrix} \sin(\theta_1)\,\sin(\theta_2)\,e^{i\phi_1} \\ \sin(\theta_1)\,\cos(\theta_2)\,e^{i\phi_2} \\ \cos(\theta_1)\,\sin(\theta_3)\,e^{i\phi_3} \\ \cos(\theta_1)\,\cos(\theta_3)\,e^{i\phi_4} \end{pmatrix}, \qquad |\psi_2\rangle \equiv \begin{pmatrix} \cos(\theta_1)\,\sin(\theta_2)\,e^{i\phi_1} \\ \cos(\theta_1)\,\cos(\theta_2)\,e^{i\phi_2} \\ -\sin(\theta_1)\,\sin(\theta_3)\,e^{i\phi_3} \\ -\sin(\theta_1)\,\cos(\theta_3)\,e^{i\phi_4} \end{pmatrix}, \\
|\psi_3\rangle &\equiv \begin{pmatrix} \sin(\theta_1)\,\cos(\theta_2)\,e^{i\phi_1} \\ -\sin(\theta_1)\,\sin(\theta_2)\,e^{i\phi_2} \\ \cos(\theta_1)\,\cos(\theta_3)\,e^{i\phi_3} \\ -\cos(\theta_1)\,\sin(\theta_3)\,e^{i\phi_4} \end{pmatrix}, \qquad |\psi_4\rangle \equiv \begin{pmatrix} \cos(\theta_1)\,\cos(\theta_2)\,e^{i\phi_1} \\ -\cos(\theta_1)\,\sin(\theta_2)\,e^{i\phi_2} \\ -\sin(\theta_1)\,\cos(\theta_3)\,e^{i\phi_3} \\ \sin(\theta_1)\,\sin(\theta_3)\,e^{i\phi_4} \end{pmatrix}.
\end{aligned} \tag{5.7}$$

Since $\hat{M}$ is a unitary matrix, which is easily verified since it is constructed from an orthonormal set of vectors, the measurement of these vectors can be obtained on chip by setting the chip-configuration such that $\hat{U}_4^\dagger \equiv \hat{M}^\dagger$. In other words, one can successfully measure $\hat{M}$ from collecting normalised coincidence counts if $\hat{U}_4^\dagger \hat{M} \approx \hat{I}_4$. By performing this calculation for the same optimal values stated above ($\Phi_{1,2,3,4} = e^{-i\phi_{1,2,3,4}}$, $\Phi_5 = e^{2i(\theta_3-\theta_2)}$, $\Phi_6 = e^{2i(\theta_2-\theta_3)}$, $X_A = \theta_2$, $X_B = 2\theta_3$ and $X_C = X_D = \theta_1$), one finds that the resulting matrix is in fact

$$\hat{U}_4^\dagger \hat{M} = \begin{pmatrix} \alpha\gamma & 0 & 0 & 0 \\ 0 & \alpha\gamma & 0 & 0 \\ 0 & 0 & \beta\delta & 0 \\ 0 & 0 & 0 & \beta\delta \end{pmatrix} \approx \hat{I}_4. \tag{5.8}$$

Which gives the desired result, up to some local complex phases where $\alpha\gamma = -e^{i(\theta_1+\theta_2)}$ and $\beta\delta = -e^{i(\theta_1+\theta_3)}$. Hence this approach can be used to efficiently measure any four-dimensional basis, an example of which is the 4D Hadamard matrix defined as

$$\hat{H}_4 = \frac{1}{2}\begin{pmatrix} 1 & 1 & 1 & 1 \\ 1 & 1 & -1 & -1 \\ 1 & -1 & 1 & -1 \\ 1 & -1 & -1 & 1 \end{pmatrix}, \tag{5.9}$$

which is achieved via the following measurement settings

$$\hat{H}_4 \rightarrow \{\theta_1 = \theta_2 = \theta_3 = \pi/4, \;\; \phi_1 = \phi_2 = \phi_3 = \phi_4 = \phi_5 = \phi_6 = 0\}. \tag{5.10}$$

The above approach that simultaneously measures each eigenvector for the 4-dimensional product bases is able to speed up the measurement collection by 16× for two ququarts. However the drawback is that this approach requires the use of eight SNSPDs compared with just two when projecting into each of the 16 eigenvectors individually. In addition, when using this approach, the probabilities of measuring coincidence events in each channel combination also depends on the relative transmission efficiencies across each of the spatial modes. Due to these reasons, and since efficient detectors are typically a scarce resource, it was chosen to use only two SNSPD detectors connected to output modes 0_A and 0_R.

5.2.5 Chip-to-chip Phase Stabilisation

The ability to generate and measure coherent superpositions of single photon states generated on-chip has been shown several times in this thesis. At the beginning of this chapter, it was shown that single qubit states that are encoded in these single photon states can even remain coherent for significant periods of time (hours) chip-to-chip. This time-preserved coherence was achieved via the conversion of qubit encoding from path to polarisation from chip-to-chip, and then to stabilise the setup such that no polarisation changes occur in time. In contrast to that approach, the goal of this section is to develop and show an on-chip active phase stabilisation protocol such that no encoding converter is required. The motivation for this is the application of chip-to-chip *high dimensional* state transfer, where no preferred encoding conversion is known due to the necessity of transporting d modes. Here the precise meaning of coherence is that the two initially identical superposition states remain identical throughout the chip-to-chip channel, such that they can be reliably interfered on the receiver circuit. That is to say that the photonic states can change during the transfer, but they must change in the same way.

When applying this to the transfer of high dimensional qudit states between chips, where the method of transfer is via different optical paths, each spatial mode must act to have the same effect on the photonic states they carry. The key challenge then, is to stabilise each optical path such that each of the (up to four) separate optical paths essentially apply the same unitary transformation to the single photon states such they cannot be distinguished at the receiver. The use of a multi-core fibre in this experiment is an attempt to produce almost identical changes in the single photon

states throughout most of the transmission. In reality, however, the dominating noise arises during the transmission throughout the initially coupled fibre array, where the different spatial modes are subject to their own noise.

The four fixed (over reasonable time-scales) polarisation changes can be easily dealt with via an external polarisation controller for each optical mode. However, the fluctuation of photon arrival times within the coherence time of the single photons generates a random phase shift between each optical path, which must be stabilised in order to measure any quantum coherence's between the two devices. In addition there is also a significant time-independent optical delay (longer than the photons coherence time) which can be mechanically controlled via four optical delay-lines. The resulting decoherence, then, is likely to be generated from local phase-drifts along the fibres.

In order to mitigate this substantial issue, a chip-to-chip active phase stabilisation protocol was designed and implemented by four on-chip thermal phase sifters. It was found that, without active stabilisation, the setup completely decohered on the order of several seconds. The on-chip phase shifters can operate at kHz frequencies ($\gg$ 1 kHz), making them perfectly adequate to stabilise the setup. The general approach to solving this problem was to utilise the pump laser (centred at $\lambda = 1549.3nm$) to monitor the relative phase changes across each channel. This was practically achieved by creating a chip-to-chip interferometer where the coupled optical power at each output port of the receiver dictates the local phase-drift. A convenient feature of the entangled state configuration is that the pump is approximately evenly split between each of the optical modes due to the on-chip AMZI filters, see figure 2.7 and 3.6. As a result, interference patterns can be achieved between chips by applying optical beam splitters (MZI set to $\pi/2$) on the receiver circuits and by varying the thermal phase shifters over a 2π range.

By monitoring the optical power at each of the output ports, it is possible to infer the relative phase of each of the optical modes. In practice, the approach was to initially characterise the classical channel by applying the beam splitters and sweeping the applied phase to obtain a 2π interference fringe. Since the random phase fluctuations vary on much longer time scales than on-chip heaters, clean interference fringes can be achieved, see figure 5.4c. Each of the phase shifters are then calibrated by applying a sinusoidal fit to the data. When repeated over several single-second time periods, the same experiment will obtain a shifted fringe due to the relative random phase drift across the different spatial modes. By using the same fitting function, the random offset can be precisely measured. The measured phase offset $\Delta\phi$ is then applied (with a sign flip, $e^{-i\Delta\phi}$) to each of the on-chip phase shifters in order to cancel the relative

phase fluctuations.

In an ideal scenario, the goal would be to apply real-time and high sample-rate phase stabilisation, which could be achieved via a phase-lock loop [193]. In practice, a standard feedback loop implementation is non-trivial given the chip design due to the inclusion of MRR single photon sources and design limitations, where four input/output modes are required - but only two input modes are present. Figure 5.4a shows a time-dependent chip-to-chip interference pattern caused by the relative phase-drift between two adjacent optical modes. Here, the two optical modes leave the transmitter and are coupled to the receiver device and interfere at an on-chip beam splitter. Between the two chips, optical fibre-coupled delay lines are utilised to match the temporal arrival of the pulsed laser. A variable spectral filter (variable FWHM) was applied to the input pulsed laser to control the coherence length of the interference, where the coherence length L_c is approximately given in terms of the central wavelength λ and optical bandwidth $\Delta\lambda$ by [194]

$$L_c \approx \frac{\lambda^2}{\Delta\lambda}. \tag{5.11}$$

Since the bandwidth of the twin beams produced by the single photon sources is around $30 \times 10^{-12} m$, it is important to choose a larger bandwidth (and therefore smaller coherence length) for the pump. A resulting coherent pump interference will then infer the coherence of single photons across the channel. In order to see high visibility interference, it is also important that the pump intensity is equal between the two spatial modes. The difference in losses across each spatial mode can be accommodated for on-chip by the inclusion of MZI attenuators, see the receiver design in figure 5.2. Figure 5.4a shows the natural relative phase drift between two modes of the chip-to-chip setup over a 700 s time period. From this it can be seen that the interference visibility is greater than 20 dB, with the optical intensity varying from -35 dBm to -59 dBm. A similar approach was taken between each pairwise combination of spatial modes to insure the simultaneous overlap of each of the four modes.

The dashed line in figure 5.4b shows an example of the interference pattern in the normalised optical due to the relative phase drift over a smaller time-scale $\approx 25\ s$. From here, an approximate time-scale of the phase-drift can be characterised. It was found that a significant phase drift occurs on the order of a few seconds. In order to stabilise the channel, it is therefore adequate to design a phase stabilisation technique that operates every second. For this approach, quantum measurements (such as collecting photon coincidence detection events) can be collected for short periods of time whilst the phase fluctuations are small. Multiple collection events can be obtained after each phase stabilisation and the results combined. The active phase

stabilisation can be seen by the data points in 5.4b which represent the normalised optical power. Crucially there is no interference pattern between each data point, suggesting that the relative phase-drift has been adequately accounted for.

The above approach was found to be enough for the time-scales at which large phase fluctuations occurred, for example see figure 5.4c which shows a phase stabilised interference fringe with both optical power and single photon coincidence counts. This plot is designed to show the level of phase control between two optical modes in the chip-to-chip setup. For each data point in the figure, the offset phase was measured and corrected for and the desired optical phase was then applied such that the set phase in each case was $\phi_{\text{set}} = \phi_{\text{desired}} - \phi_{\text{offset}}$. Here the desired phase is the one which corresponds to the initial calibration and the offset comes from the difference between the initial calibration and recently measured result. The resulting fringe shows that the phase can be stabilised both for classical and quantum coincidence counts over the whole 2π range.

The time taken for each stabilisation, i.e. to set the interferometer configuration, measure and fit the fringe offset and set the new phase, takes approximately 300 milliseconds. In the case where coincidence counts are collected, a single second integration time is acquired before measuring the phase offset again. In order to gain higher statistical significance, multiple of these measurements are repeated and combined depending on the experiment. For example, the measured coincidence counts in figure 5.4a, showing two second integration time, accounts for two datasets.

The following experiments were designed to investigate how the chip-to-chip phase stabilisation performs when transmitting qubits between chips. In each case, the maximally entangled Bell state $|\Phi^+\rangle_{A,B} \equiv |\psi_2\rangle_{A,B}$ is prepared, where photon A is measured on the receiver and photon B is measured on the transmitter. In the first experiment, the initial entangled state is measured in the basis given by $\hat{\sigma}_x \otimes (\cos(\theta)\hat{\sigma}_x + \sin(\theta)\hat{\sigma}_y)$. This basis was chosen, since the expectation value is always zero for a maximally mixed state (one which has maximally decohered). However, for the target pure state, the expectation value oscillates from 1 to -1, the measured data of which is shown in figure 5.4b. The plot shows the calculated expectation value of this operator measured on the state when varying the parameter θ from 0 to 2π. When θ is zero, the measurement basis is equal to $\hat{\sigma}_x \otimes \hat{\sigma}_x$ where only the positive eigenvalues should contribute to the measurement, and the expectation value is 1 in

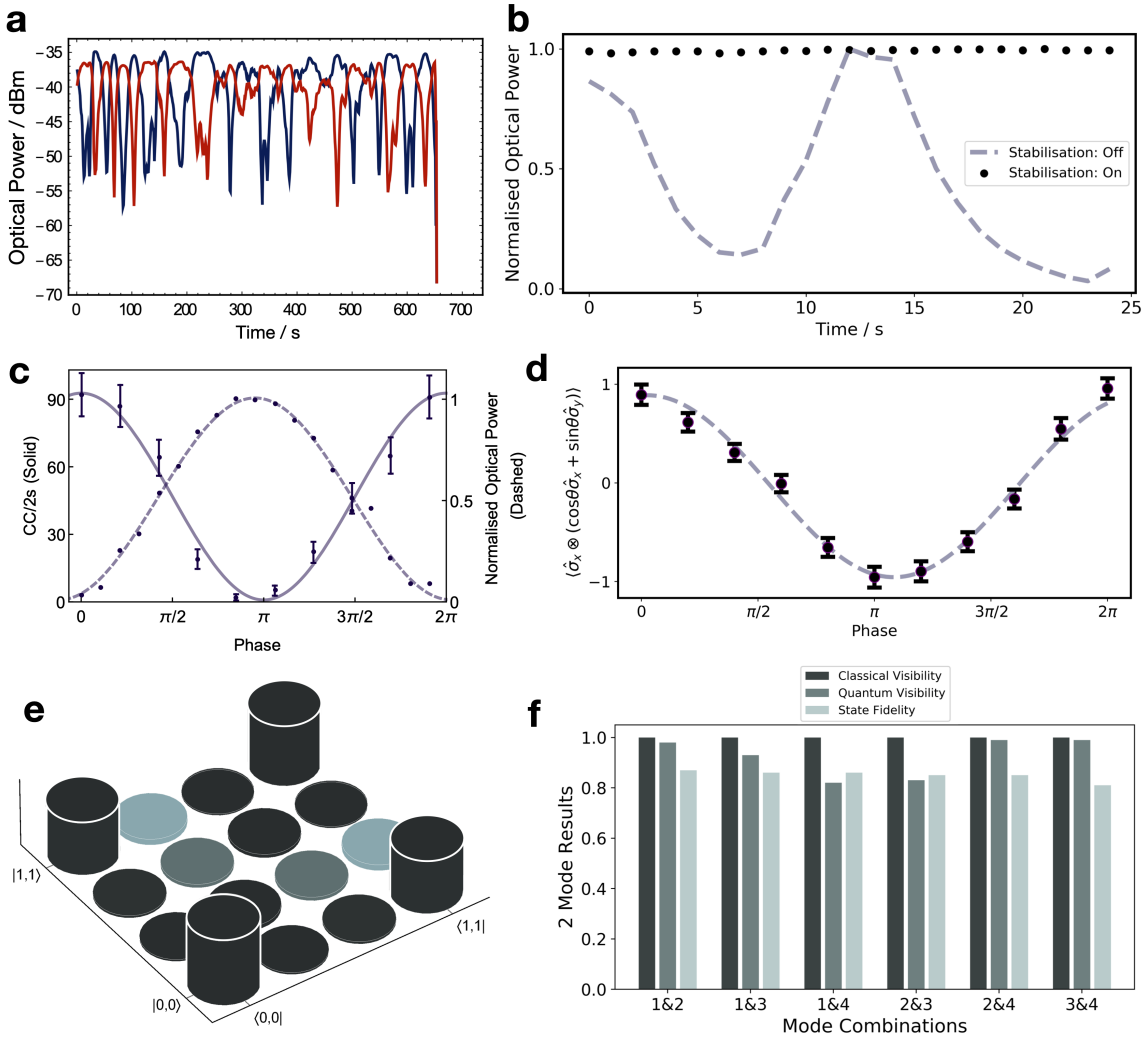

Figure 5.4: spatial Mode Phase Stabilisation Results. **a**, measured two-mode chip-to-chip interference of split pump light across two spatial modes when temporally overlapped. **b**, comparison between active phase stabilisation off/on (dashed/dots). **c**, chip-to-chip interference fringe. Data point with error bars (y-axis left) shows the chip-to-chip quantum interference fringe across modes $0_R/1_R$ and $0_A/1_A$. A zero and π relative phase shift corresponds to the measurement $(\hat{\sigma}_x^{(0,1)}\hat{\sigma}_x^{(0,1)})_{A,B}$ and $(\hat{\sigma}_x^{(0,1)}\hat{\sigma}_y^{(0,1)})_{A,R}$ bases, respectfully. Here coincidence counts are taken from the $0_A, 0_R$ modes, i.e. the positive eigenvalue. In contrast, the classical fringe (right y-axis) was recorded from output mode 1_R and is therefore π out of phase with the quantum fringe. Each data set is fit with a sinusoidal fringe using nonlinear curve fit function in python (from the scipy package). **d**, interference fringe from the expectation value of the measured operator (shown on y-axis). Modes 0/1 from each chip are projected into this basis and measured via normalised two-photon coincidence counts across the two devices. The quantum fringe from **c** shows the raw coincidence counts of the positive eigenvalue. **e**, reconstructed density matrix of the two mode entangled state between two chips, with a measured fidelity of 87%. **f,** results from **c-e** are repeated for every pairwise combination of modes across the two chips. The measured values are summarised for the classical and quantum fringe visibilities, as well as the full state fidelities which are derived from the full tomography in each case.

the ideal case. This can be seen by writing the change of basis

$$\begin{aligned} |\psi_2\rangle &= \frac{|0,0\rangle + |1,1\rangle}{\sqrt{2}} \\ &= \frac{|+,+\rangle + |-,-\rangle}{\sqrt{2}}, \end{aligned} \tag{5.12}$$

where no negative eigenvalues of $\hat{\sigma}_x \otimes \hat{\sigma}_x$ are present. In contrast, when $\theta = \pi/2, 3\pi/2$ the two qubits are measured in the mutually unbiased bases ($\pm\hat{\sigma}_x \otimes \hat{\sigma}_y$) we expect zero correlation between the positive and negative eigenvalues. As a result, the expectation value in these bases should give zero when averaged over many coincidence counts, $\langle \pm\hat{\sigma}_x \otimes \hat{\sigma}_y \rangle = 0$. The minima of the fringe is explained when measuring $\hat{\sigma}_x \otimes -\hat{\sigma}_x$, where the positive and negative eigenvalues are flipped and so a value of -1 is expected. The expected fit is a $\cos\theta$ function, which can be verified by deriving the general expectation value in the following way. The target state, $|\psi_2\rangle \equiv |\Psi^+\rangle_{A,B}$ can be rewritten in the basis of eigenstates for both operators $|\pm\rangle$ for $\hat{\sigma}_x$ and $|\pm e^{i\theta}\rangle \equiv (|0\rangle \pm e^{i\theta}|1\rangle)/\sqrt{2}$ for $(\cos(\theta)\hat{\sigma}_x + \sin(\theta)\hat{\sigma}_y)$, see section 4.4 for an explicit calculation. When written in these bases, the state becomes

$$\begin{aligned} |\psi_2\rangle = \frac{1}{\sqrt{8}}\Big[&\Big(|+\rangle|+e^{i\theta}\rangle + |-\rangle|-e^{i\theta}\rangle\Big)(1+e^{-i\theta}) \\ &+\Big(|+\rangle|-e^{i\theta}\rangle + |-\rangle|+e^{i\theta}\rangle\Big)(1-e^{-i\theta})\Big], \end{aligned} \tag{5.13}$$

and the expectation value,

$$\begin{aligned} \langle \hat{\sigma}_x \otimes (\cos(\theta)\hat{\sigma}_x + \sin(\theta)\hat{\sigma}_y)\rangle &= \mathrm{Tr}\big(\hat{\sigma}_x \otimes (\cos(\theta)\hat{\sigma}_x + \sin(\theta)\hat{\sigma}_y)|\psi_2\rangle\langle\psi_2|\big) \\ &= \mathrm{Tr}\Big[\Big(|+,+e^{i\theta}\rangle\langle+,+e^{i\theta}| + |-,-e^{i\theta}\rangle\langle+,+e^{i\theta}| \\ &\quad - |+,-e^{i\theta}\rangle\langle+,+e^{i\theta}| - |-,+e^{i\theta}\rangle\langle+,+e^{i\theta}|\Big)|\psi_2\rangle\langle\psi_2|\Big] \\ &= \big|\langle+,+e^{i\theta}||\psi_2\rangle\big|^2 + \big|\langle-,-e^{i\theta}||\psi_2\rangle\big|^2 \\ &\quad - \big|\langle+,-e^{i\theta}||\psi_2\rangle\big|^2 - \big|\langle-,+e^{i\theta}||\psi_2\rangle\big|^2 \end{aligned} \tag{5.14}$$

which evaluates as $\cos\theta$ and justifies the chosen fit. The presence (and high > 80 visibility) of the measured coherences of the Bell state suggest a high fidelity, pure qubit is transmitted between devices and confirms the phase stabilisation techniques are adequate for transmitting path entangled qubits between chips.

Figure 5.4e shows the full reconstructed density matrix of the measured chip-to-chip entangled state, yielding a fidelity of 0.87. The reconstructed density matrix was estimated via maximum likelihood techniques and over-complete topographical basis measurements, via the detection of 36 different coincidence counts corresponding to

the measurement of 36 different eigenvectors. Each coincidence measurement was composed of a 5 second integration time window, where the phase drift was stabilised every second. Each of the measurements shown in figures 5.4c-e were repeated for each of the pairwise combinations of two modes between the transmitter and receiver. The results are summarised in the bar graph which is shown in figure 5.4f. The average measured fidelities were 0.85 ± 0.02 and the average quantum fringe visibilities were 0.92 ± 0.07, where the errors represent the standard error in the mean.

5.2.6 High Dimensional State Analysis

The previous section shows that it is possible to coherently measure path encoded quantum states between two silicon devices, without the need to convert the encoded qudits as part of the transfer process. This is achieved via the active phase stabilisation between each of the separate optical paths, which is actively corrected for on the receiver device. Having previously shown this for classical and quantum measurements for prepared Bell states, sec 5.2.5, in this section we analyse the state performance on the 3D and 4D biphoton states $|\psi_{3/4}\rangle$.

In order to verify the high fidelity coherent state transfer, two key verification protocols were used and are summarised in detail in the following two sections. In the first approach, the state fidelity is directly measured by decomposing the target state into locally measurable observables. In a secondary approach, a (compressed sensing [195]) state tomography estimates and reconstructs the four-dimensional density matrix of the on-chip state $\hat{\rho}_{\text{meas}}$. Once the reconstruction is obtained, the state fidelity is then calculated as the overlap between the target pure state $|\psi_{3/4}\rangle$ and measured state, ρ as $\langle\psi_{3/4}|\,\rho\,|\psi_{3/4}\rangle$. The former approach has the advantage that it requires only a small number of measurements, however, the secondary approach has the advantage that more information is gained about the state, since the full reconstruction is achieved.

5.2.6.1 State Decomposition

Experiment Details. Here we discuss the direct measurement of the target state fidelity which can be achieved by decomposing the target states, $|\psi_{3/4}\rangle$, into local observables that Alice and Bob can each verify on their respective devices. In this scenario, Alice and Bob each have access to their own three- or four-dimensional sub-spaces, $H_A = \{\,|\,\phi_i\rangle_A\,\}$ and $H_B = \{\,|\,\phi_j\rangle_B\,\}$, where the total Hilbert space is the tensor product of these bases, $H = H_A \otimes H_B$. When written in this global product basis, the state fidelity can be obtained from only a few local measurements on the

d-dimensional state in the following manner

$$\begin{aligned} F_d &= \langle\psi_d|\,\hat{\rho}_{\text{meas}}\,|\psi_d\rangle \\ &= \text{Tr}\big(\hat{\rho}_{\text{meas}}\,|\psi_d\rangle\,\langle\psi_d|\big) \\ &= \text{Tr}\Big(\hat{\rho}_{\text{meas}}\big(\sum_{i,j}|\phi_i\rangle\,\langle\phi_i|_A\otimes|\phi_j\rangle\,\langle\phi_j|_B\big)\Big) \\ &= \sum_{i,j}\langle\phi_i,\phi_j|_{A,B}\,\hat{\rho}_{\text{meas}}\,|\phi_i,\phi_j\rangle_{A,B}\,. \end{aligned} \tag{5.15}$$

This approach directly relies on the ability to find the equivalence between the target density matrix $\hat{\rho}_{\text{target}}$ and the measurable bases in the following way

$$\hat{\rho}_{\text{target}} = |\psi_{3/4}\rangle\,\langle\psi_{3/4}| \equiv \sum_{i,j}|\phi_i\rangle\,\langle\phi_i|_A\otimes|\phi_j\rangle\,\langle\phi_j|_B\,. \tag{5.16}$$

This can be achieved by decomposing the ideal states into local measurable observables that consist of the two mode Pauli operators. As we will see, the tensor-product of these Pauli operators are each stabilizers of the high dimensional entangled states and can be combined to reproduce the target density matrices. The most straightforward example of which, is the two dimensional entangled state $|\psi_2\rangle^{(0,1)}$. Here the superscript refers to the actual optical modes which encode the two-dimensions, i.e. Alice and Bob each measure 0 and 1, but any pairwise permutation of optical modes are equivalent here. The density matrix of this state can be written as

$$\begin{aligned} \hat{\rho}_2 &= |\psi_2\rangle\,\langle\psi_2| \\ &= \frac{1}{2}\Big[\,|00\rangle\,\langle 00| + |00\rangle\,\langle 11| + |11\rangle\,\langle 00| + |11\rangle\,\langle 11|\,\Big]. \end{aligned} \tag{5.17}$$

The above state can be easily decomposed into the stabiliser formalism, which is written as the sum of the tensor product of Pauli operators. For this state, the stabilisers are $\hat{I}^{(0,1)}\otimes\hat{I}^{(0,1)}$, $\hat{\sigma}_x^{(0,1)}\otimes\hat{\sigma}_x^{(0,1)}$, $-\hat{\sigma}_y^{(0,1)}\otimes\hat{\sigma}_y^{(0,1)}$ and $\hat{\sigma}_z^{(0,1)}\otimes\hat{\sigma}_z^{(0,1)}$, and their normalised sum produces the above density matrix $\hat{\rho}_2$ in the following way,

$$\hat{\rho}_2 = \frac{1}{4}\Big[\hat{I}^{(0,1)}\otimes\hat{I}^{(0,1)}, +\hat{\sigma}_x^{(0,1)}\otimes\hat{\sigma}_x^{(0,1)} - \hat{\sigma}_y^{(0,1)}\otimes\hat{\sigma}_y^{(0,1)} + \hat{\sigma}_z^{(0,1)}\otimes\hat{\sigma}_z^{(0,1)}\Big]. \tag{5.18}$$

These four operators can be further simplified, since both operators $\hat{I}^{(0,1)}\otimes\hat{I}^{(0,1)}$ and $\hat{\sigma}_z^{(0,1)}\otimes\hat{\sigma}_z^{(0,1)}$ require only computational basis measurements. In order to stay consistent with earlier terminology, see section 4.4, these combined terms evaluate the diagonal elements of the density matrix and will be referred to as the population term, $\hat{P}$. In this case, the population term evaluates as $\hat{P} = (\hat{I}^{(0,1)}\otimes\hat{I}^{(0,1)} + \hat{\sigma}_z^{(0,1)}\otimes\hat{\sigma}_z^{(0,1)})/2$. The two coherence terms, $\hat{C}_\theta$, are given by the remaining two operators in equation 5.18

and correspond to the off-diagonal density matrix terms. We define the two coherence terms as

$$\hat{C}_x \equiv \hat{\sigma}_x \otimes \hat{\sigma}_x \tag{5.19a}$$

$$\hat{C}_y \equiv -\hat{\sigma}_y \otimes \hat{\sigma}_y, \tag{5.19b}$$

Thus the fidelity of the Bell pair can be directly measured via the sum of three expectation values each measured in a separate basis dictated by the Pauli operators

$$F_2 = \frac{\langle \hat{P} \rangle}{2} + \frac{\langle \hat{C}_x \rangle}{4} + \frac{\langle \hat{C}_y \rangle}{4}. \tag{5.20a}$$

This approach can be extended to the remaining high dimensional states, $|\psi_{3/4}\rangle$. In the case of the three-dimensional entangled state, the density matrix of which may be written as

$$\begin{aligned} \hat{\rho}_3 &= |\psi_3\rangle \langle \psi_3| \\ &= \frac{1}{3}\Big[|00\rangle \langle 00| + |00\rangle \langle 11| + |00\rangle \langle 22| \\ &\quad + |11\rangle \langle 00| + |11\rangle \langle 11| + |11\rangle \langle 22| \\ &\quad + |22\rangle \langle 00| + |22\rangle \langle 11| + |22\rangle \langle 22| \Big]. \end{aligned} \tag{5.21}$$

Again, here the diagonal elements of the density matrix can be measured when Alice and Bob project into the computational basis. Here we define the d-dimensional population term as

$$\hat{P}_d = \sum_{i=0}^{d-1} |i,i\rangle \langle i,i|/d. \tag{5.22}$$

The remaining off-diagonal elements can be determined by the tensor product of Pauli matrices acting on different optical modes. In this way, the three dimensional entangled state may be written as

$$\begin{aligned} \hat{\rho}_3 = \hat{P}_3 + \frac{1}{6}\Big[&\hat{\sigma}_x^{(0,1)} \otimes \hat{\sigma}_x^{(0,1)} - \hat{\sigma}_y^{(0,1)} \otimes \hat{\sigma}_y^{(0,1)} \\ &+ \hat{\sigma}_x^{(0,2)} \otimes \hat{\sigma}_x^{(0,2)} - \hat{\sigma}_y^{(0,2)} \otimes \hat{\sigma}_y^{(0,2)} + \hat{\sigma}_x^{(1,2)} \otimes \hat{\sigma}_x^{(1,2)} - \hat{\sigma}_y^{(1,2)} \otimes \hat{\sigma}_y^{(1,2)} \Big]. \end{aligned} \tag{5.23}$$

In the case of the four-dimensional entangled state, the density matrix is given by

$$\begin{aligned} \hat{\rho}_4 &= |\psi_4\rangle \langle \psi_4| \\ &= \frac{1}{4}\Big[|00\rangle \langle 00| + |00\rangle \langle 11| + |00\rangle \langle 22| + |00\rangle \langle 33| \\ &\quad + |11\rangle \langle 00| + |11\rangle \langle 11| + |11\rangle \langle 22| + |11\rangle \langle 33| \\ &\quad + |22\rangle \langle 00| + |22\rangle \langle 11| + |22\rangle \langle 22| + |22\rangle \langle 33| \\ &\quad + |33\rangle \langle 00| + |33\rangle \langle 11| + |33\rangle \langle 22| + |33\rangle \langle 33| \Big] \end{aligned} \tag{5.24}$$

This state can be written in a directly analogous way, relying on the population term $\hat{P}_4$ and this time 12 coherence terms which are formed by the different permutations of optical modes. The decomposed state is

$$\begin{aligned}\hat{\rho}_4 = \hat{P}_4 + \frac{1}{8}\Big[&\hat{\sigma}_x^{(0,1)}\otimes\hat{\sigma}_x^{(0,1)} - \hat{\sigma}_y^{(0,1)}\otimes\hat{\sigma}_y^{(0,1)} + \hat{\sigma}_x^{(0,2)}\otimes\hat{\sigma}_x^{(0,2)} - \hat{\sigma}_y^{(0,2)}\otimes\hat{\sigma}_y^{(0,2)} \\ &+ \hat{\sigma}_x^{(0,3)}\otimes\hat{\sigma}_x^{(0,3)} - \hat{\sigma}_y^{(0,3)}\otimes\hat{\sigma}_y^{(0,3)} + \hat{\sigma}_x^{(1,2)}\otimes\hat{\sigma}_x^{(1,2)} - \hat{\sigma}_y^{(1,2)}\otimes\hat{\sigma}_y^{(1,2)} \\ &+ \hat{\sigma}_x^{(1,3)}\otimes\hat{\sigma}_x^{(1,3)} - \hat{\sigma}_y^{(1,3)}\otimes\hat{\sigma}_y^{(1,3)} + \hat{\sigma}_x^{(2,3)}\otimes\hat{\sigma}_x^{(2,3)} - \hat{\sigma}_y^{(2,3)}\otimes\hat{\sigma}_y^{(2,3)}\Big].\end{aligned} \tag{5.25}$$

Results. When transmitting the entangled qudit state from one chip to another, two main types of noise are expected to affect the measured fidelities. Firstly, and as previously discussed, the relative phase fluctuations between optical paths (if not corrected accurately) will tend to decohere the transmitted state. This decoherence will lower contribution of the coherence terms but the population term will be unaffected. In the worst case scenario, the total expectation value of the coherence terms will be exactly zero and the measured state will be the mixed state $\hat{\rho}_{\text{mixed}} = \sum_{i=0}^{d-1} |i,i\rangle\langle i,i|/d$.

The second key source of noise is optical mode cross-talk, which will affect both the coherence and population terms. Figure 5.5a shows the experimental measurements for the population and coherence operators for the $|\psi_{3/4}\rangle$ states. Here, computational basis measurements for these two states are shown on the left, whilst the measured expectation values $\langle\hat{P}_{3/4}\rangle$, $\langle\hat{C}_{3/4}\rangle$, $\langle\hat{F}_{3/4}\rangle$ are shown to the right. The ideal population term, as defined in equation 5.22, is related to the sum of the peak probabilities when measured in the computational basis and evaluates as $\langle\hat{P}_d\rangle = 1/d$. The measured values for the three- and four-dimensional states were $\langle\hat{P}_3\rangle = 0.318 \pm 0.006$ and $\langle\hat{P}_4\rangle = 0.231 \pm 0.004$. The coherence terms for the two states are defined as

$$\begin{aligned}\hat{C}_3 = \frac{1}{6}\Big[&\hat{\sigma}_x^{(0,1)}\otimes\hat{\sigma}_x^{(0,1)} - \hat{\sigma}_y^{(0,1)}\otimes\hat{\sigma}_y^{(0,1)} \\ &+ \hat{\sigma}_x^{(0,2)}\otimes\hat{\sigma}_x^{(0,2)} - \hat{\sigma}_y^{(0,2)}\otimes\hat{\sigma}_y^{(0,2)} + \hat{\sigma}_x^{(1,2)}\otimes\hat{\sigma}_x^{(1,2)} - \hat{\sigma}_y^{(1,2)}\otimes\hat{\sigma}_y^{(1,2)}\Big], \\ \hat{C}_4 = \frac{1}{8}\Big[&\hat{\sigma}_x^{(0,1)}\otimes\hat{\sigma}_x^{(0,1)} - \hat{\sigma}_y^{(0,1)}\otimes\hat{\sigma}_y^{(0,1)} + \hat{\sigma}_x^{(0,2)}\otimes\hat{\sigma}_x^{(0,2)} - \hat{\sigma}_y^{(0,2)}\otimes\hat{\sigma}_y^{(0,2)} \\ &+ \hat{\sigma}_x^{(0,3)}\otimes\hat{\sigma}_x^{(0,3)} - \hat{\sigma}_y^{(0,3)}\otimes\hat{\sigma}_y^{(0,3)} + \hat{\sigma}_x^{(1,2)}\otimes\hat{\sigma}_x^{(1,2)} - \hat{\sigma}_y^{(1,2)}\otimes\hat{\sigma}_y^{(1,2)} \\ &+ \hat{\sigma}_x^{(1,3)}\otimes\hat{\sigma}_x^{(1,3)} - \hat{\sigma}_y^{(1,3)}\otimes\hat{\sigma}_y^{(1,3)} + \hat{\sigma}_x^{(2,3)}\otimes\hat{\sigma}_x^{(2,3)} - \hat{\sigma}_y^{(2,3)}\otimes\hat{\sigma}_y^{(2,3)}\Big],\end{aligned} \tag{5.26}$$

which in general evaluates as $\langle\hat{C}_d\rangle = 1 - \langle\hat{P}_d\rangle = (d-1)/d = 2/3, 3/4$. The measured values were 0.572 ± 0.007 and 0.642 ± 0.009, respectively. It can be seen from equation 5.15 that the fidelity of the two states is the sum of these expectation values, which evaluates as $F_3 = 0.890 \pm 0.009$ and $F_4 = 0.873 \pm 0.010$.

5.2.6.2 Compressed Sensing Tomography

Experiment Details. The most general approach to learning the quantum state of a physical system is quantum state tomography. This powerful tool has been utilised several times in this thesis and allows the reconstruction of density matrices via the measurement of many copies of a state in different bases. Despite this powerful diagnostic tool, quantum state tomography is best suited for simple quantum systems, since it carries the significant disadvantage that it requires many bases measurements, scaling badly for n d-dimensional qudits as $(d+1)^n$. Since the ultimate goal of chip-scale devices is to integrate increasingly complex quantum systems, the continued use of quantum state tomography as a general state reconstruction tool is unlikely in the near future. More recently, a substantial theoretical goal has been to develop more specialised tomographic processes that require significantly less resources in given scenarios. For example, in a given experiment it is often true that the majority of possible quantum states and experimental configurations are not of primary interest. It is therefore sensible to suppose that there may be some more optimal approaches to reconstructing specific kinds of states, such as pure or entangled states.

Compressed sensing quantum tomography is a particular example of a quantum state reconstruction tool that is designed to specifically reduce the number of measurement settings required to reconstruct an approximately pure quantum state. The details of this protocol is outlined in the original text in reference [195] and has been thoroughly experimentally explored [12, 196–198]. The uniqueness of this approach allows the more efficient reconstruction of low rank density matrices with a number of measurements far fewer than may be required otherwise by the full state tomography. Specifically, the number of measurement settings required to reproduce a given $d \times d$ density matrix of rank r is reduced from d^2 to $O(rd\ln^2 d)$, a significant saving if the measured density matrix is of low rank[7]. In addition, the required measurements are each product states obtained by projecting into each of the eigenvectors of the tensor product of different Pauli matrices, which are standard practice in quantum information science.

The exact approach in this experiment follows closely to the one outlined in reference [12]. The protocol for four-dimensions is as follows, suppose Alice and Bob each share one photon from a bi-photon state encoded into two qudits. Each party projects their qudit into a randomly chosen basis, achieved by $(\hat{\sigma}_i \otimes \hat{\sigma}_j)_A \otimes (\hat{\sigma}_k \otimes \hat{\sigma}_l)_B$ for random i,j,k,l where $\hat{\sigma}_X \in \{\hat{\sigma}_I, \hat{\sigma}_x, \hat{\sigma}_y, \hat{\sigma}_z\}$, and where $\hat{\sigma}_I$ is the 2×2 identity matrix. In the four-dimensional case there are $4^4 = 256$ total operators to choose from, where each

[7] Or highly pure, since a rank 1 state is also a pure state

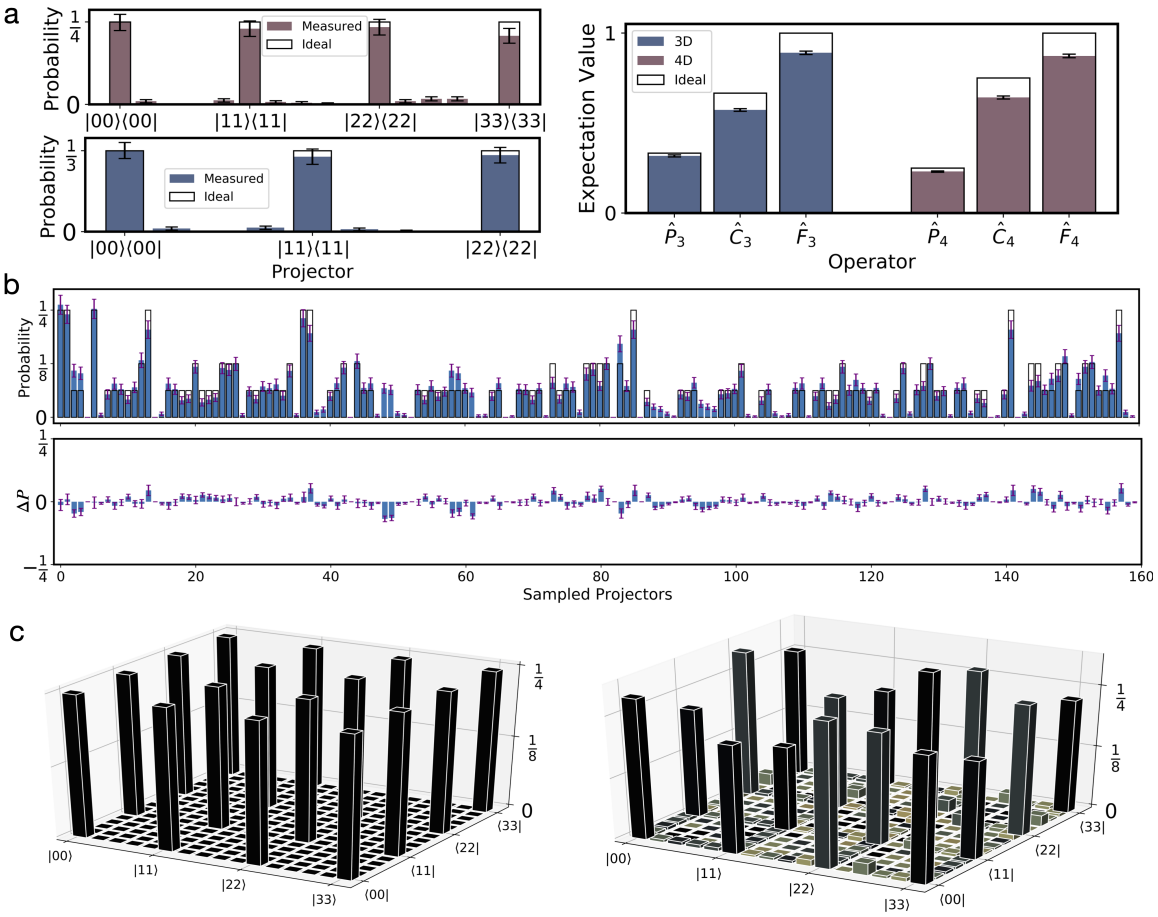

Figure 5.5: High dimensional entanglement distribution results. **a**, computational basis measurements (left) for the entangled qudits in three- and four-dimensions. The right-hand bar graph shows the measured population, coherence and fidelities against their calculated ideal values for the three- and four-dimensional entangled states. In each case the ideal probabilities are shown as colorless bars and measured probabilities are color-matched. For the computational basis measurements, each of the d^2 eigenvectors are plotted on the x axis, but labels are shown only for the cases where a non-zero probability (peak) is expected. **b**, measured vs expected eigenvector probabilities for a random sample of 160 measured eigenvectors. In total 1600 measurements were made, every 1/10 data point is represented here. The top figure shows the ideal measurements (shown in black transparent bars) and measured values (shown in blue). For the measured values the error bars are given and estimated via poissonian statistics. The lower figure shows the difference between the expected and measured probabilities for each eigenvector, along with the uncertainty of each result. **c**, ideal (left) and measured (right) density matrix of the four-dimensional entangled state. The density matrix was reconstructed via 100 bases measurements, each consisting of 16 eigenvector projectors, giving a total of 1600 measurement settings. For each measurement multiple 1s integration times were used. Phase stabilisation was applied in between each measurement. The resulting four-dimensional state fidelity was 87% between chips as calculated by the compressed sensing tomography.

measurement choice w_i should be made at random where $i \in \{1,\ldots,256\}$. The matrix reconstruction σ of the measured state ρ relies on solving a convex optimisation that minimises the trace norm of the measured state σ subject to the following constraints

$$\begin{aligned} \mathrm{Tr}(\sigma) &= 1, \\ \mathrm{Tr}(w_i\sigma) &= \mathrm{Tr}(w_i\rho), \end{aligned} \tag{5.27}$$

where σ is from the set of positive semi-definite matrices (where its vector inner products are all non-negative). Efficient numerical optimisations of this kind exist and are freely available [199]. The specific code used during this experiment was kindly provided by Dr Stefano Paesani, and is identical to the reconstruction method utilised in reference [12].

During this experiment 100 different global product bases w_i were measured at random between the two chips. This compares with the 50 bases that were measured for four-dimensional states in reference [12]. For each basis, 16 different coincidence counts were measured and normalised, giving a total of 1600 measurement settings for the compressed sensing tomography. In order to increase the statistical significance, biphoton coincidence events were integrated for a single second before being repeated five times for each eigenvector. The resulting coincidence counts were each combined and normalised. In between each single measurement, the phase stabilisation protocol was repeated and the total measurement collection time requires approximately five hours of data-collection. Figure 5.5b (top) shows a sample of one-in-ten of the total measured eigenvectors, where the measured values are coloured in blue and the target values are colourless. For clarity figure 5.5b (bottom) shows the difference between the target value and measured value for each of these 160 eigenvectors. The mean absolute difference between the target and measured probabilities is found to be $\Delta P_\mu = 0.015 \pm 0.0010$ which shows good agreement between predictions and measurement. Figure 5.5c (left/right) shows the expected and measured reconstructed density matrix. The target state fidelity was also estimated via the inner product between the target pure state and reconstructed density matrix, which gave a numerical value of $F_4 = \langle\psi_4|\,\hat{\rho}_{\mathrm{meas}}\,|\psi_4\rangle = 0.89$ and a state purity of approximately 80%. The estimated fidelity falls within close proximity to the previously measured fidelity (via decomposition into locally measurable observable) of $F_4 = 0.873 \pm 0.010$.

5.2.7 High Dimensional QKD

Quantum key distribution (QKD) is the ability for a transmitted quantum state to create shared randomness between two parties [39, 89]. This shared randomness acts

as a key resource that allows both parties to utilise powerful cryptography protocols, for example, each user is able to encrypt and decrypt strings of bits by performing an XOR between the random key and their shared message. If the shared randomness is truly unknown to any third-party, then it can be used to create a one-time single-shot key (referred to as a one-time pad). Under these assumptions, the two users are said to have unbreakable information security [200, 201]. For some protocols, this security holds even in the instances where the measurement devices are under the control of the adversary [36] or where only some of the apparatus can be trusted [45]. QKD has been shown in many platforms, and has been demonstrated with key rates above 1 MHz [202], at distances of 260 km [203] and even from Earths orbit [37].

Quantum entangled states are a convenient way of generating shared randomness between two or more parties. When measuring a quantum state, the probability of obtaining a particular measurement outcome depends on the choice of measurement. Since a biphoton entangled quantum state is encoded in two particles, with one belonging to each party member, the joint statistics of each members outcome depends largely on their *combined* measurement choice. Quantum entangled states, as we have seen many times up until now, have the peculiar phenomena that their joint statistics can be perfectly correlated when measured in the correct bases. For example, the Bell states $|\Phi^+\rangle$ is perfectly correlated when Alice and Bob both measure in the computational basis, or in the $\hat{\sigma}_x$ basis, but not at all correlated if they choose to measure in the opposite bases, i.e. when Alice measures in the computational basis and Bob measures in $\hat{\sigma}_x$. Sets of measurement bases where this is true, where both parties measurement outcomes are all uncorrelated with a flat distribution profile, are referred to as *mutually unbiased*. When each party member chooses to measure from a set of these mutually unbiased bases, then their measurement outcomes are correlated only in the instances where the members choose the same basis. Together, these sets of bases form the backbone of QKD, since each member can publicly share their choice of measurement settings (only after the measurement has been performed!) but since their random bits are encoded in the measurement outcome and not the choice of measurement, their keys remain in the private domain. Crucially, once the public announcement is made, each party member can discard the cases where they did not choose to measure in the same mutually unbiased basis, which generates an identical random key between between both parties.

Perhaps one of the most powerful aspects of QKD is that once a secure key is established between the two parties, the resulting encryption key can never be learned by a third-party. This is because the carrier of the randomness arose from an unknown quantum state, which cannot be precisely or accurately measured without produc-

ing many copies - which is forbidden under the no-cloning theorem. Hence once the quantum property has been measured, the prepared quantum state collapses to the eigenvector corresponding to the eigenvalue of the resulting outcome. This measurement cannot be repeated since the physical object is no longer in the original quantum state and so the extracted randomness cannot be learned by a third party. This leads to another desired property in the context of cryptography, the ambiguity of the quantum state to its observer presents an obstacle to any unwanted eavesdropper - since any attempt to perform measurements on the quantum system by the eavesdropper will introduce errors in the shared joint statistics that Alice and Bob measure. This fact allows both parties to compare their measured datasets and bound the amount of information any observer might have about the key. Given this information, each party can then make an informed decision about whether to share their encrypted message.

High dimensional QKD utilises high dimensional quantum states to establish shared randomness between two users. Utilising high dimensional states to generate the randomness has a few key benefits [41]. For example, in any QKD protocol, the rate of key generation typically decays exponentially with the separation distance between observers. This is due to the fact that the quantum states are encoded and transmitted in photons, where the optical transmission of those photons decays with increasing distance. High dimensional quantum states have increased information density per single photon when compared with qubits, which is a practice approach to combating the reduced rate of shared photon states over larger distances. In addition, high dimensional states have been shown to be more resilient to noise, which is practical in combating noisy communication channels [204].

In this section, it is shown that the high dimensional entangled state, $|\psi_4\rangle = \sum_{i=0}^{3} |i,i\rangle/2$, can be efficiently measured in multiple mutually unbiased bases. These mutually unbiased bases can be used by two observers to generate a random shared key in the instances where they measure the same unbiased basis. In recent work, high dimensional QKD has been successfully verified between two parties by utilising silicon photons [182]. However, in this demonstration, weak coherent pulses were utilised as information carriers. This approach typically requires so-called decoy states (pulses of varying intensities) for information security [205]. In addition, these attenuated coherent states have limited practical uses in general quantum technologies, where heralded single photon sources have many advantages. For example, the use of entangled quantum states poses the advantage that they can be used in networking scenarios to connect multiple users, where a centralised source can be routed to many different users. To complete this demonstration, the same two mutually unbiased

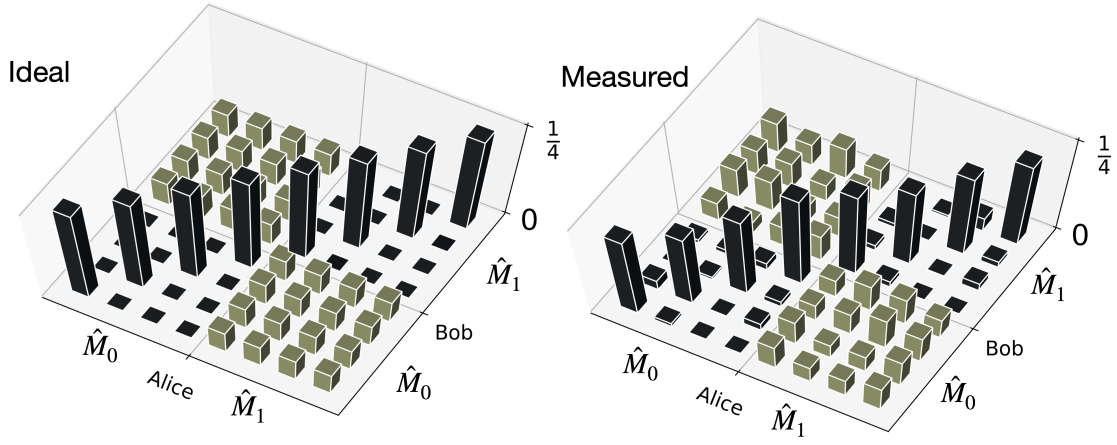

Figure 5.6: High-dimensional QKD measurements. The four dimensional entangled state $\rho_{\text{ideal}} = |\psi_4\rangle\langle\psi_4|$ was measured in one of two mutually unbiased bases $\hat{M}_0$ and $\hat{M}_1$, see equation 5.28 for basis definitions. The ideal and measured statistics are shown left and right, respectively. The average projector fidelity was 91% with an average quantum error rate of 8.8%. A key feature, is that when measuring the state in the same basis, highly correlated measurements are found in the joint probability function (and a key can be established). In the case where each user measures a different state, approximately equal (flat) probability distributions are measured across every outcome.

bases $\hat{M}_0$ & $\hat{M}_1$ as in reference [182] were used, which are defined as

$$\hat{M}_0 = \begin{pmatrix} \big(|0\rangle + |1\rangle\big)/\sqrt{2} \\ \big(|0\rangle - |1\rangle\big)/\sqrt{2} \\ \big(|2\rangle + |3\rangle\big)/\sqrt{2} \\ \big(|2\rangle - |3\rangle\big)/\sqrt{2} \end{pmatrix}, \qquad \hat{M}_1 = \begin{pmatrix} \big(|0\rangle + |2\rangle\big)/\sqrt{2} \\ \big(|0\rangle - |2\rangle\big)/\sqrt{2} \\ \big(|1\rangle + |3\rangle\big)/\sqrt{2} \\ \big(|1\rangle - |3\rangle\big)/\sqrt{2} \end{pmatrix}. \tag{5.28}$$

In order to verify the correlations in the counting statistics between both qudits, each combination of measurement bases was measured across the two devices. Figure 5.6 shows the expected (left) and measured (right) probabilities of each eigenvector in the bases. As expected, the joint counting statistics show strong correlation in the cases where both the same bases are measured, and low correlation when different bases are measured. For each eigenvector projection a quantum bit error rate was calculated, i.e. the percentage of coincidence events which measure an unexpected eigenvalue. Over the entire measured space the average error rate was found to be 8.8%, which would be expected from a state fidelity of around 91% and is roughly in line with previously measured state fidelities. In addition, this bit error rate is significantly below the error tolerance threshold value (11%) for the BB84 QKD protocol for qubits [41] and is also below the previously achieved chip-to-chip error rates utilising weak coherent pulses

[182].

5.3 Future Work

5.3.1 High-dimensional Entanglement Witness

Entanglement within high dimensional multi-partite systems has become of increasing interest in recent years both theoretically [206] and experimentally [182, 191, 204]. In many recent experiments initial work has aimed at generating the d-dimensional maximally entangled states of the form $|\psi_d\rangle$ - as is explored so far in this chapter. However, it turns out that multiple copies of smaller dimensional systems are extremely good at replicating the counting statistics of these high dimensional entangled states. For example, the state $|\psi_4\rangle$ that is explored throughout this thesis chapter can be perfectly replicated by the tensor product of two Bell pairs. This can be seen by completing the basis transformation

$$\begin{aligned} \{|0\rangle, |1\rangle, |2\rangle, |3\rangle\}_A &\rightarrow \{|00\rangle, |01\rangle, |10\rangle, |11\rangle\}_{a,b} \\ \{|0\rangle, |1\rangle, |2\rangle, |3\rangle\}_B &\rightarrow \{|00\rangle, |01\rangle, |10\rangle, |11\rangle\}_{c,d} \end{aligned} \tag{5.29}$$

such that

(5.30)

$$\begin{aligned} |\psi_4\rangle = \frac{1}{2}\big(|00\rangle + |11\rangle + |22\rangle + |33\rangle\big)_{A,B} &\rightarrow \frac{1}{2}\big(|0000\rangle + |0101\rangle + |1010\rangle + |1111\rangle\big)_{a,b,c,d} \\ &= \frac{1}{\sqrt{2}}\big(|00\rangle + |11\rangle\big)_{a,b} \otimes \frac{1}{\sqrt{2}}\big(|00\rangle + |11\rangle\big)_{c,d}. \end{aligned}$$

Despite this result, these high dimensional states can hold a tremendous amount of entanglement [12, 207], and can be an effective tool to increasing the Hilbert space of systems where multiple qubits are difficult to come by. A natural question arises, however, which categories of high dimensional entangled states cannot be represented by multiple copies of smaller systems? In recent theoretical work, a genuine multi-dimensional entanglement witness is able to certify those states which cannot be decomposed by smaller copies [208]. This contrasts with previous work [209] which was able to calculate the minimum Hilbert space size capable of reproducing the measured results. It turns out that in three- and four-dimensional bipartite systems, the maximal violation of this witness are given by the following two states

$$|\eta_1\rangle = \frac{1}{\sqrt{3}}\big(|00\rangle + |11\rangle + |22\rangle\big) \equiv |\psi_3\rangle \tag{5.31}$$

and

$$|\eta_2\rangle = \frac{\sqrt{3}}{2}|00\rangle + \frac{1}{2\sqrt{3}}\big(|11\rangle + |22\rangle + |33\rangle\big). \tag{5.32}$$

Hence, in three-dimensional systems the maximal violation is actually the maximally entangled state $|\psi_3\rangle$ which we have previously measured during this chapter. This contrasts the four-dimensional version of the state which can be fully represented by four qubits.

The measured witness operator can be constructed in terms of the state $|\eta\rangle\langle\eta|$ and the parameter α which is defined as the maximum probability that any decomposible (representable by smaller qudits) state $|\phi\rangle$ is measured as the target, i.e. $|\langle\phi||\eta\rangle|^2_{\max}$. In order to make the measurement as easy as possible, the target state $|\eta\rangle$ is chosen in a way that minimises α. Such that the target state is as far away from the decomposible states as possible. In the case of the three- and four-dimensional states above, $|\eta_1\rangle$ and $|\eta_2\rangle$, the calculated parameters are $\alpha_1 = [(3+\sqrt{5})/6]^{\frac{1}{2}} \approx 0.934$ and $\alpha_2 = [(3+\sqrt{8})/6]^{\frac{1}{2}} \approx 0.986$. By constructing the witness

$$\hat{W} = \alpha\mathbb{1} - |\eta\rangle\langle\eta| \tag{5.33}$$

one can see that the expectation value of $\hat{W}$ is negative only when the measured state fidelity is higher than α. This sets the bar high for producing high dimensional entangled states which cannot be decomposed into smaller qudit systems. This emphasises that, in general, qubits are very good at decomposing larger Hilbert spaces and reproducing their entanglement.

Unfortunately, this means that if one is required to generate a genuine high dimensional entangled state that is transmitted over a distance. The state decoherence should be not much more than 1% for a four-dimensional entangled state - a surprising result. Unfortunately, even the three-dimensional fidelity threshold $\approx 93\%$ is a significant challenge. In our experiment, chip-to-chip fidelities of around 90% were achieved, limited by the channel decoherence. If these fidelities are to significantly improve, as to violate the constructed witness, better phase stabilisation protocols should be achieved. This gap could be effectively closed by an active phase-lock loop for example. Due to the on-chip phase stability, it is highly likely based on previous bi-photon experiments in this thesis, that these fidelities could be adequately achieved on a single device, and could be demonstrated in the lab with current devices. It is for this reason that this is under the future work section of this thesis.

5.4 Discussion

This chapter contains the report of several chip-to-chip experiments in silicon quantum photonics, where single qudit ($d = 2,3,4$) logical states are successfully transferred and measured between integrated devices. When combined with the earlier work in

chapters 3 and 4 of this thesis, high quality pure single photons generated on chip are transferred between chips which enable quantum information experiments achieved for the first time in integrated devices. For example, work in reference [108] shows the first successful chip-to-chip Bell test proving the coherent transfer of qubits between chips via path-polarisation. The work in this chapter significantly improves on this demonstration via the integration of high heralding efficiency and high purity single photon sources that are capable of generating high quality multi-photon states on chip. When combined with the ability to coherently transfer qudits between devices, this has enabled the first demonstration of quantum teleportation between chips, which yielded some of the highest fidelities seen so far in the field [63]. Since quantum teleportation is the foundation of many quantum technologies, such as quantum repeaters [82] and quantum computing [63–65], this demonstration may one day play a key role in deployable quantum technologies.

Since optical losses play a key role in quantum communications experiments, the transfer of single photon states - where their quantum properties cannot be amplified due to the no-cloning theorem - is particularly fragile. Recent work has shown that the move to higher dimensional systems provides a route to both higher information density and improved noise tolerance in quantum communications [41, 182, 186, 191, 204, 206]. Many quantum communications protocols will therefore see improvements by successfully showing the coherent transfer of single photon states that encode qudits states. Since integrated photonics, despite its key advantages, provides higher optical losses, the advantages of high dimensional systems are potentially heightened in this platform. The remainder of this chapter has focused on the testing of this high-dimensional approach, in particular with entangled biphoton states. The high fidelity transfer of these states were successfully bench-marked with two methods, i.e. through the state decomposition into local measurable observable and via compressed sensing state tomography. The achieved fidelities ($\approx 90\%$) are comparable to the recent demonstration of single chip high dimensional entanglement generation on a chip [12]. The approximate few percentage discrepancy between the results reported in this thesis and the former approach is accounted for via the chip-to-chip decoherence, and can be seen from the drop in quantum visibility of bi-photon interference seen between figure 5.4f and 3.12.

CHAPTER 6

CONCLUSIONS

There is no doubt that the work contained in this thesis does not represent the end goal for integrated quantum photonics. Instead, the topics and experiments in this thesis show an incremental step towards scalable quantum technologies in the aforementioned platform. The goal of this thesis is that, by attempting to focus on the systems architecture and design of quantum information protocols in silicon photonics, we may uncover the unique applications of the platform and plan a road map ahead. This road map should focus on the underlying technologies that are required to build a truly scalable quantum photonic toolkit in silicon. The need for developing these new technologies are certainly evident from the difficulty of achieving the experiments laid out across this work, but the proof of principle demonstrations are designed to give hope to the overarching endeavour. The main positive message is that silicon quantum photonics, despite being in its infancy, is able to directly compete with more mature quantum platforms both of light and other materials. This is evidenced within this thesis by the achievement of high fidelity quantum teleportation and genuine multipartite entanglement, some of the backbones of quantum technologies. Moreover, in the final experimental chapter of this thesis we focus on experiments that are unique to light and its ability to communicate over large distances. These demonstrations, despite their proof-of-principle nature, form great promise for distributed and interconnected quantum technology platforms that may develop.

On the contrary, however, there is a great amount of work to do in developing a wide array of useful quantum machines from light. As we elude to all throughout this thesis, there are several key technology categories that require substantial development for truly scalable integrated photonic machines. The first category is single photon sources,

a particular focus of this thesis. It has been demonstrated throughout this thesis that pure single photon states can be generated on-chip with reasonable accuracy, which is evidenced by the high visibility $\approx 90\%$ quantum interference on chip. However, the reliable interference between many photons from multiple sources will require orders of magnitude smaller spectral impurities, moving from the $\approx 10\%$ implied here down to $\approx 0.1\%$ and better. Multiple schemes have now been proposed on how to achieve these orders of magnitude improvement [132, 133] and in recent works these purities are beginning to be realised on chip [130]. Once high quality and high heralding efficiency sources are developed, the remaining challenge will be to multiplex them in a way that produces near deterministic high quality photons, where methods for achieving this are known [135, 137, 138]. However, these implementations require fast-feed forward and high speed switches. Progress is currently being made on this front, where all optical switches can be constructed from resonators on-chip, though the substantial issue is that current technologies lead to a trade-off between visibility and rate [172, 173, 210, 211]. The final ingredient to develop ideal sources are optical delays, which can be achieved either through optical memories or long waveguides. Unfortunately, optical quantum memories are still far from ideal and it is therefore likely that delay lines will be a more optimal approach [170, 212].

The second main category of focus should be on systems architecture, where low-loss components come together to manipulate the generated single photons with high fidelity. Much work has been deployed on the theoretical side, which attempts to close the gap between the limits of quantum mechanics and today's available technology [64, 213, 214]. For example, in quantum computing, one of the exciting developments is the requirement for 3-GHZ resource states, where we have shown their possible implementation within this thesis [69, 170]. To the best of my knowledge, this is the first 3-GHZ state measured on-chip and was verified with genuine multipartite entanglement witnesses. However, the fidelity of gates can still be improved and optimised for lower losses. In addition, new verification schemes such as the two bases measurements in section 4.4.3 will help bridge the gap between state generation and verification once the complexity grows significantly for n d-dimensional qudits.

Finally, custom electronics systems are required to meet the demands of a growing number of active components on chip and single photon coincidence counting logic. A particular example of this is that today's best counting systems have a maximum output of approximately 10^8 counts per second. This will eventually limit the scalability of trial-until-success experiments like the ones performed in this thesis, however, multiplexed sources could move around this issue by only counting conditional clicks. Moreover, single photon detection systems themselves were a central sticking point

for photonic systems until the invention of superconducting nano-wire detectors that obtain very high efficiencies [128]. The direct integration of these detectors in silicon photonics is challenging, yet recent simulations have shown that integration is possible with near unity efficiency by utilising a resonator design [171]. As a result, optical resonators like the ones explored throughout this thesis could play a crucial role in almost all aspects of future quantum circuits, for example, sources, switches, filters and even detectors. Further study on the properties of more advanced micro-resonator designs could prove to become a gold mine of quantum optical technologies, as has been shown in the recent work on sources [132].

Despite the need for improved technologies to achieve truly scalable systems, there remains significant scope for experimental demonstrations with existing technologies by pushing their performance to the limit. For example, boson sampling is a key area of interest that requires low resources and is computationally hard to simulate [176–181]. Due to the necessity of only static devices (no programmable components), this route may allow large-scale demonstrations with low loss and higher coincidence events. A vast amount of progress towards this goal has been recently demonstrated on-chip [174, 175] and the integration of optimised sources with simultaneously high brightness, heralding efficiency and purity could already significantly improve these demonstrations. Due to these key reasons, boson sampling experiments could prove to be the first experiments to achieve quantum supremacy.

Based on current technologies it is likely that we may reach 10-photon demonstrations on chip within the next few years. A simple simulation based on equation 3.16 and calculated in section 4.5 shows that 10-fold coincidence events (5 pairs) on chip would be possible with count rates of around 1 per minute. In such a configuration, the signal to noise ratio, i.e. pure photon pairs compared with multiphoton terms, would likely have to be around 10 - with a squeezing parameter of around $x = 0.3$ and double the estimated value within the experiments in this thesis. The simulation also assumes gigahertz pumping rates and a detection probability of around 0.25, allowing for approximately 6 dB optical loss per channel. This should be achievable for passive devices in silicon with optimised gratings, and certainly once integrated detectors become available. A good suggested strategy would be to simultaneously focus on long-term technological breakthroughs, as well as to test current technologies to their limits. The concluding message of this thesis is that, despite the technical challenges ahead, never has there ever been more viable routes to success for integrated quantum photonic technologies. The rate of progress within the last decade alone has been both vast and inspiring, and it is the opinion of this thesis that there are many more reasons to be optimistic about the future of quantum photonic technologies than not.

APPENDIX A

SINGLE QUBIT UNITARIES - BOTTOM MODE

In this appendix we derive the unitary transformation for when the optical phase shift is applied to the top qubit mode, labeled $|0\rangle$ throughout this thesis. A quantitative assessment of this unitary operation can be given by summarising the linear optical transformations on each of the modes caused by each component as follows

$$\hat{U}_{\text{Phase}}(\theta) = \begin{pmatrix} e^{i\phi} & 0 \\ 0 & 1 \end{pmatrix}, \tag{A.1}$$

$$\hat{U}_{\text{MMI}} = \frac{1}{\sqrt{2}} \begin{pmatrix} i & 1 \\ 1 & i \end{pmatrix}, \tag{A.2}$$

$$\hat{U}_{\text{MZI}}(\theta) = \hat{U}_{\text{MMI}}\hat{U}_{\text{Phase}}\hat{U}_{\text{MMI}} = e^{i(\theta+\pi)/2} \begin{pmatrix} -\sin(\theta/2) & \cos(\theta/2) \\ \cos(\theta/2) & \sin(\theta/2) \end{pmatrix}. \tag{A.3}$$

Therefore the total unitary is written as

$$\begin{aligned} \hat{U}_t(\phi,\theta) &= \hat{U}_{\text{Phase}}(\phi)\hat{U}_{\text{MZI}}(\theta) \\ &= e^{i(\theta+\pi)/2} \begin{pmatrix} -e^{i\phi}\sin(\theta/2) & e^{i\phi}\cos(\theta/2) \\ \cos(\theta/2) & \sin(\theta/2) \end{pmatrix}. \end{aligned} \tag{A.4}$$

As a result, the general mapping of computational basis states as a function of the two phases θ and ϕ is written as

$$\hat{U}_t(\phi,\theta)|0\rangle = e^{i(\theta+\pi)/2}\big(-e^{i\phi}\sin(\theta/2)|0\rangle + \cos(\theta/2)|1\rangle\big), \tag{A.5a}$$

$$\hat{U}_t(\phi,\theta)|1\rangle = e^{i(\theta+\pi)/2}\big(e^{i\phi}\cos(\theta/2)|0\rangle + \sin(\theta/2)|1\rangle\big). \tag{A.5b}$$

Hence the magnitude of the $\{0,1\}$ superposition states can be easily controlled by the parameter θ and the relative phase of the $\{0,1\}$ states can be controlled via the external phase ϕ. These bases therefore form an arbitrary orthonormal basis set, spanning the entire two dimensional space, under the conditions that each of the states are orthonormal with one another, i.e.

$$\left(-e^{i\phi}\sin(\theta/2)|0\rangle+\cos(\theta/2)|1\rangle\right)^{\dagger}\left(e^{i\phi}\cos(\theta/2)|0\rangle+\sin(\theta/2)|1\rangle\right)=0 \tag{A.6a}$$

$$\left(e^{i\phi}\cos(\theta/2)|0\rangle+\sin(\theta/2)|1\rangle\right)^{\dagger}\left(-e^{i\phi}\sin(\theta/2)|0\rangle+\cos(\theta/2)|1\rangle\right)=0 \tag{A.6b}$$

$$\left(-e^{i\phi}\sin(\theta/2)|0\rangle+\cos(\theta/2)|1\rangle\right)^{\dagger}\left(-e^{i\phi}\sin(\theta/2)|0\rangle+\cos(\theta/2)|1\rangle\right)=1 \tag{A.6c}$$

$$\left(e^{i\phi}\cos(\theta/2)|0\rangle+\sin(\theta/2)|1\rangle\right)^{\dagger}\left(e^{i\phi}\cos(\theta/2)|0\rangle+\sin(\theta/2)|1\rangle\right)=1, \tag{A.6d}$$

which is to say that $\hat{U}_t(\phi,\theta)$ is unitary such that $\hat{U}_t^{\dagger}(\phi,\theta)\hat{U}_t(\phi,\theta)=\mathbb{1}$, since this would imply that for $i,j\in\{0,1\}$

$$\begin{aligned}\left(\hat{U}_t(\phi,\theta)|i\rangle\right)^{\dagger}\hat{U}_t(\phi,\theta)|j\rangle&=\langle i|\hat{U}_t^{\dagger}(\phi,\theta)\hat{U}_t(\phi,\theta)|j\rangle\\&=\delta_{i,j}.\end{aligned} \tag{A.7}$$

To test the condition, we can directly calculate $\hat{U}_t^{\dagger}(\phi,\theta)\hat{U}_t(\phi,\theta)$, applying $\hat{A}^{\dagger}=\hat{A}^{T*}$

$$\begin{aligned}\hat{U}_t^{\dagger}(\phi,\theta)\hat{U}_t(\phi,\theta)&=\begin{pmatrix}-e^{-i\phi}\sin\theta/2 & \cos\theta/2\\ e^{-i\phi}\cos\theta/2 & \sin\theta/2\end{pmatrix}\begin{pmatrix}-e^{i\phi}\sin\theta/2 & e^{i\phi}\cos\theta/2\\ \cos\theta/2 & \sin\theta/2\end{pmatrix}\\&=\begin{pmatrix}1&0\\0&1\end{pmatrix},\end{aligned} \tag{A.8}$$

where the global phases immediately cancel.

For projective measurements, where arbitrary qubits are rotated back into the computational basis to be accurately measured, one can simply perform the adjoint transformation $\hat{U}_t^{\dagger}(\phi,\theta)$. By performing this projection back in to the computational basis, one can infer the statistical likelihood of particular eigenvalues only by measuring photon detection events in each mode. By utilizing this method one can infer the measured eigenvalues, as can be seen in the following approach

$$\hat{U}_t^{\dagger}(\phi,\theta)\left(-e^{i\phi}\sin(\theta/2)|0\rangle+\cos(\theta/2)|1\rangle\right)=\hat{U}_t^{\dagger}(\phi,\theta)\hat{U}_t(\phi,\theta)|0\rangle=|0\rangle, \tag{A.9a}$$

$$\hat{U}_t^{\dagger}(\phi,\theta)\left(e^{i\phi}\cos(\theta/2)|0\rangle+\sin(\theta/2)|1\rangle\right)=\hat{U}_t^{\dagger}(\phi,\theta)\hat{U}_t(\phi,\theta)|1\rangle=|1\rangle. \tag{A.9b}$$

By utilizing the mathematical identity $(\hat{A}\hat{B})^{\dagger}=\hat{B}^{\dagger}\hat{A}^{\dagger}$, evaluating $\hat{U}_t^{\dagger}$ becomes straightforward under the following approach

$$\begin{aligned}\hat{U}_t^{\dagger}(\phi,\theta)&=\left(\hat{U}_{\text{Phase}}(\phi)\hat{U}_{\text{MZI}}(\theta)\right)^{\dagger}\\&=\hat{U}_{\text{MZI}}^{\dagger}(\theta)\hat{U}_{\text{Phase}}^{\dagger}(\phi)\\&=e^{-i(\theta+\pi)}\hat{U}_{\text{MZI}}(\theta)\hat{U}_{\text{Phase}}(-\phi).\end{aligned} \tag{A.10}$$

Hence the ability to project any qubit system back into the computational basis can be efficiently achieved by reversing the physical operation order $\hat{U}_{\text{Phase}} \leftrightarrow \hat{U}_{\text{MZI}}$ and also reversing the sign of the phase applied to the $|0\rangle$ mode, $\hat{U}_{\text{Phase}}(\phi) \rightarrow \hat{U}_{\text{Phase}}(-\phi)$.

APPENDIX B

SFWM UNITARY TRANSFORMATION

B.1 Unitary Derivation

The mechanism of SWFM, see sections 2.2.3 and 3.2.1, is well-known and the goal in modern quantum optics experiments is to achieve greater control over the characteristics of this phenomena. In order to elaborate on why this is, it is essential to have a deeper discussion about the underlying physical process. As we have mentioned in sections 2.2.3 and 3.2.1 of this thesis, SFWM arises due to the nonlinear interaction of two pump photons in a particular medium of interaction length L. Such a process gives rise to a interaction Hamiltonian of the following form [114]

$$\hat{H}_{\mathrm{SFWM}} = \int_{-L/2}^{L/2} \mathrm{d}z \chi^{(3)} \hat{E}_{\mathrm{p}}(z,t) \hat{E}_{\mathrm{p'}}(z,t) \hat{E}_{\mathrm{s}}^{\dagger}(z,t) \hat{E}_{\mathrm{i}}^{\dagger}(z,t) + \mathrm{h.c.}, \tag{B.1}$$

where an interaction along the z axis of length L is considered at time t and where $\hat{E}_x(z,t)$ represents the electric field operators of the FWM photons. A standard description of the resulting unitary transformation may be derived analytically by taking two Gaussian-shaped pump fields represented as strong classical waves of wavenumber k_p and frequency ω_p, of the form

$$\hat{E}_p(z,t) = \int \mathrm{d}\omega_p e^{i\left(k_p(\omega_p)z + \omega_p t\right)} \alpha_p(\omega_p), \tag{B.2}$$

where $\alpha(\omega_p)$ represents a Gaussian profile centred at μ_p with width σ_p attributed to a pulsed laser source of the following form

$$\alpha_p(\omega_p) = A_p e^{(\omega_p - \mu_p)^2/2\sigma_p^2}, \tag{B.3}$$

which describes a gated classical source with amplitude A_p. For the signal and idler fields we have the following contribution

$$\hat{E}_x^\dagger(z,t) = A_x \int \mathrm{d}\omega_x e^{-i\left(k_x(\omega_x)z+\omega_x t\right)} \hat{a}_x^\dagger(\omega_x) \tag{B.4}$$

written in terms of the creation operators $\hat{a}_x$ and where the coefficient A_x contains any constants. The unitary transformation which takes place may be described in terms of the Hamiltonian in the following way

$$\hat{U} = \exp\Big[-\frac{i}{\hbar}\int_{-\infty}^{\infty} \hat{H}(t)\mathrm{d}t\Big]. \tag{B.5}$$

By performing the substitutions and combining the exponents we may arrive at the unitary transformation which describes the SFWM interaction giving rise to the non-degenerate photon pairs measured in this thesis,

$$\begin{aligned}\hat{U} = \exp\Bigg[-\frac{i}{\hbar}\Bigg(A\int_{-L/2}^{L/2}\mathrm{d}z\int \mathrm{d}t\mathrm{d}\omega_p\mathrm{d}\omega_{p'}\mathrm{d}\omega_s\mathrm{d}\omega_i e^{i\left(k_p(\omega_p)+k_{p'}(\omega_{p'})-k_s(\omega_s)-k_i(\omega_i)\right)z} \\ \times e^{i\left(\omega_p+\omega_{p'}-\omega_s-\omega_i\right)t}\alpha(\omega_p)\alpha(\omega_{p'})\hat{a}_s^\dagger\hat{a}_i^\dagger + \mathrm{h.c.}\Bigg)\Bigg].\end{aligned} \tag{B.6}$$

Here the integration over time gives rise to a dirac delta function in frequency, and gives the condition that the signal and idler photons conserve energy in the process

$$\int \mathrm{d}t e^{i\left(\omega_p+\omega_{p'}-\omega_s-\omega_i\right)t} = 2\pi\delta(\omega_p+\omega_{p'}-\omega_s-\omega_i). \tag{B.7}$$

By integrating over the interaction length, one arrives at a sinc profile

$$\int_{-L/2}^{L/2}\mathrm{d}z e^{i\left(k_p(\omega_p)+k_{p'}(\omega_{p'})-k_s(\omega_s)-k_i(\omega_i)\right)z} \approx \mathrm{sinc}\Big(\frac{\Delta kL}{2}\Big) \tag{B.8}$$

where we have defined the parameter $\Delta k = \left(k_p(\omega_p)+k_{p'}(\omega_{p'})-k_s(\omega_s)-k_i(\omega_i)\right)$. This is usually referred to as the phase matching condition, since the maximum amplitude corresponds to when $\Delta k = 0$. Combining these results, the overall unitary reduces to

$$\hat{U} = \exp\Bigg[-\frac{i}{\hbar}\Bigg(A\int \mathrm{d}\omega_s\mathrm{d}\omega_i f_{\mathrm{SFWM}}(\omega_s,\omega_i)\hat{a}_s^\dagger(\omega_s)\hat{a}_i^\dagger(\omega_i) + \mathrm{h.c.}\Bigg)\Bigg], \tag{B.9}$$

where we have defined the so-called joint-spectral amplitude f_{SFWM} as

$$f_{\mathrm{SFWM}} = \int \mathrm{d}\omega_p\,\alpha(\omega_p)\alpha(\omega_s+\omega_i-\omega_p)\ \mathrm{sinc}\Big(\frac{\Delta kL}{2}\Big), \tag{B.10}$$

which describes both the phase matching condition and energy conservation of the SFWM process. When combined, these processes describe the correlations between the measured signal and idler photons, and by tuning the properties of this function, one may attain spectral shapes of varying spectral purity. The significance of this will is explored in the context of multi-photon quantum interference in section 3.2.4.2. Moreover, section 3.2.2 shows how this unitary gives rise to multi-mode twin-beam squeezed states that can be used to approximate single photon sources - one of the primary technologies used in this thesis.

B.2 Bi-photon Approximation

The SFWM unitary transformation, summarised in equation B.9, acts on the vacuum state $|\text{vac}\rangle$ to produce twin-beam squeezed states across multiple spectral modes, see section 3.2.2 for details. The multi-pair behaviour of the four-wave mixing can be seen directly by tailor expanding the exponential of an operator $e^{\hat{X}}$ as

$$e^{\hat{X}}|\text{vac}\rangle = \left[1 + \hat{X} + \frac{\hat{X}^2}{2!} + \ldots\right]|\text{vac}\rangle\,, \tag{B.11}$$

where in this case $\hat{X}$ is defined as

$$\hat{X} \equiv -\frac{i}{\hbar}\left(A\int \mathrm{d}\omega_s \mathrm{d}\omega_i f_{\text{SFWM}}(\omega_s,\omega_i)\hat{a}_s^\dagger(\omega_s)\hat{a}_i^\dagger(\omega_i) + \text{h.c.}\right). \tag{B.12}$$

Here the higher order terms in the tailor expansion give rise to multi-photon terms. However, where the SFWM is small, and therefore A is small, the high order terms are negligible and the unitary evolution can be approximated as

$$\begin{aligned} e^{\hat{X}}|\text{vac}\rangle &\approx \left[1+\hat{X}\right]|\text{vac}\rangle \\ &= |\text{vac}\rangle - \frac{i}{\hbar}\left(A\int \mathrm{d}\omega_s \mathrm{d}\omega_i f_{\text{SFWM}}(\omega_s,\omega_i)\hat{a}_s^\dagger(\omega_s)\hat{a}_i^\dagger(\omega_i) + \text{h.c.}\right)|\text{vac}\rangle\,. \end{aligned} \tag{B.13}$$

Hence, in the event that two photons are detected at signal and idler frequency, the vacuum term is post-selected away and the state (after re-normalisation) is approximately the bi-photon state [78]

$$|\psi\rangle = \int \mathrm{d}\omega_s \mathrm{d}\omega_i f_{\text{SFWM}}(\omega_s,\omega_i)\hat{a}_s^\dagger(\omega_s)\hat{a}_i^\dagger(\omega_i)|\text{vac}\rangle\,. \tag{B.14}$$

This bi-photon approximation is useful for describing path encoded qubits on chip and holds where the multi-photon emission is low.

BIBLIOGRAPHY

[1] M D Barrett, J Chiaverini, T Schaetz, J Britton, W M Itano, J D Jost, E Knill, C Langer, D Leibfried, R Ozeri, and D J Wineland.
Deterministic quantum teleportation of atomic qubits.
Nature, 429:737–739, 2004.

[2] D. Stick, W. K. Hensinger, S. Olmschenk, M. J. Madsen, K. Schwab, and C. Monroe.
Ion trap in a semiconductor chip.
Nature Physics, 2:36–39, 2005.

[3] L Steffen, Y Salathe, M Oppliger, P Kurpiers, M Baur, C Lang, C Eichler, G Puebla-Hellmann, A Fedorov, and A Wallraff.
Deterministic quantum teleportation with feed-forward in a solid state system.
Nature, 500:319–322, 2013.

[4] Alberto Politi, Martin J. Cryan, John G. Rarity, Siyuan Yu, and Jeremy L. O'Brien.
Silica-on-silicon waveguide quantum circuits.
Science, 320(5876):646–649, 2008.

[5] Benjamin J. Metcalf, Justin B. Spring, Peter C. Humphreys, Nicholas Thomas-Peter, Marco Barbieri, W. Steven Kolthammer, Xian-Min Jin, Nathan K. Langford, Dmytro Kundys, James C. Gates, Brian J. Smith, Peter G. R. Smith, and Ian A. Walmsley.
Quantum teleportation on a photonic chip.
Nature Photonics, 8:770–774, 2014.

[6] Jacques Carolan, Christopher Harrold, Chris Sparrow, Enrique Martín-López, Nicholas J Russell, Joshua W Silverstone, Peter J Shadbolt, Nobuyuki Matsuda, Manabu Oguma, Mikitaka Itoh, Graham D Marshall, Mark G Thompson, Jonathan C F Matthews, Toshikazu Hashimoto, Jeremy L O'Brien, and Anthony Laing.

Universal linear optics.
Science, 349:711–716, 2015.

[7] Ranjeet Kumar, Jun Rong Ong, Marc Savanier, and Shayan Mookherjea.
Controlling the spectrum of photons generated on a silicon nanophotonic chip.
Nature Communications, 5:5489, 2014.

[8] Xiyuan Lu, Qing Li, Daron A. Westly, Gregory Moille, Anshuman Singh, Vikas Anant, and Kartik Srinivasan.
Chip-integrated visible-telecom entangled photon pair source for quantum communication.
Nature Physics, 2019.

[9] Christian Reimer, Michael Kues, Piotr Roztocki, Benjamin Wetzel, Fabio Grazioso, Brent E. Little, Sai T. Chu, Tudor Johnston, Yaron Bromberg, Lucia Caspani, David J. Moss, and Roberto Morandotti.
Generation of multiphoton entangled quantum states by means of integrated frequency combs.
Science, 351(6278):1176–1180, 2016.

[10] Ming Zhang, Lan-Tian Feng, Zhi-Yuan Zhou, Yang Chen, Hao Wu, Ming Li, Guo-Ping Guo, Guang-Can Guo, Dao-Xin Dai, and Xi-Feng Ren.
Generation of multiphoton entangled quantum states with a single silicon nanowire.
arXiv, page 1803.01641, 2018.

[11] Jeremy C. Adcock, Caterina Vigliar, Raffaele Santagati, Joshua Siverstone, and Mark Thompson.
Programmable four-photon graphy states on a silcion chip.
arXiv, page 1811.03023, 2018.

[12] Jianwei Wang, Stefano Paesani, Yunhong Ding, Raffaele Santagati, Paul Skrzypczyk, Alexia Salavrakos, Jordi Tura, Remigiusz Augusiak, Laura Mančinska, Davide Bacco, Damien Bonneau, Joshua W. Silverstone, Qihuang Gong, Antonio Acín, Karsten Rottwitt, Leif K. Oxenløwe, Jeremy L. O'Brien, Anthony Laing, and Mark G. Thompson.
Multidimensional quantum entanglement with large-scale integrated optics.
Science, 360(6386):285–291, 2018.

[13] Jianwei Wang, Stefano Paesani, Raffaele Santagati, Sebastian Knauer, Antonio A Gentile, Nathan Wiebe, Maurangelo Petruzzella, Jeremy L O rsquor Brien, John G Rarity, Anthony Laing, and Mark G Thompson.
Experimental quantum Hamiltonian learning.
Nature Physics, 13:551–555, 2017.

[14] Nicholas C Harris, Gregory R Steinbrecher, Mihika Prabhu, Yoav Lahini, Jacob Mower, Darius Bunandar, Changchen Chen, Franco N C Wong, Tom Baehr-Jones, Michael Hochberg, Seth Lloyd, and Dirk Englund.
Quantum transport simulations in a programmable nanophotonic processor.
Nature Photonics, 11:447–452, 2017.

[15] J. W. Silverstone.
Entangled light in silicon waveguides.
PhD thesis, University of Bristol, 2015.

[16] J. Wang.
Generating, manipulating, distributing and analysing light's quantum states using integrated photonic circuits.
PhD thesis, University of Bristol, 2016.

[17] Maximilian Schlosshauer.
Decoherence, the measurement problem, and interpretations of quantum mechanics.
Reviews of Modern Physics, 76(4):1267–1305, Feb 2005.

[18] Tameem Albash and Daniel A. Lidar.
Decoherence in adiabatic quantum computation.
Physical Review A, 91(6), Jun 2015.

[19] A Buzzelli, P Cabella, G de Gasperis, and N Vittorio.
Polarization of cosmic microwave background.
Journal of Physics: Conference Series, 689:012003, Feb 2016.

[20] Frank Leymann, Johanna Barzen, Michael Falkenthal, Daniel Vietz, Benjamin Weder, and Karoline Wild.
Quantum in the cloud: Application potentials and research opportunities, 2020.

[21] Arya K. Babbush R. et al Arute, F.
Quantum supremacy using a programmable superconducting processor.
Nature, 574:505–510, 2019.

[22] Philip Sibson, Chris Erven, Mark Godfrey, Shigehito Miki, Taro Yamashita, Mikio Fujiwara, Masahide Sasaki, Hirotaka Terai, Michael G. Tanner, Chandra M. Natarajan, Robert H. Hadfield, Jeremy L. O'Brien, and Mark G. Thompson.
Chip-based quantum key distribution, 2015.

[23] Philip Sibson, Jake E. Kennard, Stasja Stanisic, Chris Erven, Jeremy L. O'Brien, and Mark G Thompson.
Integrated silicon photonics for high-speed quantum key distribution, 2016.

[24] Vittorio Giovannetti, Seth Lloyd, and Lorenzo Maccone.
Advances in quantum metrology.
Nature Photonics, 5(4):222–229, Mar 2011.

[25] William Buchanan.
Public Key, pages 143–166.
2017.

[26] Percus Allon.
Computational Complexity and Statistical Physics, pages 3–61.
Oxford University Press, 2006.

[27] Lance Fortnow.
The status of the p versus np problem.
Commun. ACM, 52(9):78–86, September 2009.

[28] Nils Gura, Arun Patel, Arvinderpal Wander, Hans Eberle, and Sheueling Chang Shantz.
Comparing elliptic curve cryptography and rsa on 8-bit cpus.
In Marc Joye and Jean-Jacques Quisquater, editors, *Cryptographic Hardware and Embedded Systems - CHES 2004*, pages 119–132, Berlin, Heidelberg, 2004. Springer Berlin Heidelberg.

[29] Joshua Fried, Pierrick Gaudry, Nadia Heninger, and Emmanuel Thomé.
A kilobit hidden snfs discrete logarithm computation.
Advances in Cryptology – EUROCRYPT 2017, page 202–231, 2017.

[30] P. W. Shor.
Algorithms for quantum computation: discrete logarithms and factoring.
In *Proceedings 35th Annual Symposium on Foundations of Computer Science*, pages 124–134, 1994.

[31] Peter W. Shor.
Polynomial-time algorithms for prime factorization and discrete logarithms on a quantum computer.
SIAM Journal on Computing, 26(5):1484–1509, Oct 1997.

[32] Enrique Martín-López, Anthony Laing, Thomas Lawson, Roberto Alvarez, Xiao-Qi Zhou, and Jeremy L. O'Brien.
Experimental realization of shor's quantum factoring algorithm using qubit recycling.
Nature Photonics, 6(11):773–776, Oct 2012.

[33] A. Politi, J. C. F. Matthews, and J. L. O'Brien.
Shor's quantum factoring algorithm on a photonic chip.
Science, 325(5945):1221–1221, Sep 2009.

[34] Lieven M. K. Vandersypen, Matthias Steffen, Gregory Breyta, Costantino S. Yannoni, Mark H. Sherwood, and Isaac L. Chuang.
Experimental realization of shor's quantum factoring algorithm using nuclear magnetic resonance.
Nature, 414(6866):883–887, Dec 2001.

[35] B. P. Lanyon, T. J. Weinhold, N. K. Langford, M. Barbieri, D. F. V. James, A. Gilchrist, and A. G. White.
Experimental demonstration of a compiled version of shor's algorithm with quantum entanglement.
Phys. Rev. Lett., 99:250505, Dec 2007.

[36] Hoi-Kwong Lo, Marcos Curty, and Bing Qi.
Measurement-device-independent quantum key distribution.
Phys. Rev. Lett., 108:130503, Mar 2012.

[37] Cai W. Liu W. et al. Liao, S.
Satellite-to-ground quantum key distribution.
Nature, 549:43–47, 2017.

[38] H. J. Kimble.
The quantum internet.
Nature, 453:1023 – 1030, 2008.

[39] Charles Bennett and Gilles Brassard.
Withdrawn: Quantum cryptography: Public key distribution and coin tossing.

volume 560, pages 175–179, 01 1984.

[40] Nicolas Gisin, Grégoire Ribordy, Wolfgang Tittel, and Hugo Zbinden.
Quantum cryptography.
Reviews of Modern Physics, 74(1):145–195, Mar 2002.

[41] S. Pirandola, U. L. Andersen, L. Banchi, M. Berta, D. Bunandar, R. Colbeck, D. Englund, T. Gehring, C. Lupo, C. Ottaviani, J. Pereira, M. Razavi, J. S. Shaari, M. Tomamichel, V. C. Usenko, G. Vallone, P. Villoresi, and P. Wallden.
Advances in quantum cryptography, 2019.

[42] Daniel J. Bernstein.
Introduction to post-quantum cryptography, pages 1–14.
Springer Berlin Heidelberg, Berlin, Heidelberg, 2009.

[43] Jonathan Barrett, Lucien Hardy, and Adrian Kent.
No signaling and quantum key distribution.
Physical Review Letters, 95(1), Jun 2005.

[44] Dominic Mayers and Andrew Yao.
Quantum cryptography with imperfect apparatus, 1998.

[45] Cyril Branciard, Eric G. Cavalcanti, Stephen P. Walborn, Valerio Scarani, and Howard M. Wiseman.
One-sided device-independent quantum key distribution: Security, feasibility, and the connection with steering.
Phys. Rev. A, 85:010301, Jan 2012.

[46] Lars Lydersen, Carlos Wiechers, Christoffer Wittmann, Dominique Elser, Johannes Skaar, and Vadim Makarov.
Thermal blinding of gated detectors in quantum cryptography.
Optics Express, 18(26):27938, Dec 2010.

[47] Valerio Scarani and Christian Kurtsiefer.
The black paper of quantum cryptography: real implementation problems, 2009.

[48] Hong-Wei Li, Shuang Wang, Jing-Zheng Huang, Wei Chen, Zhen-Qiang Yin, Fang-Yi Li, Zheng Zhou, Dong Liu, Yang Zhang, Guang-Can Guo, and et al.
Attacking a practical quantum-key-distribution system with wavelength-dependent beam-splitter and multiwavelength sources.
Physical Review A, 84(6), Dec 2011.

[49] Vadim Makarov, Andrey Anisimov, and Johannes Skaar.
Effects of detector efficiency mismatch on security of quantum cryptosystems.
Physical Review A, 74(2), Aug 2006.

[50] Chi-Hang Fred Fung, Kiyoshi Tamaki, Bing Qi, Hoi-Kwong Lo, and Xiongfeng Ma.
Security proof of quantum key distribution with detection efficiency mismatch, 2008.

[51] R.P. Feynman.
Simulating physics with computers.
Int J Theor Phys, 21:467–488, 1982.

[52] Chao Song, Kai Xu, Wuxin Liu, Chui-ping Yang, Shi-Biao Zheng, Hui Deng, Qiwei Xie, Keqiang Huang, Qiujiang Guo, Libo Zhang, Pengfei Zhang, Da Xu, Dongning Zheng, Xiaobo Zhu, H. Wang, Y.-A. Chen, C.-Y. Lu, Siyuan Han, and Jian-Wei Pan.
10-qubit entanglement and parallel logic operations with a superconducting circuit.
Phys. Rev. Lett., 119:180511, 2017.

[53] Matthew Neeley, Markus Ansmann, Radoslaw C. Bialczak, Max Hofheinz, Erik Lucero, Aaron D. O'Connell, Daniel Sank, Haohua Wang, James Wenner, Andrew N. Cleland, Michael R. Geller, and John M. Martinis.
Emulation of a quantum spin with a superconducting phase qudit.
Science, 325(5941):722–725, 2009.

[54] M. H. Devoret and R. J. Schoelkopf.
Superconducting circuits for quantum information: An outlook.
Science, 339(6124):1169–1174, 2013.

[55] David D. Awschalom, Lee C. Bassett, Andrew S. Dzurak, Evelyn L. Hu, and Jason R. Petta.
Quantum spintronics: Engineering and manipulating atom-like spins in semiconductors.
Science, 339(6124):1174–1179, 2013.

[56] Xi-Lin Wang, Yi-Han Luo, He-Liang Huang, Ming-Cheng Chen, Zu-En Su, Chang Liu, Chao Chen, Wei Li, Yu-Qiang Fang, Xiao Jiang, Jun Zhang, Li Li, Nai-Le Liu, Chao-Yang Lu, and Jian-Wei Pan.

18-qubit entanglement with six photons' three degrees of freedom.
Phys. Rev. Lett., 120:260502, 2018.

[57] Xi-Lin Wang, Luo-Kan Chen, W. Li, H.-L. Huang, C. Liu, C. Chen, Y.-H. Luo, Z.-E. Su, D. Wu, Z.-D. Li, H. Lu, Y. Hu, X. Jiang, C.-Z. Peng, L. Li, N.-L. Liu, Yu-Ao Chen, Chao-Yang Lu, and Jian-Wei Pan.
Experimental ten-photon entanglement.
Physical Review Letters, 117:210502, 2016.

[58] Dik Bouwmeester, Jian-Wei Pan, Klaus Mattle, Manfred Eibl, Weinfurter, and Aton Zeilinger.
Experimental quantum teleportation.
Nature, 390:575–579, 1997.

[59] Raju Valivarthi, Marcel li Grimau Puigibert, Qiang Zhou, Gabriel H Aguilar, Varun B Verma, Francesco Marsili, Matthew D Shaw, Sae Woo Nam, Daniel Oblak, and Wolfgang Tittel.
Quantum teleportation across a metropolitan fibre network.
Nat. Photon., 10(10):676–680, 2016.

[60] M. Veldhorst, C. H. Yang, J. C. C. Hwang, W. Huang, J. P. Dehollain, J. T. Muhonen, S. Simmons, A. Laucht, F. E. Hudson, K. M. Itoh, A. Morello, and A. S. Dzurak.
A two-qubit logic gate in silicon.
Nature, 526:410–414, 2015.

[61] J. W. Silverstone, R. Santagati, D. Bonneau, M. J. Strain, M. Sorel, J. L. O'Brien, and M. G. Thompson.
Qubit entanglement between ring-resonator photon-pair sources on a silicon chip.
Nature Communications, 6:7948 EP –, Aug 2015.
Article.

[62] J.M. Hornibrook, J.I. Colless, I.D. Conway Lamb, S.J. Pauka, H. Lu, A.C. Gossard, J.D. Watson, G.C. Gardner, S. Fallahi, M.J. Manfra, and et al.
Cryogenic control architecture for large-scale quantum computing.
Physical Review Applied, 3(2), Feb 2015.

[63] S Pirandola, J Eisert, C Weedbrook, A Furusawa, and S L Braunstein.
Advances in quantum teleportation.
Nature Photonics, 9:641–652, 2015.

[64] E. Knill, R. Laflamme, and G. J. Milburn.
A scheme for efficient quantum computation with linear optics.
Nature, 409:46–52, 2000.

[65] Daniel Gottesman and Isaac L Chuang.
Demonstrating the viability of universal quantum computation using teleportation and single-qubit operations.
Nature, 402:390–393, 1999.

[66] Jeremy L. O'Brien.
Optical quantum computing.
Science, 318(5856):1567–1570, 2007.

[67] Michael A. Nielsen.
Optical quantum computation using cluster states.
Phys. Rev. Lett., 93:040503, 2004.

[68] Pieter Kok, W. J. Munro, Kae Nemoto, T. C. Ralph, Jonathan P. Dowling, and G. J. Milburn.
Linear optical quantum computing with photonic qubits.
Reviews of Modern Physics, 79(1):135–174, Jan 2007.

[69] Daniel E. Browne and Terry Rudolph.
Resource-efficient linear optical quantum computation.
Phys. Rev. Lett., 95:010501, Jun 2005.

[70] Stefanie Barz, Elham Kashefi, Anne Broadbent, Joseph F. Fitzsimons, Anton Zeilinger, and Philip Walther.
Demonstration of blind quantum computing.
Science, 335(6066):303–308, 2012.

[71] M. Fox.
Quantum Optics : An Introduction.
Oxford University Press, Incorporated, Oxford, 2006.

[72] Marlan O. Scully and M. Suhail Zubairy.
Quantum theory of radiation, page 1–45.
Cambridge University Press, 1997.

[73] Marlan O. Scully and M. Suhail Zubairy.
Coherent and squeezed states of the radiation field, page 46–71.
Cambridge University Press, 1997.

[74] Marlan O. Scully and M. Suhail Zubairy.
Quantum distribution theory and partially coherent radiation, page 72–96.
Cambridge University Press, 1997.

[75] Christopher Gerry and Peter Knight.
Coherent states, page 43–73.
Cambridge University Press, 2004.

[76] Christopher Gerry and Peter Knight.
Nonclassical light, page 150–194.
Cambridge University Press, 2004.

[77] Christopher Gerry and Peter Knight.
Nonclassical light, page 150–194.
Cambridge University Press, 2004.

[78] Peter J. Mosley, Jeff S. Lundeen, Brian J. Smith, Piotr Wasylczyk, Alfred B. U'Ren, Christine Silberhorn, and Ian A. Walmsley.
Heralded generation of ultrafast single photons in pure quantum states.
Physical Review Letters, 100(13), Apr 2008.

[79] Martin B. Plenio and S. Virmani.
An introduction to entanglement measures, 2005.

[80] V. Vedral, M. B. Plenio, M. A. Rippin, and P. L. Knight.
Quantifying entanglement.
Physical Review Letters, 78(12):2275–2279, Mar 1997.

[81] Daniel M. Greenberger, Michael A. Horne, and Anton Zeilinger.
Going beyond bell's theorem, 2007.

[82] Saikat Guha, Hari Krovi, Christopher A. Fuchs, Zachary Dutton, Joshua A. Slater, Christoph Simon, and Wolfgang Tittel.
Rate-loss analysis of an efficient quantum repeater architecture.
Physical Review A, 92(2), Aug 2015.

[83] Zheng-Da Li, Rui Zhang, Xu-Fei Yin, Li-Zheng Liu, Yi Hu, Yu-Qiang Fang, Yue-Yang Fei, Xiao Jiang, Jun Zhang, Li Li, and et al.
Experimental quantum repeater without quantum memory.
Nature Photonics, 13(9):644–648, Jun 2019.

[84] Mark Hillery, Vladimír Bužek, and André Berthiaume.
Quantum secret sharing.
Physical Review A, 59(3):1829–1834, Mar 1999.

[85] Sudhir Kumar Singh and R. Srikanth.
Generalized quantum secret sharing.
Physical Review A, 71(1), Jan 2005.

[86] Asher Peres.
Delayed choice for entanglement swapping.
Journal of Modern Optics, 47(2-3):139–143, Feb 2000.

[87] Yoon-Ho Kim, Rong Yu, Sergei P. Kulik, Yanhua Shih, and Marlan O. Scully.
Delayed "choice" quantum eraser.
Physical Review Letters, 84(1):1–5, Jan 2000.

[88] Charles H. Bennett, Gilles Brassard, and Seth Breidbart.
Quantum cryptography ii: How to re-use a one-time pad safely even if p=np.
Natural Computing, 13(4):453–458, Oct 2014.

[89] Artur K. Ekert.
Quantum cryptography based on bell's theorem.
Phys. Rev. Lett., 67:661–663, Aug 1991.

[90] Marco Lucamarini, Giuseppe Vallone, Ilaria Gianani, Paolo Mataloni, and Giovanni Di Giuseppe.
Device-independent entanglement-based bennett 1992 protocol.
Physical Review A, 86(3), Sep 2012.

[91] Anthony Laing, Valerio Scarani, John G. Rarity, and Jeremy L. O'Brien.
Reference-frame-independent quantum key distribution.
Physical Review A, 82(1), Jul 2010.

[92] C. K. Hong, Z. Y. Ou, and L. Mandel.
Measurement of subpicosecond time intervals between two photons by interference.
Physical Review Letters, 59:2044–2046, 1987.

[93] Yuanyuan Chen, Sebastian Ecker, Sören Wengerowsky, Lukas Bulla, Siddarth Koduru Joshi, Fabian Steinlechner, and Rupert Ursin.
Polarization entanglement by time-reversed hong-ou-mandel interference.
Physical Review Letters, 121(20), Nov 2018.

[94] J W Silverstone et al.
On-chip quantum interference between silicon photon-pair sources.
Nat. Photon., 8:104–108, 2013.

[95] Alexander E. Ulanov, Ilya A. Fedorov, Demid Sychev, Philippe Grangier, and A. I. Lvovsky.
Loss-tolerant state engineering for quantum-enhanced metrology via the reverse hong–ou–mandel effect.
Nature Communications, 7(1), Jun 2016.

[96] Jun Chen, Kim Fook Lee, and Prem Kumar.
Deterministic quantum splitter based on time-reversed hong-ou-mandel interference.
Phys. Rev. A, 76:031804, Sep 2007.

[97] N. Bergamasco, M. Menotti, J.E. Sipe, and M. Liscidini.
Generation of path-encoded greenberger-horne-zeilinger states.
Physical Review Applied, 8(5), Nov 2017.

[98] Imad I. Faruque, Gary F. Sinclair, Damien Bonneau, John G. Rarity, and Mark G. Thompson.
On-chip quantum interference with heralded photons from two independent micro-ring resonator sources in silicon photonics.
Opt. Express, 26(16):20379–20395, Aug 2018.

[99] William S. C. Chang.
The formation and analysis of optical waveguides, page 1–38.
Cambridge University Press, 2009.

[100] José David Doménech, Javier S. Fandiño, Bernardo Gargallo, and Pascual Muñoz.
Arbitrary coupling ratio multimode interference couplers in silicon-on-insulator, 2014.

[101] P. D. Trinh, S. Yegnanarayanan, and B. Jalali.
Integrated optical directional couplers in silicon-on-insulator.
Electronics Letters, 31(24):2097–2098, 1995.

[102] G. B. Cao, F. Gao, J. Jiang, and F. Zhang.
Directional couplers realized on silicon-on-insulator.
IEEE Photonics Technology Letters, 17(8):1671–1673, 2005.

[103] G. Hofmann D. Heinert J. Komma, C. Schwarz and R. Nawrodt.
Thermo-optic coefficient of silicon at 1550nm and cryogenic temperatures.
Appl. Phys. Lett., 101(041905), 2012.

[104] C. M. Wilkes, X. Qiang, J. Wang, R. Santagati, S. Paesani, X. Zhou, D. A. B. Miller, G. D. Marshall, M. G. Thompson, and J. L. O'Brien.
60db high-extinction auto-configured mach–zehnder interferometer.
Optics Letters, 41(22):5318, Nov 2016.

[105] D Bonneau, E Engin, K Ohira, N Suzuki, H Yoshida, N Iizuka, M Ezaki, C M Natarajan, M G Tanner, R H Hadfield, and et al.
Quantum interference and manipulation of entanglement in silicon wire waveguide quantum circuits.
New Journal of Physics, 14(4):045003, Apr 2012.

[106] W. Bogaerts, P. De Heyn, T. Van Vaerenbergh, K. De Vos, S. Kumar Selvaraja, T. Claes, P. Dumon, P. Bienstman, D. Van Thourhout, and R. Baets.
Silicon microring resonators.
Laser & Photonics Reviews, 6(1):47–73, 2012.

[107] Yunhong Ding, Christophe Peucheret, Haiyan Ou, and Kresten Yvind.
Fully etched apodized grating coupler on the soi platform with -0.58 db coupling efficiency.
Optics Letters, 39(18):5348–5350, 2014.

[108] Jianwei Wang, Damien Bonneau, Matteo Villa, Joshua W Silverstone, Raffaele Santagati, Shigehito Miki, Taro Yamashita, Mikio Fujiwara, Masahide Sasaki, Hirotaka Terai, et al.
Chip-to-chip quantum photonic interconnect by path-polarization interconversion.
Optica, 3:407–413, 2016.

[109] Daniel Llewellyn, Yunhong Ding, Imad I. Faruque, Stefano Paesani, Davide Bacco, Raffaele Santagati, Yan-Jun Qian, Yan Li, Yun-Feng Xiao, Marcus Huber, and et al.
Chip-to-chip quantum teleportation and multi-photon entanglement in silicon.
Nature Physics, 16(2):148–153, Dec 2019.

[110] Y Ding, H Ou, and C Peucheret.
Ultra-high-efficiency apodized grating coupler using fully etched photonic crystals.

Optics Letters, 38:2732–2734, 2013.

[111] William R. Clements, Peter C. Humphreys, Benjamin J. Metcalf, W. Steven Kolthammer, and Ian A. Walmsley.
An optimal design for universal multiport interferometers, 2016.

[112] Michael Reck, Anton Zeilinger, Herbert J. Bernstein, and Philip Bertani.
Experimental realization of any discrete unitary operator.
Phys. Rev. Lett., 73:58–61, Jul 1994.

[113] P. Walther, K. J. Resch, T. Rudolph, E. Schenck, H. Weinfurter, V. Vedral, M. Aspelmeyer, and A. Zeilinger.
Experimental one-way quantum computing.
Nature, 2005.

[114] Andreas Christ, Kaisa Laiho, Andreas Eckstein, Katiúscia N Cassemiro, and Christine Silberhorn.
Probing multimode squeezing with correlation functions.
New Journal of Physics, 13(3):033027, Mar 2011.

[115] Wolfgang Mauerer, Malte Avenhaus, Wolfram Helwig, and Christine Silberhorn.
How colors influence numbers: Photon statistics of parametric down-conversion.
Physical Review A, 80(5), Nov 2009.

[116] Jungsang Kim, Shigeki Takeuchi, Yoshihisa Yamamoto, and Henry H. Hogue.
Multiphoton detection using visible light photon counter.
Applied Physics Letters, 74(7):902–904, 1999.

[117] Danna Rosenberg, Adriana E. Lita, Aaron J. Miller, and Sae Woo Nam.
Noise-free high-efficiency photon-number-resolving detectors.
Phys. Rev. A, 71:061803, Jun 2005.

[118] D. Rosenberg, A. E. Lita, A. J. Miller, S. Nam, and R. E. Schwall.
Performance of photon-number resolving transition-edge sensors with integrated 1550 nm resonant cavities.
IEEE Transactions on Applied Superconductivity, 15(2):575–578, 2005.

[119] Adriana E. Lita, Aaron J. Miller, and Sae Woo Nam.
Counting near-infrared single-photons with 95% efficiency.
Opt. Express, 16(5):3032–3040, Mar ts , url = http://www.opticsexpress.org/abstract.cfm?URI=oe-16-5-3032, doi = 10.1364/OE.16.003032.

[120] Daiji Fukuda, Go Fujii, Takayuki Numata, Kuniaki Amemiya, Akio Yoshizawa, Hidemi Tsuchida, Hidetoshi Fujino, Hiroyuki Ishii, Taro Itatani, Shuichiro Inoue, and Tatsuya Zama.
Titanium-based transition-edge photon number resolving detector with 98% detection efficiency with index-matched small-gap fiber coupling.
Opt. Express, 19(2):870–875, Jan ts , url = http://www.opticsexpress.org/abstract.cfm?URI=oe-19-2-870, doi = 10.1364/OE.19.000870.

[121] Clinton Cahall, Kathryn L. Nicolich, Nurul T. Islam, Gregory P. Lafyatis, Aaron J. Miller, Daniel J. Gauthier, and Jungsang Kim.
Multi-photon detection using a conventional superconducting nanowire single-photon detector.
Optica, 4(12):1534–1535, Dec ts , url = http://www.osapublishing.org/optica/abstract.cfm?URI=o 4-12-1534, doi = 10.1364/OPTICA.4.001534.

[122] Konrad Banaszek and Ian A. Walmsley.
Photon counting with a loop detector.
Opt. Lett., 28(1):52–54, Jan ts , url = http://ol.osa.org/abstract.cfm?URI=ol-28-1-52, doi = 10.1364/OL.28.000052.

[123] M. J. Fitch, B. C. Jacobs, T. B. Pittman, and J. D. Franson.
Photon-number resolution using time-multiplexed single-photon detectors.
Phys. Rev. A, 68:043814, Oct 2003.

[124] Leaf A. Jiang, Eric A. Dauler, and Joshua T. Chang.
Photon-number-resolving detector with 10 $bits$ of resolution.
Phys. Rev. A, 75:062325, Jun 2007.

[125] Chandra M. Natarajan, Lijian Zhang, Hendrik Coldenstrodt-Ronge, Gaia Donati, Sander N. Dorenbos, Val Zwiller, Ian A. Walmsley, and Robert H. Hadfield.
Quantum detector tomography of a time-multiplexed superconducting nanowire single-photon detector at telecom wavelengths.
Opt. Express, 21(1):893–902, Jan ts , url = http://www.opticsexpress.org/abstract.cfm?URI=oe-21-1-893, doi = 10.1364/OE.21.000893.

[126] Rajveer Nehra, Chun-Hung Chang, Qianhuan Yu, Andreas Beling, and Olivier Pfister.

Photon-number-resolving segmented detectors based on single-photon avalanche-photodiodes, 2017.

[127] Brice Calkins, Paolo L. Mennea, Adriana E. Lita, Benjamin J. Metcalf, W. Steven Kolthammer, Antia Lamas-Linares, Justin B. Spring, Peter C. Humphreys, Richard P. Mirin, James C. Gates, Peter G. R. Smith, Ian A. Walmsley, Thomas Gerrits, and Sae Woo Nam.
High quantum-efficiency photon-number-resolving detector for photonic on-chip information processing.
Opt. Express, 21(19):22657–22670, Sep 2013.

[128] F. Marsili, V. B. Verma, J. A. Stern, S. Harrington, A. E. Lita, T. Gerrits, I. Vayshenker, B. Baek, M. D. Shaw, R. P. Mirin, and et al.
Detecting single infrared photons with 93% system efficiency.
Nature Photonics, 7(3):210–214, Feb 2013.

[129] Kevin Zielnicki, Karina Garay-Palmett, Daniel Cruz-Delgado, Hector Cruz-Ramirez, Michael F. O'Boyle, Bin Fang, Virginia O. Lorenz, Alfred B. U'Ren, and Paul G. Kwiat.
Joint spectral characterization of photon-pair sources.
Journal of Modern Optics, 65(10):1141–1160, Feb 2018.

[130] Borghi M. Signorini S. et al. Paesani, S.
Near-ideal spontaneous photon sources in silicon quantum photonics.
Nat Commun, 11(2505), 2020.

[131] Massimo Borghi.
Phase-resolved joint spectra tomography of a ring resonator photon pair source using a silicon photonic chip.
Optics Express, 28(5):7442, Feb 2020.

[132] Z. Vernon, M. Menotti, C. C. Tison, J. A. Steidle, M. L. Fanto, P. M. Thomas, S. F. Preble, A. M. Smith, P. M. Alsing, M. Liscidini, and et al.
Truly unentangled photon pairs without spectral filtering.
Optics Letters, 42(18):3638, Sep 2017.

[133] J. B. Christensen, J. G. Koefoed, K. Rottwitt, and C. J. McKinstrie.
Engineering spectrally unentangled photon pairs from nonlinear microring resonators by pump manipulation.
Optics Letters, 43(4):859, Feb 2018.

[134] Fumihiro Kaneda and Kwiat Paul.
High-efficiency single-photon generation via large-scale active time multiplexing.
arXiv, page 1803.04803, 2017.

[135] Damien Bonneau, Gabriel J Mendoza, Jeremy L O'Brien, and Mark G Thompson.
Effect of loss on multiplexed single-photon sources.
New Journal of Physics, 17(4):043057, Apr 2015.

[136] Mikkel Heuck, Mihir Pant, and Dirk R Englund.
Temporally and spectrally multiplexed single photon source using quantum feedback control for scalable photonic quantum technologies.
New Journal of Physics, 20(6):063046, Jun 2018.

[137] Ferenc Bodog, Matyas Mechler, Matyas Koniorczyk, and Peter Adam.
Optimization of multiplexed single-photon sources operated with photon-number-resolving detectors, 2020.

[138] Agustina G. Magnoni, Ignacio H. López Grande, Laura T. Knoll, and Miguel A. Larotonda.
Performance of a temporally multiplexed single-photon source with imperfect devices.
Quantum Information Processing, 18(10), Aug 2019.

[139] P Grünwald.
Effective second-order correlation function and single-photon detection.
New Journal of Physics, 21(9):093003, sep 2019.

[140] Xiong C. Eggleton B. et al Caspani, L.
Integrated sources of photon quantum states based on nonlinear optics.
Light Sci Appl, 6, 2017.

[141] M. Beck.
Comparing measurements of g(2)(0) performed with different coincidence detection techniques.
J. Opt. Soc., 24:2972–2978, 2007.

[142] S. Clemmen, K. Phan Huy, W. Bogaerts, R. G. Baets, Ph. Emplit, and S. Massar.
Continuous wave photon pair generation in silicon-on-insulator waveguides and ring resonators.

Optics Express, 17(19):16558, Sep 2009.

[143] J. G. Rarity, P. R. Tapster, E. Jakeman, T. Larchuk, R. a. Campos, M. C. Teich, and B. E. A. Saleh.
Two-photon interference in a mach-zehnder interferometer.
Physical Review Letters, 65(11):1348–1351, 1990.

[144] I. I. Faruque, G.F. Sinclair, D. Bonneau, J. G. Rarity, and M. G. Thompson.
On-chip quantum interference with heralded photons from two independent micro-ring resonator sources in silicon photonics.
Optics Express, 26(16):20379–20395, 2018.

[145] Massimo Borghi.
Phase-resolved joint spectra tomography of a ring resonator photon pair source using a silicon photonic chip.
Optics Express, 28(5):7442, Feb 2020.

[146] Annamaria Dosseva, Łukasz Cincio, and Agata M. Brańczyk.
Shaping the joint spectrum of down-converted photons through optimized custom poling.
Physical Review A, 93(1), Jan 2016.

[147] Francesco Graffitti, Jérémy Kelly-Massicotte, Alessandro Fedrizzi, and Agata M. Brańczyk.
Design considerations for high-purity heralded single-photon sources.
Physical Review A, 98(5), Nov 2018.

[148] J. B. Christensen, J. G. Koefoed, K. Rottwitt, and C. J. McKinstrie.
Engineering spectrally unentangled photon pairs from nonlinear microring resonators by pump manipulation.
Optics Letters, 43(4):859, Feb 2018.

[149] Daniel F. V. James, Paul G. Kwiat, William J. Munro, and Andrew G. White.
Measurement of qubits.
Physical Review A, 64(5), Oct 2001.

[150] Reinier W. Heeres, Philip Reinhold, Nissim Ofek, Luigi Frunzio, Liang Jiang, Michel H. Devoret, and Robert J. Schoelkopf.
Implementing a universal gate set on a logical qubit encoded in an oscillator.
Nature Communications, 8(1), Jul 2017.

[151] Sergey Bravyi and Alexei Kitaev.
Universal quantum computation with ideal clifford gates and noisy ancillas.
Physical Review A, 71(2), Feb 2005.

[152] Chui-Ping Yang, Shih-I Chu, and Siyuan Han.
Possible realization of entanglement, logical gates, and quantum-information transfer with superconducting-quantum-interference-device qubits in cavity qed.
Physical Review A, 67(4), Apr 2003.

[153] M. Veldhorst, C. H. Yang, J. C. C. Hwang, W. Huang, J. P. Dehollain, J. T. Muhonen, S. Simmons, A. Laucht, F. E. Hudson, K. M. Itoh, and et al.
A two-qubit logic gate in silicon.
Nature, 526(7573):410–414, Oct 2015.

[154] Charles H. Bennett, Gilles Brassard, Claude Crépeau, Richard Jozsa, Asher Peres, and William K. Wootters.
Teleporting an unknown quantum state via dual classical and einstein-podolsky-rosen channels.
Phys. Rev. Lett., 70:1895–1899, Mar 1993.

[155] Thomas Jennewein, Gregor Weihs, Jian-Wei Pan, and Anton Zeilinger.
Experimental nonlocality proof of quantum teleportation and entanglement swapping.
Physical Review Letters, 88(1), Dec 2001.

[156] Vahid Karimipour, Alireza Bahraminasab, and Saber Bagherinezhad.
Entanglement swapping of generalized cat states and secret sharing.
Phys. Rev. A, 65:042320, Apr 2002.

[157] M. Barbieri, G. Vallone, P. Mataloni, and F. De Martini.
Complete and deterministic discrimination of polarization bell states assisted by momentum entanglement.
Physical Review A, 75(4), Apr 2007.

[158] Carsten Schuck, Gerhard Huber, Christian Kurtsiefer, and Harald Weinfurter.
Complete deterministic linear optics bell state analysis.
Phys. Rev. Lett., 96:190501, May 2006.

[159] Ryo Okamoto, Jeremy L. O'Brien, Holger F. Hofmann, and Shigeki Takeuchi.

Realization of a knill-laflamme-milburn controlled-not photonic quantum circuit combining effective optical nonlinearities.
Proceedings of the National Academy of Sciences, 108(25):10067–10071, 2011.

[160] T. C. Ralph.
Scaling of multiple postselected quantum gates in optics.
Phys. Rev. A, 70:012312, Jul 2004.

[161] Qi Zhao, Gerui Wang, Xiao Yuan, and Xiongfeng Ma.
Efficient and robust detection of multipartite greenberger-horne-zeilinger-like states.
Physical Review A, 99(5), May 2019.

[162] Ryszard Horodecki, Paweł Horodecki, Michał Horodecki, and Karol Horodecki.
Quantum entanglement.
Reviews of Modern Physics, 81(2):865–942, Jun 2009.

[163] Charles H. Bennett, Herbert J. Bernstein, Sandu Popescu, and Benjamin Schumacher.
Concentrating partial entanglement by local operations.
Physical Review A, 53(4):2046–2052, Apr 1996.

[164] Sandu Popescu and Daniel Rohrlich.
Thermodynamics and the measure of entanglement, 1996.

[165] William K. Wootters.
Entanglement of formation of an arbitrary state of two qubits.
Physical Review Letters, 80(10):2245–2248, Mar 1998.

[166] Zhi-Hao Ma, Zhi-Hua Chen, Jing-Ling Chen, Christoph Spengler, Andreas Gabriel, and Marcus Huber.
Measure of genuine multipartite entanglement with computable lower bounds.
Physical Review A, 83(6):062325, 2011.

[167] Jessica Bavaresco, Natalia Herrera Valencia, Claude Klöckl, Matej Pivoluska, Paul Erker, Nicolai Friis, Mehul Malik, and Marcus Huber.
Measurements in two bases are sufficient for certifying high-dimensional entanglement.
Nature Physics, 14:1032–1037, 2018.

[168] P Erker, M Krenn, and Marcus Huber.

Quantifying high dimensional entanglement with two mutually unbiased bases.
Quantum, 1:22, 2017.

[169] Xinlun Cai, Jianwei Wang, Michael J. Strain, Benjamin Johnson-Morris, Jiangbo Zhu, Marc Sorel, Jeremy L. O'Brien, Mark G. Thompson, and Siyuan Yu.
Integrated compact optical vortex beam emitters.
Science, 338:363–366, 2012.

[170] Terry Rudolph.
Why i am optimistic about the silicon-photonic route to quantum computing.
APL Photonics, 2(3):030901, 2017.

[171] Nicola A. Tyler, Jorge Barreto, Gerardo E. Villarreal-Garcia, Damien Bonneau, Döndü Sahin, Jeremy L. O'Brien, and Mark G. Thompson.
Modelling superconducting nanowire single photon detectors in a waveguide cavity.
Opt. Express, 24(8):8797–8808, Apr 2016.

[172] Gan, Grawert, Schley, Akiyama, Michel, Wada, Kimerling, and Kartner.
Design of all-optical switches based on carrier injection in si/sio/sub 2/ split-ridge waveguides (srws).
Journal of Lightwave Technology, 24(9):3454–3463, 2006.

[173] Jason S. Pelc, Kelley Rivoire, Sonny Vo, Charles Santori, David A. Fattal, and Raymond G. Beausoleil.
Picosecond all-optical switching in hydrogenated amorphous silicon microring resonators.
Optics Express, 22(4):3797, Feb 2014.

[174] Stefano Paesani, Yunhong Ding, Raffaele Santagati, Levon Chakhmakhchyan, Caterina Vigliar, Karsten Rottwitt, Leif Oxenløwe, Jianwei Wang, Mark Thompson, and Anthony Laing.
Generation and sampling of quantum states of light in a silicon chip.
Arxiv, page 1812.03158, 2018.

[175] Justin B. Spring, Benjamin J. Metcalf, Peter C. Humphreys, W. Steven Kolthammer, Xian-Min Jin, Marco Barbieri, Animesh Datta, Nicholas Thomas-Peter, Nathan K. Langford, Dmytro Kundys, James C. Gates, Brian J. Smith, Peter G. R. Smith, and Ian A. Walmsley.
Boson sampling on a photonic chip.
Science, 339(6121):798–801, 2013.

[176] Hui Wang, Yu He, Yu-Huai Li, Zu-En Su, Bo Li, He-Liang Huang, Xing Ding, Ming-Cheng Chen, Chang Liu, Jian Qin, Jin-Peng Li, Yu-Ming He, Christian Schneider, Martin Kamp, Cheng-Zhi Peng, Sven Höfling, Chao-Yang Lu, and Jian-Wei Pan.
High-efficiency multiphoton boson sampling.
Nature Photonics, 11:361–365, 2017.

[177] Justin B. Spring, Benjamin J. Metcalf, Peter C. Humphreys, W. Steven Kolthammer, Xian-Min Jin, Marco Barbieri, Animesh Datta, Nicholas Thomas-Peter, Nathan K. Langford, Dmytro Kundys, James C. Gates, Brian J. Smith, Peter G. R. Smith, and Ian A. Walmsley.
Boson sampling on a photonic chip.
Science, 339:798–801, 2013.

[178] Han-Sen Zhong, Yuan Li, Wei Li, Li-Chao Peng, Zu-En Su, Yi Hu, Yu-Ming He, Xing Ding, Weijun Zhang, Hao Li, Lu Zhang, Zhen Wang, Lixing You, Xi-Lin Wang, Xiao Jiang, Li Li, Yu-Ao Chen, Nai-Le Liu, Chao-Yang Lu, and Jian-Wei Pan.
12-photon entanglement and scalable scattershot boson sampling with optimal entangled-photon pairs from parametric down-conversion.
Physical Review Letters, 121:250505, 2018.

[179] Joonsuk Huh, Gian Giacomo Guerreschi, Borja Peropadre, Jarrod R. McClean, and Alán Aspuru-Guzik.
Boson sampling for molecular vibronic spectra.
Nature Photonics, 9:615 –620, 2015.

[180] Marco Bentivegna, Nicolò Spagnolo, Chiara Vitelli, Fulvio Flamini, Niko Viggianiello, Ludovico Latmiral, Paolo Mataloni, Daniel J. Brod, Ernesto F. Galvão, Andrea Crespi, Roberta Ramponi, Roberto Osellame, and Fabio Sciarrino.
Experimental scattershot boson sampling.
Science Advances, 1(3):e1400255, 2015.

[181] Matthew A. Broome, Alessandro Fedrizzi, Saleh Rahimi-Keshari, Justin Dove, Scott Aaronson, Timothy C. Ralph, and Andrew G. White.
Photonic boson sampling in a tunable circuit.
Science, 339(6121):794–798, 2013.

[182] Bacco D. Dalgaard K. *et al* Ding, Y.

High-dimensional quantum key distribution based on multicore fiber using silicon photonic integrated circuits.
npj Quantum Inf, 3(25), 2017.

[183] J. S. Bell.
On the einstein podolsky rosen paradox.
Physics Physique Fizika, 1:195–200, Nov 1964.

[184] S. Massar and S. Popescu.
Amount of information obtained by a quantum measurement.
Phys. Rev. A, 61:062303, May 2000.

[185] Zurek W. Wootters, W.
A single quantum cannot be cloned.
Nature, 299(299):802–803, 1982.

[186] Leach J. Buller G. et al Dada, A.
Experimental high-dimensional two-photon entanglement and violations of generalized bell inequalities.
Nature Phys, 7(7):677–680, 2011.

[187] Reimer C. Roztocki P. et al Kues, M.
On-chip generation of high-dimensional entangled quantum states and their coherent control.
Nature, 546(546):622–626, 2017.

[188] C. Senko, P. Richerme, J. Smith, A. Lee, I. Cohen, A. Retzker, and C. Monroe.
Realization of a quantum integer-spin chain with controllable interactions.
Phys. Rev. X, 5:021026, Jun 2015.

[189] Valentina Parigi, Vincenzo D'Ambrosio, Christophe Arnold, Lorenzo Marrucci, Fabio Sciarrino, and Julien Laurat.
Storage and retrieval of vector beams of light in a multiple-degree-of-freedom quantum memory.
Nature Communications, 6(1), Jul 2015.

[190] Dong-Sheng Ding, Wei Zhang, Shuai Shi, Zhi-Yuan Zhou, Yan Li, Bao-Sen Shi, and Guang-Can Guo.
High-dimensional entanglement between distant atomic ensemble memories, 2014.

[191] Yi-Han Luo, Han-Sen Zhong, Manuel Erhard, Xi-Lin Wang, Li-Chao Peng, Mario Krenn, Xiao Jiang, Li Li, Nai-Le Liu, Chao-Yang Lu, Anton Zeilinger, and Jian-Wei Pan.
Quantum teleportation in high dimensions.
Phys. Rev. Lett., 123:070505, Aug 2019.

[192] Yonggi Jo, Hee Park, Seung-Woo Lee, and Wonmin Son.
Efficient high-dimensional quantum key distribution with hybrid encoding.
Entropy, 21(1):80, Jan 2019.

[193] S. Ristic, A. Bhardwaj, M. J. Rodwell, L. A. Coldren, and L. A. Johansson.
An optical phase-locked loop photonic integrated circuit.
Journal of Lightwave Technology, 28(4):526–538, 2010.

[194] Mark Fox.
Oxford University Press, 2006.

[195] David Gross, Yi-Kai Liu, Steven T. Flammia, Stephen Becker, and Jens Eisert.
Quantum state tomography via compressed sensing.
Phys. Rev. Lett., 105:150401, Oct 2010.

[196] A Steffens, C A Riofrío, W McCutcheon, I Roth, B A Bell, A McMillan, M S Tame, J G Rarity, and J Eisert.
Experimentally exploring compressed sensing quantum tomography.
Quantum Science and Technology, 2(2):025005, may 2017.

[197] T. *et al* Monz.
Experimental quantum compressed sensing for a seven-qubit system.
Nature Communications, 8(1):2041–1723, may 2017.

[198] Steven T Flammia, David Gross, Yi-Kai Liu, and Jens Eisert.
Quantum tomography via compressed sensing: error bounds, sample complexity and efficient estimators.
New Journal of Physics, 14(9):095022, sep 2012.

[199] Johan Löfberg.
A toolbox for modeling and optimization in matlab.
pages 284 – 289, 10 2004.

[200] Peter W. Shor and John Preskill.
Simple proof of security of the bb84 quantum key distribution protocol.
Phys. Rev. Lett., 85:441–444, Jul 2000.

[201] D. Gottesman, H. . Lo, N. Lutkenhaus, and J. Preskill.
Security of quantum key distribution with imperfect devices.
In *International Symposium onInformation Theory, 2004. ISIT 2004. Proceedings.*, pages 136–, 2004.

[202] A. R. Dixon, Z. L. Yuan, J. F. Dynes, A. W. Sharpe, and A. J. Shields.
Gigahertz decoy quantum key distribution with 1 mbit/s secure key rate.
Optics Express, 16(23):18790, Oct 2008.

[203] Shuang Wang, Wei Chen, Jun-Fu Guo, Zhen-Qiang Yin, Hong-Wei Li, Zheng Zhou, Guang-Can Guo, and Zheng-Fu Han.
2 ghz clock quantum key distribution over 260 km of standard telecom fiber.
Optics Letters, 37(6):1008, Mar 2012.

[204] Nicolas J. Cerf, Mohamed Bourennane, Anders Karlsson, and Nicolas Gisin.
Security of quantum key distribution using d-level systems.
Physical Review Letters, 88(12), Mar 2002.

[205] Hoi-Kwong Lo, Xiongfeng Ma, and Kai Chen.
Decoy state quantum key distribution.
Phys. Rev. Lett., 94:230504, Jun 2005.

[206] Manuel Erhard, Mario Krenn, and Anton Zeilinger.
Advances in high dimensional quantum entanglement, 2019.

[207] Anthony Martin, Thiago Guerreiro, Alexey Tiranov, Sébastien Designolle, Florian Fröwis, Nicolas Brunner, Marcus Huber, and Nicolas Gisin.
Quantifying photonic high-dimensional entanglement.
Phys. Rev. Lett., 118:110501, Mar 2017.

[208] Tristan Kraft, Christina Ritz, Nicolas Brunner, Marcus Huber, and Otfried Gühne.
Characterizing genuine multilevel entanglement.
Physical Review Letters, 120(6), Feb 2018.

[209] Jamie Sikora, Antonios Varvitsiotis, and Zhaohui Wei.
Minimum dimension of a hilbert space needed to generate a quantum correlation.
Physical Review Letters, 117(6), Aug 2016.

[210] Barrios C. Panepucci R. et al Almeida, V.

All-optical control of light on a silicon chip.
Nature, 431(431):1081–1084, 2004.

[211] Ying Li, Peter C. Humphreys, Gabriel J. Mendoza, and Simon C. Benjamin.
Resource costs for fault-tolerant linear optical quantum computing.
Phys. Rev. X, 5:041007, Oct 2015.

[212] A. I. Lvovsky, B. C. Sanders, and W. Tittel.
Optical quantum memory, 2010.

[213] Sean D. Barrett and Thomas M. Stace.
Fault tolerant quantum computation with very high threshold for loss errors.
Physical Review Letters, 105(20), Nov 2010.

[214] R Raussendorf, J Harrington, and K Goyal.
Topological fault-tolerance in cluster state quantum computation.
New Journal of Physics, 9(6):199–199, jun 2007.